

EVOLUTION OF COASTAL DEPOSITIONAL SYSTEMS OF THE KRKA RIVER ESTUARY IN RESPONSE TO THE LATE PLEISTOCENE-HOLOCENE SEA-LEVEL CHANGES

Smrkulj, Natalia

Doctoral thesis / Doktorski rad

2024

Degree Grantor / Ustanova koja je dodijelila akademski / stručni stupanj: **University of Zagreb, Faculty of Science / Sveučilište u Zagrebu, Prirodoslovno-matematički fakultet**

Permanent link / Trajna poveznica: <https://um.nsk.hr/um:nbn:hr:217:311125>

Rights / Prava: [In copyright](#)/[Zaštićeno autorskim pravom.](#)

Download date / Datum preuzimanja: **2025-03-01**



Repository / Repozitorij:

[Repository of the Faculty of Science - University of Zagreb](#)





University of Zagreb

Faculty of Science
Department of Geology

Natalia Smrkulj

**EVOLUTION OF COASTAL
DEPOSITIONAL SYSTEMS OF THE
KRKA RIVER ESTUARY IN RESPONSE
TO THE LATE PLEISTOCENE-
HOLOCENE SEA-LEVEL CHANGES**

DOCTORAL THESIS

Zagreb, 2024



University of Zagreb

Faculty of Science
Department of Geology

Natalia Smrkulj

**EVOLUTION OF COASTAL
DEPOSITIONAL SYSTEMS OF THE
KRKA RIVER ESTUARY IN RESPONSE
TO THE LATE PLEISTOCENE-
HOLOCENE SEA-LEVEL CHANGES**

DOCTORAL THESIS

Supervisors: Dr. Slobodan Miko

Prof. George Papatheodorou

Zagreb, 2024



Sveučilište u Zagrebu

Prirodoslovno-matematički fakultet
Geološki odsjek

Natalia Smrkulj

**RAZVOJ OBALNIH TALOŽNIH OKOLIŠA
ESTUARIJA RIJEKE KRKE TIJEKOM
KASNOPLEISTOCENSKO-
HOLOCENSKIH PROMJENA MORSKE
RAZINE**

DOKTORSKI RAD

Zagreb, 2024



Sveučilište u Zagrebu

Prirodoslovno-matematički fakultet
Geološki odsjek

Natalia Smrkulj

**RAZVOJ OBALNIH TALOŽNIH OKOLIŠA
ESTUARIJA RIJEKE KRKE TIJEKOM
KASNOPLEISTOCENSKO-
HOLOCENSKIH PROMJENA MORSKE
RAZINE**

DOKTORSKI RAD

Mentori: Dr. sc. Slobodan Miko

Prof. dr. sc. George Papatheodorou

Zagreb, 2024

This doctoral thesis was conducted at the Croatian Geological Survey (Department for Mineral Resources and Marine Geology) under the supervision of Dr. Slobodan Miko and Prof. George Papatheodorou (University of Patras) as part of the doctoral study of Geology at the Faculty of Science, University of Zagreb. This research was fully supported by the Croatian Science Foundation, grants: „Young Researchers' Career Development – Training New Doctoral Students“ (DOK-01-2020) and Project “Sediments between source and sink during a Late Quaternary eustatic cycle: The Krka river and the Mid Adriatic Deep System” (QMAD) (HRZZ IP-04-2019-8505), under the mentorship of Dr. Slobodan Miko.

Some of the doctoral thesis data are published in the following articles:

Hasan, O., Smrkulj, N., Miko, S., Brunović, D., Ilijanić, N. & Šparica Miko, M. (2023): Integrated Reconstruction of Late Quaternary Geomorphology and Sediment Dynamics of Prokljan Lake and Krka River Estuary, Croatia. // *Remote sensing*, 15 (10), <https://doi.org/10.3390/rs15102588>, 2588 doi:10.3390/rs15102588.

Smrkulj, N., Hasan, O., Brunović, D., Miko, S., Ilijanić, N. (2024): Holocene palaeoenvironmental development of Prokljan Lake (Krka River, Croatia): Evolution from a calcareous tufa barrier system to a karst estuary. // *Marine Geology*, 476, <https://doi.org/10.1016/j.margeo.2024.107370>.

Acknowledgments

Over the four years of this research, I have had the privilege of working and meeting with a wide range of people, all of whom have benefitted my PhD.

First and foremost, I would like to thank my supervisor, Dr. Slobodan Miko, for his guidance, knowledge, many many ideas, constructive criticism, and support throughout my PhD. For allowing me to work on his Project and with its amazing, hardworking team, especially Dr. Ozren Hasan, Dr. Dea Brunović and Dr. Nikolina Ilijanić, who all helped me in overcoming many scientific fields that include geophysics, marine geology, sedimentology, and geochemistry. I am grateful for their help.

I am also very grateful to Prof. George Papatheodorou (University of Patras) for taking on the role of the secondary supervisor and his Oceanus-Lab team for discussions, for the kind words, enjoyable fieldwork, and seismic equipment and software, without which one part of this research would not have been possible. I want to thank Dr. Maria Geraga, Dr. Dimitris Christodoulou, Maria Papakonstantinou, and Alexandros Menegatos for their fieldwork help and geophysical interpretation and for making me comfortable during my stay in Patras.

I want to thank my thesis committee members Prof. Hana Fajković, Dr. Igor Felja and Dr. Ozren Hasan for their insightful comments and suggestions, which helped to improve this work. I would also like to thank my academic advisor, Prof. Hana Fajković, who helped me with all administrations regarding my doctoral study.

I am very thankful to my colleagues from the Department for Mineral Resources and Marine Geology and Croatian Geological Survey for their wonderful collaboration and discussions, especially my „roommates“ Ivona Ivkić Filipović and Petra Hus for their help, performing micropalaeontological analyses and inspiring conversations during coffee time. I would like to acknowledge Msc. Martina Šparica Miko for CN analysis, Msc. Anamaria Heski for particle size analysis, Dr. Valentina Hajek Tadesse for performing the ostracod analysis, and Hrvoje Burić and Marko Copic, who helped during the fieldwork. I would like to thank Dr. Ivan Razum (Croatian Natural History Museum) for help during fieldwork and statistical analysis.

I want to express my sincere gratitude to Dr. Michael Strasser, Dr. Jyh-Jaan Steven Huang, and Msc. Marcel Ortler of the Austrian Core Facility laboratory (University of Innsbruck) for their help during the XRF analysis.

Finally, I would like to express my deepest gratitude to my huge Family, consisting of two-legged and four-legged members. To my father, mother, brother, and husband, Viktor, for providing me with unconditional love, sacrifices, and support throughout my life. To put up with me throughout my PhD. I would like to extend my gratitude to my beloved Pomeranians, Chester (I miss you terribly every single day), Ellie, Amidala, Aurora, Pjenko, Baileys, Lily, Vulpix, and Porsche. Their unwavering companionship, boundless energy, and unconditional love have been constant sources of joy, happiness, and comfort throughout this journey. Their loyal presence has provided much-needed breaks. Thank you, my furry loves, for always being there for me. Therefore, I dedicate this thesis to my family.

BASIC DOCUMENTATION CARD

University of Zagreb
Faculty of Science
Department of Geology

Doctoral Thesis

EVOLUTION OF COASTAL DEPOSITIONAL SYSTEMS OF THE KRKA RIVER ESTUARY IN RESPONSE TO THE LATE PLEISTOCENE-HOLOCENE SEA-LEVEL CHANGES

NATALIA SMRKULJ

Croatian Geological Survey, Sachsova 2, 10 000 Zagreb

Abstract: Climate and sea-level changes strongly controlled the evolution of shallow coastal settings worldwide during the Quaternary Period. The shallow coastal region has been subjected to repeated alternations between the subaerial and marine conditions. The Krka River mouth area located in central Dalmatia along the microtidal Eastern Adriatic coast represents a suitable environmental setting for studying palaeoenvironments and relative sea-level changes. An evolutionary model of the Krka River coastal depositional system was reconstructed by combining high-resolution acoustic methods and a multiproxy analysis of sediment cores. The acoustic methods (bathymetrical and seismic studies) provided insight into the submerged geomorphology and up to 30 m thick sediment sequences preserved in the study area. The multiproxy analysis was conducted on six sediment cores and included physical, sedimentological, geochemical, and micropalaeontological analyses supported by 24 radiocarbon dates (^{14}C) to obtain data on benthic communities, hydrological, and depositional processes related to sea level and climatic conditions and timing of events. The results indicated fluvial incision and sediment bypass towards the shelf area during the period of low sea level (lowstand), whereas during the transgressive phase, the shelf area and subsequently the River canyon were flooded. A system of calcareous tufa barriers started to form in the upstream tract of the recent Krka River estuary. The calcareous tufa barrier system, together with sea-level and climate oscillations, had the main influence on the palaeoenvironmental development of the area. The Holocene sea-level rise progressively flooded the tufa barriers with the formation of estuarine conditions during the Late Holocene. Human activity intensified after 600 cal yr BP.

Keywords: karst estuary, Krka River, sea-level changes, palaeoenvironmental changes, seismic stratigraphy, Eastern Adriatic Coast, late Pleistocene-Holocene

Thesis contains: 287 pages, 106 figures, 35 tables, 6 appendices, 2 plates and 305 references.

Original in: English

Thesis deposited in: Library of the Croatian Geological Survey, National and University Library in Zagreb and Central Library of Department of Geology, Faculty of Science

Supervisors: Dr. Slobodan Miko, Prof. George Papatheodorou

Reviewers: Prof. Hana Fajković

Dr. Igor Felja

Dr. Ozren Hasan

Thesis accepted: 11.10.2024.

TEMELJNA DOKUMENTACIJSKA KARTICA

Sveučilište u Zagrebu
Prirodoslovno-matematički fakultet
Geološki odsjek

Doktorska disertacija

RAZVOJ OBALNIH TALOŽNIH OKOLIŠA ESTUARIJA RIJEKE KRKE TIJEKOM KASNOPLEISTOCENSKO-HOLOCENSKIH PROMJENA MORSKE RAZINE

NATALIA SMRKULJ

Hrvatski geološki institut, Sachsova 2, 10 000 Zagreb

Sažetak: Klimatske promjene te promjene morske razine tijekom kvartara znatno su utjecale na evoluciju obalnih okoliša. Plitka obalna područja pod utjecajem su stalnih izmjena kopnenih i marinskih uvjeta. Područje ušća rijeke Krke koje se nalazi u središnjoj Dalmaciji na Istočnoj jadranskoj obali, predstavlja pogodno područje za istraživanje paleookolišnih promjena te relativnih promjena morske razine. Primjenom visoko-rezolucijskih akustičnih metoda te „multiproxy“ analizom sedimentnih jezgri rekonstruiran je evolucijski model taložnih obalnih okoliša rijeke Krke. Akustične metode (batimetrijska i seizmička istraživanja) dale su uvid u potopljenu geomorfologiju istraživnog područja te u sedimentnu sekvencu debljine otprilike 30 m. „Multiproxy“ analiza provedena je na 6 sedimentnih jezgri, a uključivala je fizičke, sedimentološke, geokemijske i mikropaleontološke analize kako bi se dobili rezultati o bentičkim zajednicama, hidrološkim i taloženim procesima koji ukazuju na promjene morske razine te klimatske uvjete. Kronologija jezgri zasnivala se na datiranju 24 uzorka metodom radioaktivnog ugljika (^{14}C). Rezultati su ukazali na riječno usijecanje te transport sedimenta na područje šelfa tijekom razdoblja niske razine mora, dok tijekom transgresije dolazi do potapanja šelfnog područja, a uzvodno na području današnjeg estuarija formirao se sustav sedrenih barijera. Sedrene barijere, u kombinaciji s oscilacijama morske razine i klime, imale su glavnu ulogu na paleookolišni razvoj područja. Porast morske razine tijekom holocena uzorkuje potapanje sedrenih barijera te formiranje estuarijskih uvjeta tijekom kasnog holocena. U posljednjih 600 godina u estuarijskim sedimentima zabilježena je pojačana antropogena aktivnost i erozija sliva rijeke Krke.

Ključne riječi: krški estuarij, rijeka Krka, promjene morske razine, paleookolišne promjene, seizmička stragrafija, Istočna jadranska obala, kasni Pleistocen-Holocen

Rad sadrži: 287 stranica, 106 slika, 35 tablica, 6 priloga, 2 table i 305 literaturnih navoda.

Jezik izvornika: engleski

Rad je pohranjen u: knjižnici Hrvatskog geološkog instituta, Nacionalnoj i sveučilišnoj knjižnici u Zagrebu, te Središnjoj knjižnici Geološkog odsjeka Prirodoslovno-matematičkog fakulteta.

Mentori: Dr. sc. Slobodan Miko, Prof. dr. sc. George Papatheodorou

Ocjenjivači: Izv. prof. dr. sc. Hana Fajković

Doc. dr. sc. Igor Felja

Dr. sc. Ozren Hasan

Rad prihvaćen: 11.10.2024.

TABLE OF CONTENTS

1. INTRODUCTION	1
2. LITERATURE OVERVIEW	3
2.1 River mouths	3
2.2 Climate and sea-level changes during the Quaternary	14
2.2.1 Last Glacial sea-level and climate changes in the Adriatic	15
3. STUDY AREA	20
3.1 Morphology and geology of the Krka River watershed area	22
3.2 Krka River estuary, Prokljan Lake and the continental shelf area	26
4. MATERIALS AND METHODS	29
4.1 Fieldwork surveys	29
4.1.1 High-resolucional acoustic methods	29
4.1.2 Sediment sampling.....	35
4.2 Laboratory analyses	38
4.2.1 Grab samples and sediment cores.....	38
4.2.2 Radiocarbon dating.....	42
4.2.3 Color Spectrophotometry and Munsell color system.....	46
4.2.4 Gamma Density.....	47
4.2.5 Magnetic Susceptibility.....	47
4.2.6 Inorganic elemental analysis (ITRAX XRF core scanner and ICP-MS)	48
4.2.7 Stable isotope geochemistry and organic elemental analysis.....	51
4.2.8 Particle size analysis.....	55
4.2.9 Mineralogical analysis.....	56
4.2.10 Foraminiferal and ostracod analysis.....	58
4.2.11 Data analysis	60
5. RESULTS	62
5.1 Description of seafloor geomorphology in study areas.....	62
5.1.1 Krka River estuary	62
5.1.2 Middle Adriatic shelf area.....	73
5.2 Seismic stratigraphy	78
5.2.1 Krka River estuary	78
5.2.2 Middle Adriatic shelf area.....	91
5.3 Lithostratigraphy.....	101
5.3.1 Chronology.....	105

5.3.2 Initial core description and physical properties	107
5.3.3 Particle size analysis.....	115
5.3.4 Mineralogical analysis.....	130
5.3.5 Geochemical analysis.....	133
5.3.6 Organic elemental analysis and stable isotope geochemistry	155
5.3.7 Micropalaeontological analysis.....	169
6. DISCUSSION	182
6.1 Acoustic and core data interpretation of the Pleistocene Krka River incised valley and deltaic deposits	182
6.2 Acoustic and core data interpretation of the Krka River estuary.....	194
6.3 Seabed sediment composition, dynamics and assessment of human impact.....	208
6.3.1 Geochemical record of environmental change during the past 600 years caused by human activities	215
6.3.2 Anthropogenic influence on heavy metal contents in the past 150 years.....	216
6.4 Late Quaternary palaeoenvironmental history of the Krka River mouth area in response to sea-level fluctuations: From a river valley to a karst estuary.....	219
7. CONCLUSIONS	236
8. EXTENDED ABSTRACT.....	239
9. REFERENCES.....	242
10. APPENDICES.....	279
11. CURRICULUM VITAE	284

LIST OF ABBREVIATIONS

EAC	Eastern Adriatic Coast
LGM	Last Glacial Maximum
kyr	kiloyears
BP	before present
MBES	Multibeam echosounder
SSS	Sidescan sonar
SBP	Subbottom profiler
PSA	Particle size analysis
MS	Magnetic susceptibility
TC	Total carbon
TOC	Total organic carbon
TN	Total nitrogen
TIC	Total inorganic carbon
IR	Insoluble residue
MSCL	Geotek Multi-Sensor Core Logger
XRF	X-Ray Fluorescence
AMS	Accelerated Mass Spectrometry
cal	calendar age
ICP-MS	Inductively coupled plasma atomic emission spectroscopy
VSMOW	Vienna Standard Mean Ocean Water
VPDB	Vienna Pee Dee Belemnite
OM	Organic matter
TOC/TN	Total organic carbon to total nitrogen ratio
XRD	X-ray diffraction
PCA	Principal component analysis
EF	Enrichment factor
bsl	below sea level
OBIA	Object-Based Image Analysis
TWTT	Two-way travel time
LIA	Little Ice Age

1. INTRODUCTION

Climate and sea-level changes controlled the evolution of shallow coastal settings worldwide during the Quaternary period. The shallow coastal region has been subjected to repeated alternations between the subaerial and marine conditions. Typical environments in coastal and shelf regions include incised valley systems, estuaries, and deltas. These settings develop during transgressive-regressive cycles of sea-level change, where the incised valleys form during the relative sea-level fall with a river incision and formation of fluvially eroded palaeogeographic lows, and estuaries and deltas form when these valleys are flooded and infilled with sediment during subsequent relative sea-level rise (Zaitlin et al., 1994; Posamentier and Allen, 1999; Blum et al., 2013). Additionally, present-day estuaries are of considerable economic and ecological importance because large cities, ports, industries, and human populations are situated in these environments, which are strongly related to ongoing sea-level changes (Kennish, 2016). Therefore, these environments provide important archives of stratigraphic information on environmental, sea-level, and climatic changes in coastal regions (Dalrymple et al., 1992).

The Adriatic Sea also experienced significant environmental change during the Quaternary period. Since most of the Adriatic is shallow, with depths less than 100 m, sea level and climate changes have greatly influenced its evolution (Correggiari et al., 1996). These changes have been well-studied through numerous research efforts along the Western Adriatic Coast (Alberico et al., 2017), where vertical repetitions of transgressive-regressive cycles and the development of larger river systems occur (e.g., Correggiari et al., 1996; Amorosi et al., 2016; Trobec et al., 2017; Pellegrini et al., 2018; Ronchi et al., 2018). However, along the Eastern Adriatic Coast (EAC), such studies have been lacking, despite the increasing number of recent studies that have shown a different palaeoenvironmental development. Thus, the Western and Eastern Adriatic coasts are geomorphologically very different. The EAC is characterized by intense karst processes and limited sediment supply to the sea (Surić, 2002). Unlike the rivers along the western coast, karst river mouths along the EAC have developed specific karst salt-wedge estuaries or intra-estuarine deltas if the sediment supply is somewhat greater (Pikelj and Juračić, 2013; Felja, 2017; Hasan, 2017; Hasan et al., 2023; Smrkulj et al., 2024).

The fundamental purpose of this research is to provide a detailed geomorphological reconstruction and informations on palaeoenvironmental changes of the Krka River during the global eustatic rise that followed the Last Glacial Maximum (LGM), through geophysical investigations and multi-proxy analyses of sediment cores. To achieve this general objective, the specific objectives of this research are summarized as follows.

1. To describe submerged landscapes and geomorphology of the study area based on geophysical data
2. To determine the Late Quaternary stratigraphic sequence and palaeoenvironmental changes of the study area based on sedimentological and seismic data
3. To analyze the evolution of stratigraphic infill in the context of sea-level changes and changes in palaeoenvironments and palaeohydrology of the study area
4. To determine the main processes that influenced the evolution and stratigraphy of the study area
5. To determine the timing of marine flooding in the study area and the timing of the formation of recent estuarine conditions
6. To reconstruct the relative sea-level changes of the study area and to compare them with other research data along the EAC
7. To determine the potential anthropogenic influence on estuarine sediments.

The research hypotheses are as follows:

During the last low sea-level stage (30–19 kyr BP (kiloyears before present)), the Krka River originated as an incised valley with a developed delta at its river mouth. With postglacial sea-level rise, the Krka River mouth area was flooded by the sea with the development of estuarine environments during the Holocene. During the late Holocene, present estuarine conditions commenced. Climate and sea-level changes, and calcareous tufa deposition, controlled the sedimentation in the study area. Multiproxy analyses of sediment cores coupled with geophysical data enable the determination of palaeoenvironmental changes and anthropogenic influence in the present-day Krka River mouth area.

2. LITERATURE OVERVIEW

The second chapter provides an overview of the published literature on the research topics explored in this work: 1) an overview of the morphology, architecture, and sedimentology of incised valleys, estuaries, and deltas; external processes (such as sea-level changes, climate, and tectonics) that influence these environments; the evolution of estuarine systems along the EAC; and 2) an overview of sea-level research during the Last Glacial in the Adriatic.

2.1 River mouths

River mouths encompass the lower part of a river's course (often a developed delta) and coastal areas where sediment deposition predominates. The hydrological regime in this area is complex and variable, with a combination of different physical, chemical, and biological properties. Owing to such hydrological conditions, various geomorphological forms and areas with alternating fluvial, marine, and lacustrine sediments can arise. Additionally, these areas harbor typical flora and fauna that are highly ecologically sensitive (Dalrymple et al., 1994).

Estuaries, deltas, and incised valleys, as well as their sedimentary infills, represent one of the most economically and ecologically important coastal environments. They develop at river mouths during transgressive-regressive cycles, and their evolution is mainly controlled by climate and relative sea-level changes and sediment supply (Boyd et al., 1992). Regarding their locations at land-sea transition and numerous processes (fluvial, estuarine, and marine) that influence their formation and infill, they are considered one of the most geomorphologically complex coastal environments (Boyd et al., 1992; Zaitlin et al., 1994). Therefore, the classification of coastal environments is very complex, and the most effective method to classify these environments is to use a subdivision into regressive and transgressive categories based on the dominant coastal processes (Boyd et al., 1992; Fig. 2.1). The most recent development in coastal models involves facies models, that is, sequence stratigraphy (Mitchum et al., 1977; Posamentier and Vail, 1988), which places the coastal facies in a classification defined by transgressive and regressive stacking geometries and relative sea-level variations.

When the rate of sediment supply exceeds the rate of relative sea-level rise or sediment accumulates during a relative sea-level fall, regression results, and deltaic

environments (lobate shoreline) or tidal flat forms (linear shoreline) (Fig. 2.1). Transgression occurs when the rate of relative sea-level rise exceeds the rate of sediment supply and the formation of estuaries and lagoons occur (Dalrymple et al., 1992) (Fig. 2.1).

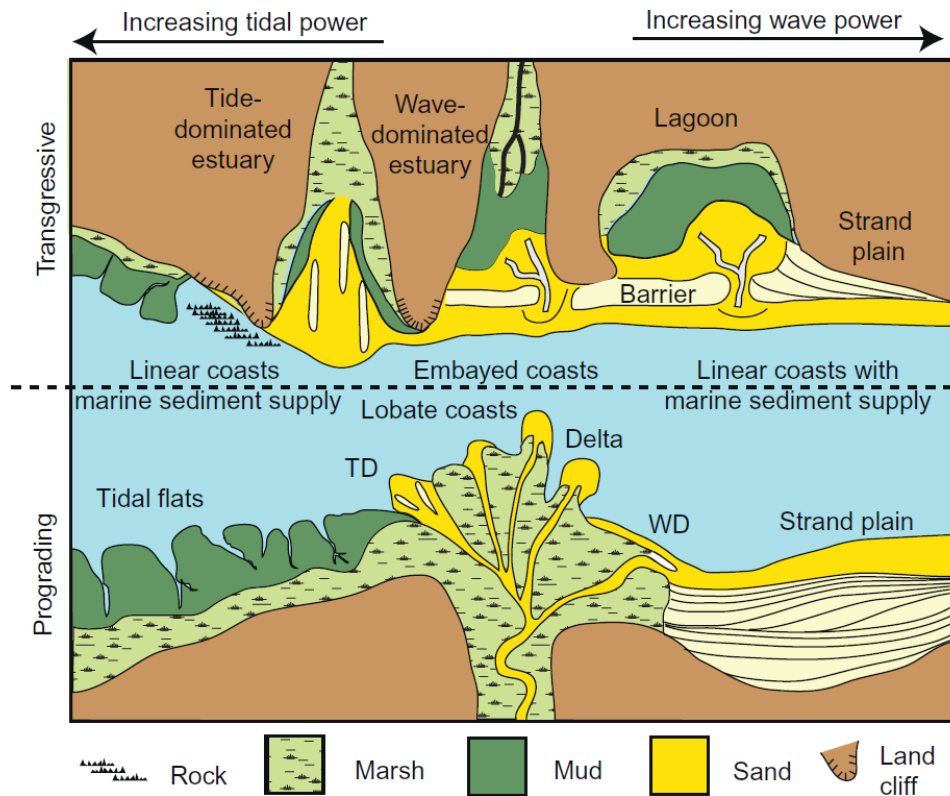


Figure 2.1 Transgressive and progradational geomorphological environments (Harris, 2012).

Fluctuations at the base level, in combination with different coastal and upstream factors, can result in vertical river incision and the creation of deep incised valleys. An incised valley is defined as "a fluvially eroded, elongate topographic low that is larger than a single channel form, and is characterised by an abrupt seaward shift of depositional facies across a regionally mappable sequence boundary at its base. The fill typically begins to accumulate during the next base-level rise, and may contain deposits of the following highstand and subsequent sealevel cycles" (Zaitlin et al., 1994).

Incised-valley systems are common features in coastal and shelf regions. They are characterized by their elongated shape and often lack significant flooding from smaller tributaries due to the valley's depth. A fundamental aspect of incised valleys is their formation during the two episodes. The first is incision during the relative base-level lowering (lowstand

period) and erosion with the formation of a basal erosional surface, which is considered a sequence boundary (Posamentier and Vail, 1988; Van Wagoner et al., 1990). During that period, regressive facies (terrestrial sediment) were deposited at their base overlying the distal facies (marine), or a bypass of sediment through the valley occurred, and the sediment was deposited at the lowstand coastline. Thus, incised valleys play a significant role in transporting sediments from terrestrial areas to deep marine environments, facilitating the formation of lowstand deltas (shelf-edge deltas) or basin-floor fans during periods of low relative sea level (Mitchum et al., 1977; Van Wagoner et al., 1990; Posamentier, 2001; Blum and Törnqvist, 2000).

Shelf-margin or shelf-edge deltas are prominent features on Quaternary shelves related to falling and lowstand sea level (Fig. 2.2). The shelf edge is considered a key environment in which to determine the influence of sea-level changes on shelf-margin sedimentation (Lobo et al., 2005) since these environments are significant for identifying the palaeo shelf edge (formed at the morphologic shelf break), which in modern systems is recorded at water depths from 20 to over 200 m (Emery, 1981). Additionally, they offer insight into the distribution of significant volumes of sediment between the shelf edge, slope, and basin-floor settings (Porębski and Steel, 2003).

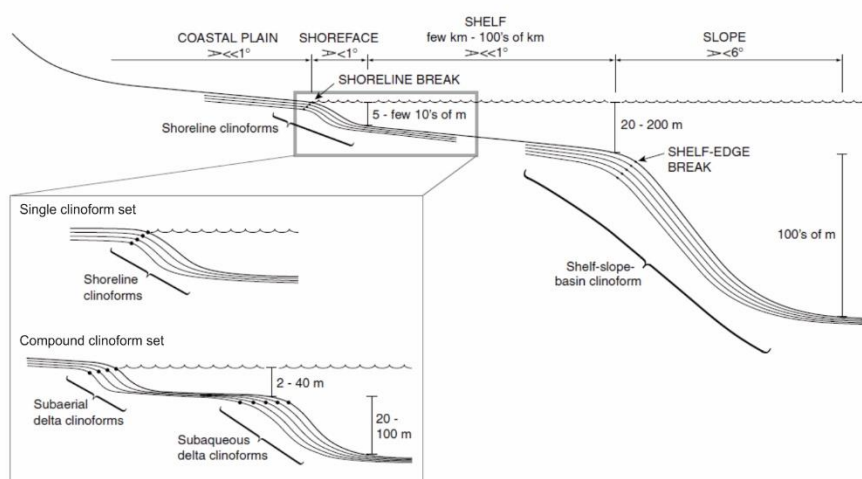


Figure 2.2 Regional cross-section of continental shelf highlighting slope characteristics, deltaic shoreline clinoforms and shelf-edge clinoforms (Adapted from Helland-Hansen and Hampson, 2009).

These shelf-margin deltas typically create extensive (tens of kilometers), elevated (hundreds of meters), and steep (3–6°) clinoforms (Figs. 2.2, and 2.3), which often form elongated wedges that initially thicken basinward just beyond the shelf edge (Porębski and Steel, 2003). As these deltas approach the shelf edge, their foresets downlap onto the existing outer shelf surface (Trincardi and Field, 1991). Below the shelf edge, the deltaic foresets become longer, steeper (3–6°), and more susceptible to turbidite deposition, downlapping onto the pre-existing slope of the shelf margin. The clinoform series resulting from this transition from outer-shelf to shelf-margin deltas typically exhibit a horizontal-to-downward trajectory, whereas in the most distal segments, a pattern of aggrading to backstepping occurs as the relative sea level starts to rise. Atop the shelf-edge wedges, an erosional unconformity develops at the beginning of sea-level fall. Clinoforms, particularly at or below the shelf margin, are discontinuous and discordant with wedge-shaped units of chaotic, mounded, and transparent seismic facies, interpreted as mass gravity processes that cause re-sedimentation, that is, gravity-driven soft-sediment deformation (Porębski and Steel, 2003; Helland-Hansen and Hampson, 2009). Shelf-edge deltas often transition landward and connect to a network of submerged river channels (incised valleys or delta distributary channels; Porębski and Steel, 2003).

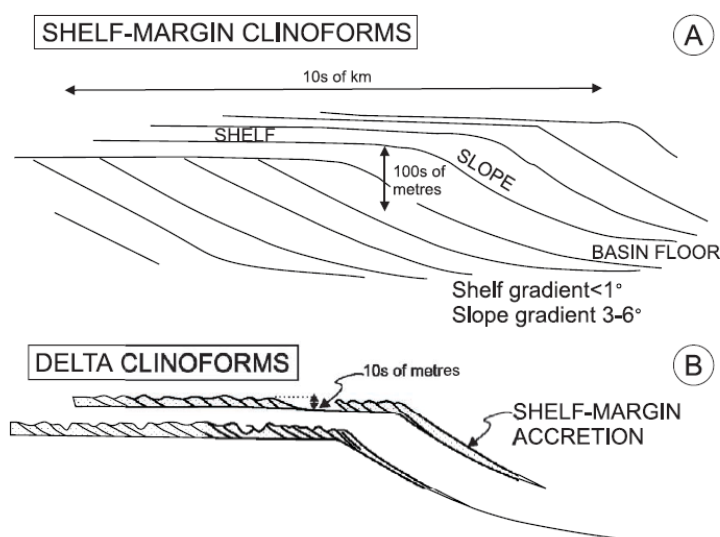


Figure 2.3 Differentiation between shelf-edge clinoforms and prograding shelf delta (modified after Porębski and Steel, 2003).

The subsequent flooding of lowstand deltas and incised valleys and their infill occur during the base level rise, with deposition of marine facies on top of the terrestrial (regressive) facies and the formation of estuaries or deltas (Zaitlin et al., 1994; Boyd et al., 2006). Incised valleys are characterized by a mixture of sedimentary facies, including terrestrial, estuarine, and marine deposits, which vary greatly.

Palaeovalley systems can be categorized into four main types (Fig. 2.4 A, B) based on their location within source-to-sink systems and the dominant processes that influence them: bedrock, mixed bedrock-alluvial, coastal-plain, and cross-shelf incised valleys (Blum et al., 2013). The bedrock-alluvial segments are incised and cut across bedrock, which is of significantly older age and displays an overall degradational structure, while the coastal plain and cross-shelf valleys form during the relative sea-level fall as river systems cut through the shelf area and extend basinward. The coastal-plain and cross-shelf segments mainly form in response to a relative sea-level fall (Fig. 2.4 C, D). Following incision and cross-shelf expansion, lateral migration of channels and concurrent deposition of channel belts result in the formation of valley-scale features. The physiography of incised valleys can be divided into two types according to Zaitlin et al. (1994): piedmont incised-valley systems (linked to steep mountainous areas) and coastal-plain incised-valley systems (restricted to low-gradient coastal areas). The piedmont-type incised valley is influenced by structural factors and exhibits a stronger fluvial impact and numerous sea-level fluctuations. In contrast, the coastal-plain incised valley is very sensitive to coastal processes and changes due to shifts in the coastline position (Boyd et al., 2006).

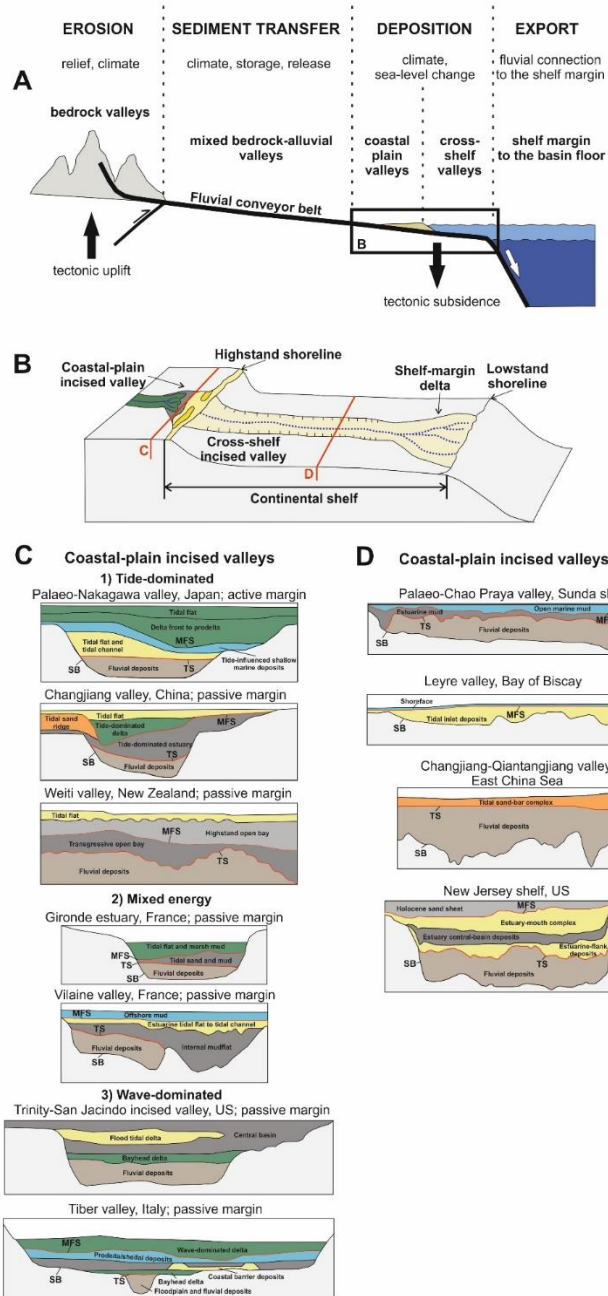


Figure 2.4 A Sketch depicts the classification of fluvial valley systems, highlighting the predominant processes and controls from the source region to the depositional basin. The Inset sketch shows the placement of coastal-plain incised valleys and cross-shelf incised valleys in a plan-view profile. C, D Illustrative stratigraphic configurations of incised valley infills along some of the late-Quaternary coastal-plain and cross-shelf valley infills (redrawn from Wang, 2020; Wang et al., 2020; A originally from Blum and Hattier-Womack, 2009).

According to their sedimentary infill, incised valleys can be classified as simple or compound depending on the identification of one or more sequence boundaries (Zaitlin et al., 1994). Simple fill corresponds to a single cycle of base-level change and incised valley infilling. A compound fill is the result of multiple cycles of base level change and with the

recognition of multiple sequence boundaries (similar physiography and sedimentary infill have the eastern Adriatic rivers). Generally, piedmont incised-valleys systems show a compound fill, whereas coastal-plain incised-valley systems tend to have a simple fill (Zaitlin et al., 1994).

Classical facies models (e.g., Dalrymple et al., 1992; Allen and Posamentier, 1993; Zaitlin et al., 1994) regarding incised-valley deposits often associate the sedimentary infills within valleys with the development of estuarine facies sequences (Fig. 2.5). These sequences typically emerge during shoreline transgression, which corresponds to an increase in relative sea level.

Zaitlin et al. (1994) proposed a conceptual facies model for incised valley fill based on a longitudinal distribution of environments divided into three segments that reflect several phases of development, such as erosion, deposition and progradation (Fig. 2.6). The outer incised valley (seaward segment) is characterized by deposition of fluvial and estuarine deposits (lowstand to transgressive) at the valley mouth, overlain by marine sediment (transgressive). The middle incised valley consists of a drowned-valley estuarine complex, that is, at the basal sequence, a deposition of fluvial sediments occurs during the lowstand or early transgression and is overlaid by a typical estuarine deposition (Dalrymple et al., 1992). The inner incised valley (landward segment) extends inland from the estuarine–marine limit, and this part of the river valley is isolated from the influence of relative sea-level changes (completely fluvial); however, the fluvial style can change with changes in the base level. In this incised valley segment the climatic, tectonic and sediment supply factors are more pronounced and control fluvial deposition.

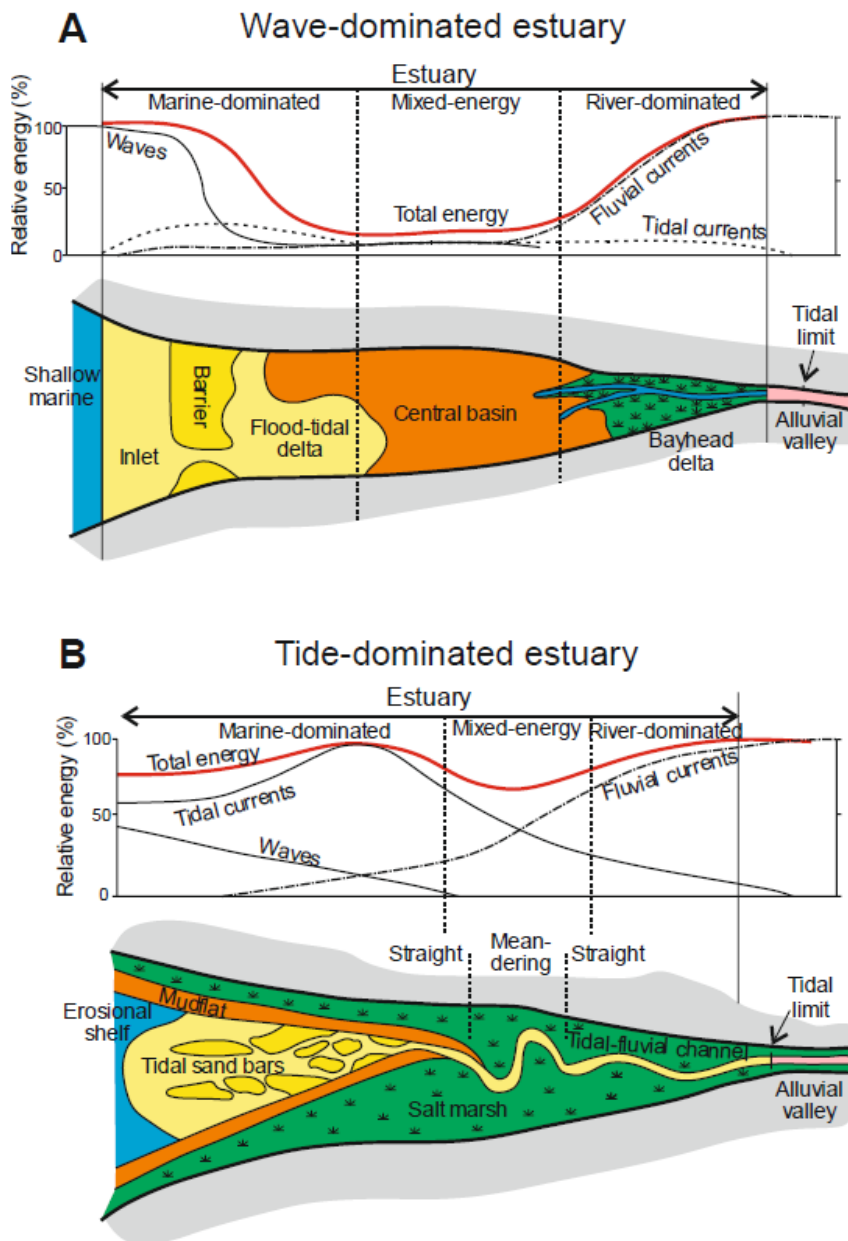


Figure 2.5 A Energy distribution and morphological components of a wave-dominated estuary. B Energy distribution and morphological components of a tide-dominated estuary (Wang, 2020).

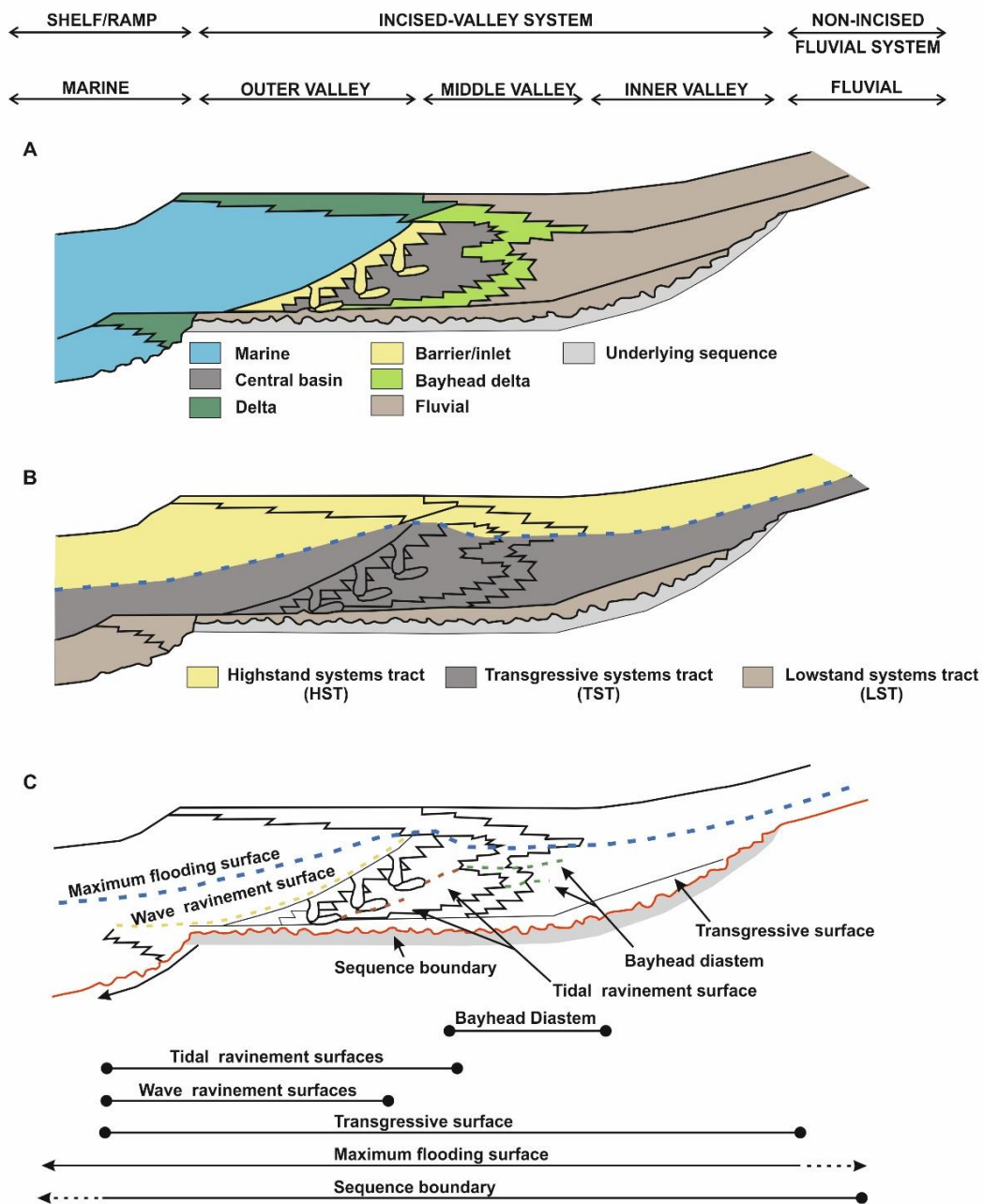


Figure 2.6 Longitudinal section of a simple incised valley. Distribution of (A) sedimentary environments within the incised-valley, (B) system tracts and (C) stratigraphic surfaces (modified after Boyd et al. (2006), originally from Zaitlin et al. (1994).

Estuaries generally meet the criteria outlined above, and the study of both estuaries and incised-valleys is linked. Therefore, the study of estuarine facies is typically approached from an incised valley perspective by applying conceptual models (for example, Dalrymple et

al., 1992; Allen and Posamentier, 1993; Boyd et al., 2006; Chaumillon et al., 2008; Chaumillon et al., 2010).

Estuaries are considered submerged river mouths, or semi-enclosed coastal water bodies connected to the sea, within which the water is brackish (Kennish, 2016), and both fluvial and marine sediment inputs are present (Dalrymple et al., 1992). Geographically, estuaries are usually sheltered coastal areas that are less exposed to marine influence than other river mouths. Additionally, wave impact is reduced, allowing for the development of large ports and industries in these areas. They can typically be divided into three parts based on environmental energy, morphology, and sediment type, namely: upper or fluvial estuary, middle or central estuary, and lower or marine estuary (Dalrymple et al., 1992). The upper estuary is predominantly influenced by the river and daily tides, with the fluvial influence weakening towards the sea. In the central estuary, there is an intense mixing of fresh water and saltwater, meaning that both tides and rivers have a strong influence. The lower estuary is predominantly under marine influence with strong tidal and wave impacts (Masselink and Hughes, 2014). The inner and outer estuaries are the most energetic parts of the estuary with the highest sediment transport.

Today, there are numerous classifications and divisions of estuaries based on physical and geological characteristics, dominant wave or tide influences, sediment supply, hydrodynamics, and so on (Hayes, 1975; Dalrymple et al., 1992; Perillo, 1995; Cooper et al., 2012). The numerous terminologies and classifications are due to the many transitional sedimentary environments influenced by different processes, for which a single classification cannot be applied. One peculiar type of estuary is the karst estuary, which is characterized with freshwater inflows either through direct surface flows in the karst or through diffuse flow across a porous karst matrix and sea level (Menning et al., 2015).

Similar to other rivers worldwide (e.g., Nordfjord et al., 2006; Chaumillon et al., 2010; Maselli and Trincardi, 2013; Gomes et al., 2016; Bufarale et al., 2017; Qiu et al., 2019, De Falco et al., 2022), the karst rivers along the EAC were formed during the Pleistocene, carving their fluviokarst valleys into the bedrock (Juračić and Prohić, 1991). As postglacial sea levels rose, the sea flooded the lower reaches of these karst river mouths, leading to the formation of salt-wedge estuaries (Žutić and Legović, 1987; Sondi et al., 1995; Burić et al., 2007) or intra-

estuarine delta (Sondi et al., 1995; Felja et al., 2015). Unlike estuaries with high sediment supply, most karst estuaries along the EAC have low sediment input, causing them to become submerged and preserving their incised valleys (Pikelj and Juračić, 2013; Hasan et al., 2020; Hasan et al., 2023). Hence, the classification of "give up" estuaries proposed by Cooper et al. (2012) is applicable to this type of estuary. Additionally, some karst rivers, such as the Krka and Zrmanja Rivers, have developed calcareous tufa barriers along their canyons, which are now submerged due to rising sea levels (Hasan et al., 2020; Smrkulj et al., 2024).

Calcareous tufas are freshwater carbonates (Pentecost, 1995; Ford and Pedley, 1996), which form exclusively during the warm interglacial phases of the Quaternary, whereas their formation is interrupted or stopped during the cold glacial phases. They are typical for cool freshwater and open-air environments where water splashes against river rapids or lakes, and particularly thrive in areas with changing slope gradients, such as barriers or cascades (Chen et al., 2004). Furthermore, biochemical processes lead to CO₂ outgassing, facilitating the formation of calcareous tufa (Pedley, 1990; Pentecost, 2005). Moreover, plants act as substrates aiding calcite precipitation on their outer surfaces, contributing to the characteristic porous structure of calcareous tufas (García-del-Cura et al., 2012). Their morphology often divides river flows, reducing erosional power and leading to lake formation, allowing for sediment accumulation and altering sediment transport to the sea (Pavlović et al., 2002; Golubić et al., 2008; Hasan et al., 2023). They can grow relatively tall and rapidly, potentially providing detailed records of climatic events. Thus, calcareous tufas are considered excellent palaeoenvironmental and palaeoclimatic archives (Domínguez-Villar et al., 2000; Domínguez-Villar et al., 2011).

Consequently, the sheltered karst Krka River estuary and its Pleistocene palaeo-mouth present suitable settings for studying the Quaternary geomorphology, palaeoenvironments, and sea-level changes. An important consideration arises when examining climate change and sea-level fluctuations within local or regional contexts, which often prove far more intricate than what is reflected in the global perspective. Local to regional shifts in relative sea level can exhibit notable deviations from eustatic changes in sea level, and the causes of these differences include factors such as local tectonic activity, land subsidence, sediment compaction, and hydrodynamics.

2.2 Climate and sea-level changes during the Quaternary

During the Quaternary period, which began approximately 2.4 million years ago and continues to the present, the Earth experienced significant climate and sea-level changes (Murray-Wallace and Woodroffe, 2014). These changes have had profound impacts on Earth's ecosystems, geomorphology, and human evolution. The Quaternary is characterized by repeated glacial and interglacial cycles (Imbrie et al., 1984). It can be subdivided into the Pleistocene and the Holocene epochs (Hafsten, 1970). Emiliani (1955) initially proposed the transition between Pleistocene glacial and interglacial periods based on variations in oxygen isotope ratios in planktonic and benthic foraminifera, dividing the Quaternary period into Marine isotope stages (MIS), giving the glacial periods even numbers (oceans enriched with ^{18}O) and interglacials odd numbers (oceans depleted with ^{18}O). Each warmer and colder phase, or subphase, is marked by alphabetical letters or numbers. During glacial periods, large ice sheets expanded over the continents, lowering global (eustatic) sea levels and causing cooler and drier climates. Interglacial periods, however, were warmer and wetter, with reduced ice coverage. The Milankovitch theory of climate change is believed to be a significant driver of the glacial-interglacial cycles during the Quaternary. The Milankovitch cycles are variations in Earth's orbit, axial tilt, and precession that influence the distribution and intensity of solar radiation reaching the Earth (Fairbanks, 1989), therefore influencing the eustatic sea-level changes (Lambeck and Chappell, 2001). Currently, the Earth's eccentricity cycles with a period of approximately 100 kyr, whereas obliquity has a period of about 43 kyr and precession periodicity of 23 kyr and 19 kyr. The origins of these fluctuations can be broadly categorized as eustatic, glacio-hydro-isostatic, or tectonic, with tectonic factors posing a significant challenge to measurement. Eustatic alterations are global sea-level changes that are directly influenced by the release or accumulation of water from ice sheets, thereby serving as a universal determinant of sea-level shifts (Fairbanks, 1989; Fleming et al., 1998). Alterations in the relative sea level and land surfaces typically signify vertical shifts in landmasses, alterations in ocean volume, or often, a combination of both (Lambeck and Chappell, 2001; Surić et al., 2014; Rovere et al., 2016). The relative sea level is primarily invoked when examining past sea levels and their impact on continental shelves and coastal communities. This investigation of the relative position of past sea level is facilitated by studying palaeoenvironmental sea-level indicators or proxies (Benjamin et al., 2017).

2.2.1 Last Glacial sea-level and climate changes in the Adriatic

The latest glacial cycle comprises five Marine Isotope Stages (MIS 1–5; Fig. 6.7A) (Siddall et al., 2003). MIS 1 represents the current warm period or the Holocene (Fig. 6.7), while the previous similar peak occurred during MIS 5e, approximately 123 kyr BP (Shackleton et al., 2003). During the MIS 5e substage (128 to 116 kyr BP), the global sea level was higher than today (Rovere et al., 2016a). After the LGM lowstand (Clark et al., 2009), when the sea level was 120 m lower than today (Fairbanks, 1989), up to 134 m (Lambeck et al., 2014), warming occurred with sea level rise (Clark et al., 2004). This transition from the LGM to the most recent period (Fig. 6.7), the Holocene, was not continuous but occurred in distinct stages (Clark et al., 2012). Colder and drier climatic conditions prevailed during the Meltwater pulses from continental ice sheets (Younger Dryas; Fairbanks, 1989), which led to the slowdown of the Atlantic thermocline circulation. The opposite scenario occurred under warmer conditions (the Bølling-Allerød period) (Fig. 6.7B).

During the MIS 5 interglacial, the Adriatic basin had similar physiography as the modern one, with a shoreline somewhat landward of the recent position (approximately 10 m higher than its present position; Waelbroeck et al., 2002). The following periods of sea-level fall (MIS 4 and 3) and sea-level lowstand (MIS 2) are glacial periods marked by cold climatic conditions, which had a dominant role in shaping the Adriatic basin. Then, the shoreline was located more seaward, leaving most of the basin exposed to subaerial conditions (Amorosi et al., 2016; Benjamin et al., 2017), with the prevalence of erosional processes and reworking the pre-existing deposits. In addition to erosion, the dominant were fluvial (Po Plain–Adriatic Sea alluvial system; Amorosi et al., 2004; Amorosi et al., 2016; Pellegrini et al., 2017; Pellegrini et al., 2018) and aeolian processes, as well as weathering and karstification of coastal areas (Benjamin et al., 2017). In the area of the MAD, marine sedimentation continued (Piva et al., 2008). Many submerged caves with speleothems were detected along the EAC, where the speleothems were deposited during the MIS 4 and MIS 3 periods (Surić et al., 2005; Surić and Juračić, 2010). During the transition to the MIS 2 period, the sea level dropped by approximately 130 m (maximum lowstand; Lambeck et al., 2014), and extensive glaciers capped the alpine chain with sediment transport and deposition in the Po River alluvial plain, which debouched into the Middle Adriatic Depression (MAD) basin (Correggiari et al., 1996; Pellegrini et al., 2017). The sediment supply from the EAC during that

period was negligible because of the karstic nature of Dinarides. However, many karst rivers along the EAC incised their canyon-like valleys during the previous low sea level, with the most significant erosion of older deposits and/or further incising of their valleys during the LGM sea-level lowstand (Felja, 2017).

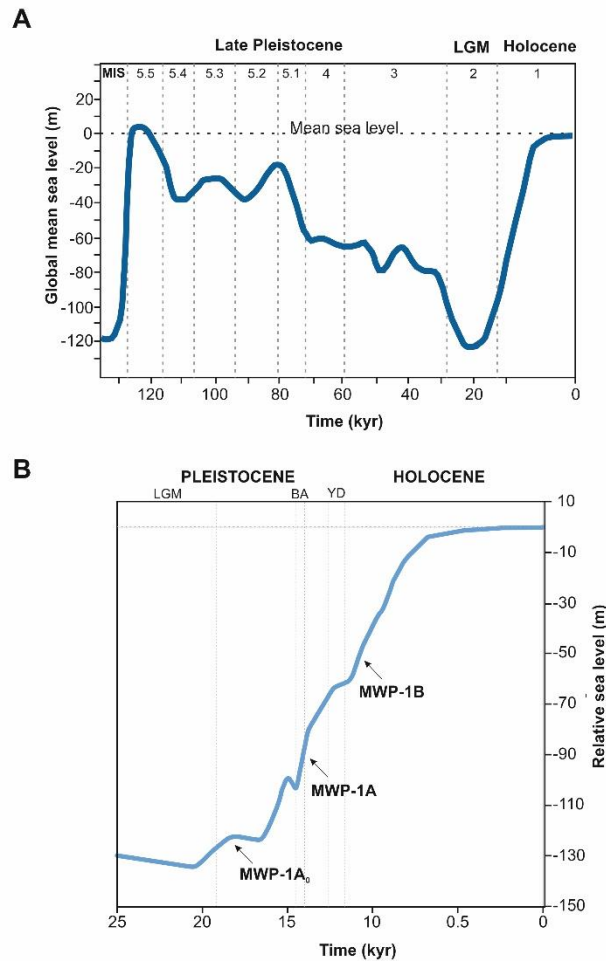


Figure 2.7 A Sea-level change curve (in dark blue) during the late Pleistocene and Holocene based on stable oxygen isotopes (simplified and modified after Benjamin et al., 2017). B Global eustatic sea-level curve since the LGM (modified after Lambeck et al., 2014). Also shown are the major climate events in this period (LGM, the Bølling-Allerød warm period, and the Younger Dryas cold period), as well as the timing of Meltwater pulses 1A₀, 1A and 1B.

Since the end of the LGM, significant volumes of meltwater have been released into the global oceans due to the melting of ice sheets, resulting in a global sea-level rise of approximately 120 m (Fig. 6.7B) (Fairbanks, 1989; Edwards, 2006; Clark et al., 2009). The first significant sea-level rise of 10–15 m occurred approximately 19 kyr BP and lasted

approximately 500 years (Fig. 6.7B) (Clark et al., 2004). The following and even more significant rise in global sea level occurred during the warm Bølling-Allerød period (14.5–14.0 kyr BP) and is known as Meltwater Pulse 1A (Fig. 6.7B). At that time, the rise in global sea level was up to 20 m (Lambeck et al., 2014). The sea-level rise reduced in the following cooling period of Younger Dryas dated to approximately 12.5–11.5 kyr BP. Afterward, during the early Holocene (11.7–8.5 kyr BP; Meltwater pulses 1B; Fig. 6.7B), the sea-level rise was higher (Lambeck et al., 2002), and this period is characterized by higher temperatures and warm and humid climate with increased precipitation (Holocene Climatic Optimum; approximately 9 kyr BP; Lionello, 2012). Additionally, during the early Holocene, a pluvial period was identified along the Dalmatian coast (Wunsam et al., 1999; Schmidt et al., 2000; Combourieu-Nebout et al., 2013; Brunović et al., 2020; Razum et al., 2021). The sea level decreased notably during the middle and late Holocene (up to 2.5 kyr BP). However, in the last 100 to 150 years, there has been a distinct increase in sea level (Lambeck et al., 2014).

Numerous studies of sea-level changes based on multiproxy analyses during the post-LGM have been conducted in the Adriatic, especially on the Northern and Western sides of the Adriatic, and numerous studies have been carried out extensively on the EAC (references summarized in Brunović, 2020; Brunović et al., 2020; Hasan et al., 2020; Razum et al., 2020). According to Correggiari et al. (1996), the sea level of the Adriatic Sea aligns well with the global sea level rise curve (Fairbanks, 1989). The Adriatic Basin was flooded stepwise with the formation of incised-valley fills, lagunar and estuarine environments, and barrier islands on the western and northern sides of the Adriatic, which record relative sea-level changes (e.g., Correggiari et al., 1996; Kent et al., 2002; Cattaneo and Steel, 2003; Amorosi et al., 2008; Antonioli et al., 2009; Maselli et al., 2010; Maselli and Trincardi, 2013; Moscon et al., 2015; De Falco et al., 2022). Around 7000 yr BP, the Adriatic Sea reached its approximate present-day configuration, with sea levels stabilizing after significant submersion (Lambeck et al., 2014). The decrease in the rise of sea level prompted the development of the extensively formed deltaic complex of the Po River in the northern Adriatic (Correggiari et al., 1996).

Along the EAC, palaeoenvironmental reconstructions of coastal environments and sea-level changes were studied by combining sediment cores and geophysical methods, as

well as using different sea-level proxies (geomorphological and erosional indicators, biogenic structures, archaeological indicators).

During periods of low sea level, karst Adriatic rivers were eroding and further incising their canyons into the bedrock, and their mouths were flooded during the Holocene sea-level rise (early to middle) with the formation of estuaries; therefore, alteration of terrestrial, brackish, and marine environments was detected (Felja et al., 2015; Hasan et al., 2020). The estuaries have exhibited varying degrees of filling during the last 7500 years. Palaeoenvironmental reconstructions were made on the island of Mljet (Veliko and Malo jezero lakes, Stupa embayment), where the authors detected marine sedimentation in the lakes at approximately 5.0 kyr BP (Wunsam et al., 1999), while in Veliko jezero lake at approximately 2.3 kyr BP. Razum (2018) identified the marine sedimentation in Stupa embayment at 9.8 kyr BP (Razum, 2018). However, marine intrusion through karstified bedrock occurs earlier (Wunsam et al., 1999). Submerged karst basins, such as Lošinj Bay and Koločep Bay, represent valuable resources for investigating sea-level fluctuations and climate changes because they are basins filled with sediments and were isolated with a karst sill (Brunović et al., 2020, Šolaja et al., 2022). In the Lošinj Bay, multiple sea-level fluctuations were identified with a formation of the present bay at 10.5 kyr BP (Brunović et al., 2020; Brunović et al., 2024), while the karst polje developed within the present Koločep Bay was flooded prior to 12.1 kyr BP (Šolaja et al., 2022). Brunović et al. (2019) made palaeoreconstructions of marine ponds that developed in the coastal karst dolines along the island of Cres. The authors suggested progressive marine inundation during the Holocene sea-level rise, with the existence of a palaeo-marine pond in the Sonte embayment up to 6.61 kyr BP, while the marine pond in the Jaz embayment was formed at 711 yr BP. Relative sea-level changes were investigated on the coast of Istria (Faivre et al., 2011; Furlani et al., 2011). Faivre et al. (2011) detected that the sea level was approximately 1.7–1.9 meters lower than the present sea level in the period of 2.0 kyr BP, suggesting tectonic subsidence.

Among geomorphological indicators, the formation of speleothems has been extensively studied. In the area of the present-day eastern Adriatic coast, many submerged caves (Surić et al., 2014) have been detected with speleothem sedimentation that occurred during the period of >37-22 kyr BP (Surić et al., 2005). During the Holocene, an increase in sea

level resulted in the cessation of speleothem formation at numerous sites along the eastern Adriatic coast (Surić et al., 2005; Surić and Juračić, 2010). The speleothems then become incrustated by marine organisms suitable for dating. Research results in the area of the Zečice Spring confirmed that the sea level was lower than 41.5 meters around 9.2 kyr BP (Surić and Juračić, 2010). Additionally, numerous studies have used tidal notches as indicators of relative sea-level changes (Surić et al., 2014 and references therein). The difficulty in studying tidal notches lies in their inability to be absolutely dated, yet they serve as good relative indicators of coastal tectonic movements (Surić et al., 2014).

In addition to tidal notches, algal rims have been investigated as bio-constructive indicators of relative sea level. Faivre et al. (2013, 2024) reconstructed relative sea-level changes over the past 1500 years on Vis Island, based on algal rims of the alga *Lithophyllum byssoides*, and detected four major phases of relative sea-level change.

Archaeological findings located along the coastline or submerged by the sea are numerous along the EAC (Šegota and Filipčić, 1991; Antonioli et al., 2007; Faivre et al., 2010; Boetto and Radić Rossi, 2012; Bekić et al., 2016; Jerbić, 2019; Bechor et al., 2020, 2023). Some of these findings have enabled the reconstruction of past sea level changes (Šegota and Filipčić, 1991; Jerbić, 2019; Bechor et al., 2020, 2023). An extensive overview of archaeological findings along the EAC is given in the doctoral thesis of Jerbić (2019), and by Radić Rossi et al., (2020).

On the EAC, the environmental impact of human activities during the Anthropocene in the Krka River estuary has been intensively studied by many authors (e.g., Prohić and Kniewald, 1987; Prohić and Juračić, 1989; Elbaz-Poulichet et al., 1991; Seyler and Martin, 1991; Kwokal and Lovrić, 2006; Cukrov et al., 2020; Marcinek et al., 2022; Parać et al., 2022; Cukrov et al., 2024).

3. STUDY AREA

In this doctoral dissertation, the area of the present-day Krka River estuary was investigated, encompassing the middle Adriatic Sea's shelf region up to the eastern slope of the MAD (Fig. 3.1). The research area is located in Croatia in the central part along the EAC. The Adriatic Sea is an epicontinental semi-enclosed prolongation of the central Mediterranean Sea (Fig. 3.1). It stretches in the northwest-southeast direction for more than 800 km, and its width is approximately 200 km. Generally, the Adriatic Sea is divided into three different depth areas: the shallow northern Adriatic shelf with depths of approximately 80 m, a somewhat wider middle Adriatic shelf with depths of approximately 270 m (MAD), and an approximately 1200 m deep southern Adriatic. The western coast and the eastern coast of the Adriatic differ significantly in morphology (Pikelj and Juračić, 2013). The western coast is characterized by a low-lying morphology and is mainly alluvial or terraced, whereas the EAC is highly indented with numerous islands and islets with pronounced karst topography.

The approximately five km thick carbonates along the EAC were deposited during the Mesozoic on the isolated Adriatic Carbonate Platform. At the end of the Cretaceous, a large part of the platform gradually disintegrated and was marked by regional emergence (Vlahović et al., 2005). During the Late Eocene to Oligocene epochs, significant tectonic uplift occurred in the Dinarides, leading to the deposition of molasse in the thrust-top basins (Babić and Zupanič, 2012). The Dinarides experience compressional tectonics, with the primary stress direction being NE-SW (Vlahović et al., 2005). The movement of the Adriatic microplate interacts with the alpine orogenic systems, contributing to the ongoing tectonic activity in the Adriatic region (Anderson and Jackson, 1987). Compared to the seismically active Northern and Southern Adriatic, the Central Adriatic is often regarded as stable, undeformed, and relatively quiet seismically. However, the Adriatic offshore is currently considered seismically active. Neotectonic activity is concentrated around the islands of Vis, Jabuka, and Palagruža, with the Jabuka-Andrija thrust system identified as a primary source of this activity (Herak et al., 2005). Nevertheless, seismic profiles in the central Adriatic region have not shown SW–NE-oriented faults (Herak et al., 2005). According to Faivre et al. (2013), the central Adriatic region has remained seismically stable over the past 1500 years.

During the Cenozoic, the sedimentation of carbonate and clastic deposits continued on distal foreland basins (Korbar, 2009) and thrust-top basins (Babić and Zupanić, 2012). During the Quaternary period, erosion and karstification led to present-day relief (Dinaric karst), while the karstified and folded relief flooded during the late Pleistocene and Holocene (Benac and Juračić, 1998; Surić, 2002). Because the carbonate rocks are subject to erosion, various karst features have been formed, such as sinkholes, karst poljes, karst river canyons, uvalas, and caves. Considering that a large part of the Adriatic Sea is very shallow (<100 m depth), the palaeoenvironmental development in that area was strongly influenced by sea-level changes during the Quaternary.

Along the EAC, only a few karst rivers flow into the Adriatic, carrying low amounts of terrigenous sediment. Flooding of their river mouths occurred during the Quaternary, with the development of karst estuaries (Pikelj and Juračić, 2013; Felja et al., 2015; Felja, 2017; Hasan et al., 2020; Hasan et al., 2023). The estuaries are mostly composed of carbonate bedrock, they comprise a low tidal energy (microtidal estuaries) and a limited terrigenous supply. Furthermore, some rivers, such as the Krka and Zrmanja Rivers, have developed calcareous tufa deposits along their stream, further lowering the erosional power of the rivers and limiting sediment supply (Hasan et al., 2023). In addition, some other rivers and their estuaries along EAC (e.g., Neretva, Mirna, Raša) experienced higher sediment supply during the Holocene and, therefore, developed an intra-estuarine delta (Felja et al., 2015; Felja, 2017).

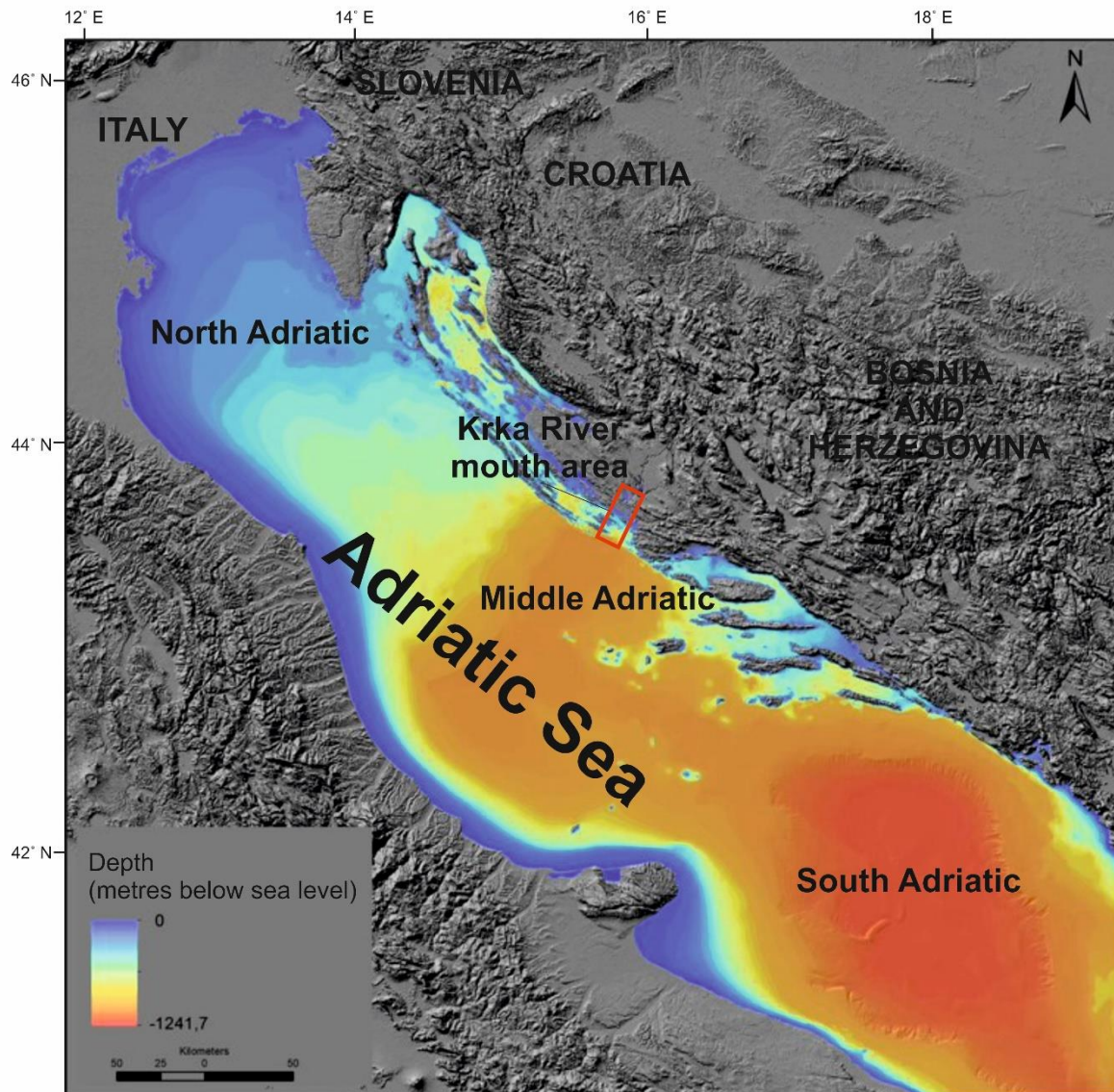


Figure 3.1 Adriatic Sea and the area of research indicated by a red square.

3.1 Morphology and geology of the Krka River watershed area

The Krka River is a relatively small karst river, with a length of approximately 73 km and is situated in the central Dalmatia along the EAC. Part of the river course is within Krka National Park (Krka NP) and, therefore, has been the focus of scientific research in a variety of fields.

During the lowstand periods, the river incised its canyon-shaped valley into the karst bedrock (Juračić and Prohić, 1991), vertically intersecting major geological structures (NW–SE-trending reverse faults). Based on bathymetry, the palaeo-Krka River canyon can be traced

from the Sveti Ante Channel towards the area between the mainland and the island of Zlarin, with its mouth at a depth of 65 m. The Krka River is considered to have developed a delta in the shelf area (one of the hypotheses of this research). The shelf area is characterised by the presence of numerous islands of variable dimensions, the most important being the islands of Zlarin and Žirje (Fig. 3.2A). At depths ranging from 65 to 200 meters, sediment was transported in the delta area and towards the slope leading to the MAD.

The resistant bedrock defines the channel morphology of the valley, which is narrow and relatively deep, except for the two wider basins, Visovac Lake and Prokljan Lake (Fig. 3.2). The river drains a catchment area of approximately 2500 m², and varies seasonally and annually (Bonacci et al., 2006). The first 49 km of the river course is freshwater, and the last 24 km is the estuary. Krka springs are located near the town of Knin, with its largest spring located beneath the 22 m high Topoljski buk waterfall of the Krčić River (Bonacci et al., 2017). This northernmost area is mostly composed of Permian and Triassic carbonate and clastic deposits (Mamužić 1975). The river enters the Adriatic Sea near Šibenik. Most of its drainage basin is composed of Jurassic and Cretaceous carbonates, Paleogene limestones, and flysch deposits (Mamužić 1975). Because of the carbonate composition of the coast and islands (Fig. 3.2A), the input of terrigenous material by the river and its tributaries in this area is not significant.

The river flow rates vary significantly, ranging from 0.2 to 5 m³/s up to 565 m³/s, with an average annual flow between 40 and 60 m³/s (Liu et al., 2019). The freshwater part of the river ends with a 46 m-high tufa barrier at Skradinski Buk (Fig. 3.2B). During the postglacial period, favorable climatic and geochemical conditions developed with the growth of calcareous tufa deposits along the river course. Numerous barriers, waterfalls, and part of the estuary (from the foot of the Skradinski Buk barrier and Skradin) lie within the boundaries of the Krka NP. Krka River waters are characterized by low concentrations of nutrients (Legović et al., 1994) and low input of terrigenous material (Juračić and Prohić, 1991). The river is supersaturated with carbonate, enabling tufa barrier formation (Horvatinčić et al., 2000). The input of terrigenous material is limited because of the presence of tufa lakes and barriers upstream.

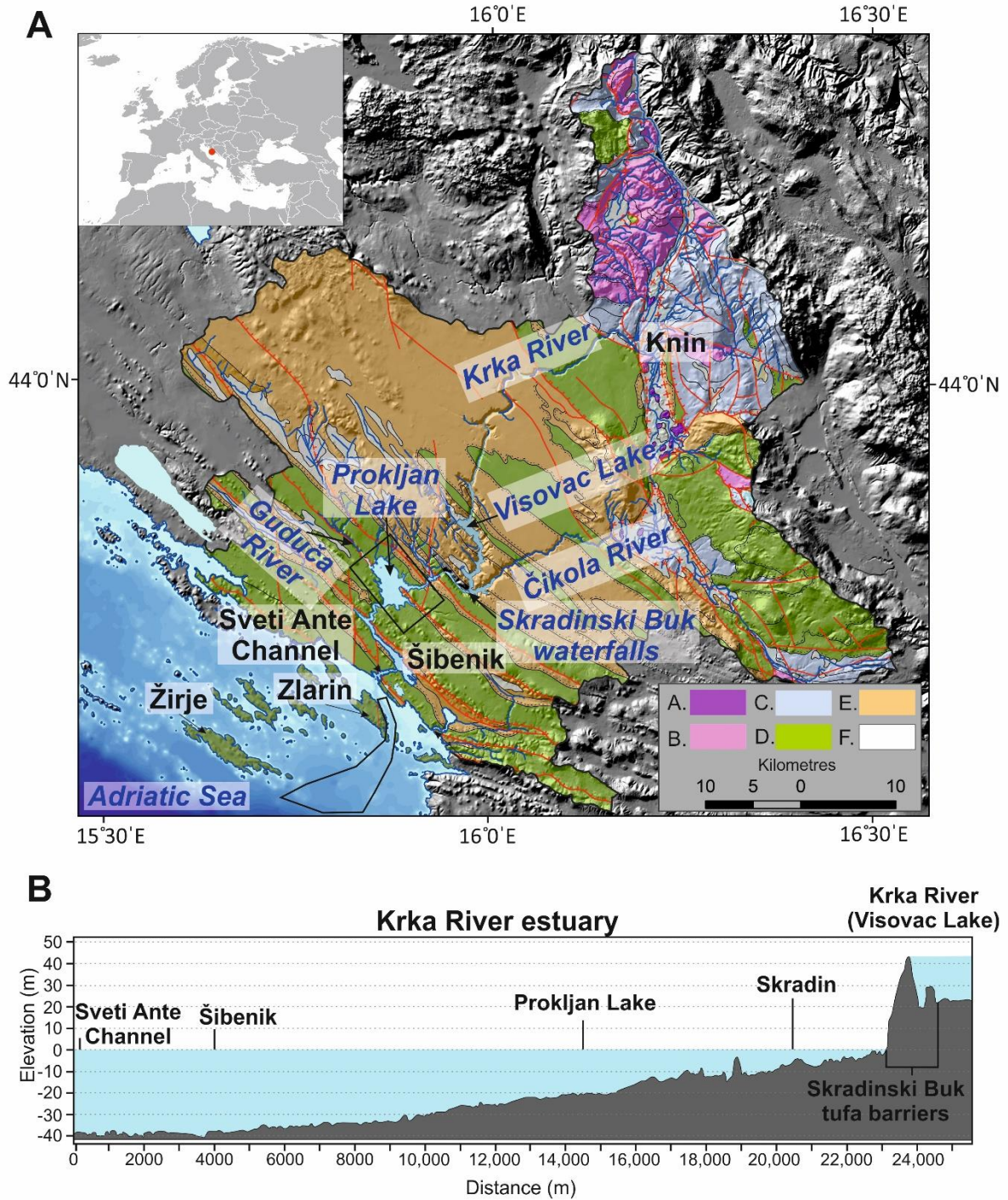


Figure 3.2 A. General location map of the study area showing the geology of the Krka River watershed area. The geology consists of the following deposits: A. Permian evaporites, B. Triassic limestones and clastic rocks, C. Jurassic dolomites and limestones, D. Cretaceous limestones, E. Eocene flysch and limestones, F. Holocene alluvial and lake sediments, terra rossa (Modified from Geological Map of the Republic of Croatia 1:300000). B. Profile showing the bottom morphology of the Krka River estuary from Sveti Ante Channel to Skradinski Buk.

The river is located at the interface of marine and terrestrial ecosystems, coupled with indented coastline. Therefore, the climate in this area is twofold. According to Köppen's climate classification, the area at the base of Dinara Mountain, where the source of the Krka River is located, belongs to the Cfa climate category (moderately warm humid climate). The Krka River mouth area falls under the Csa climate category, characterized by a Mediterranean climate featuring dry, hot summers, and short, mild winters (Filipčić, 2000). In the most landward part of the Krka River valley (near the town of Knin), the average annual air temperature is 13°C, while in the most seaward part of the Krka River estuary, the average annual air temperature is approximately 2°C higher (15°C in the Šibenik area). July is the warmest month with an average temperature of 25.1°C, while January marks the coldest month with an average temperature of 6.9°C in the Krka River valley. The highest recorded temperature was 39.2°C in Šibenik, and 39.6°C in Knin, while the lowest temperature in Šibenik was -10.2°C, and in Knin -18.3°C (Zaninović, 2007). Less rainfall occurs from May to August, while more falls from October to February. The peak precipitation occurs in late autumn, specifically in November, with an average of 112 mm. The driest month is July with the lowest precipitation levels averaging 29.74 mm (Perica et al., 2005). The predominant wind in the Šibenik area is the bora, which reaches its peak frequency and velocity during winter. Furthermore, southerly winds are consistently strong throughout the year, whereas southwest winds are most common during the summer months.

The Krka River region has been identified as a zone of unique botanical significance and is listed in Croatia's Important Plant Areas (Milović, 2016). The path of the Krka River traverses the transitional area between the evergreen Mediterranean and deciduous sub-Mediterranean vegetation zones. Due to its geographical location and a variety of habitats, including travertine barriers, flowing and stagnant aquatic environments, cliffs, rocky landscapes, and human-influenced areas, the plant diversity around the Krka River is notably rich. Within the current boundaries of Krka NP, a total of 1509 species and subspecies of vascular plants have been documented. This national park boasts richer flora than other protected areas in Croatia, partly due to frequent and ongoing botanical research (Hršak et al., 2023). The most prominent plant families include Compositae, Poaceae, and Fabaceae, with dominant chorotypes being South-European and Eurasian. The vascular flora of Krka NP falls between the typical Mediterranean and central European ranges, underscoring the sub-

Mediterranean phytogeographical position of the area (Hršak et al., 2023). The vegetation on the karst plateau is limited, primarily consisting of low maquis shrubs and grasses.

The catchment area of the Krka River is characterized by numerous archaeological sites, with at least 20 sites spanning various historical periods (from prehistoric epochs to the Middle Ages) located within the Krka NP. The oldest traces of human habitation are found in cave sites such as Jazinka and Oziđana pećina, which were inhabited during the Late Stone Age (from the Early Neolithic period, around 6000 before Christ, inhabited continuously until around 1500 before Christ) (Mendušić and Marguš, 2007). Prehistoric sites predominantly consist of hill forts, with the most renowned being the hill fort at Puljani, which Pliny the Elder mentioned among the "fortresses famed for their battles". In the Roman Empire era, the Burnum military camp stood out as particularly significant. It was built across the hill fort of Puljani. Located on the right bank of the Krka River near the present-day village of Ivoševci, the remains of Burnum feature arches from the Pretoria (camp command) building and amphitheater (Boschi, 2011; Cesarik, 2018).

3.2 Krka River estuary, Prokljan Lake and the continental shelf area

The Krka River estuary is a karst oligotrophic salt-wedge estuary (Žutic and Legović, 1987). It experiences microtidal conditions, with a maximum tidal range of approximately 30 cm at the head and 40 cm at the mouth of the estuary (Legović et al., 1994). The estuary has an ENE–WSW orientation perpendicular to the coast extending to the fortress of Sveti Nikola (Fig. 3.2A, B). The Holocene transgression led to the flooding of the valley and the formation of the recent estuary, where the freshwater (or brackish) part moves seawards, and the bottom seawater layer moves inland, as a countercurrent (Buljan, 1969; Cindrić et al., 2015). The thin upper water layer (up to 2.5 m) is nearly homogenous and freshwater, with a salinity of 0.2% (Liu et al., 2019). A sharp halocline separates the upper freshwater/brackish water from the bottom seawater layer, and the salinity reaches 37.5‰ during summer (Liu et al., 2019). The depth of the halocline depends strongly on the river inflow and can vary from 0.2 to 6.3 m (Legović, 1991). The exchange time of the freshwater layer during the winter high river discharge is between 6 and 20 days, and during the summer, when the river discharge is lower, the exchange time is up to 80 days. The exchange time of seawater is longer, between

50 and 100 days in the winter period and up to 250 days in the summer (Legović, 1991). In summer, when the inflow of the river is reduced, the lowermost part of the estuary behaves as a partially mixed estuary (Gržetić et al., 1991). In addition, hypoxic conditions were observed during the autumn months in Prokljan Lake (Legović et al., 1991), when the mixing of water layers is slow and phytoplankton is decomposed below the halocline.

The 46 m-high Skradinski Buk waterfalls prevent further inland flooding. The estuarine valley is relatively narrow, steep-sided, except for two broader areas, i.e., Prokljan Lake and Šibenik harbor area, which are parallel to geological structures. The estuary depth gradually increases from 5 m at Skradinski Buk to 43 m at the mouth of the estuary at the entrance of the Sveti Ante Channel (Fig. 3.2B).

The terrigenous input into the estuary is low because of the karstic drainage area and system of tufa deposits, which reduces transport and retains much of the sediment upstream of the estuary (Hasan et al., 2023). The primary freshwater input into the estuary is from the Krka River, the small torrential Guduča River, and numerous other torrential streams that enter Prokljan Lake. Most of the estuarine sediment accumulates in Prokljan Lake, where the recent sedimentation rate varies from 2 to 5 mm/year, whereas in Šibenik Bay, the sedimentation of authigenic carbonate with a rate less than 1 mm/year dominates (Cukrov and Barišić, 2006). The primary nutrient source of the estuary is the decomposition of freshwater phytoplankton upstream of Visovac Lake (Viličić et al., 1989). Furthermore, the distribution and concentrations of total dissolved trace metals (Pb, Cd, Cu, Ni, and Fe) are low, typically in unpolluted rivers and mostly in carbonate catchments (Elbaz-Poulichet et al., 1991).

Prokljan Lake is situated in the upper part of the estuary and extends in a NW-SE direction, covering an area of 11.1 km². The lake is 6.7 km long and up to 2.8 km wide, and it is connected to the sea by a narrow channel that leads to Šibenik Harbor. The northern part is very shallow, with depths of approximately 1 to 2 m, while the southern part is deeper, with depths up to 25 m (Legović, 1991).

The continental shelf area is situated offshore from the city of Šibenik in central Dalmatia, along the EAC. This region encompasses the submerged palaeochannel of the Krka River and the continental shelf, reaching depths of up to 100 m along the middle section of

the EAC. The palaeochannel, which has been submerged, extends from the Šibenski Channel in a north-south orientation, bordered by Zlarin Island on the west and several smaller islands (Drvenik, Rakitan, Dvanka) on the east. To the south of Zlarin Island, the shelf widens to approximately 8 km in the east-west direction, stretching roughly 7.5 km until it reaches the shelf break at a depth of approximately 70–80 m towards the eastern slope of the Middle Adriatic Depression (MAD). The formation of the MAD occurred during the Late Quaternary due to the combined effects of sediment deposition and tectonic subsidence, as noted by Maselli et al. (2010).

4. MATERIALS AND METHODS

This chapter covers the methodology used in this doctoral research based on a multiproxy approach. It consists of the acquisition, processing, and interpretation of bathymetry, seismic, sedimentological, geochemical, and micropalaeontological data. The methodology is subdivided into fieldwork surveys and laboratory methods.

4.1 Fieldwork surveys

4.1.1 High-resolution acoustic methods

High-resolution acoustic (geophysical) methods are among the most significant and fundamental remote sensing methods for seafloor observations. Geophysical methods have numerous advantages because they are non-destructive and enable the mapping of large areas in a relatively short time, as well as areas that are often otherwise inaccessible.

Due to the wide range of available seabed mapping technologies, geophysical methods are typically classified into four main categories: single-beam echosounders, multibeam echosounders (MBES), and side-scan sonar (SSS), which measure depths and record the seabed properties, and sub-bottom profilers (SBP), whose acoustic waves penetrate the into the sediment, providing information about the subsurface structure of the deposits.

Geophysical methods rely on the propagation of acoustic signals through seawater and their interaction with the seabed. A short signal, in the range of a few milliseconds (ms), is transmitted and travels through the water column, creating an echo when it comes into contact with the seabed. The echo then travels back at a certain angle towards the sonar, which records its return time and intensity (backscatter) (Blondel, 2009). The backscatter intensity depends on the physical properties of the seabed sediment, its structure (roughness), and the characteristics of the acoustic signal (angle of incidence and frequency) (Collier and McGonigle, 2011). Hence, these methods are used to obtain seafloor maps, sediment distribution and sediment physical properties (backscatter) or geomorphological and geological classifications of the seabed (Deiana et al., 2021).

The MBES transmits multiple acoustic beams. The system comprises two arrays of transducers, or transmitters, aligned with the movement of the research vessel and a receiver positioned perpendicular to it (MGDAPAI, 2013). Both transducers send a fan-shaped beam through the water column to the seabed. Furthermore, SSS has been employed for geomorphological studies and for assessing sediment properties, presenting findings as a high-resolution 2D image (sonograph) of the seabed (Blondel, 2009). The sound velocity propagation in marine environments depends on the salinity, pressure, temperature, and water pH but is additionally affected by seawater bubbles and suspended sediment (Blondel, 2009; Kuperman and Roux, 2007).

The subsurface geology and internal structure of the sediment were surveyed using sub-bottom profilers. Seismic waves are reflected, refracted, or diffracted by their propagation through the subsurface when there is an elastic contrast (acoustic impedance; Schock et al., 1989) at the boundary of two layers, rock masses, or any other sediment feature (for example lithology, porosity, pore saturation, compaction), but also when it comes into contact with anthropogenic objects (Morang et al., 1997). Seismic waves then propagate back to the surface, where they record in the form of seismic profiles of the sedimentary succession, which provides insight into the structure of the subsurface, the thickness of the layers and depositional conditions (e.g., Coggan et al., 2007; MGDAPAI, 2013; Wu et al., 2021).

The selection of the wavelength of echosounders and sub-bottom profilers is important, as it determines the resolution (and penetration depth) of structures and objects detected on the seabed and in sediment stratigraphy. The resolution of the obtained data depends on the frequency used by the echosounders and sub-bottom profilers (Blondel, 2009). A higher frequency of the device will provide a higher data resolution but lower penetration of waves into the sediment and vice versa. Hence, selecting the correct frequency is crucial to ensure the highest accuracy and precision in data resolution and interpretation (Blondel, 2009). Furthermore, the water depth, weather conditions, and boat speed greatly influence the data quality during acquisition (MGDAPAI, 2013).

The first phase of fieldwork included high-resolution acoustic methods, which enabled accurate seafloor mapping and geomorphological investigations of the study areas, providing insight into subsurface geology. The instruments used for the bathymetrical surveys were

WASSP S3 MBES (Furuno ENL, Auckland, New Zealand; Fig. 4.1A) and Humminbird 999ci HD SI SSS (Fig. 4.1B), while for the subsurface geological investigations and stratigraphical sequence, SBP profilers were applied (parametric subbottom profiler Innomar SES-2000 light and „Chirp“ Kongsberg GeoPulse Plus subbottom profiler) (Figs. 4.1C, D, E).

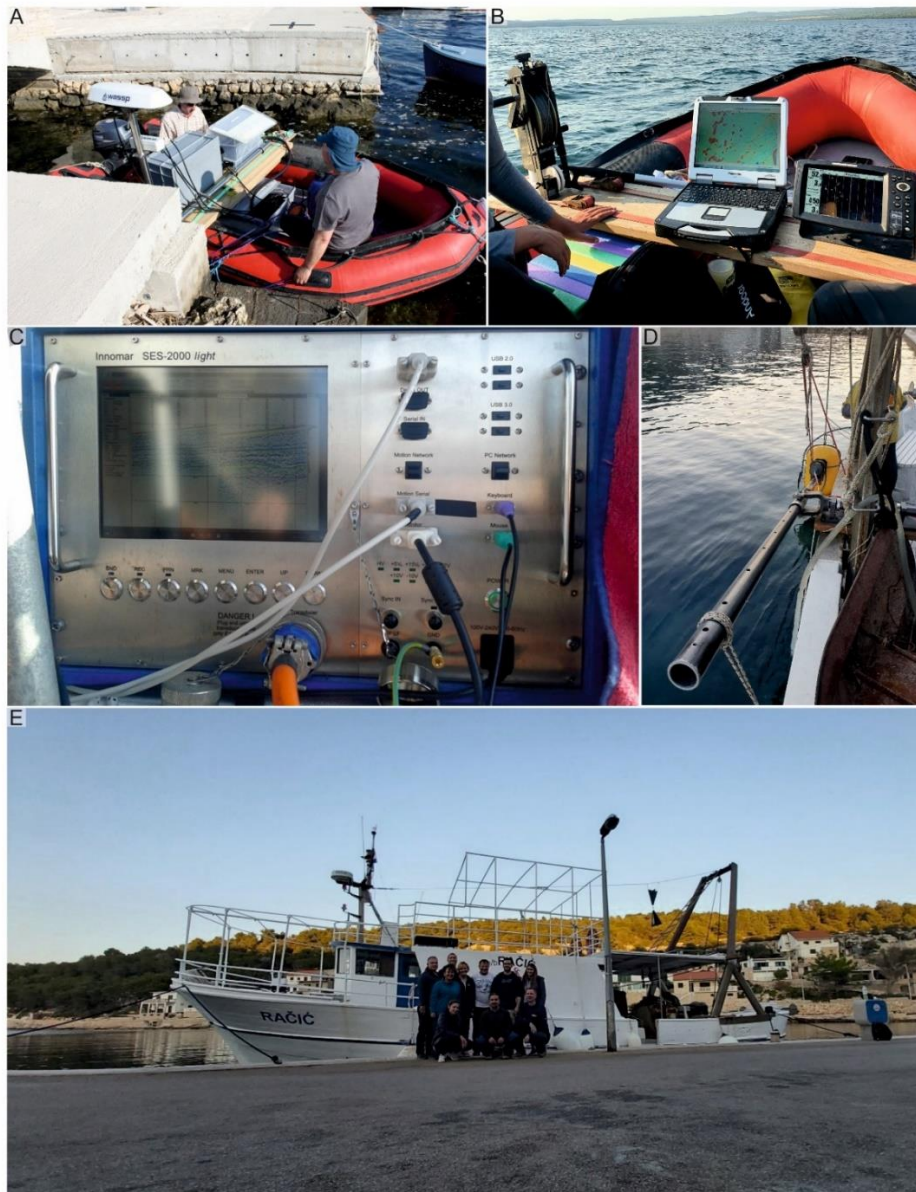


Figure 4.1 Fieldwork survey. A. Multibeam echosounder WASSP S3 MBES. B. Sidescan sonar Humminbird 999ci HD SI. C. Subbottom profiler Innomar SES-2000 light. D. „Chirp“ Kongsberg GeoPulse Plus subbottom profiler. E Boat „Račić“ and its crew during subbottom profiler survey.

The bathymetric data in the Krka River estuary area were obtained using the MBES in June 2020 (Fig. 4.1A). The MBES was side-mounted on a zodiac boat, moving at 3–4 knots.

The MBES survey was done in June 2020 on the boat „Corina“, in the area between the Šibenik harbor and the islands of Zlarin and Žirje. The MBES operational frequency was 160 kHz, producing 224 beams at a 120 °angle swath. The positional data were provided using a Hemisphere V103 GPS GNSS antenna with SBAS motion corrections, and the WASSP Sensorbox (Furuno ENL, Auckland, New Zealand) inertial measuring unit was used for the pitch, roll, and heave motions. WASSP CDX software (version 3.9, Furuno ENL, Auckland, New Zealand) was used for device control as well as for recording the MBES data, whereas post-processing of the data was performed with BeamworX Autoclean v2020.2 software.

The SSS survey was conducted in the Krka River estuary in September 2020 using a Humminbird 999 Si HD depth SSS (Fig. 4.1B). The SSS emits sound pulses with a frequency of 80 kHz and/or 200 kHz toward the seabed. It uses an NMEA0183 GPS/WAAS antenna with a direction sensor for positioning, which enables high-quality positioning during the measurement. The sonar was side-mounted on a vessel with an outboard engine, moving at 3.5 to 4 knots. The mosaic was created using ReefMaster 2.0.

The seismic survey was carried out at three locations: in the area of the Krka River estuary, the shelf area between the islands of Zlarin, Drvenik, and Žirje, and the eastern MAD slope. The SBP survey of the Krka River estuary and the area between the islands of Zlarin and Drvenik was carried out in June and November of 2020 on the vessel Prvić 25 (ŠB 268291) (Figs. 4.1C and 4.2A). The vessel was equipped with a differential GPS device, parametric Innomar SES-2000 light SBP, and an inertial measuring unit. All work and navigation devices were integrated using a PC laptop. The SBP consists of a main unit (transceiver) located on the vessel and a side-mounted transmitter (transducer) attached to an aluminum support, which is partially located below sea level. Two low frequencies (6 and 10 kHz) were used during the survey. By combining low frequencies, a high frequency is obtained using a parametric SBP. A lower frequency enables better penetration of the subsurface, whereas a higher frequency results in better bathymetric reflection.

The SBP survey of the shallow Adriatic shelf between the islands of Zlarin and Žirje and the eastern MAD slope was conducted in October 2021. The survey was carried out on the 17 m long vessel Račić (Figs. 4.1E and 4.2B). The vessel was equipped with a differential GPS device and Chirp Kongsberg GeoPulse Plus SBP (Fig. 4.1D). The SBP consists of a main unit

(transceiver) on board and a transmitter (transducer). The transmitter consisted of four transducers in series with a hydrophone and was side-mounted on the vessel and partially submerged in water. The chirp SBP can use frequencies in the range of 1.5–18 kHz, whereby penetration of up to 80 m into clayey sediments and up to 6 m into the sand and coarse-grained deposits can be achieved, with a maximum vertical resolution of 10 cm. The Leica GS08 RTK GNSS navigation system was used for vessel positioning and data georeferencing, SMC IMU-108 inertial unit for the relative motion of the vessel, and HYPACK software for vessel navigation. All work and navigation devices were integrated using a PC laptop. Seismic profiles were processed and interpreted in SB-Interpreter–TritonImaging Inc. software at the University of Patras in the Laboratory of Marine Geology and Physical Oceanography under the leadership of Prof. George Papatheodorou and associates to reconstruct the geomorphology of the submerged Pleistocene Krka River mouth.

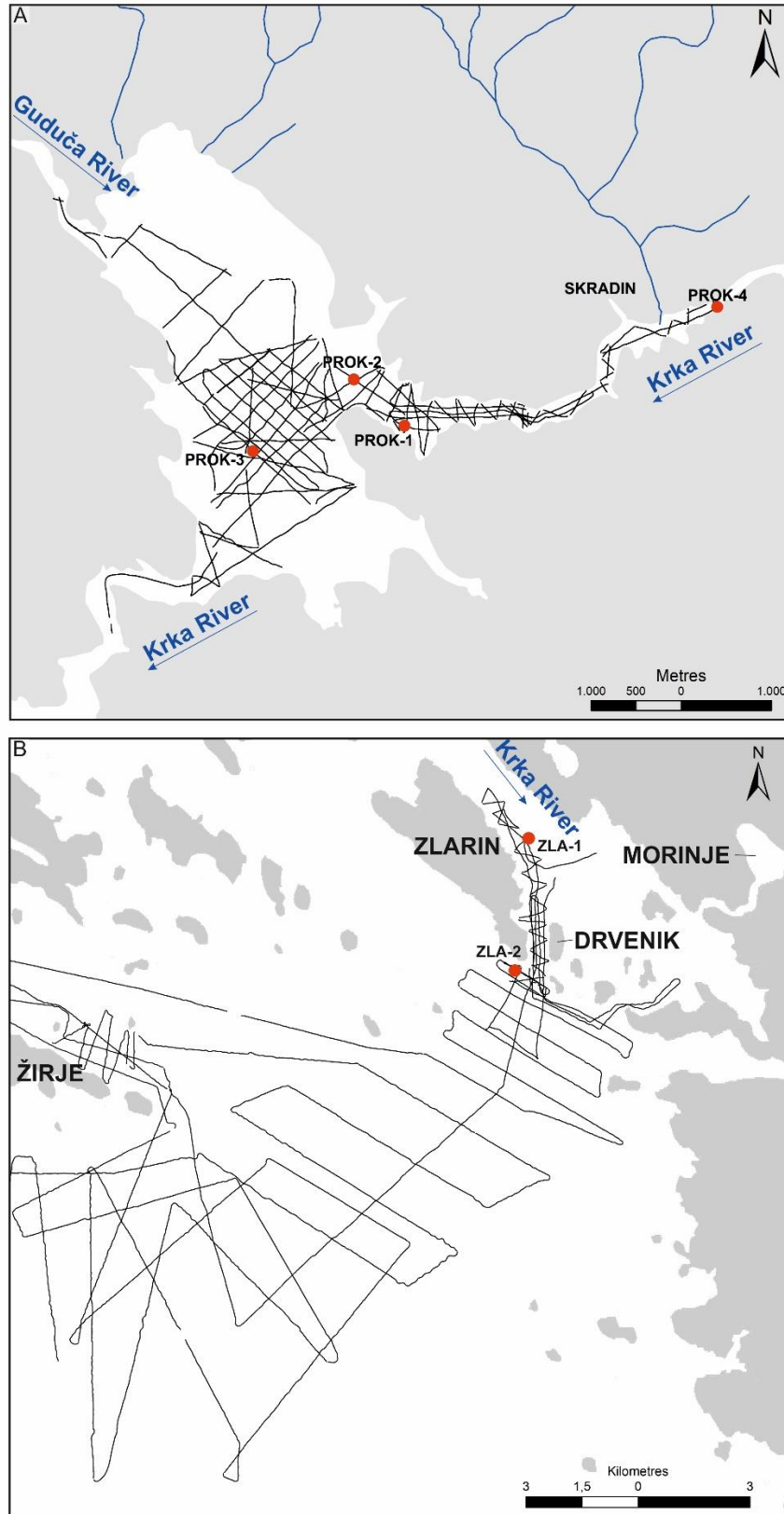


Figure 4.2 A. Position map of seismic lines and sediment core locations in the Krka River estuary. B. Position map of seismic lines and sediment cores location in the submerged Krka River canyon and shelf area of the Pleistocene Krka River delta.

4.1.2 Sediment sampling

Several coring locations were selected in the study area based on high-resolution seismic and bathymetric data. The sediment cores were recovered using a floating research coring platform with a tower, winches, and a 6 cm wide and 3 m long piston corer (Niederreiter piston corer; Fig. 4.3A). This method of sediment sampling can enable the collection of sediment cores up to 15 m in length. The recovered sediment cores were then transported to the Croatian Core Repository in the Croatian Geological Survey and stored at a temperature of +4°C. Four sediment cores were recovered from the Krka River estuary in September 2020, and two from the palaeocanyon of the Krka River near the island of Zlarin in April 2022 (Fig. 4.2B, 4.3B and C; Table 4.1).



Figure 4.3 Sediment coring. A. Floating research coring platform „Q2“. B. Sediment cores PROK collected in the Krka River estuary. C. Sediment cores ZLA collected in the area of the submerged Pleistocene delta.

Table 4.1 Collected sediment cores (see Fig. 4.2 for the core locations).

Core	Latitude	Longitude	Core length (m)	Water depth (m)
PROK-1	451011.5163	4851927.561	8.475	12.7
PROK-2	450449.6936	4852439.801	4.375	15.6
PROK-3	449332.2268	4851644.986	5.245	17.9
PROK-4	454480.6718	4853247.986	5.72	7.54
ZLA-1	449399.6329	4838593.145	3.73	48
ZLA-2	449026.1582	4835276.703	2.85	61

The locations for surface sediment sampling with Van Veen grab were determined in the Krka River estuary based on the obtained bathymetric and backscatter maps. A total of 35 grab samples were collected, whereas at 27 sampled locations, sea bottom videos were taken with a SeaViewer underwater drop camera (Figs. 4.4A and B; Table 4.2).



Figure 4.4 A. Grab sediment collection with Van Veen grab. B. Seafloor observations with SeaViewer underwater drop camera.

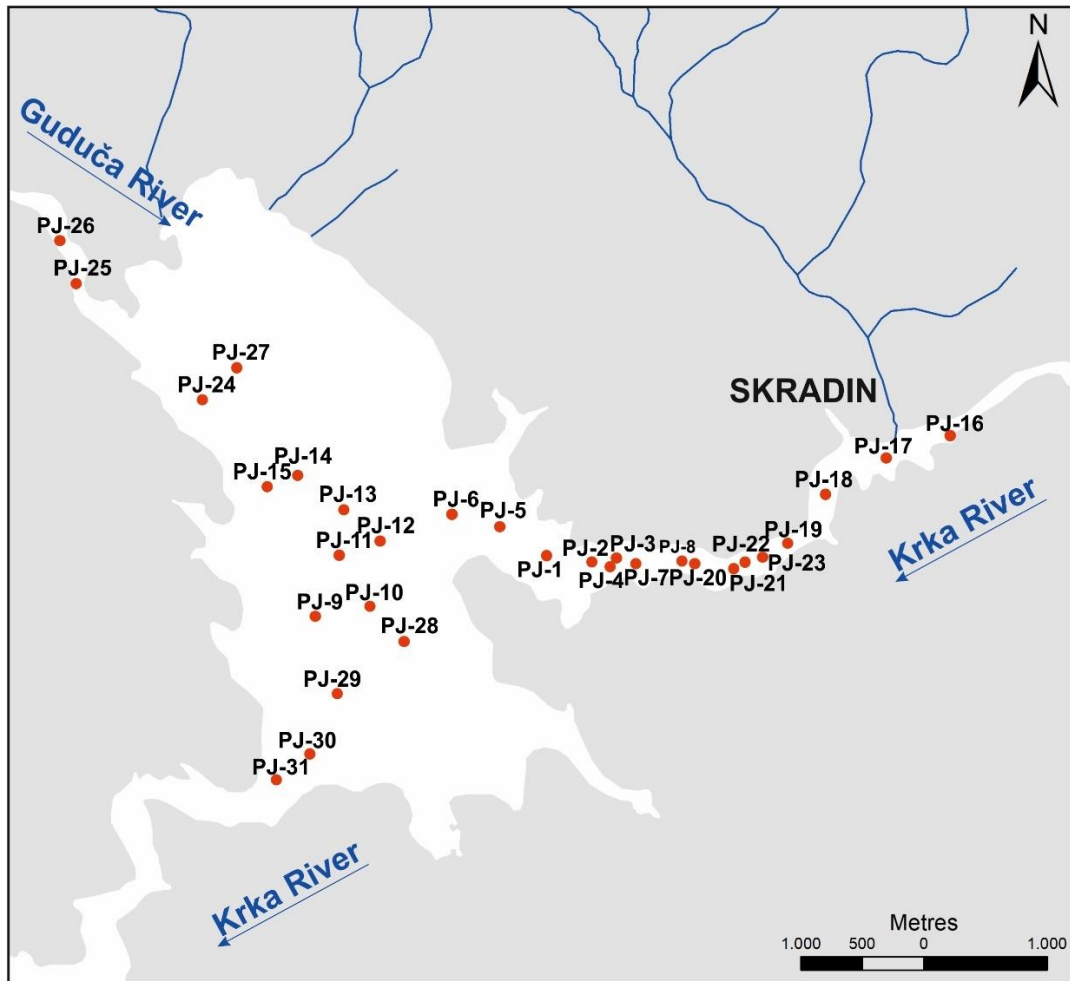


Figure 4.5 Position map of grab samples from the Krka River estuary.

Table 4.2 Collected grab samples (see Fig. 4.5 for grab sample locations).

Grab	Latitude	Longitude	Water depth (m)
PJ-1	451021.328	4852141.844	8.6
PJ-2	451387.7216	4852092.158	11.9
PJ-3	451586.5673	4852123.458	9.3
PJ-4	451537.6352	4852052.895	8.5
PJ-5	450640.4593	4852377.328	14.3
PJ-6	450251.0085	4852479.575	8.8
PJ-7	451744.376	4852077.741	12.8
PJ-8	452123.5399	4852105.105	10.6
PJ-9	449142.7689	4851651.528	10.1
PJ-10	449585.8545	4851733.147	12.6
PJ-11	449323.3133	4852136.533	16.3
PJ-12	449668.0913	4852261.574	14.6
PJ-13	449339.5817	4852514.729	17.6
PJ-14	448997.8307	4852796.081	18.4
PJ-15	448750.3451	4852705.743	12.8
PJ-16	454298.4065	4853119.191	7.2
PJ-17	453778.8065	4852935.529	5.1
PJ-18	453286.8144	4852641.634	9.5
PJ-19	452979.9549	4852243.05	11.4
PJ-20	452223.5203	4852076.229	13.7
PJ-21	452540.968	4852035.939	13.1
PJ-22	452631.4822	4852090.168	12.5
PJ-23	452776.3391	4852129.664	11.9
PJ-24	448224.8724	4853410.144	12.9
PJ-25	447199.609	4854352.798	10.9
PJ-26	447069.1194	4854702.642	9.5
PJ-27	448504.9449	4853668.698	14.6
PJ-28	449862.4655	4851445.576	17.6
PJ-29	449320.5644	4851022.485	14.1
PJ-30	449099.8238	4850531.021	11.8
PJ-31	448824.7749	4850323.471	22.7

4.2 Laboratory analyses

4.2.1 Grab samples and sediment cores

The collected grab sediment samples (31) were analyzed for particle size (PSA), magnetic susceptibility (MS), mineralogical composition, total carbon (TC), total organic carbon (TOC), total nitrogen (TN), total inorganic carbon (TIC), and insoluble residue (IR) content at Croatian Geological Survey. The analyses are described in the following subsections.

Sediment cores collected during the surveys were analyzed in different laboratories because all analyses using a multi-proxy approach could not be performed in one laboratory. In the laboratory of the Croatian Geological Survey, cores PROK-1, PROK-2, PROK-3, and PROK-4 were cut into 1.4 m long segments (Fig. 4.6A) and initially processed, and analyzed using non-destructive analysis techniques (Geotek Multi-Sensor Core Logger (MSCL) and COX Analytics ITRAX X-ray Fluorescence (XRF) core scanner) at the Austrian Core Facility, Institute of Geology, University of Innsbruck. Before opening, the sediment cores were analyzed using a MSCL (Fig. 4.6B and C). MSCL gathers physical properties of sediment cores in a non-destructive way, such as the attenuation of gamma rays (gamma density), the velocity of compressional waves (P-wave velocities), the amount of MS (MS2C and MS2E), and color reflectance using a spectrophotometer ($L^*a^*b^*$). MSCL can analyze split cores or whole rounds up to 150 cm in length and about 6 to 15 cm in diameter. The cores were automatically pushed by a powerful ball screw to geophysical sensors at different resolutions. The gamma-ray density and MS2C (loop sensor) were measured at a resolution of 5 mm for all cores, whereas the $L^*a^*b^*$ parameters and MS2E (point sensor) were measured on opened cores with a resolution of 2 mm. The sediment cores were then cut longitudinally using a core splitter (Fig. 4.7A and B). One half of each core was archived and the other half was smoothed (4.7 C). Afterwards, the cores were photographed and scanned using a XRF core scanner (Fig. 4.7 D and E).



Figure 4.6 A. Cutting the sediment cores into 1.4 m long segments. B. Geotek Multi-Sensor Core Logger. C. Analysis of PROK sediment cores with a core logger.

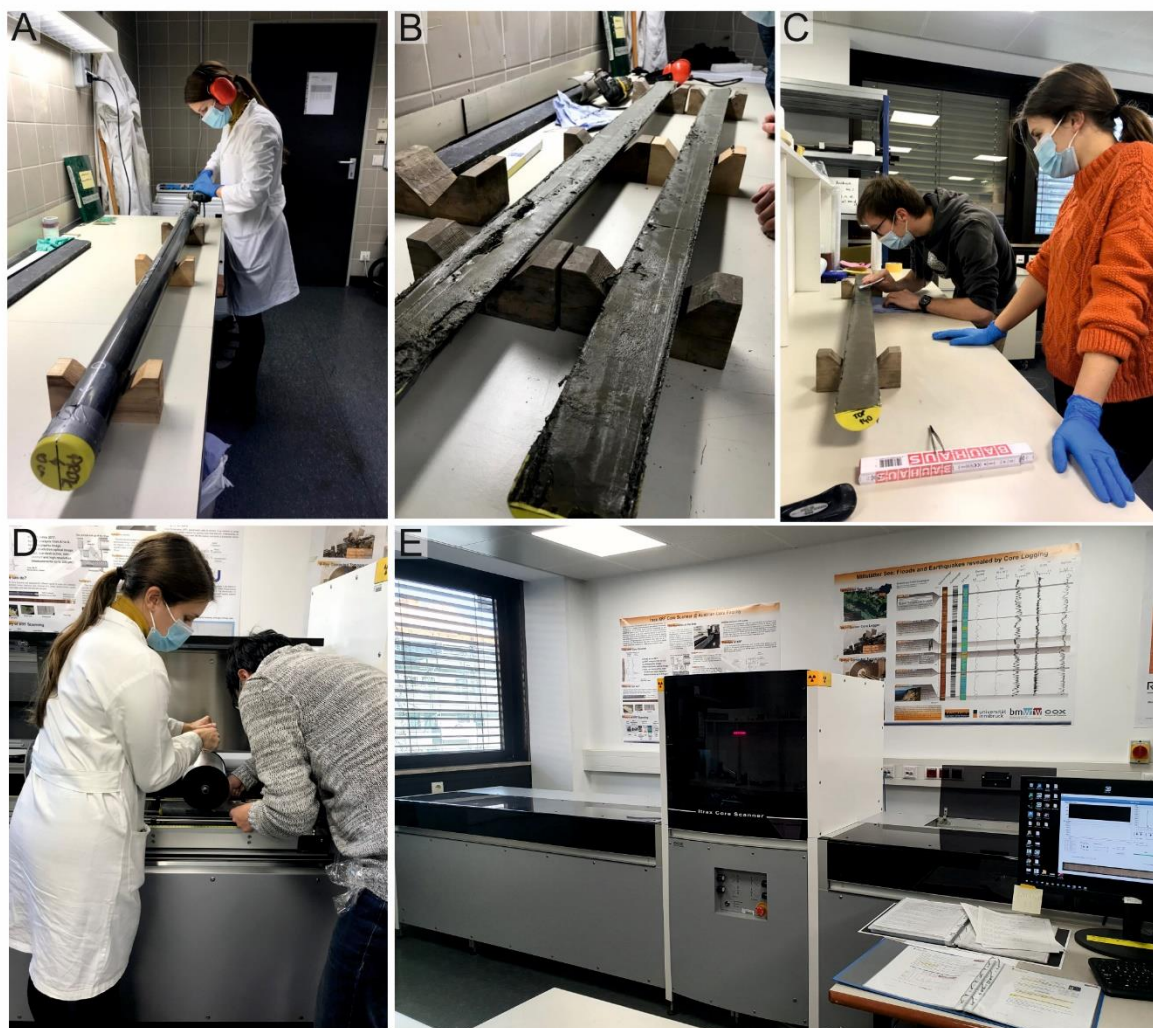


Figure 4.7 A, B, C. PROK sediment cores were cut longitudinally and smoothed for XRF analysis. D. Putting an ultrathin foil on the core surface prior to analysis. E. COX Analytics ITRAX XRF core scanner.

Sediment cores ZLA-1 and ZLA-2 were opened and analyzed in the laboratory of the Department of Mineral Resources and Marine Geology at the Croatian Geological Survey. Sediment cores were cut longitudinally and then smoothed, visually described, and photo-documented using a Canon EOS 500D camera.

Afterward, all sediment cores were subsampled in centimeter intervals for the particle size, inorganic and organic geochemistry, mineralogy, micropalaeontology, stable isotope analysis, and radiocarbon dating (Accelerated Mass Spectrometry (AMS) ^{14}C) at Croatian Geological Survey. The samples were frozen and freeze-dried in an SP Scientific VirTis BenchTop Pro Freeze Dryer (Fig. 4.8).



Figure 4.8 SP Scientific VirTis BenchTop Pro Freeze Dryer.

4.2.2 Radiocarbon dating

Radiocarbon dating is one of the oldest and most widely used methods for measuring the decay of radioactive ^{14}C . It allows the dating of materials younger than 50,000 years, since the half-life of ^{14}C is approximately 5730 ± 40 years. Radioactive ^{14}C is a naturally occurring carbon isotope formed in the upper atmosphere where it is oxidized, forming $^{14}\text{CO}_2$. After oxidation, CO_2 enters the carbon cycle, i.e., it is assimilated in plants through photosynthesis and then in animals. Although ^{14}C constantly decays, it is renewed in the atmosphere, from which the hypothesis of an approximately constant share of the global ^{14}C reservoir over time arises. When organisms die, they are no longer in equilibrium with the atmosphere and biosphere, and the unstable ^{14}C will start to decay with a half-life of 5730 ± 40 years (Walker, 2005). Samples that are older than 50,000 years can be measured but with the possibility of a higher

influence of contamination because the amount of remaining ^{14}C is minor and difficult to measure (Walton, 1967). Radiocarbon dating can be performed on various samples and materials from wood, peat, coal, lake sediments, plant remains, shells, corals, and various archaeological artifacts such as pieces of clothing, tools, and fossil pigments. There are two ways to measure the radioactive age of ^{14}C , and these are beta particle counting, which includes the detection and counting of radioactive decay products that are thought to reflect residual ^{14}C , and AMS, where the relative amount of ^{14}C is counted using a particle accelerator acting as a mass spectrometer of atoms in the sample.

The samples were prepared and measured at the Beta Analytic Laboratory (Miami) using the AMS method. AMS is performed by accelerating ions from samples subjected to a magnetic field and separating a rare isotope from an abundant neighboring mass (e.g., ^{14}C from ^{12}C ; Walker, 2005). The AMS method does not measure the absolute number of ^{14}C atoms but rather determines the isotopic ratio of ^{14}C to the stable isotopes ^{12}C or ^{13}C . The age is determined by comparing the ratio with a standard of known ^{14}C content.

It is generally accepted that the half-life of ^{14}C can be reliably and precisely determined, similar to the natural value of ^{14}C in the atmosphere. This problem is represented by the remaining three assumptions that lead to certain errors in radiometric ^{14}C measurement. Some of the sources of these errors are contamination, isotopic fractionation, reservoir effect, and long-term variations in ^{14}C production (Walker, 2005). Contamination refers to the addition of older or younger ^{14}C to the sample in various ways, which can cause significant errors in the obtained dates. Contamination can occur with the bioturbation of organisms owing to the penetration of plant roots and the production of organic acids containing younger ^{14}C , or simply during sample preparation (Walker, 2005).

Isotopic fractionation implies the distribution of different isotopes of carbon in nature. In the process of photosynthesis, plants prefer lighter isotopes ^{12}C and even ^{13}C and, therefore, will have higher concentrations of lighter isotope and lower concentrations of the heavier isotope ^{14}C . This means that the plant will have a lower ^{14}C activity than the atmosphere at the same time, and dating fossil plants will a higher age because they have less ^{14}C . Isotopic fractionation also depends on the species, so different parts of the biosphere will have different ^{14}C ages. By dating marine organisms, the reverse values are obtained because

seawater prefers the absorption of the heavier ^{14}C isotope with a deficit of ^{12}C , which is transferred to marine organisms (shells, corals) having a higher ^{14}C activity, leading to a younger ^{14}C age. Isotopic fractionation is corrected in laboratories based on the fact that the heavier isotope ^{14}C is twice as abundant as ^{13}C . The ^{12}C and ^{13}C isotopes are stable and can be directly measured in fossil material samples using AMS, and this ratio is compared to that of a standard PDB limestone, yielding $\delta^{13}\text{C}$. The $\delta^{13}\text{C}$ value is expressed in per mille (‰) and allows accurate measurement of the isotopic fractionation which is reflected in the fossil sample. Most materials have negative $\delta^{13}\text{C}$ values (Walker, 2005; Lowe and Walker, 2014).

One of the basic assumptions of the ^{14}C method is the uniform concentration of ^{14}C in the biosphere through space and time. However, it has been recognized that the concentration of ^{14}C (both in the atmosphere and living organisms) varies significantly over time within and between ^{14}C reservoirs (Ulm, 2002). This leads to a discrepancy between the radiocarbon and calendar ages (Walker, 2005). The reservoir effect can be different in marine and lake systems. In marine systems, for example, the mixing of older and younger seawater occurs mainly due to marine circulation and is especially pronounced in the oceans, where the age of water can be measured in thousands of years. This means that marine organisms will potentially incorporate older ^{14}C into their shells, resulting in a false or apparent age (Walker, 2005). The marine reservoir effect has been documented primarily through the dating of marine shells of known historical age (Reimer and Reimer, 2001) with an agreed global calibration correction of 405 years. To accommodate for the difference between the Adriatic sea reservoir age and the model, an additional regional difference (ΔR) was added. The results from the eastern coast of the Adriatic indicated the existence of an average marine reservoir effect of 424 ± 57 years ($\Delta R = 77 \pm 57$) (Favre et al., 2015). The reservoir correction should, therefore, be applied to all samples.

Estuarine environments are even more complicated because estuarine organisms can obtain carbon from the dissolved CO_2 in terrestrial rainwater runoff (Ulm, 2002). Many other processes, such as relative sea-level changes, hinterland geology, local circulation patterns, precipitation, and sedimentation patterns, influence fluctuations in ^{14}C over time, resulting in an estuarine reservoir ^{14}C age of up to several hundred years (Ulm, 2002).

In lakes and rivers, the chemical composition of water primarily depends on the composition of the lake catchment area and the composition of the atmosphere. The samples from the lake sediments are composed of ^{14}C originating from the atmosphere (which reflects the actual age of ^{14}C) and ^{14}C originating from carbonate rocks that make up the catchment area. These rocks are older than 50,000 years (the upper limit of the ^{14}C method), which means that they will contribute to increasing the age of the lake sediments. In lake systems, the reservoir effect is called the hard water effect. When dating, it is necessary to first determine the extent to which the effect of hard water is for a particular area because it can vary considerably. This can be done by sampling dissolved inorganic carbon or the surface layer of the sediment with which the initial ^{14}C activity in the carbonate part of the sediment can be approximated. The organic part of the sediment can be determined from the ^{14}C activity of completely submerged aquatic plants or aquatic fauna and the organic part of the surface sediment (Walker, 2005; Philippsen, 2013). Therefore, it is desirable to find dating materials in the sediment core that are not subject to the reservoir effect, such as charcoal or plant material.

Radiocarbon age calibration was performed to convert the conventional radiocarbon age into a calendar age (cal) to avoid larger regional variations. Calibration was performed using calibration curves that described past ^{14}C atmospheric concentrations of dated materials, such as corals, foraminifera, and tree rings (Hua, 2009). Today, the Northern and Southern hemisphere calibration curves IntCal20, SHCal20, and Marine20 are in use (2020).

The AMS radiocarbon dating method (^{14}C) of 28 samples from all studied sediment cores collected during the PhD fieldwork was performed at Beta Analytic Laboratory (Miami). To calibrate all dates into calendar years, Northern Hemisphere calibration curves were adopted. For marine bivalves and gastropods, the Marine20 (Heaton et al., 2020) calibration curve was used, whereas for bulk sediment, charcoal, and freshwater gastropods, the Intcal20 (Reimer et al., 2020) calibration curve was used. For the marine samples, a local marine reservoir age correction of 319 ± 43 years ($\Delta R = -167 \pm 21$ yr) (Faivre, 2015) was adopted. Age-depth models for PROK sediment cores were reconstructed by linear interpolation using the statistical software R and a Bayesian age-modeling program (Bacon v. 4.1.3; Blaauw and Christen, 2011). Ages are reported as calendar years before the present (cal yr BP; present= 1950 AD). Using

the Bacon software, accumulation rates were calculated and expressed as mm/yr. Two dates, Beta-599507 and Beta-599508, were excluded from further interpretation regarding ages older than the surrounding dates.

4.2.3 Color Spectrophotometry and Munsell color system

After the sediment core opening in two longitudinal halves, one of the first analyses is measuring sediment color reflectance since the color of sediment could change while exposed to air. Sediment color variation is a reflection of various environmental changes and processes, such as changes in material supply or erosion in the catchment.

The color reflectance with the spectrophotometer ($L^*a^*b^*$) was measured on PROK sediment cores using a Geotek Multi-Sensor Core Logger (MSCL) at 5 mm resolution (Fig. 4.6B and C), whereas the color of the sediment cores ZLA-1 and ZLA-2 was determined using the Munsell Color system (*Munsell Color*, 1994).

The spectrophotometer measures the reflected light from the surface of the sediment at wavelengths ranging from 400 to 700 nm (visible spectrum). The reflected spectrum describes the scanned color of the sample and converts the spectral data into the CIE $L^*a^*b^*$ color space. The CIE $L^*a^*b^*$ (CIELAB) model is the most complete color space determined by the International Illumination Commission ("Commission Internationale de l'Eclairage"). L^* parameter ranges from 0 (black) to 100 (white), a^* is in the range from +60 (red) to -60 (green), and b^* ranges from +60 (yellow) to -60 (blue) (St-Onge et al., 2007). These parameters can be used as high-resolution geochemical proxies, for example, L^* is used as an indicator of changes in organic carbon or carbonate content (e.g., Balsam et al., 1999; Ortiz et al., 1999), a^* is often used for changes in the concentration of Fe minerals (red minerals; Helmke et al., 2002), such as hematite, whereas b^* can indicate anoxic conditions and conditions (Debret et al., 2006).

On sediment cores ZLA-1 and ZLA-2, the color of the wet sediment was determined according to Munsell's color atlas (*Munsell Color*, 1994) and classified according to their hue (Munsell Hue), lightness (Munsell Value), and saturation (Munsell Chroma). Color

determination using Munsell's color atlas is generally fast, but subjective and depends greatly on lighting (Wolf, 2011). The color was determined for different lithological units of studied cores.

4.2.4 Gamma Density

Gamma density (wet bulk sediment density) was measured on all of the PROK sediment cores using the Geotek instrument at 5 mm resolution (Fig. 4.6B and C). Bulk density is defined as the mass of particles divided by the total volume occupied (St-Onge et al. 2007). It depends greatly on the particle size, mineral composition of sediments, degree of compaction, and porosity; therefore, it is a widely used method in multi-proxy studies (St-Onge et al., 2007). Most MSCLs use a radioactive ^{137}C source and a NaI(Tl) detector. A narrow beam of collimated gamma rays a few millimeters in diameter is emitted to measure sediment density based on emitted gamma-ray attenuation, allowing a downcore spatial resolution at the centimeter scale. The instrument is calibrated using a standard of known density in distilled water to obtain precise data.

4.2.5 Magnetic Susceptibility

Magnetic susceptibility (MS) is the degree of magnetization of a material as a result of its exposure to a magnetic field (Thompson and Oldfield, 1986). Positive high values of MS indicate ferrimagnetic minerals, such as magnetite, while lower positive values indicate ferromagnetic (hematite) and paramagnetic minerals (pyrite and clay minerals). Negative values of MS include diamagnetic minerals (e.g., calcite, quartz, and halite) and organic matter. The measurement of MS is often used to correlate cores based on lithological changes or to identify rapidly deposited layers (e.g., Heinrich events) (GEOTEK, 2014; St-Onge et al., 2007). Furthermore, the variations in MS values could be the result of changes in sediment supply or the production of magnetic minerals in marine and lake environments (Thompson and Oldfield, 1986; Dearing, 1987).

Two sensors are available for MS measuring by the Geotek MSCL and those are a loop sensor (MS2C; core scanning sensor) and a point sensor (MS2E; high-resolution surface scanning sensor). The Bartington MS2C sensor is used for high-resolution volume MS measurements on the whole cores, while the Bartington MS2E sensor is applied for high-resolution MS measurements along split sediment cores (GEOTEK, 2014). Both MS2C and MS2E sensors were used for MS measurements of the PROK sediment cores. MS2C was measured at a resolution of 5 mm, whereas MS2E was measured at a resolution of 2 mm.

The split ZLA-1 and ZLA-2 sediment cores were measured using an MS2E point sensor at the Croatian Geological Survey at a resolution of 1 cm. Multisus2 software was used for the MS measurements. Additionally, for the MS measurements of sediment samples, soils, or rocks, the Bartington MS2B dual-frequency sensor was used. The MS2B sensor was used to measure the MS of grab samples collected in the Krka River Estuary, which were stored in small containers.

4.2.6 Inorganic elemental analysis (ITRAX XRF core scanner and ICP-MS)

Element assemblages in sedimentary records present key indicators of palaeoenvironmental conditions because they are the product of catchment lithology, erosion and transportation processes, vegetation, groundwater, etc., that prevail at the time of their deposition or afterward (Gopal et al., 2023). Climate is one of the major factors that influence weathering and erosional processes; thus, geochemical composition can be indicative of certain climate conditions, such as increased moisture, aridity, or windier conditions. Anthropogenic activities (industry, agriculture and landuse change) have had a significant influence on the chemical composition of sediment (inorganic and organic contaminants, nutrient loading).

Two different methods were used in this research to quantify the elemental composition of sediments: X-ray fluorescence (XRF) and inductively coupled plasma atomic emission spectroscopy (ICP-MS).

The smoothed halves of the PROK cores were covered with ultrathin foil to avoid contamination and then subjected to non-destructive analyses using an ITRAX XRF core

scanner (Cox Analytical Systems) at the Austrian Core Facility, Institute of Geology, University of Innsbruck (Fig 4.7D and E). XRF core scanner gathers optical images from an RGB line camera with crossed polarizing filters, radiographic images (X-ray line camera), and micro-X-ray fluorescence spectrometry elemental profiles in the range SI-U downcore with XRF detection system (Croudace et al., 2006). The working principle of the XRF core scanner is explained in Croudace et al. (2006) and Tjallingii (2007) and is based on the emission of X-rays. X-rays penetrate the sediment surface and ionize the elements within the sediment. Subsequently, secondary fluorescent X-rays were generated and measured for geochemical composition. The ITRAX XRF core scanner utilizes X-rays generated from a molybdenum (Mo) source to analyze sediment cores.

The sampling resolution of the XRF core scanner can reach sub-millimetre, providing a continuous high-resolution chemical composition of the sedimentary records. Thus, high-resolution chemical data allows the reconstruction of palaeoenvironmental changes at annual or sub-annual scales (Croudace and Rothwell, 2015). However, the analytical precision of the XRF core scanner varies with the element intensity and is linked to various lithological and physical properties of the sediment, such as particle size, density, and organic matter content (Croudace et al., 2006; Tjallingii, 2007), which can affect the obtained results.

Measurements of PROK sediment cores were performed at 1 mm resolution operated with a Molybdenum X-ray tube at 30 kV tube voltage, 50 mA tube current, and an exposure time of 5 s. Outliers caused by the division of the cores into several sections and the core catcher zone were removed from the data. Based on the bulk data quality check, only the elements that showed high R2 values between two duplicate runs were considered reliable for scientific research: K, Ca, Ti, Fe, Br, Rb, Sr, and $Mo_{Inc/Coh}$.

ICP-MS is based on inductively coupled plasma, in which the atoms of most chemical elements are ionized and then emerge from the plasma into the mass spectrometer, where they are separated based on their mass and charge ratios. In total 93 samples from the sediment core PROK-1 and 64 samples from the PROK-3 core were analyzed using ICP-MS. First, the samples were freeze-dried, and approximately 2g of sample were ground into very fine powder. Powdered samples were sent to Bureau Veritas Commodities Canada Ltd (Vancouver) for simultaneous multielement analysis by ICP-MS. Before measurement, 0.25 g

of the sample is heated to 200 °C in a mixture of concentrated acids HNO₃-HClO₄-HF until evaporation. The residue was then dissolved in HCl. The following 45 elements were analyzed: Mo, Cu, Pb, Zn, Ag, Ni, Co, Mn, Fe, As, U, Th, Sr, Cd, Sb, Bi, V, Ca, P, La, Cr, Mg, Ba, Ti, Al, Na, K, W, Zr, Ce, Sn, Y, Nb, Ta, Be, Sc, Li, S, Rb, Hf, In, Re, Se, Te and Tl.

Before interpreting the results of the XRF and ICP-MS measurements, it was necessary to normalize the data to eliminate the effects on the chemical component content because different parameters can influence the obtained results (Croudace et al., 2006). This is often done using the ratios of different elements (Tribovillard et al., 2006; Tjallingii, 2007). The obtained results can be normalized to Ti, which is redox-insensitive and less susceptible to diagenic effects (Löwemark et al., 2011). Fe and Al are often used for normalization; however, Fe is easily dissolved, whereas Al can be affected by matrix effects (Croudace and Rothwell 2015).

Major elements, such as Fe, Ti, Al, K, and Si, occur mainly in terrigenous silicates and oxides and are indicative of detrital components, typically through the erosion of continental rocks and sediment transport from land to the deep sea (Croudace and Rothwell, 2015). For example, Ti/Al and Fe/Al ratios are mainly associated with silicates and often serve as proxies for detrital input into the system (Kylander et al., 2011). The relative downcore variation of terrigenous and marine influence can be approximated from the Ti/Ca ratio, where the slightly negative log(Ti/Ca) is indicative of marine carbonates and higher values of log(Ti/Ca) are typical for higher detrital input (Tjallingii, 2007).

Calcium may be biogenic or detrital, and its downcore variation usually reflects the CaCO₃ content (Croudace and Rothwell, 2015; Piva et al., 2008). It typically anti-correlates with Ti, Fe, and other terrigenous elements. However, if it correlates with a terrigenous element, it might suggest a detrital Ca origin (Röhl et al., 2004). Therefore, it may be used to predict authigenic carbonates and their δ¹⁸O records. In addition, the Ca/Sr ratio can indicate biogenic and detrital carbonates because Sr is fixed by calcifying organisms simultaneously as Ca. Lower Ca concentrations may indicate carbonate dissolution or dilution by terrigenous components (Croudace and Rothwell, 2015). The Sr/Ca ratio is often used as a proxy for marine influence and to discriminate between marine and terrestrial carbonates because

high-Sr aragonite requires a shallow-water source. Therefore, higher Sr/Ca ratios indicate marine carbonates (Croudace et al., 2006).

4.2.7 Stable isotope geochemistry and organic elemental analysis

Stable isotope geochemistry has long been applied to marine and lake sediments and fossils as palaeoenvironmental and palaeoclimate indicators (Leng, 2006), providing data about palaeotemperatures, palaeoprecipitation, evaporation rates, palaeosalinity, productivity, food webs, and evaporation rates as well as glacial ice volumes (Leng and Marshall, 2004).

The composition of authigenic carbonates and fossils is often used to infer changes in temperature or the oxygen composition of water systems and to reconstruct local hydrology (Leng and Marshall, 2004; Zanchetta et al., 2007), which might be a valuable proxy for climate changes. Along with stable isotopes of oxygen and carbon in carbonates, stable isotopes of carbon and nitrogen in organic matter are used to decipher productivity and nutrient cycling within the aquatic environment, which are often climatically induced (Leng and Marshall, 2004). However, a wide range of interlinked processes can influence the stable isotope composition of sediments and fossils, for example, the rate of evaporation, isotope composition of rainfall, and temperature change. Thus, it is preferable to integrate isotope data with other multiproxy analyses.

Concentrations of stable isotopes are represented by the relative abundance ratios of the heavy to the light isotopes in each sample compared to the ratio of a known standard and reported as the relative difference between the sample and standard (δ) in ‰. The values of δ can be positive or negative, that is, positive values show an enrichment of heavier isotopes relative to the standard, while negative values show depletion of heavier isotopes relative to the standard (Ellam, 2016). Vienna Standard Mean Ocean Water (VSMOW) is the global standard used for the isotope composition of water samples (H and O), and Vienna Pee Dee Belemnite (VPDB) is used for the isotope composition of carbonate and organic matter (C).

4.2.7.1 Stable oxygen ($\delta^{18}\text{O}$) and carbon ($\delta^{13}\text{C}$) isotopes of carbonates

Stable $\delta^{18}\text{O}_{\text{cal}}$ and $\delta^{13}\text{C}_{\text{cal}}$ isotopes of authigenic carbonates are often used for local palaeoclimate and palaeohydrology reconstructions (Leng & Marshall, 2004). The precipitation of authigenic carbonate occurs when the water is supersaturated with CaCO_3 , and CO_2 is removed from the system by algae mainly in the summer months when the phytoplankton productivity in the surface waters is at its maximum (Jones and Marshall, 2002; Leng and Marshall, 2004). It is assumed that authigenic calcite precipitates in equilibrium with the surrounding environment and that its oxygen isotopic composition depends primarily on the ambient temperature and the isotopic composition of the local water. Therefore, the sedimentary record will preferentially record changes in summer/surface conditions. Furthermore, the interpretation of stable isotope conditions is complicated and may or may not be affected by climate change.

Distinguishing between authigenic and detrital carbonates is often challenging, especially in karst riverine and estuarine environments where detrital carbonates are transported by runoff processes (Leng et al., 2010). Therefore, the changes in $\delta^{18}\text{O}_{\text{cal}}$ of precipitated carbonates can be influenced by detrital carbonates (limestones and dolomites having $\delta^{18}\text{O}_{\text{cal}}$ of approx. 0‰) and the evaporation effect. Both detrital carbonate intake and evaporation result in higher $\delta^{18}\text{O}_{\text{cal}}$ values. Unlike closed lakes at low latitudes, evaporation effects are likely to be minimal in temperate conditions, especially in environments with short residence times, which react rapidly to changes in climate. Thus, information regarding carbonate precipitation conditions in aquatic environments is critical for understanding sediment records.

For the stable oxygen and carbon isotopes of authigenic carbonates, approximately 1 cm^3 of the wet bulk samples was primarily treated with 6% hydrogen peroxide for 8 h and then sieved at 45 μm underwater flow to collect the authigenic carbonates. The samples were treated with bleach (5% sodium hypochlorite (NaClO)) for 4 h to purify the carbonate fraction and stirred occasionally with a spatula for the bleaching reaction. Afterward, the samples were rinsed with nano-pure water four to five times and freeze-dried. The $\delta^{18}\text{O}_{\text{cal}}$ and $\delta^{13}\text{C}_{\text{cal}}$ values were measured for 45 carbonate samples from core PROK-1 at the Stable Isotope Laboratory (Northern Illinois University). The standard deviation of the measured samples

was 0.04 ‰ for $\delta^{13}\text{C}_{\text{cal}}$ and 0.08 ‰ for $\delta^{18}\text{O}_{\text{cal}}$. The stable isotope compositions of oxygen and carbon in authigenic carbonates are expressed as δ values per mil (‰) relative to VPDB (defined by NBS-18 and NBS-19).

4.2.7.2 Stable carbon ($\delta^{13}\text{C}_{\text{org}}$) and nitrogen ($\delta^{15}\text{N}_{\text{org}}$) isotopes of organic matter and TOC/TN analysis

Organic matter (OM) represents a minor, but important biochemical component of sediments, especially in lake sediments, and is often used to reconstruct palaeoenvironments of aquatic systems and regional climate changes (Meyers and Teranes, 2001). It originates from a mixture of different organic materials (e.g., proteins, lipids, and carbohydrates) mainly produced by organisms living in aquatic systems and their watersheds (Meyers and Teranes, 2001). The majority of OM is sourced from vascular nitrogen-poor plants (grasses, shrubs, trees, and macrophytes) or non-vascular nitrogen-rich plants (algae) in and around aquatic environments (Meyers and Ishiwatari, 1993). Phytoplankton is the dominant autochthonous source of OM in lakes, while estuarine environments receive sediment from different sources (fluvial and marine) and, therefore, the OM is under the interplay of many processes (Lamb et al., 2006). In addition, the concentration of OM in sediments depends on several factors, such as sedimentation rate, preservation potential during transport burial, alteration during sinking and sedimentation (mineralization), and degradation. (Meyers, 1994). However, the bulk stable isotope ratios ($\delta^{13}\text{C}_{\text{org}}$ and $\delta^{15}\text{N}_{\text{org}}$) and the carbon to nitrogen ratio (TOC/TN) of OM have become increasingly used to study sources of organic matter (by discriminating between terrestrial and marine sources) and the processes of transformation of organic carbon (Lamb et al., 2006; Liu et al., 2006; Li et al., 2016). Terrestrial OM has lower and depleted values of $\delta^{13}\text{C}_{\text{org}}$ and $\delta^{15}\text{N}_{\text{org}}$ compared to marine OM (Vizzini et al., 2005; Lamb et al., 2006).

TOC/TN is frequently measured alongside $\delta^{13}\text{C}_{\text{org}}$ and $\delta^{15}\text{N}_{\text{org}}$ to improve source identification accuracy (Li et al., 2016). Low TOC/TN values (4–10) are indicative of algal material (Meyers, 1994), which is mainly composed of proteins and is, therefore, rich in nitrogen (Bianchi and Canuel, 2011). Higher TOC/TN ratios (>12) generally reflect terrestrial vegetation (Prah et al., 1980; Lamb et al., 2006) that is rich in carbon, such as cellulose. $\delta^{13}\text{C}_{\text{org}}$

often accompanies TOC/TN as a biplot and serves as a potentially good indicator of changes in the sources of organic matter, especially in estuaries (Lamb et al., 2006).

A total of 381 samples from the studied sediment cores and grab samples were analyzed for TOC, TC, TN, TIC, and IR using a Thermo Fisher Scientific (Flash 2000; NC Analyzer (Fig. 4.9). Two grams of bulk sediment were freeze-dried and ground. The samples were packed into tin capsules for the TC and TN analyses. The carbonate component was removed using 8 mL of 4.2M HCl to measure TOC. TIC was calculated as the difference between TC and TOC. The TOC/TN ratio was calculated by dividing TOC and TN. The insoluble residue was calculated as the mass difference between the sample treated with HCl and untreated sediment mass. The amount of insoluble matter in the sediment was used as a measure of the noncarbonate mineral matter in the sediment samples. The analytical precision of this method was controlled by repeated measurements of the individual samples and the standard reference material, Soil NC Reference Material (%N = 0.21 and %C = 2.29).

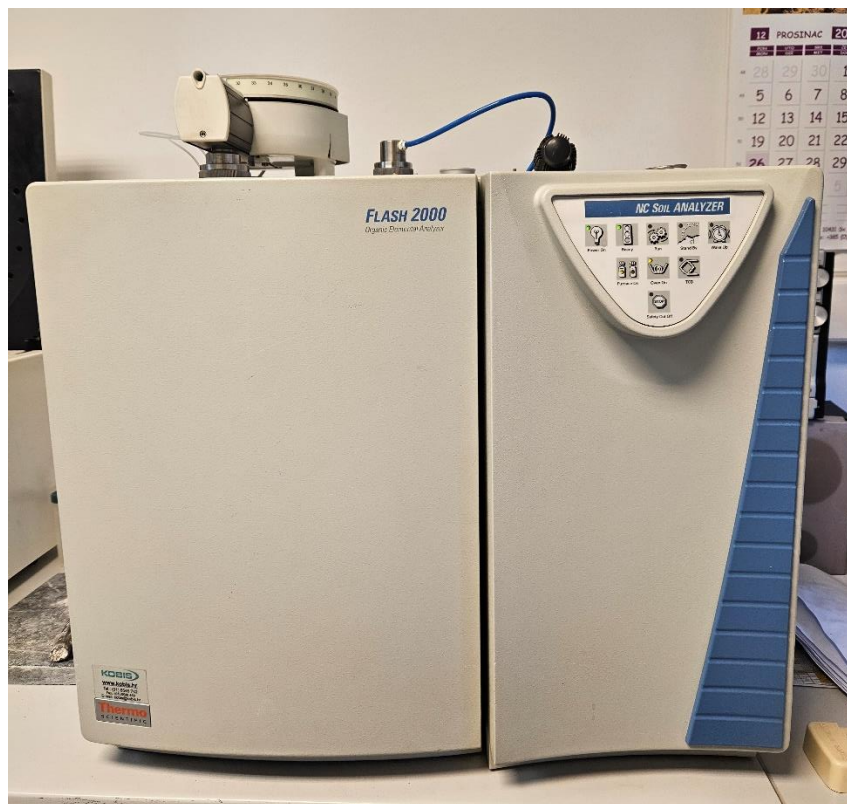


Figure 4.9 Thermo Fisher Scientific (Waltham, MA, USA) Flash 2000 NC Analyzer.

In total, 109 decarbonated samples from sediment cores PROK-1 and PROK-3 were analyzed for $\delta^{13}\text{C}_{\text{org}}$ and $\delta^{15}\text{N}_{\text{org}}$ using an Elementar Vario EL Cube or Micro Cube elemental analyzer (Elementar Analysensysteme GmbH, Hanau, Germany) interfaced with Isoprime VISION IRMS (Elementar UK Ltd, Cheadle, UK) or a PDZ Europa 20-20 isotope ratio mass spectrometer (Sercon Ltd., Cheshire, UK) at the UC Davis Stable Isotope Facility. During the analysis, samples were interspersed with several replicates of at least four different laboratory reference materials. The long-term standard deviations were 0.2 ‰ for ^{13}C and 0.3 ‰ for ^{15}N . The data are expressed relative to international standards VPDB (Vienna Pee Dee Belemnite) and Air for carbon and nitrogen.

4.2.8 Particle size analysis

Particle size is one of the most significant properties of sediments. Sediment particle size can provide information on variations in the transport mechanisms, aquatic energy conditions, and depositional location, all of which are relevant to understanding climate change. Therefore, PSA has proven vital in palaeoenvironmental studies.

Sediment cores were sampled at different intervals (every 3, 5, or 10 cm). In total, 381 samples were taken and prepared for particle size analysis from all studied cores and grab samples. Approximately 0.1–0.2 g of dry bulk sediment was used for the PSA. The samples were treated with hydrogen peroxide (H_2O_2) and left overnight to remove the organic matter. Because most of the samples in this karst environment are predominantly composed of carbonate material, they were not pretreated with hydrochloric acid (HCl). Fossil shells were manually removed from the samples. The last step of sample preparation was adding the Calgon (sodium hexametaphosphate ($(\text{NaPO}_3)_6$)) to prevent particle aggregation and thereby ensure a better dispersion of the analyzed material (Sperazza et al., 2004). The samples were placed on a shaker for 30 min before measurement with a particle size analyzer. The PSA was carried out with the Shimadzu SALD-2300 laser diffraction particle size analyzer that measures particles in the size range from 0.017 to 2500 μm , and the accompanying software program WingSALD II (Fig. 4.10). During the measurement, the analyzer used a laser with a wavelength of 680 nm, which was based on the interaction between light and sediment particles. When a light beam collides with a sediment particle, it is partially absorbed and diffracted by the

particle. The Fraunhofer theory was used to calculate the distribution of particle sizes from the samples, according to which light scattering depends on the particle size. The diffraction angle will be larger for fine-grained particles, while a smaller diffraction angle indicates coarser-grained particles (Murray, 2002; Blott and Pye, 2001). All measurements were performed in distilled water and repeated at least three times to ensure reproducible results. The suspended samples were continuously stirred using a pump to ensure that the sediment particles were randomly dispersed. The obtained data were statistically processed within the software GRADISTAT 8, and for the sediment classification, the Folk and Ward (1957) method was applied. The PSA results were graphically presented using C2 software (Juggins, 2003).



Figure 4.10 Shimadzu SALD-2300 laser diffraction particle size analyzer.

4.2.9 Mineralogical analysis

Qualitative analysis of the bulk mineralogical composition by X-ray diffraction (XRD) was performed on 86 powdered PROK sediment cores and grab samples. The analysis was performed using a PANalytical X' Pert Powder X-ray diffractometer (Fig. 4.11). It was equipped with Ni-filter CuK radiation, a vertical goniometer with a θ/θ geometry, divergence and anti-

scatter slits of 1/4, and a PIXcel detector. Data were evaluated with HighScore X'Pert Plus software using the International Centre for Diffraction Data database (PDF-4/Minerals).

The XRD method is a fundamental nondestructive analytical technique used for mineral composition identification. XRD is based on constructive interference of X-rays and a crystalline sample (Moore and Reynolds Jr, 1997). X-rays are generated by a cathode ray tube and directed toward the sample. The interaction of the incident rays with the sample produces constructive interference (and a diffracted ray) according to Bragg's Law ($n\lambda=2d \sin \theta$), which relates the wavelength of electromagnetic radiation to the diffraction angle and the lattice spacing in a crystalline sample. Conversion of the diffraction peaks to d-spacings allows identification of the mineral because each mineral has a set of unique d-spacings.

The analyzed material is finely ground into powder, and the average bulk composition is determined at a voltage of 45kV and a current of 40 mA. The step size was $0,02^{\circ}2\theta$, while each measurement lasted 4 s.



Figure 4.11 X-ray diffractometer PANalytical X'Pert Powder.

4.2.10 Foraminiferal and ostracod analysis

Foraminifera are unicellular testate organisms that are found only in brackish and marine environments. These tests, primarily composed of calcium carbonate or agglutinated materials, are commonly preserved in sediments. Owing to the large number and variety of species, they are valuable proxies for past sea-level reconstructions and are often used in palaeoecological and biostratigraphic research (Scott et al., 2001). In addition, foraminifera have relatively short life cycles and are sensitive to environmental changes, giving them an importance in palaeoenvironmental studies. However, it takes a significant amount of time to isolate and identify 300 individuals from each sample.

The samples were prepared using the wet sieve method. From each selected interval of the PROK-1 and PROK-3 cores, 10 cm³ of sediment was subsampled for analysis using a syringe. The sediment was soaked in distilled water and then sieved with a stream of water through a set of sieves with perforations of 0.263 mm, 0.125 mm, and 0.063 mm in diameter. The samples were then decanted through filter paper and placed in a dryer at 40°C or air-dried. The microfossil content of the samples was determined based on the total fraction of >0.063 mm according to the taxonomic criteria of Cimerman and Langer (1991) and Loeblich and Tappan (1988), while their ecological preferences were determined by Murray (2006). The classifications and descriptions of most genera and species are based on the characteristics of their tests (e.g., the morphology of the test, composition, perforations, aperture shape, and position). In every sample, 300 individuals were isolated and observed using a Euromex stereomicroscope.

In total, 20 selected samples from the sediment core PROK-1 and 17 from the PROK-3 core were studied for foraminifera. Selected intervals were chosen based on the differences in the lithology or geochemistry of the sediment cores. The determination of foraminifera and their assemblages, as well as the calculated biodiversity indices of the sediment core PROK-3, are described in the master thesis of Hus (2023).

Ostracods are small crustaceans with a bivalve-like valve (carapace) composed of chitin or low-magnesium calcium carbonate (Horne et al., 2002). Due to their high reproductive rates since the Paleozoic era, these organisms became some of the most prevalent microfossils found in the fossil record. (Siveter et al., 2007). The actual number of living and fossil species is estimated to be approximately 33,000 (Horne et al., 2002). They successfully inhabit all environments (marine, freshwater, and semi-terrestrial) and are typically benthic. In addition, ostracods are highly sensitive to seasonal variability and respond rapidly to environmental changes (Mesquita-Joanes et al., 2012). Regarding these characteristics, ostracods have been used in numerous studies for palaeoecological and palaeosalinity studies (Horne, 2002).

The ostracod analyses were made on eight samples from the sediment core ZLA-2 to determine the palaeoenvironmental conditions. Samples were selected at these intervals based on changes in the lithology of the sediment cores. The preparation of sediment for the

ostracod analysis was the same as for the foraminiferal analysis described above. The selected samples were wet-sieved and dried. Ostracods were isolated and determined according to the classification described by Meisich (2000).

4.2.11 Data analysis

Geochemical data serve as an illustrative instance of compositional data, where the focus lies in the relationships between components rather than their individual values (Aitchison, 1982). This interconnected nature of components means that issues with geochemical data inherently involve multiple variables (Chayes, 1960). The mathematical representation of compositional data is known as the simplex (Aitchison, 1986). For proper examination of compositional data, log-ratio transformations come into play (Aitchison, 1986; (Egozcue et al., 2003), reshaping the data into Euclidean space. Although certain restrictions are applied based on a specific transformation, this transformation facilitates the use of conventional multivariate methods (Pawlowsky-Glahn and Buccianti, 2011; Pawlowsky-Glahn et al., 2015). In this research, the center log ratio transformation (CLR) was applied to investigate data variations using the compositional biplot technique (Aitchison and Greenacre, 2002). CLR is defined as:

$$clr(x) = \left[\ln \frac{x_1}{g_m(x)}, \ln \frac{x_2}{g_m(x)}, \dots, \ln \frac{x_D}{g_m(x)} \right],$$

where $g_m(x)$ represents the geometric mean of the components in x . The compositional biplot serves as a graphical depiction of principal component analysis (PCA), relying on the covariance matrix of the centered log ratio transformed data. Its interpretation differs slightly from traditional PCA methods (Pawlowsky-Glahn et al., 2015).

Trace metal (Cu, Pb, Zn, Cr, and Ni) profiles in PROK sediment cores were investigated to assess background values, depositional trends, and contamination levels in the most upstream tract of the Krka River estuary. The enrichment factors (EF) were calculated to determine the extent of anthropogenic contamination in the sediment cores. The Enrichment Factor (EF) serves as a measure of sediment contamination relative to baseline conditions (i.e., pre-impact), taking into account sediment composition. It reduces the variability in contaminant levels linked to clay-rich mud/sand ratios by normalizing the contaminant

content using a reference element (in this study, Al concentration was used as a reference element because of its conservative nature and its presence as a major constituent in clay minerals) as a proxy for the sediment's clay content (Abraham and Parker, 2007). The EFs were calculated using the following equation adapted from Weiss et al. (1999):

$$EF = \frac{\left(\frac{\text{Contaminant mg/kg}}{\text{Al \%}}\right)_{\text{sediment}}}{\left(\frac{\text{Contaminant mg/kg}}{\text{Al \%}}\right)_{\text{background}}},$$

where sediment is the sediment layer in the post-impact interval of interest and background is the sediment interval considered pre-impact. The average concentrations of the three deepest samples in each core were chosen as representatives of the natural background values.

According to several studies, EF values indicate the level of enrichment: EF < 1 indicates no enrichment; EF= 1–3 indicates minor enrichment; EF= 3–5 indicates moderate to severe enrichment; EF= 10–25 signifies severe enrichment; EF= 25–50 indicates very severe enrichment; and EF >50 represents extremely severe enrichment (Vreca and Dolenc, 2005; Wang et al., 2007).

5. RESULTS

5.1 Description of seafloor geomorphology in study areas

5.1.1 Krka River estuary

5.1.1.1 Bathymetric and sidescan sonar results

Multibeam and sidescan sonar surveys were conducted in Prokljan Lake and the upstream section of the submerged canyon extending up to the town of Skradin, covering the bathymetric depth range of approximately 5 to 26.6 m below sea level (bsl.; Fig. 5.1). The mean depth value is 14.7 m bsl. (Fig. 5.1). The coastal areas within Prokljan Lake and near the town of Skradin were too shallow to be mapped efficiently. Consequently, an area of approximately 6 km² of seabed was surveyed.

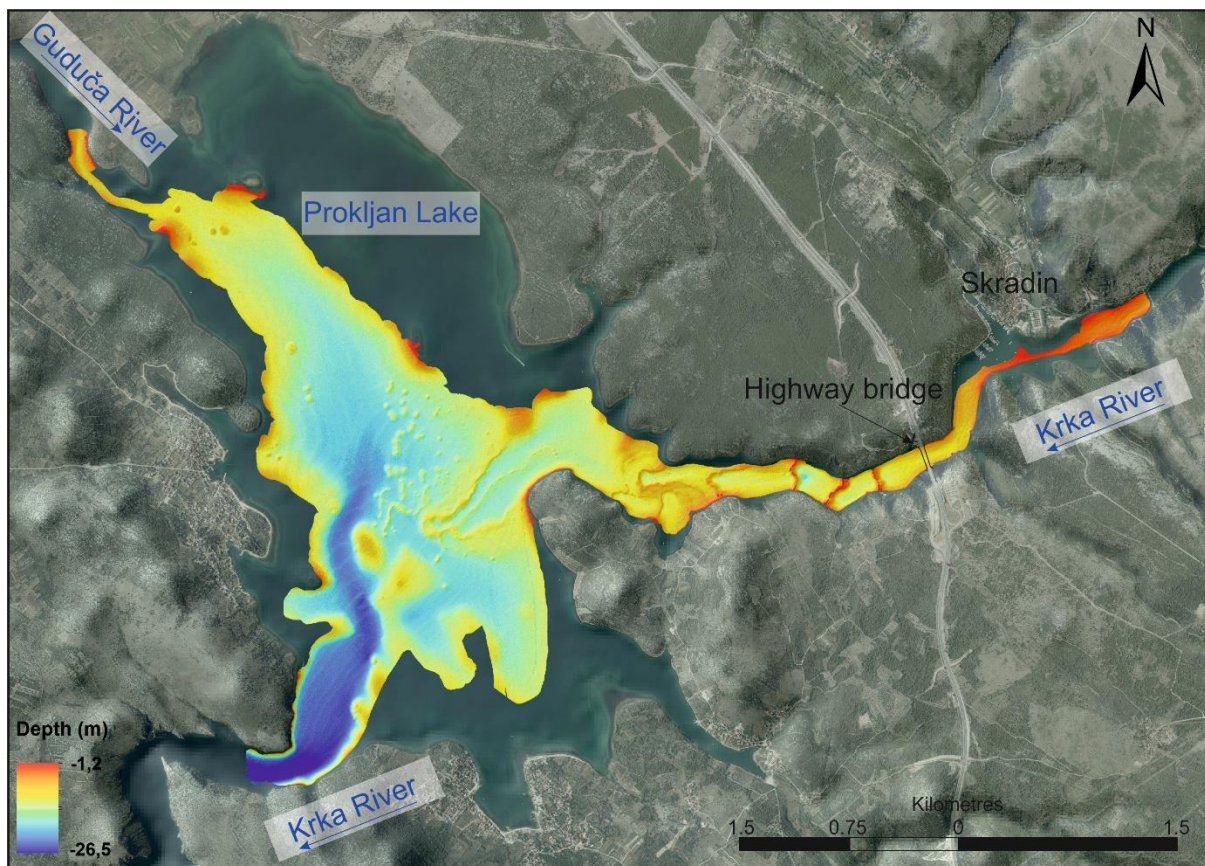


Figure 5.1 Bathymetry map of Prokljan Lake and upstream tract of the Krka River estuary representing the results obtained from the MBES survey.

The study area exhibits two morphologically distinct regions: the Krka River canyon, with an elongated geometry and steep slopes, and the broad Prokljan Lake, with various seabed forms (Fig. 5.1). The shallowest part lies at the north-eastern end of the canyon (near Skradin), where the water depth is less than 5 m (Fig. 5.1). The canyon deepens in its central part, where the average depth reaches 10 m bsl., whereas it reaches 13–15 m bsl at its end, where the canyon meets Prokljan Lake (Fig. 5.1). The shallowest part of Prokljan Lake is on the northern side, where the Guduča River enters Prokljan Lake, with a depth of approximately 12 m bsl. In the SW part of Prokljan Lake, the bottom deepens toward the exit into another part of the Krka River canyon (Fig. 5.1). The depths at the exit of the lake reach up to 25 m bsl (Fig. 5.1). An incised canyon (N–E) can be tracked in Prokljan Lake from its central part toward the exit from lake (Fig. 5.1). The incised valley is bounded on both sides by carbonate rocks that extend from land. The promontory protrudes into the lake from the south toward the center.

Furthermore, a series of submerged barriers can be observed in the central and western parts of the canyon, extending into Prokljan Lake (Fig. 5.1). The barriers are elongated and extend from one canyon side to the other. They are 150 m to 2000 m long and approximately 50 m to 100 m wide at the base, thinning upward to only several meters at the top (Fig. 5.2). The most landward barrier, or Barrier 1 (Fig. 5.2), is located 350 m east of the highway bridge in the central part of the canyon and its depth at the crest is approximately 4.6 m bsl with two distinct 9-to 11 m-wide gaps in the central-to-southern part of the 150 m-wide barrier (Figs. 5.1 and 5.2). The bottoms of the gaps reach 8 and 9 m bsl, respectively. The second barrier is approximately 200 m downstream or barrier 2 (Fig. 5.1), whose crest reaches a depth of 4.6 m bsl at the centerline (Fig. 5.2). Additional gaps exist in the central-to-southern part of Barrier 2 at depths of 9.1 m bsl (Fig. 5.2). Further downstream (250 m) lies the third barrier, or Barrier 3 (Fig. 5.1), with its crest at depths of 4.6 m bsl. This barrier is slightly S-shaped and approx. 250 m long, with two 10–15 m-wide gaps at depths of 7.6 and 8 m bsl (Fig. 5.2). Additionally, a 65 m-wide opening is present and reaches 8.2 m bsl (Fig. 5.2). The fourth barrier, Barrier 4, is located approximately 500 m downstream and is U-shaped with a total length of more than 400 m (Figs. 5.1 and 5.2). Its tip is pointing in the Krka River flow direction towards Prokljan Lake (Fig. 5.1). The barrier has a very irregular surface (Fig. 5.1) with a crest depth in the range from 8.2 m to 10 m b.s.l. (Fig. 5.2). Barrier 5 (Fig. 5.1) is situated

approx. 75 m downstream from Barrier 4. It is generally U-shaped (Fig. 5.2, B5) and makes a system of (at least) five barriers that branch out from the central to the southern part. The longest centerline over the crest is more than 750 m long, with an irregular surface (Fig. 5.2). In the northern and central parts, the crest of the barrier is at depths between 8.6 and 9 m bsl, while the depth at the southern varies from 9.5 and 10 m bsl (Fig. 5.2). A 15 m gap can be observed in the northern tip of the barrier, reaching a depth of 10.5 m bsl. The most seaward and prominent barrier, Barrier 6, starts 500 m to the west and extends from the Krka River canyon into the broad Prokljan Lake (Figs. 5.1 and 5.2). The basin formed by the barrier is divided in the middle by a thin barrier of 900 m in length (Figs. 5.1 and 5.2). Barrier 6 has an irregular surface and is generally U-shaped, with a length over the crest centerline of almost 2000 m. The crest depth varies from 11.2 m to 13.3 m bsl (Fig. 5.2), while the crest depth of the barrier that divides Barrier 6 varies from 12.6 m in the NE part to 15.2 m bsl in the southern part (Fig. 5.2). Two additional barriers branch out from Barrier 6 toward the south and west. The southern barrier is partially preserved, with a crest depth of 14.5 m bsl and a large opening reaching 17 m bsl (Fig. 5.2). The western branch is better preserved, and its crest depth is between 13.5 m and 14.5 m bsl (Fig. 5.2). Only 50 m to the west is the final barrier, or Barrier 7 (Figs. 5.1 and 5.2), which lies at depths of 15 to 16 m bsl. Several mounds are situated north of Barriers 6 and 7, and certain mounds can be delineated (Barrier 8, Figs. 5.1 and 5.2). The tips of the mounds lie at depths of 13.5 m bsl to 14.3 m bsl (Fig. 5.2). There are several mounds located toward the Guduča River inlet. They have a slightly weaker response than those in the central part of Prokljan Lake (Fig. 5.1). This area extends from the southern end towards the center of Prokljan Lake, encompasses Barriers 6 and 7, and is bounded by the valley leading to the exit from Prokljan Lake (Fig. 5.1).

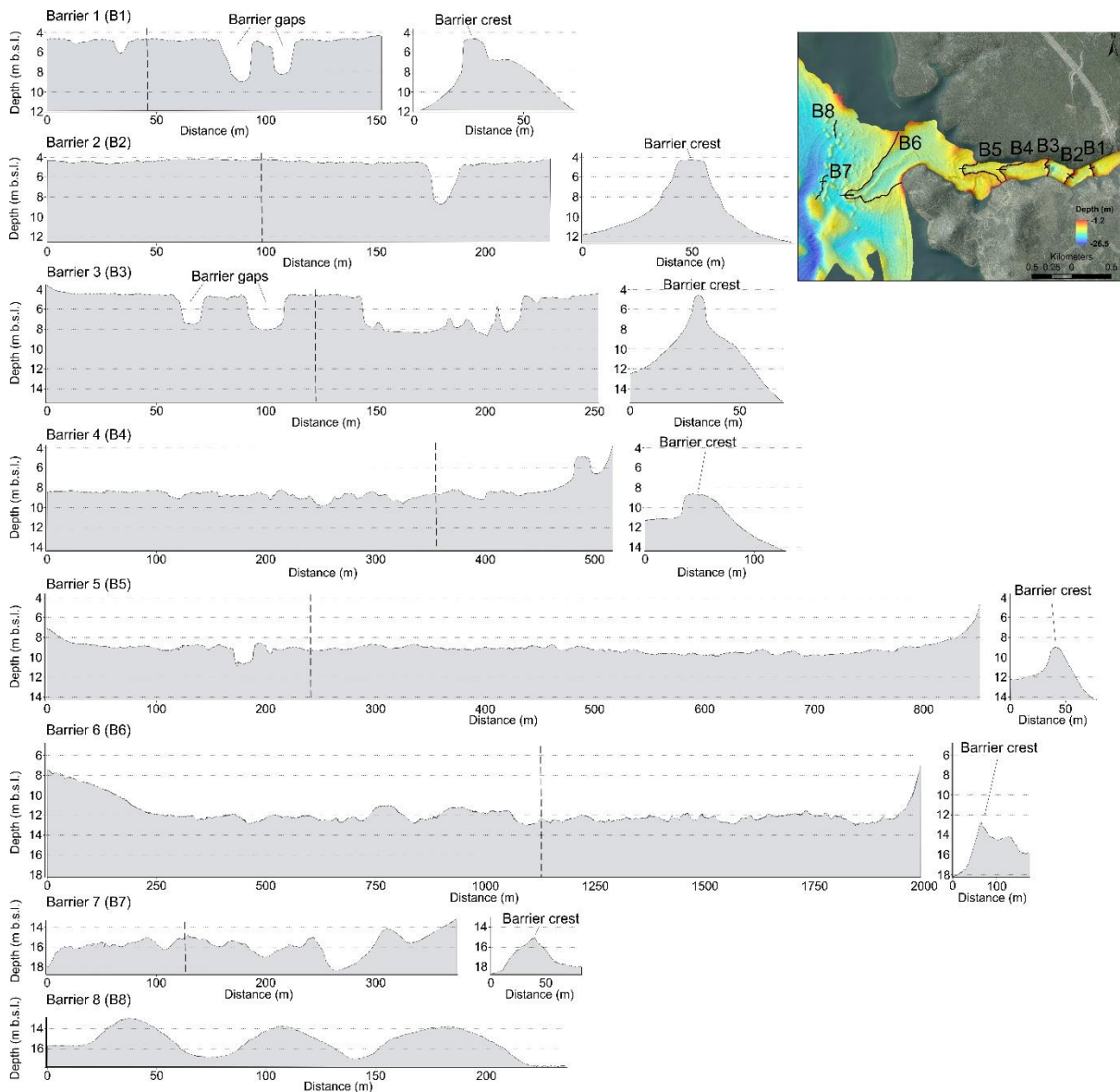


Figure 5.2 Profiles of selected barriers in the study area representing their shapes and depths, where the long profiles are located along the crests of the barriers and the short ones are perpendicular to long profiles. Locations of perpendicular profiles are marked with the dashed line on the long profile. The horizontal scale varies.

The MBES backscatter intensity ranged from -16 to -57 dB for 99.9% of the collected data (Fig. 5.3). The backscatter physiography of the survey area consisted of low acoustic backscatter surfaces on the flat bottom, whereas the well-defined barriers, mounds, and canyon sides exhibited high surface backscatter responses (Fig. 5.3). The area near the Skradin shows the lowest backscatter values (below -35 dB). Additionally, the sediments around the highway bridge (Fig. 5.3) have low backscatter responses, while the area directly below the

bridge shows high backscatter response, with values of -25 to -28 dB (Fig. 5.3). Downstream of the bridge lies the detected pipeline, with strong backscatter surrounded by areas of low backscatter response (Fig. 5.3). Barriers 1, 2, and 3 have high BS responses (-25 to -30 dB). Although the backscatter values of both Barrier 4 and the more complex Barrier 5 were less pronounced within the surrounding low-BS response medium, they could still be successfully delineated (Fig. 5.3). The backscatter response of the complex Barrier 6 is less pronounced than Barriers 4 and 5, but some parts have a strong backscatter response, varying from -25 to -29 dB (Fig. 5.3). The round mounds have a very contrasting and high backscatter response (-22 dB) compared to the surrounding low-BS-response medium (Fig. 5.3). The SE part of Prokljan Lake features deeper areas with a less pronounced backscatter response, while the southern shallower area has higher backscatter intensity (Fig. 5.3).

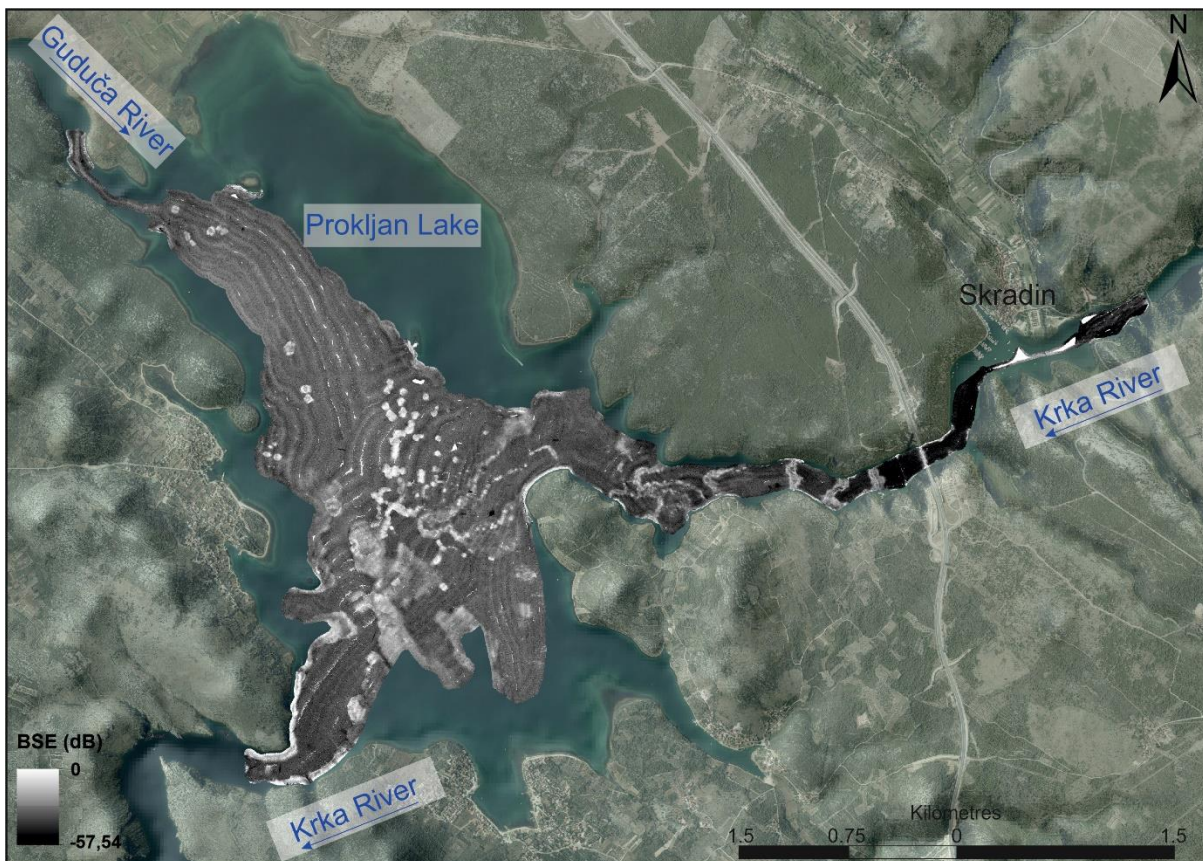


Figure 5.3 Backscatter distribution map of Prokljan Lake and the upstream tract of the Krka River.

The SSS mosaic analysis assisted in interpreting the geomorphological characteristics of the MBES and SBP data. The upper part of the Krka River canyon around Skradin has a

uniform bottom with higher reflectivity (Fig. 5.4). As the canyon develops steeper sides downstream of Skradin, bottom reflectivity decreases (Fig. 5.4). The pipe near the highway bridge is well visible at the bottom, and 150 m downstream, the first barrier is visible. The barrier has a high reflectivity of the SSS mosaic and a very irregular and rough surface of barrier crests. Downstream of the barrier, the bottom is uniform with low reflectivity, reaching the next barrier. The SSS mosaic shows that Barrier 2 branches in the northern part into two parts. Low-reflectivity flat sediments and high-reflectivity barriers occur throughout the canyon (Fig. 5.4). A similar pattern is present in Prokljan Lake, where high reflectivity is appointed to barriers, mounds, and rocky sides of Prokljan Lake, while flat bottom sediments cause low reflectivity in the mosaic (Fig. 5.4). The darkest hues are present in the incised valley toward the exit from Prokljan Lake (Fig. 5.4).



Figure 5.4 SSS map of Prokljan Lake and the upstream tract of the Krka River estuary.

5.1.1.2 Surface sediment characterization

The mass magnetic susceptibility (MS) values of the grab samples in the study area ranged from low values of $2.3 \times 10^{-8} \text{ m}^3/\text{kg}$ to moderate values of $26.1 \times 10^{-8} \text{ m}^3/\text{kg}$, with an average

of $13.3 \times 10^{-8} \text{ m}^3/\text{kg}$ (Fig. 5.5). The sample PJ-19, retrieved under the highway bridge (Fig. 5.5), measures a high MS value of $95.9 \times 10^{-8} \text{ m}^3/\text{kg}$. MS values varied between 0 and 9.2%. The lowest MS values, $<5.1 \times 10^{-8} \text{ m}^3/\text{kg}$, were recorded in 10 samples retrieved from barriers, mounds, and the shallow uppermost part of the study area. Measurements of MS ranged from 5.1 to $17.6 \times 10^{-8} \text{ m}^3/\text{kg}$ (Fig. 5.5) in 29 samples collected from the central deeper areas of Prokljan Lake and the smaller basins behind the barriers. Values $>17.6 \times 10^{-8} \text{ m}^3/\text{kg}$ (Fig. 5.5) occurred in seven seabed samples located in the NNW part of Prokljan Lake, where the Guduča River enters Prokljan Lake and at the exit of the lake.

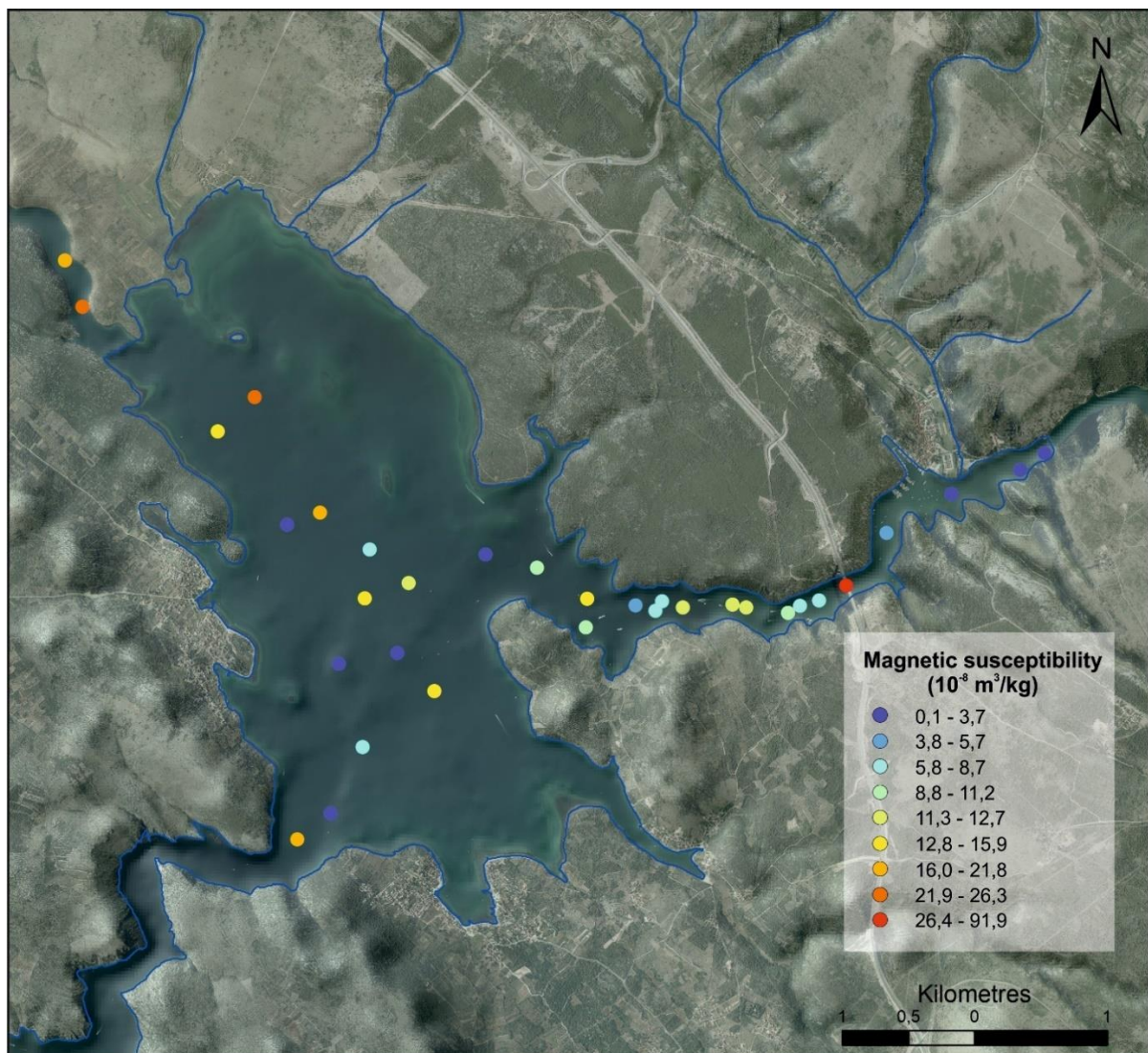


Figure 5.5 Distribution magnetic susceptibility (χ_{lf}) measured in surface sediments.

The collected sediment samples in Prokljan Lake are predominantly of silt and sand size (Fig. 5.6). The mean particle sizes range from fine silt to coarse sand (4.5–575.6 μ m; Appendix 1). Medium to coarse silts dominate sediments in the upper area of the Krka River estuary and near Skradin. The tufa barriers, carbonate mounds, and shallower parts of Prokljan Lake are mainly composed of medium silt to coarse sand. Deeper water estuarine parts of the lake are predominantly composed of fine to medium silt (Fig. 5.6; Appendix 1). The distribution of silty samples is unimodal and poorly sorted, whereas the sandy samples exhibit bimodal or trimodal distributions with very poor sorting (Appendix 1).

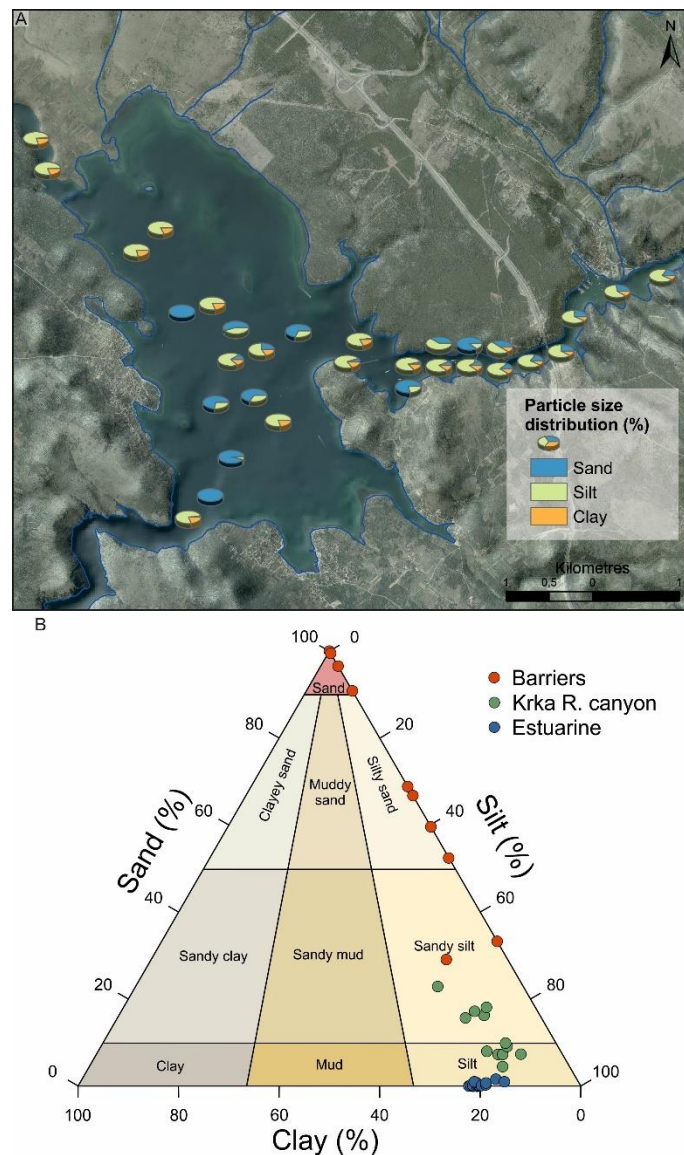


Figure 5.6 A. Particle size distribution (in %) of surface sediments. B Ternary diagram showing the PSA distribution of surface sediments according to their locations in the study area: barriers and mounds (red), Krka River canyon (green), or plain estuarine areas (blue).

The mineral composition of the grab samples is of carbonate and noncarbonate fractions. The carbonate fraction contains calcite, aragonite, magnesium calcite, and dolomite, while the noncarbonate fraction consists of quartz, halite, muscovite/illite, kaolinite, and amphibole (Appendix 1). The predominant mineral phase found in all surface samples was calcite. Additionally, aragonite and magnesium calcite dominate in samples PJ-15, PJ-29, and PJ-30. The samples from the barriers and carbonate mounds contain two minor minerals: aragonite and magnesium calcite.

Figure 5.7 shows the distribution of organic carbon in the study area, while Appendix 1 summarizes the results for TOC, TIC, TN, TC, IR, and TOC/TN. The TOC values range from 0.25 to 2.18%, with a mean of 1.36%. A lower TOC content (<1%) was measured in the samples taken from barriers and mounds, while values >1% are present in the muddy sediments from the deeper part of the Krka River estuary (Fig. 5.7). The TIC values range from 1.84 to 7.95%, with a mean of 3.99% (Appendix 1). The TN contents vary between 0.05% and 0.28% and show a similar pattern to TOC content (Appendix 1). The TOC/TN ratio ranges from 4.5 to 8.85 (Appendix 1).

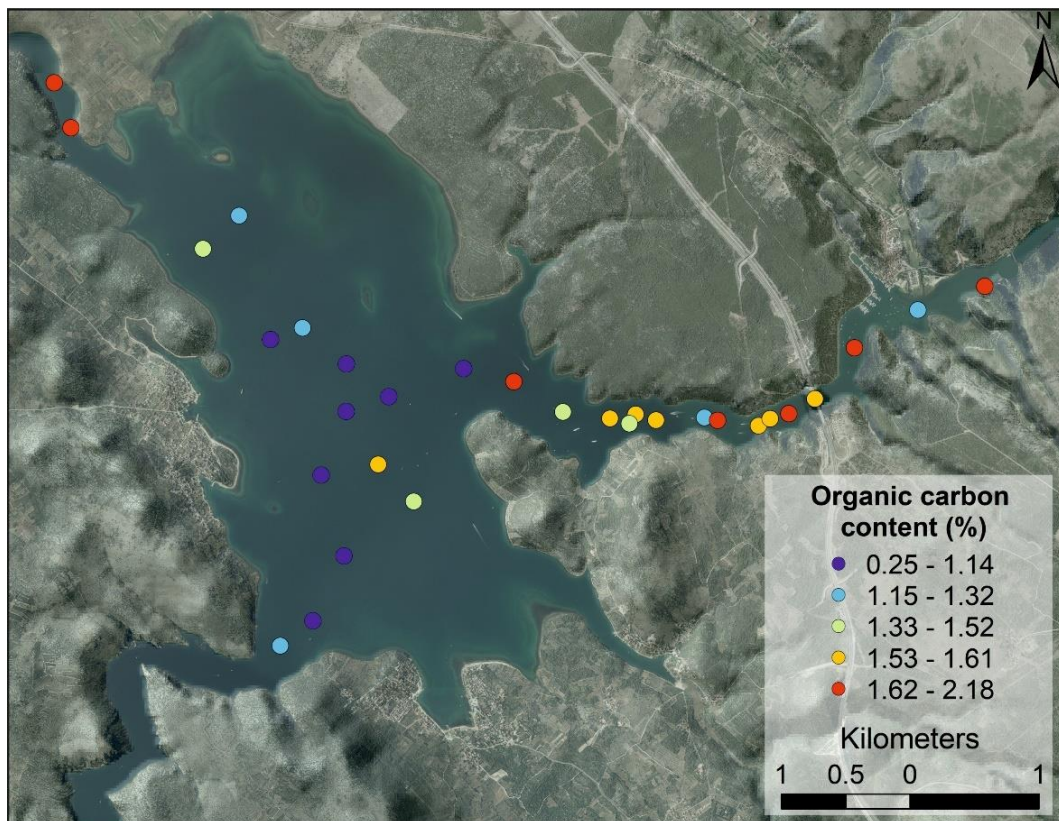


Figure 5.7 Distribution of organic carbon content in surface sediments.

5.1.1.3 Seabed classifications based on bathymetry analyses

Based on MBES backscatter data and classified results of the sediment PSA, Object-Based Image Analysis (OBIA) maps of sediment PSA distribution were created and divided into four or seven classes (Fig. 5.8). A four-class map classifies silt, sandy silt, silty sand, and sand fraction (Fig. 5.8). The silt fraction predominates in the study area with 84.8%, the sandy silt occupies 4.1% of sediments, the area covered with silty sand amounts to 7.3%, and the sandy sediment is present with 3.1%.

In the seven-class map, the dominant particle size is fine silt, which covers 77.6% of the area (Fig. 5.8), with the other silt subclasses as follows: medium silt (10.1%), coarse silt (0.9%) and very coarse silt (0.8%). Among the sand-sized fractions, very fine sand occupies the area with 8.1%, medium sand covers 2.2% of the seafloor, and coarse sand covers 0.3% of the entire study area. Overall accuracy assessments were made for both classifications. A fairly simple four-class classification map had a satisfactory accuracy assessment of 93.3%, while a more complex seven-class map had a lesser accuracy assessment of 86.7%.

Respective Kappa coefficients ranged from 0.9 for a four-class and 0.83 for a seven-class classification. The accuracy assessment for the most dominant silt fraction in a four-class classification was 100%, whereas it was the lowest for the sand with 75%. In a seven-class classification map, a dominant sediment type is fine silt, which has an excellent accuracy assessment, but it was lower for classes of medium silt and very coarse silt, with values of 67%. A limited discriminatory power of backscatter data between different coarse sediment classes is visible in a seven-class map (Fig. 5.8). Very coarse silt, medium sands, and coarse sand are indistinguishable virtually based only on MBES backscatter. The reason for the effect is probably a low number of samples for specific substrate types.

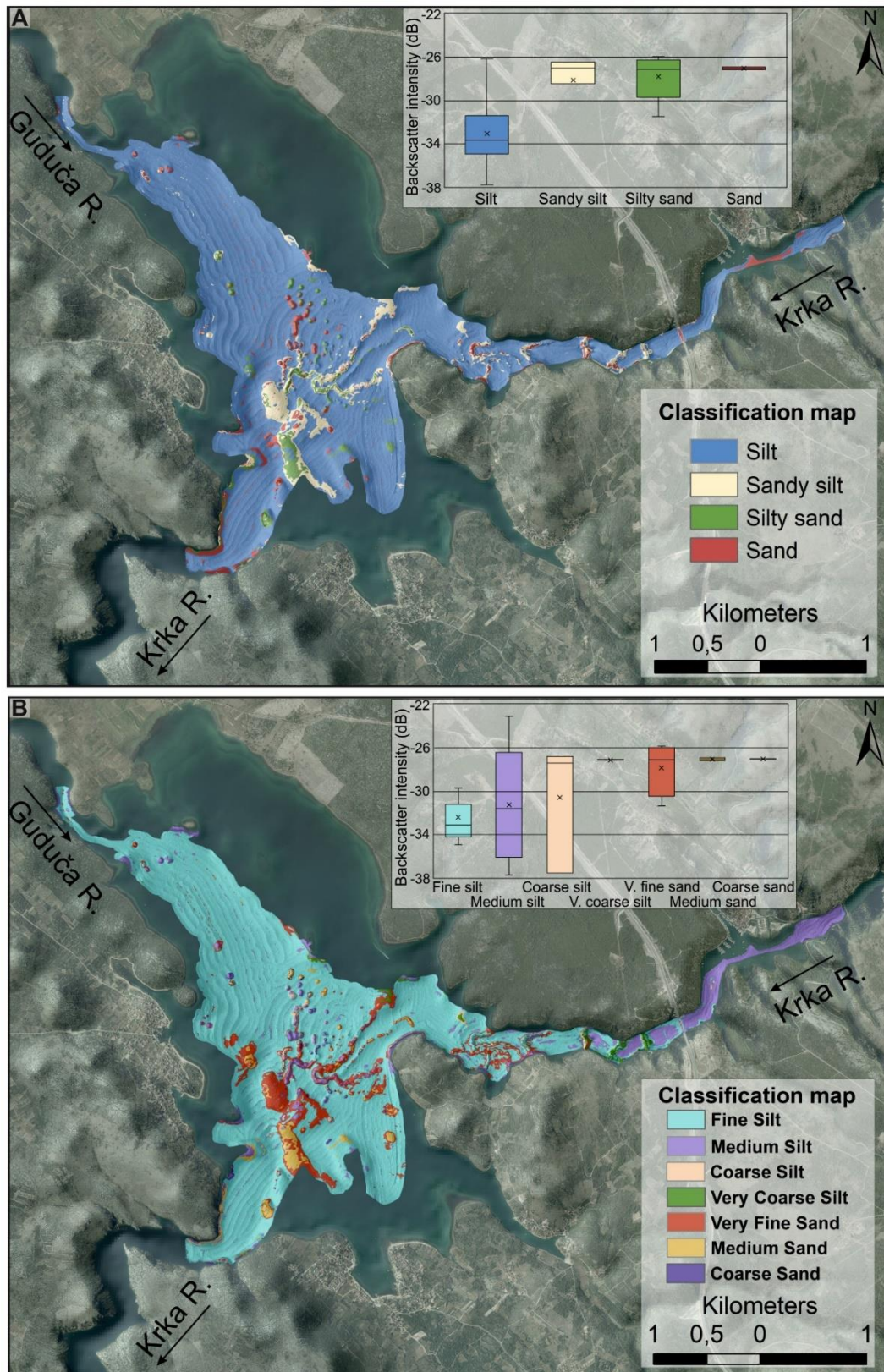


Figure 5.8 The map illustrates sediment distribution in the study area, derived from OBIA of MBES backscatter data and PSA. The distribution is categorized into two sets: (A) comprising four classes and (B) comprising seven classes. Additionally, box-and-whisker plots depict the mean backscatter intensity across these classes.

5.1.2 Middle Adriatic shelf area

The studied area consists of several morphological units, the palaeochannel from sv. Ante Channel to the south-eastern shore of Zlarin island, the shelf (submerged Krka delta plain) between Zlarin and Žirje islands and Primošten on the east (Fig. 5.9). The northernmost part of the surveyed area encompasses a submerged Krka River channel heading in the N-S direction (Fig. 5.9). The submerged channel features steep sides and a flat sea bottom, with the island of Zlarin bounding it on its western flank. The channel is 400 m to 600 m wide, and the flat seabed is between 380 m and 400 m wide. It extends approximately 7500 m from the end of the Sveti Ante Cannal to the tip of Zlarin Island (Fig. 5.9). The area widens into a shelf to the south and spreads to the west until the seamount (an extension of the small island of Komoriga; Fig. 5.9). The central part of the shelf is 2 to 3 m lower than the surroundings and forms an extension of the channel to the south until it reaches the submerged island that protrudes from the shelf area at -71 m bsl for 45 meters (Fig. 5.9). An additional channel is visible south of the seamount, incised up to 4 m to the flat. A SW part of the shelf has a semi-circle-shaped edge that slopes into a 5-6 m deeper flat seafloor towards the west (Fig. 5.9). Two seamounts are present in this shelf area, which slope gently to the south until the depth of 88 m where steeper, semi-circled slope occurs, oriented generally towards SW (Fig. 5.9). The western edge features another seamount with two flat-top peaks reaching depths of -53 to -55 m bsl (Fig. 5.9). In the southernmost part of the survey area, a seamount occurs on the shelf slope at a depth of 105m b.s.l. and protrudes to 88 m bsl (Fig. 5.9).

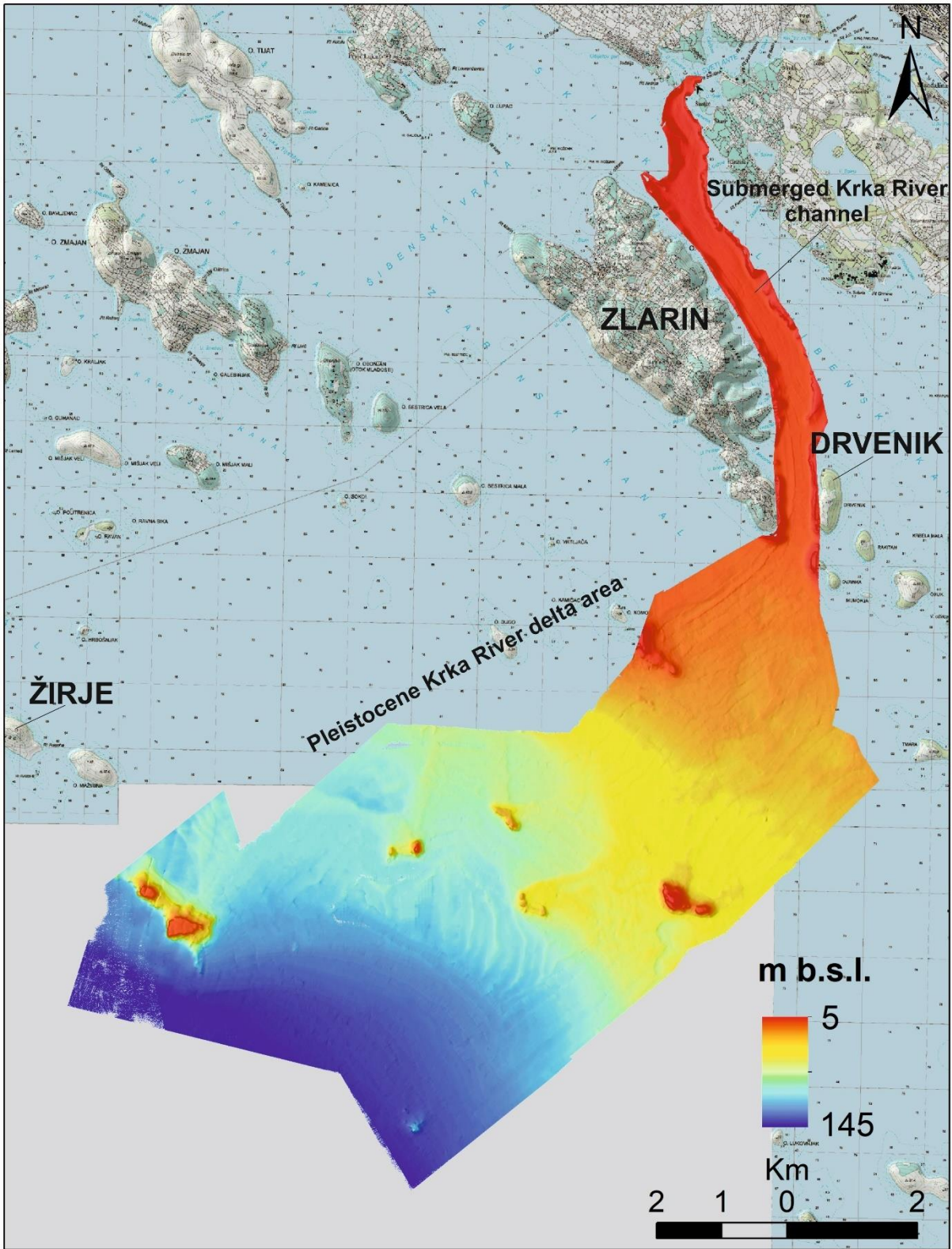


Figure 5.9 Bathymetry map of the submerged Krka River channel between the mainland and the island of Zlarin, and the Pleistocene Krka River delta area, representing the results obtained from the MBES survey.

The MBES backscatter (BS) intensity ranged from -9 to -49 dB (Fig. 5.10). The backscatter physiography of the survey area consisted of low (black), acoustic backscatter surfaces on the flat bottom, whereas the rocky parts and canyon sides exhibited high surface backscatter responses (Fig. 5.10). The submerged Krka River channel between the mainland and the island of Zlarin shows lowest backscatter values (<-30 dB), as well as the flat seafloor across the shallow shelf area. The rocky areas show high backscatter response, with values >-25 dB (Fig. 5.10).

The unsupervised classification allowed the division of sediments into three classes, representing softer (finer-grained) sediments (Class 1), coarser sediments (Class 2), and rocky areas or rocks covered with thin amounts of sediment (Class 3) (Fig. 5.11). A submerged channel in the northernmost part of the surveyed area mainly consists of rocky, steep sides, while a central part consists of a mosaic of fine-grained and coarse-grained sediment (Fig. 5.11). At the exit from the channel (the south-eastern edge of Zlarin Island), a strip of fine-grained sediment along the channel extends towards the south (Fig. 5.11). A mosaic of coarser-grained sediments, together with rocky seafloor and a pair of seamounts as an extension of the islet Komoriga, surrounds this area. The fine-grained zone is situated amidst elongated rocky outcrops at the southern end and rises approximately 1 meter above the seafloor (Fig. 5.11). The central-to-eastern part of the survey area is characterized by a slightly elevated (2-5 m) rocky plateau with two protruding rocky seamounts, one eastern, more prominent, extending out for 50 m, and the other western extending for 10 m (Fig. 5.11). Soft sediment surrounds the rocky plateau, which extends towards the west where another rocky seamount is visible, extending upwards for 20 m (Fig. 5.11). The rocky zone extends westward till the edge of the surveyed area. The southern part of the survey area has a smooth morphology covered with coarser sediment. On the slope, furthest to the south is yet another rocky seamount 25 m high. The southeastern region of the survey area shows two flat-top rocky seamounts 33 m high.

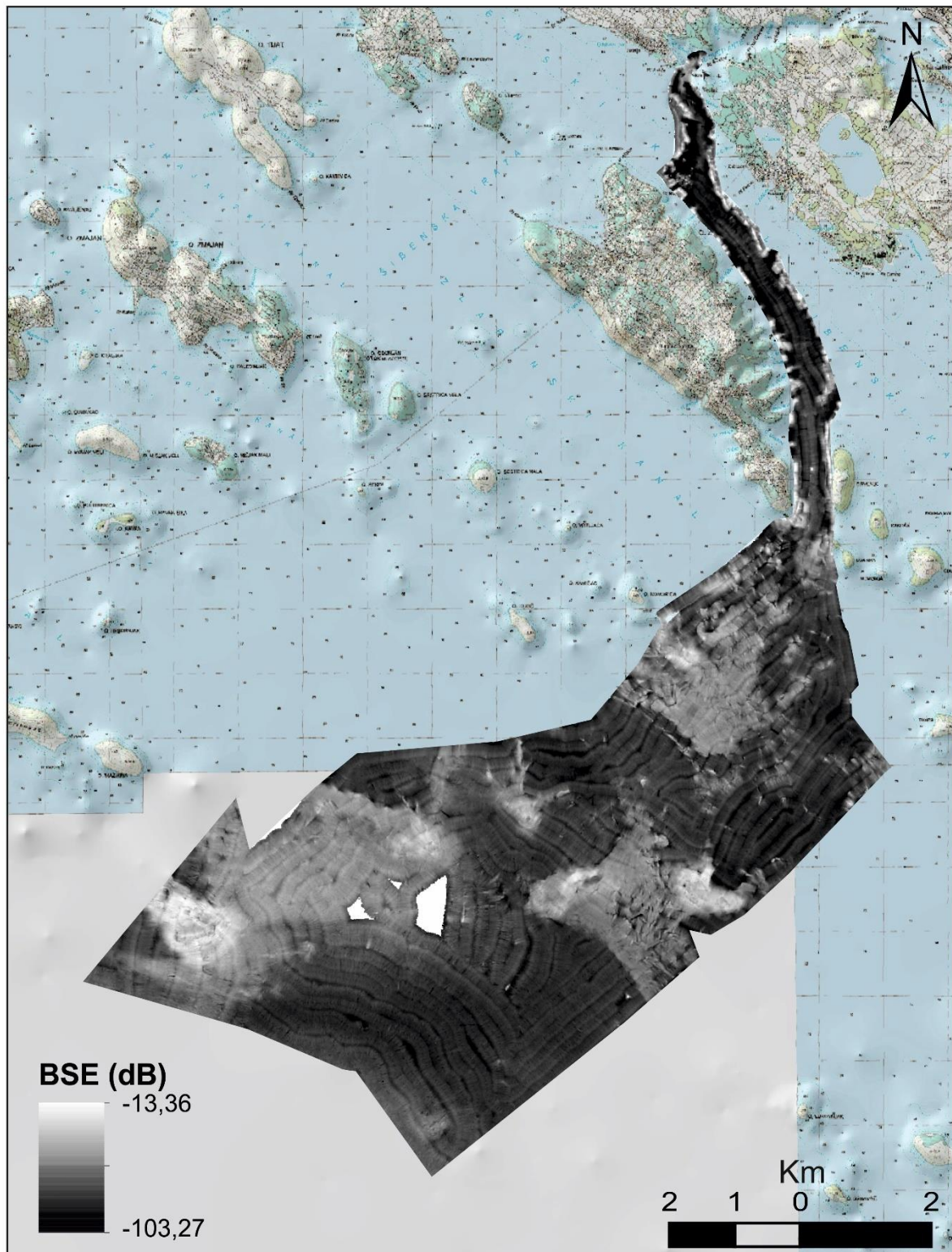


Figure 5.10 Backscatter distribution map of the submerged Krka River channel between the mainland and the island of Zlarin and the Pleistocene Krka River delta area.

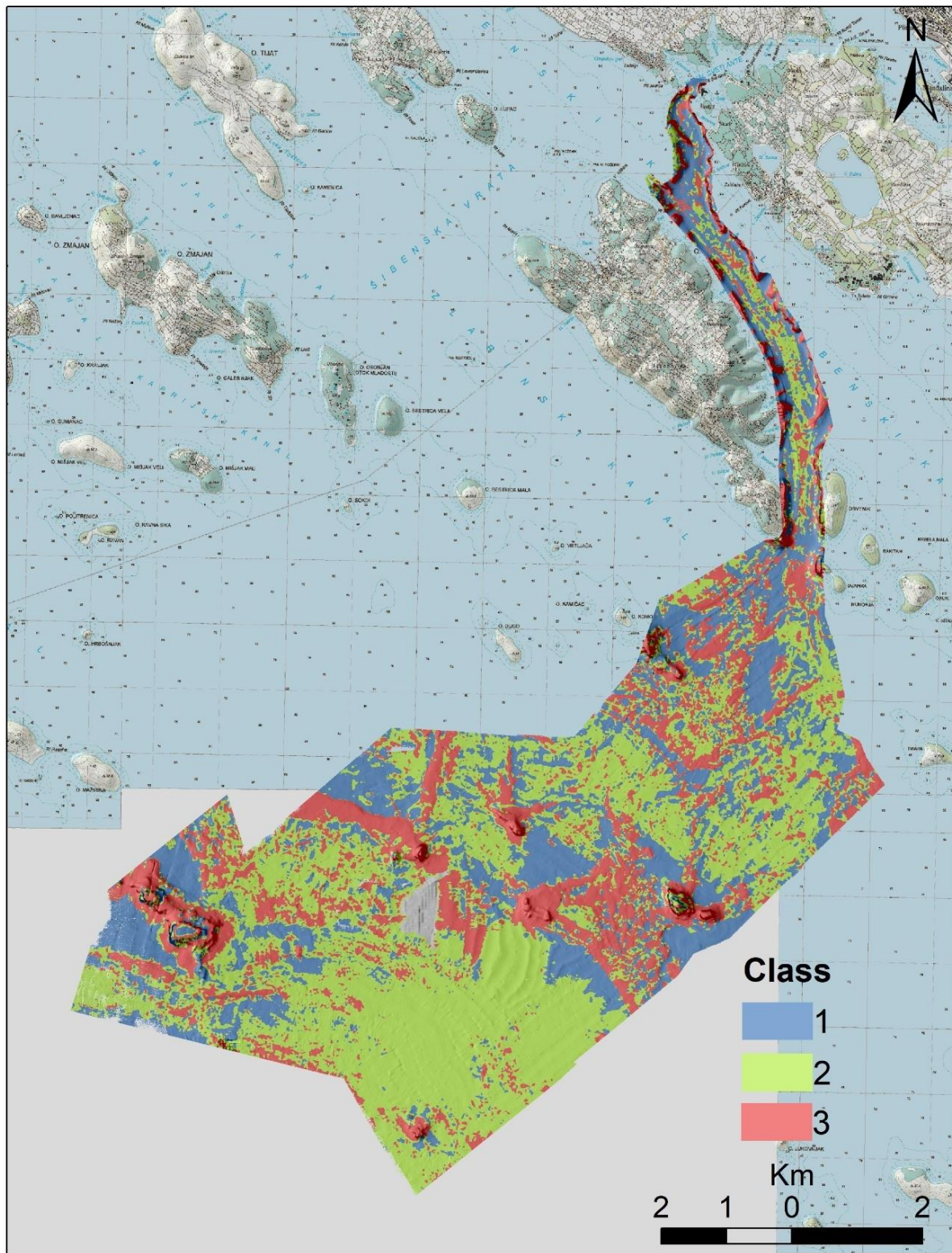


Figure 5.11 The map illustrates sediment distribution in the study area, derived from unsupervised classification of MBES backscatter data.

5.2 Seismic stratigraphy

The reflection patterns vary between the recent estuary and the Pleistocene incised valley and deltaic deposits. Therefore, the following seismostratigraphic description and interpretation is divided into two subchapters: the Krka River estuary and the Middle Adriatic shelf area. These exceptional conditions present a unique opportunity for conducting a detailed study of a complex karst environment located along a microtidal coast with limited sediment supply.

5.2.1 Krka River estuary

High-resolution seismic profiles (128), with a total length of 129.4 km, were recorded within the Krka River estuary (Fig. 4.2A). Seismic data showed up to 20 m of sedimentary infill of the estuary to the acoustic basement. Based on the concept of seismic stratigraphy by Mitchum et al. (1977) and Xu and Haq (2022), five main seismic facies and gas accumulations were identified (Fig. 5.12) and assembled into five seismic units: the acoustic basement (SU0) and four seismostratigraphic units (SU1-4) bounded by a basal erosion surface or palaeorelief (p) and unconformity surface SH1 and SH2 (Figs. 5.13–5.21). The interpreted horizons and units were correlated with the core lithostratigraphy. A constant acoustic velocity of 1500 msec⁻¹ was assumed and adopted for the seismic-to-core correlation.


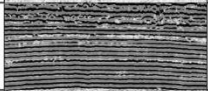


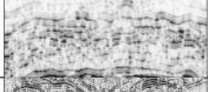




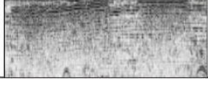
UNIT	FACIES	SEISMIC PATTERN	CONTINUITY	AMPLITUDE	FREQUENCY	REFLECTOR CONFIGURATION	INTERPRETATION
SU4	F4d		Low	High	Low	Seismic diffractions	Coarse-grained deposits?
	F4c		High	High	High	High frequency parallel	Marine/estuarine deposits
	F4b		Medium to low	Medium to low	Low to medium	Medium frequency parallel	
	F4a					Noisy chaotic to transparent	
SU3	F3b		Low	Low	Low	Chaotic	Fluvio-lacustrine to brackish deposits
	F3a		Low to medium	Medium to high	Low	Chaotic to wavy subparallel to parallel	Fluvio-lacustrine deposits
SU2	F2					Reflection free to noisy chaotic with high amplitude upper reflector	Tufa deposits
SU1	F1					Reflection free	Fluvial deposits
SU0	F0					Reflection free to noisy chaotic with high amplitude upper reflector	Cretaceous limestones
Gas			Very low			Acoustic blanking or enhanced reflections	Gas buildup

Figure 5.12 Description of seismic units and facies identified in the seismic profiles recorded within the Krka River estuary.

A major erosional palaeorelief surface (p) is identifiable in most areas of the Krka River estuary. The palaeorelief surface corresponds to the base of the depositional basin (top of the acoustic basement (SU0)) (Fig. 5.13–5.21). The basement and palaeorelief can be mapped at the margins of the estuarine valley, in the palaeochannels of the Krka and Guduča Rivers. In some areas, the basement is not recognized due to the limited system penetration or is masked by multiple reflections. The acoustic basement is characterized by reflection-free to noisy chaotic seismic facies (F0; Fig. 5.12). Furthermore, in the palaeochannels of the Krka and Guduča Rivers, the basement forms an angular unconformity with the overlying onlapping seismic units. The bedrock surface is irregular in the palaeochannels, while in the other areas of the river valley, the palaeorelief surface is smooth.

Seismic unit 1 (SU1)

Above the palaeorelief surface, four seismic units compose the sedimentary infill of the Krka River estuary (Figs. 5.13–5.21). The SU1 unit exhibits transparent facies (F1; Fig. 5.12) and overlays the acoustic basement. SU1 is not recognized in all seismic profiles and is locally thin (up to 4.5 m; Figs. 5.17–5.21). Its lower boundary is the palaeorelief surface, and the upper boundary is the SH1 horizon of the SU3 unit.

Seismic unit 2 (SU2)

SU2 overlays the acoustic basement, or SU1, with a thickness varying from 8 ms to approximately 24 ms two-way travel time (TWTT; ~6–20 m). SU2 is very pronounced and protrudes from the basement and adjacent units (Figs. 5.15–5.21). Owing to poor acoustic penetration, this unit exhibits seismically transparent or noisy chaotic facies (F2; Fig. 5.12) with no visible lower boundary in the seismic profiles. In some areas of the estuary, SU3 and SU4 overlie SU2. SU2 is present only in the narrow area of the estuarine valley and in the central part of Prokljan Lake.

Seismic unit 3 (SU3)

SU3 predominated in most study areas, extending from the acoustic basement to SU4 (Figs. 5.13–5.21). The thickness of this unit is highly variable, varying from 1.5–20 ms (0.8–15 m). Its lower boundary is an unconformable palaeorelief surface (p) or SH1, while SH2 is its upper boundary, which is also an unconformity surface. SH2 is a strong reflection and the most prominent surface identified in all seismic profiles. It is irregular, showing erosive scours, which are present in the small basins in SU2; these scours are up to ~130 m wide and have smoothed sides cutting into the lower SU3 (Figs. 5.15–5.19). SU3 consists of irregular wavy aggradational parallel to subparallel (concave up) or chaotic reflectors (F3a and F3b; Fig. 5.12). Reflectors are laterally continuous in some locations; however, in other areas, they show low continuity and are intercalated with acoustically semi-transparent parts. SU3 can be further divided into two subunits, SU3a and SU3b (Figs. 5.15, 5.17, 5.18), although those subunits may not be clearly identified in all seismic profiles. Therefore, in some seismic profiles, only

the SU3 unit is indicated. SU3a composes most of the SU3 unit and exhibits strong irregular wavy aggradational reflectors (F3a; Fig. 5.12). SU3b is a very thin subunit with facies characteristics similar to those of SU3a, but the reflectors have lower amplitudes (F3b; Fig. 5.12).

Seismic unit 4 (SU4)

SU4 is the uppermost unit of the estuary (Figs. 5.13–5.21). Its thickness varies from 0.7 ms to 18 ms (0.5 and 15 m) and represents the thickest unit in the palaeochannels of the Krka and Guduča Rivers. The small depositional basins developed above the acoustic basement and SU2. SU4 overlies unit SU3 and, in some parts, SU0 and SU1, and is bounded by an erosional SH2 surface and a subhorizontal seafloor reflector (SF). The acoustic facies of SU4 exhibit four types of subfacies (F4a, F4b, F4c, and F4d; Fig. 5.12). F4a is present locally in the palaeochannels as the noisy chaotic to seismically transparent facies. F4b demonstrates low frequency aggradational parallel reflectors, which show low to medium continuity and amplitude. F4b gradually transitions into subfacies F4c, which exhibits aggradational parallel reflectors of high continuity, amplitude, and frequency. Subfacies F4d demonstrated a series of lateral diffractions in most areas. Additionally, acoustic blanking due to gas (free methane in the sediments) can be observed in this unit (Figs. 5.13–5.15).

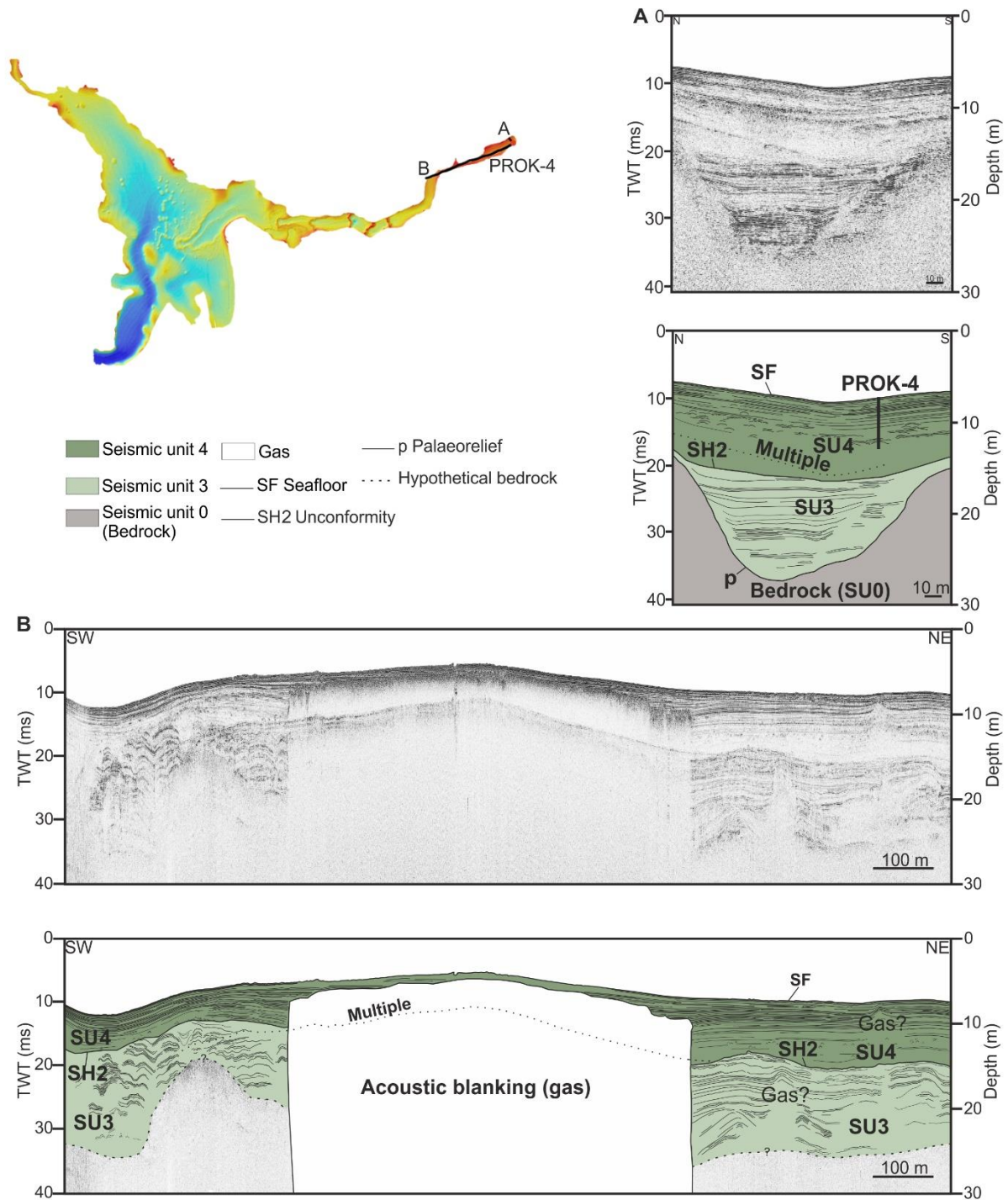


Figure 5.13 A, B. Processed seismic profiles and their corresponding stratigraphic interpretation of the Krka River estuary from the upstream and narrow tract of the estuary. The sediment core PROK-4 is plotted on a seismic profile (B).

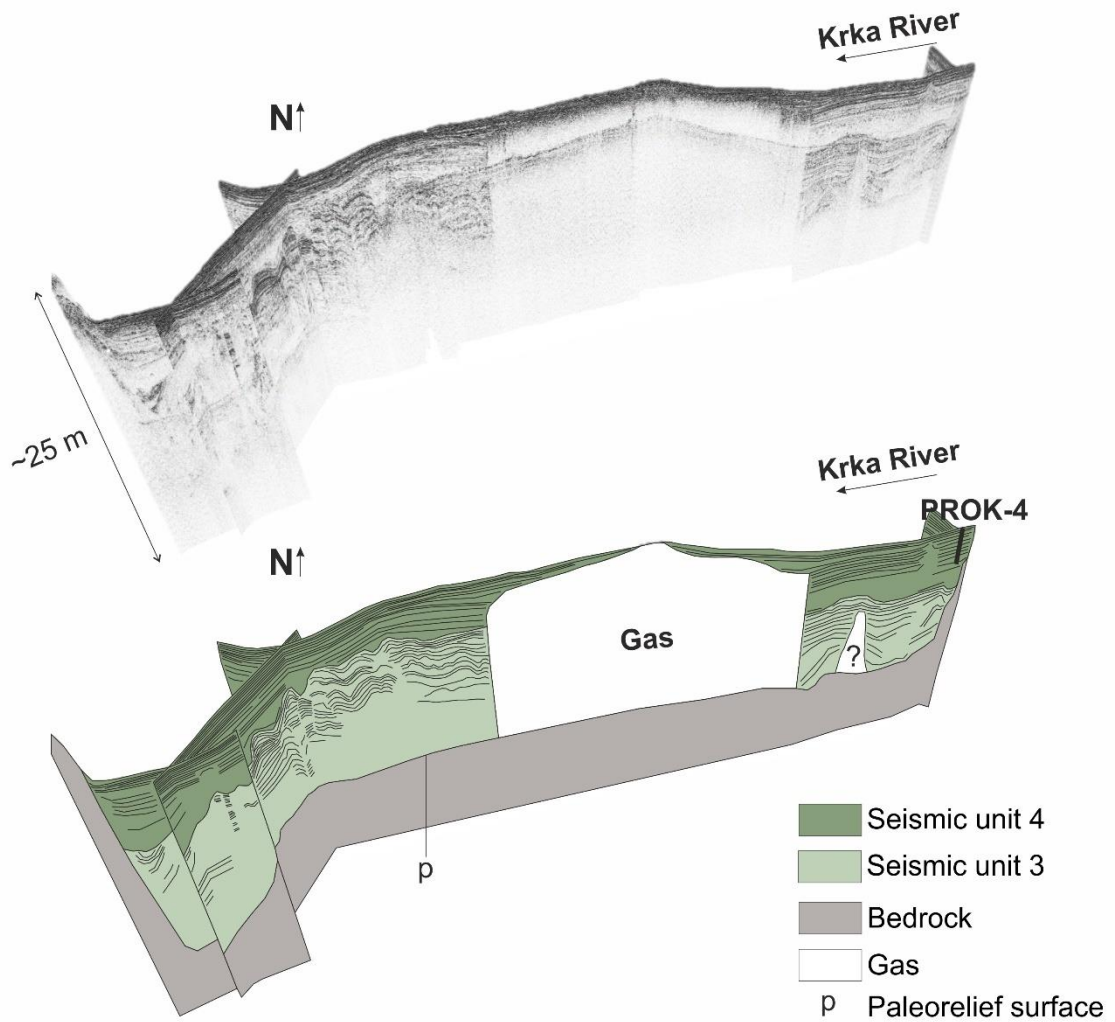
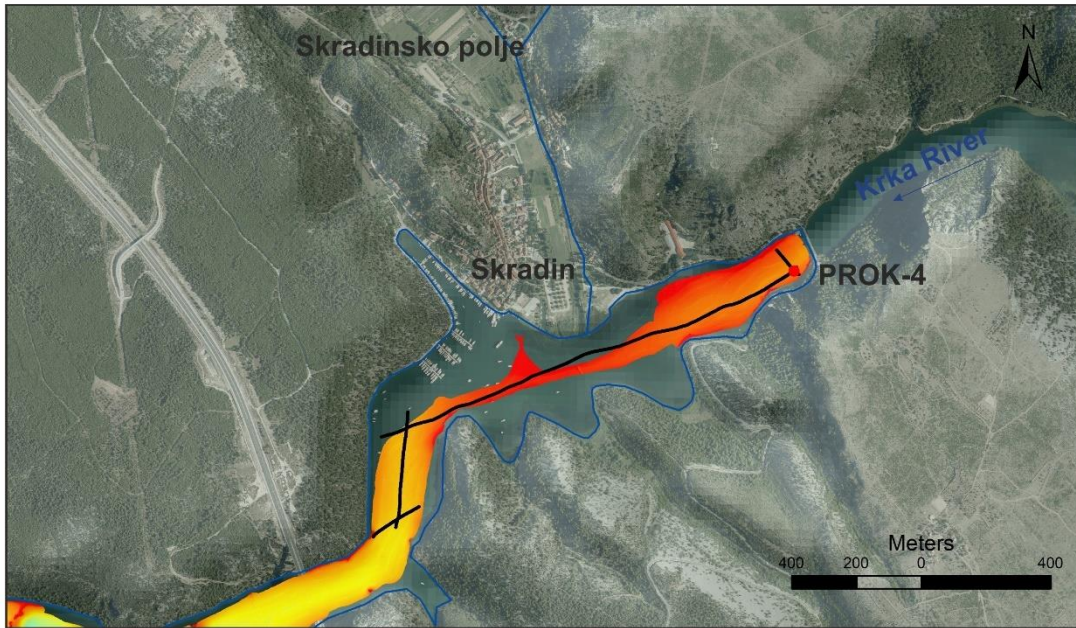


Figure 5.14 A detailed multibeam bathymetric image of the upper part of the Krka River estuary, along with a fence diagram of 3D and interpreted seismic profiles, illustrates the distribution of seismic units and areas shadowed by gas accumulation.

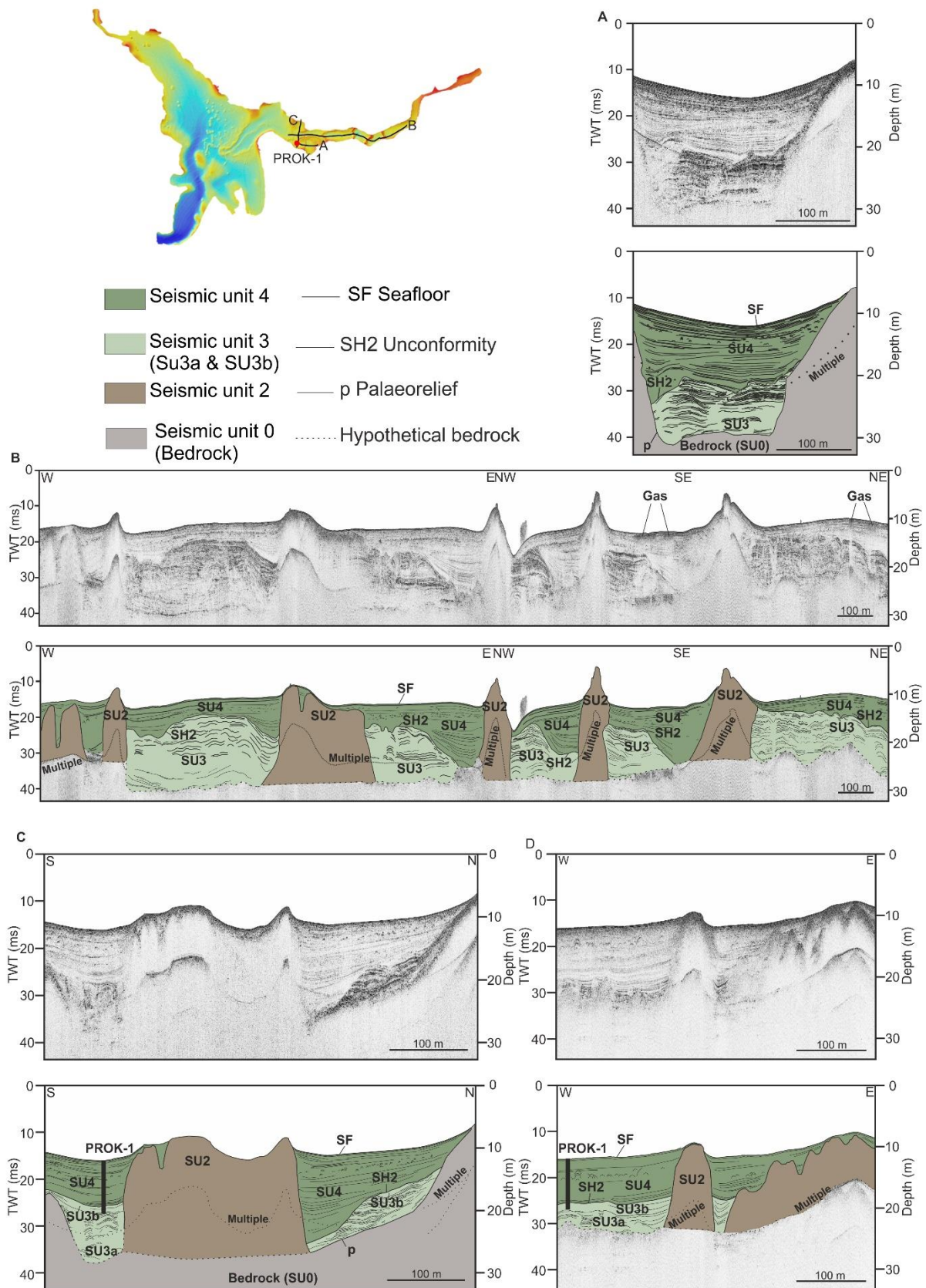


Figure 5.15 A, B, C. Processed seismic profiles and their corresponding stratigraphic interpretation of the Krka River estuary from the upstream and narrow tract of the estuary. The sediment core PROK-1 is plotted on seismic profiles (A) and (B).

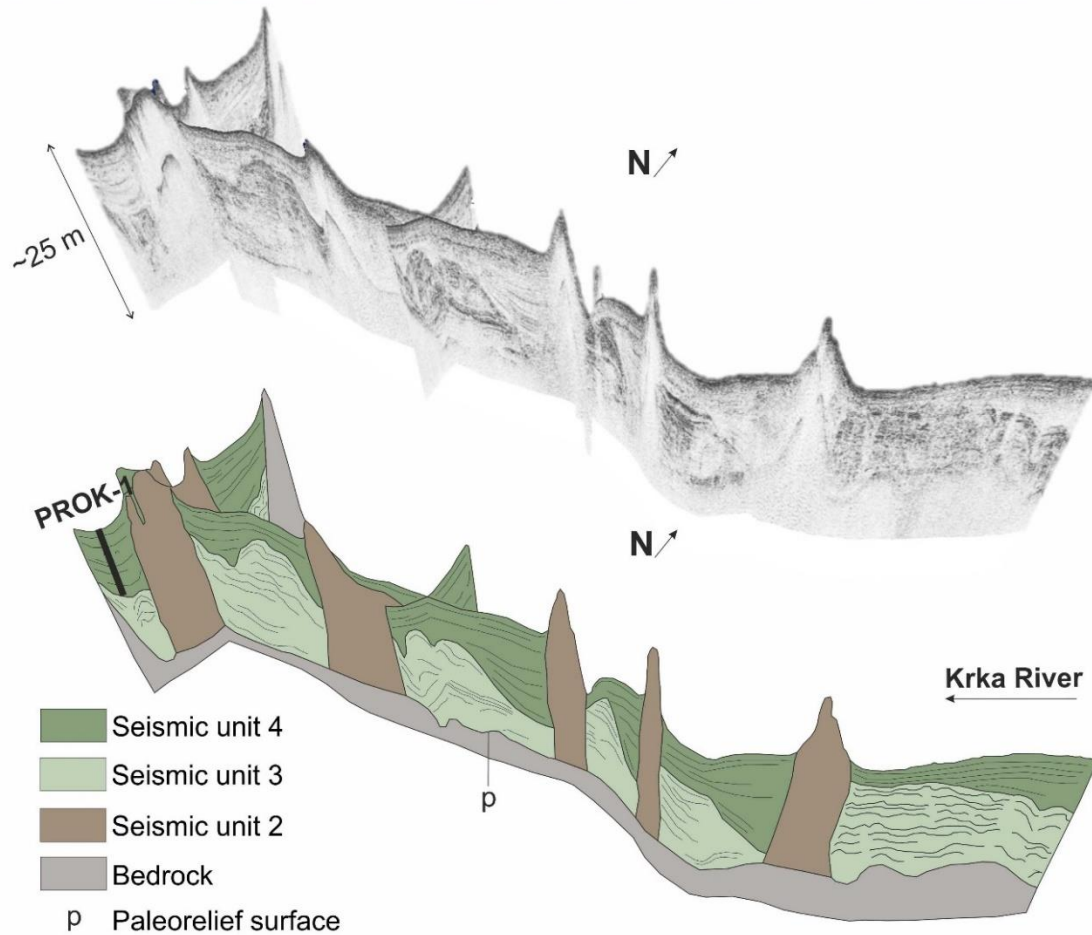
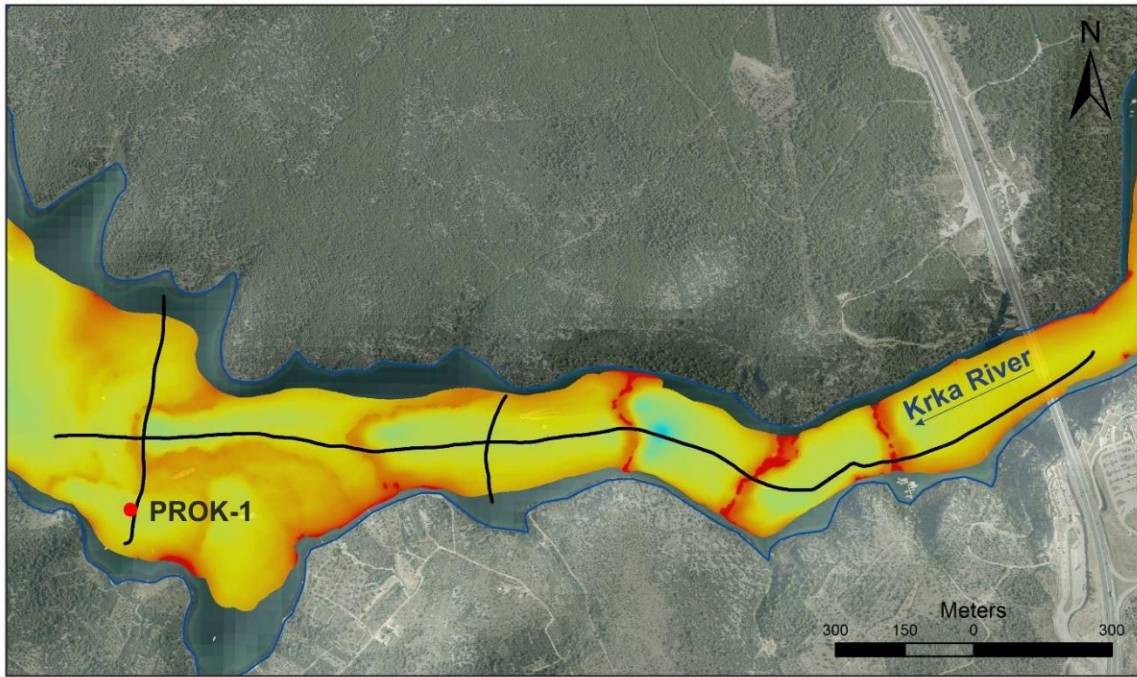


Figure 5.16 A detailed multibeam bathymetric image of the narrow central part of the Krka River estuary, along with a fence diagram of 3D and interpreted seismic profiles, illustrates the distribution of seismic units.

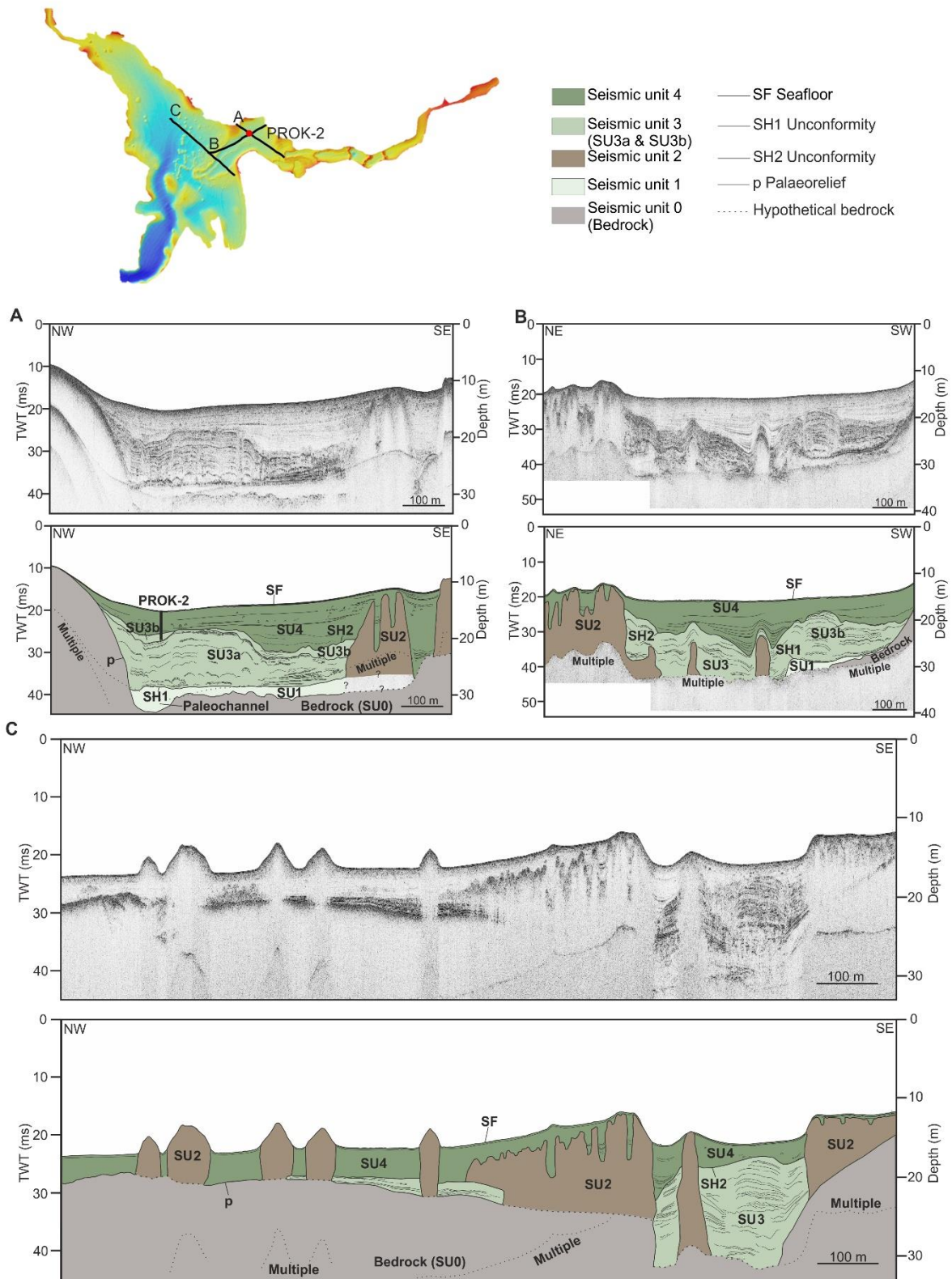


Figure 5.17 A, B,C. Processed seismic profiles and their corresponding stratigraphic interpretation of the Krka River estuary from the central part of the estuary. The sediment core PROK-2 is plotted on a seismic profile (A).

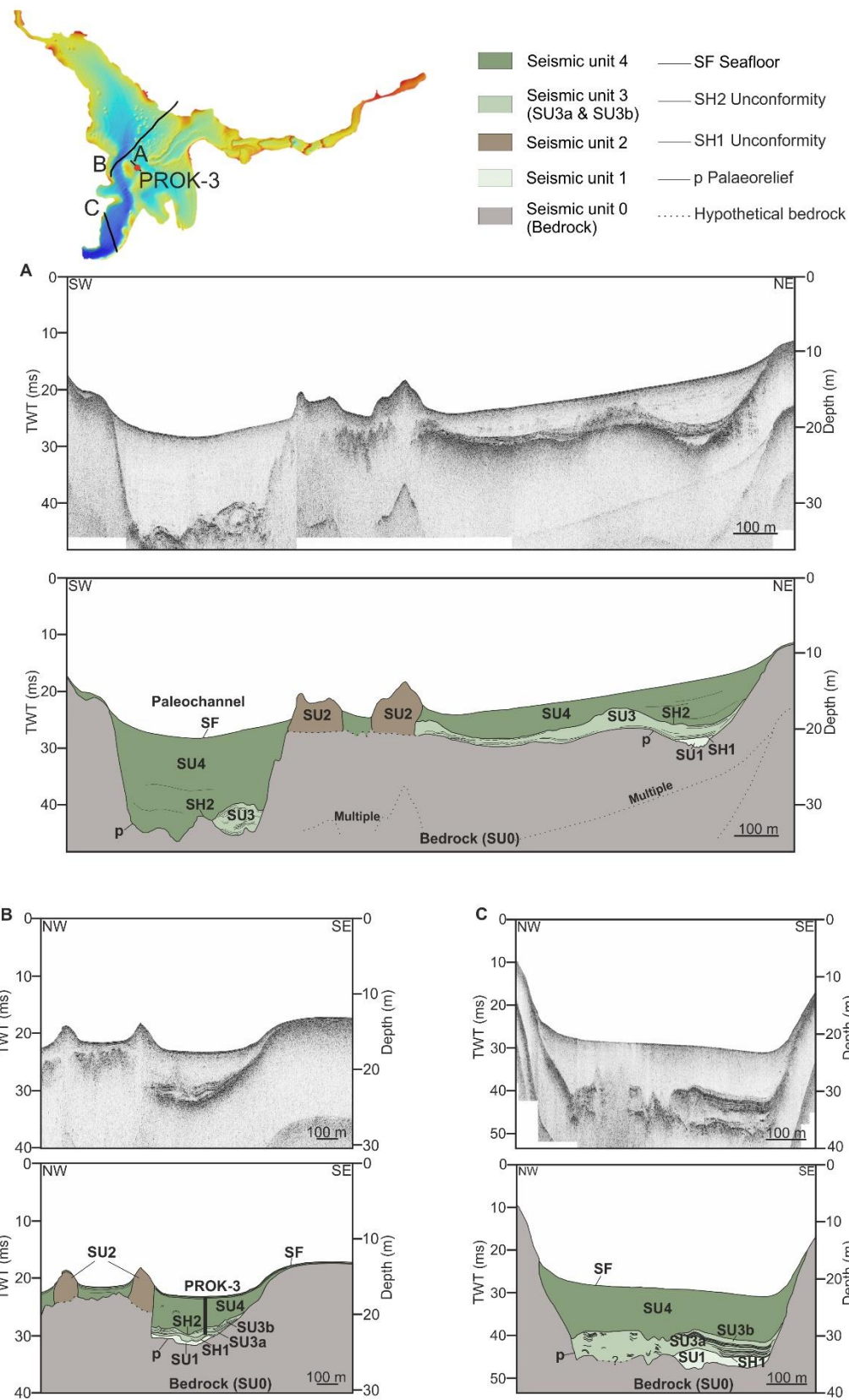


Figure 5.18 A, B, C. Processed seismic profiles and their corresponding stratigraphic interpretation of the Krka River estuary from the central and southern part of the estuary. The sediment core PROK-3 is plotted on a seismic profile (B).

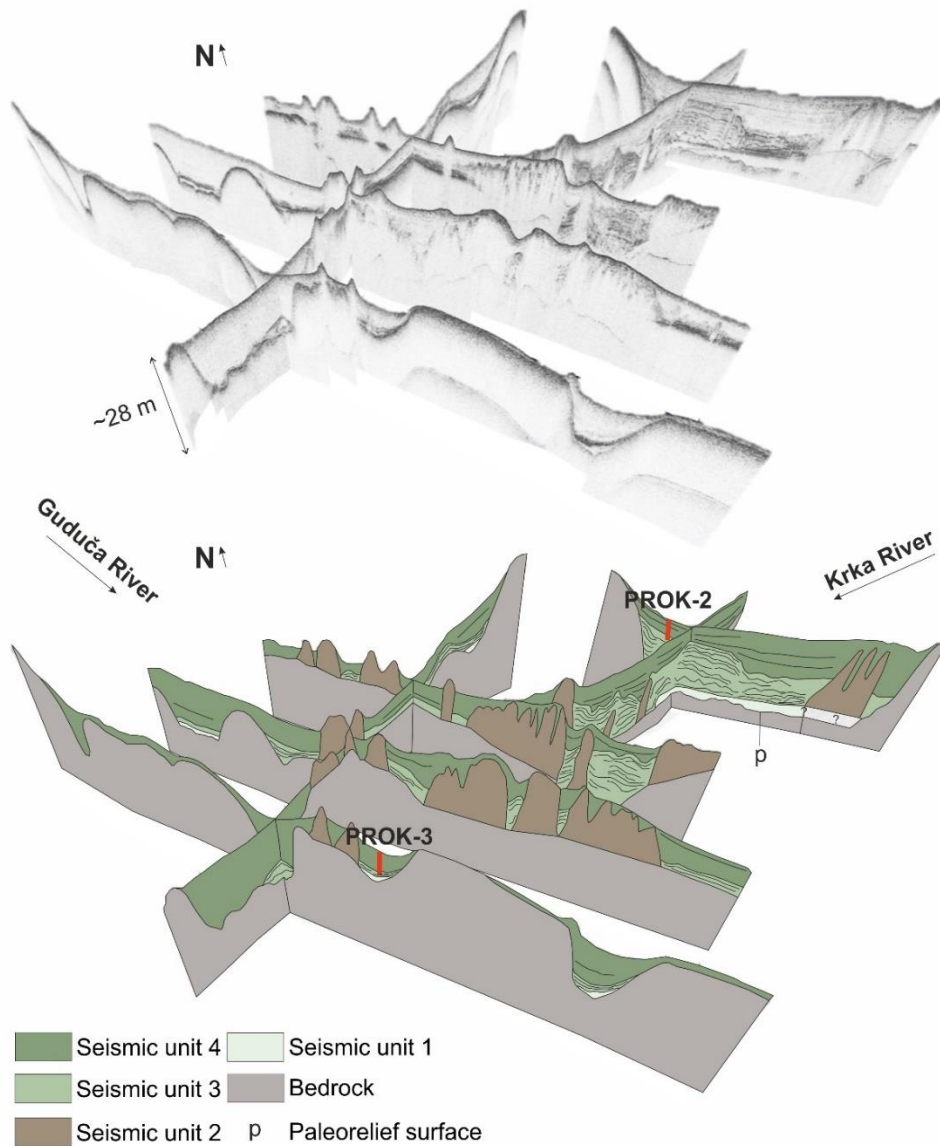
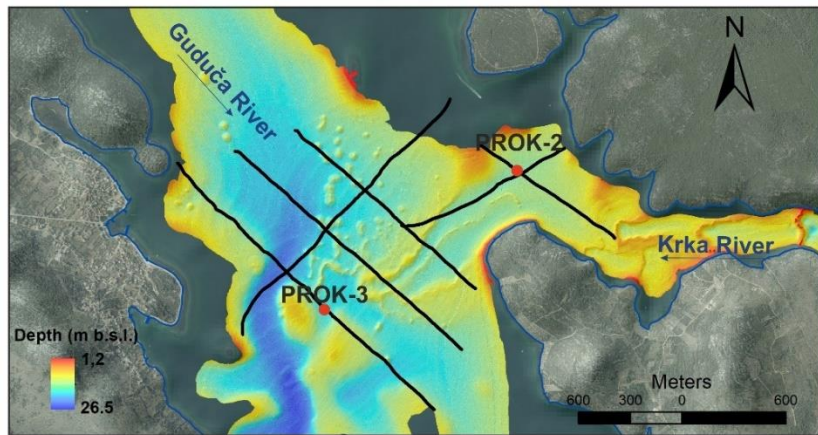


Figure 5.19 A detailed multibeam bathymetric image of the central part of Prokljan Lake, along with a fence diagram of 3D and interpreted seismic profiles, illustrates the distribution of seismic units.

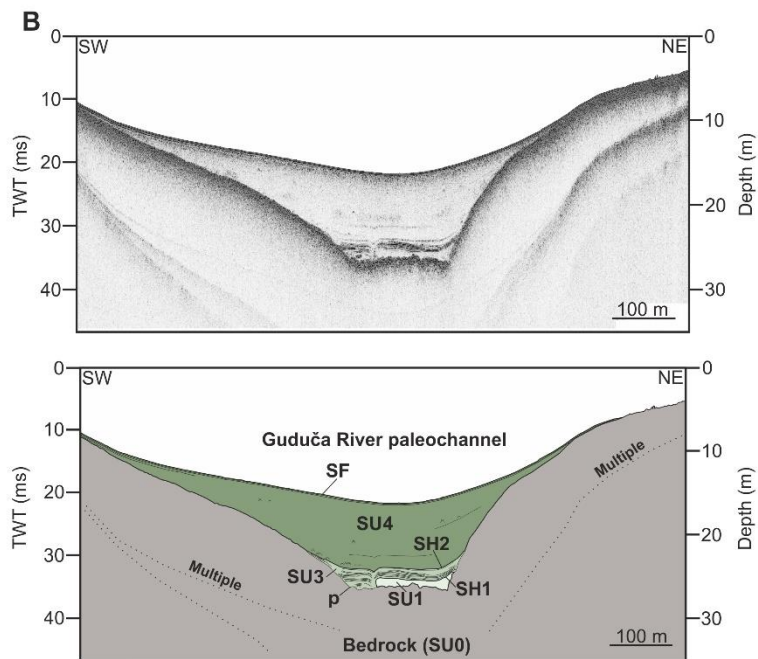
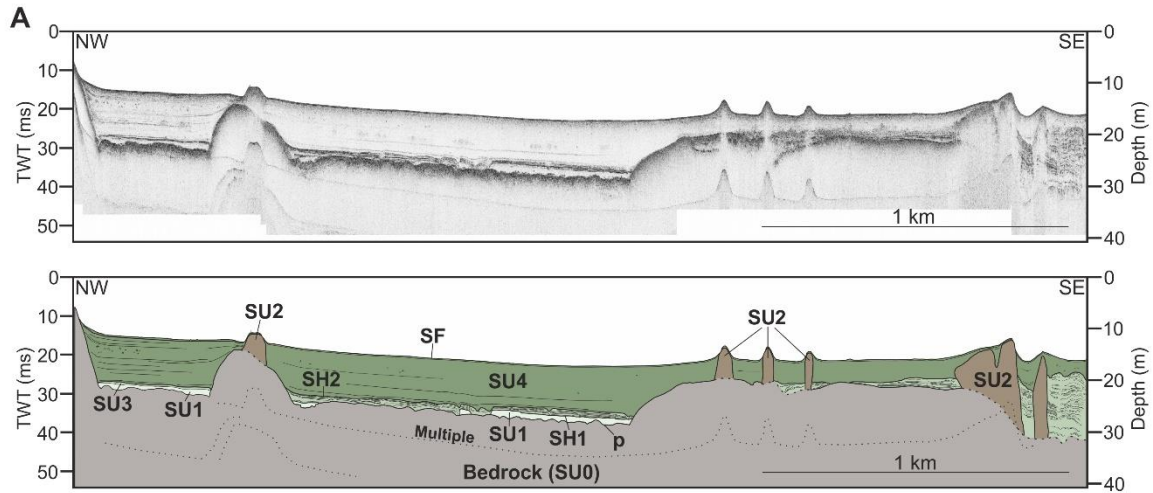


Figure 5.20 A, B. Processed seismic profiles and their corresponding stratigraphic interpretation of the central and northwestern part of Prokljan Lake.

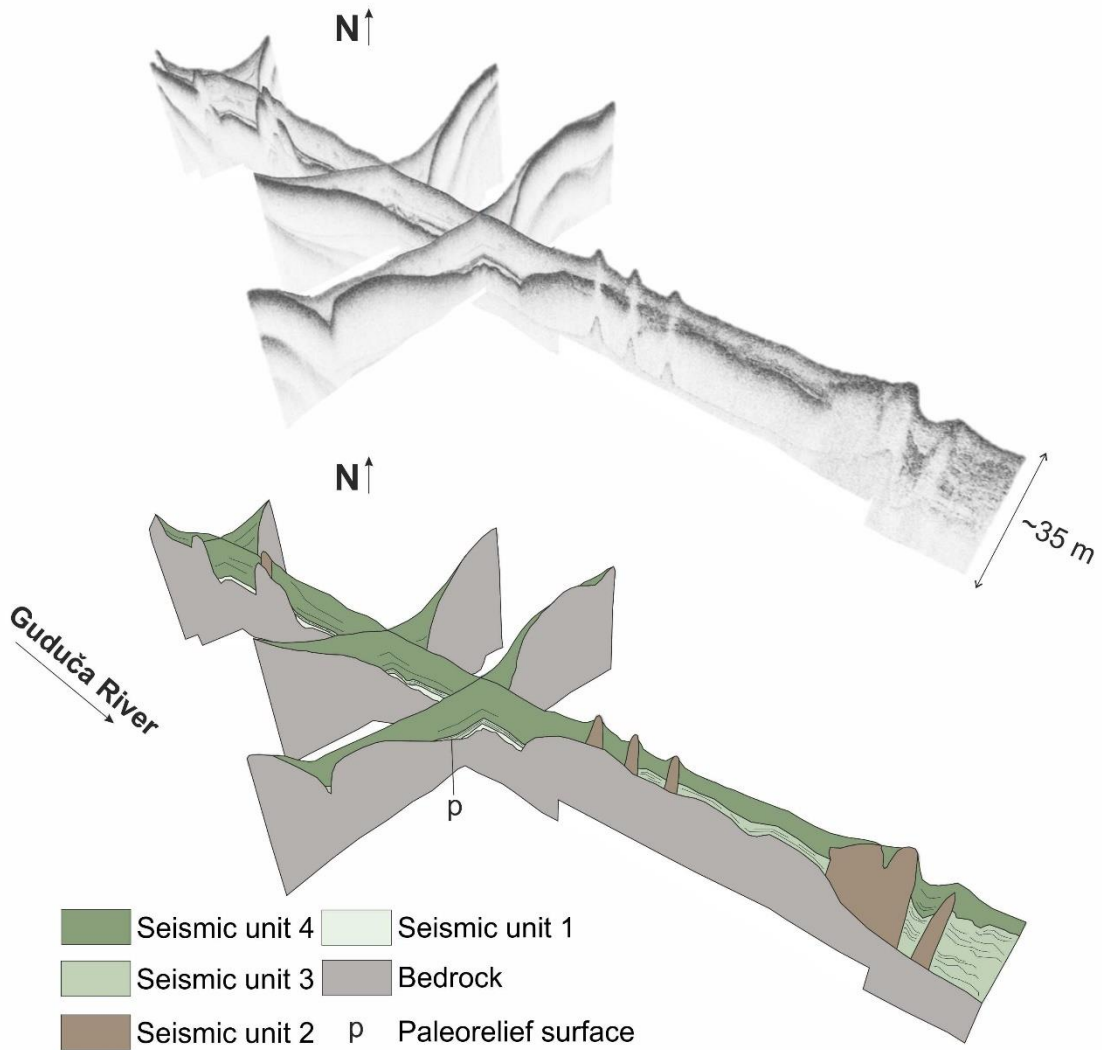
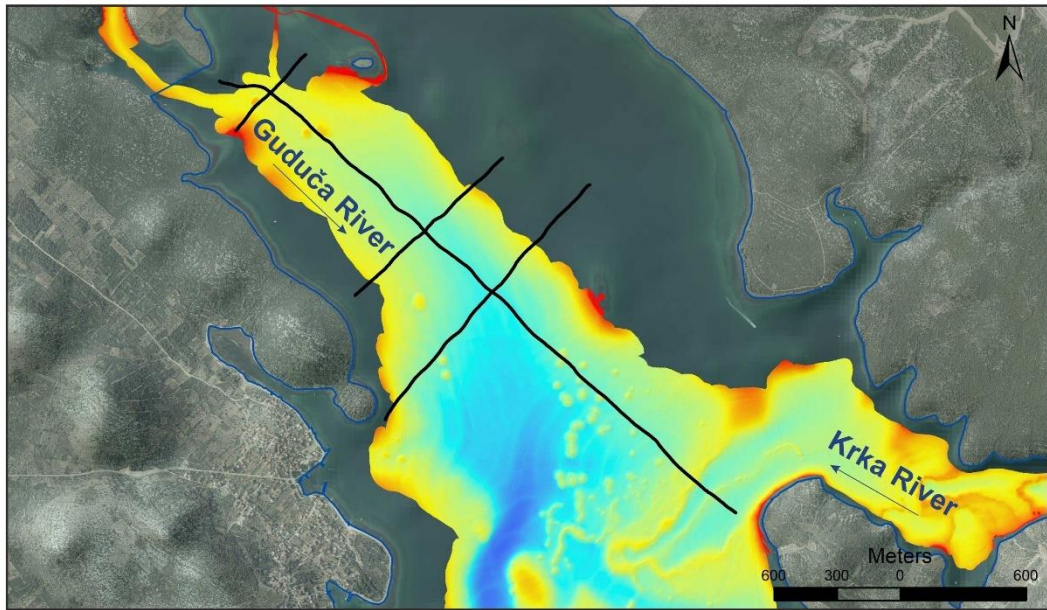


Figure 5.21 A detailed multibeam bathymetric image of the central and northwestern part of Prokljan Lake, along with a fence diagram of 3D and interpreted seismic profiles, illustrates the distribution of seismic units.

5.2.2 Middle Adriatic shelf area

High-resolution seismic profiles (147), with a total length of 552.95 km, were recorded within the submerged Krka River canyon between the mainland and the southern part of the island of Zlarin, and the Pleistocene Krka River delta (shallow shelf area). A key stratigraphic surface of regional extent and several seismic facies, described below, were recognized in this area, considering the shape, continuity, and frequency of the reflectors (Fig. 5.22). These reflection configurations were used to interpret the lithotypes, environments and depositional processes. A constant acoustic velocity of 1515 msec^{-1} (the average speed of sound in the water column was determined using the Valeport SWIFT CTD probe during the survey) was adopted for the seismic-to-core correlation (Novak et al., 2019).

Seismic facies AB (Acoustic basement)

An acoustic basement is detected in seismic profiles as high-amplitude discontinuous reflections without any internal characteristics (acoustically opaque; Figs. 5.22–5.28). This seismic facies corresponds to the base of the depositional basins, where the upper limit of this facies is marked by a discontinuous surface. This surface was interpreted as a subaerial erosional surface that was configured during subaerial exposure at the maximum sea level fall. It can be traced across the shelf from water depths between 60 and 180 m. SF AB is sometimes obscured by acoustic masking but is visible along the shelf of the central part of the study area where it crops out on the contemporary sea floor.

Seismic facies F (Fluvial deposits)

Seismic facies F is characterized by a reflection free to discontinuous parallel reflectors of very low amplitude and frequency (Fig. 5.22). This facies is recognized in the incised part of the Krka River palaeochannel above the acoustic basement (Figs. 5.23 and 5.24). Its lower boundary is the subaerial erosional surface and its upper is another erosional surface. The thickness of this facies goes up to approx. 7 m. These deposits were not reached by coring.

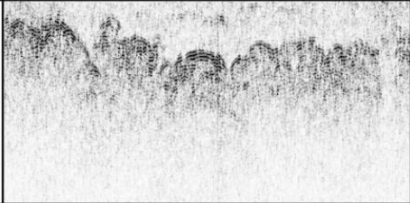
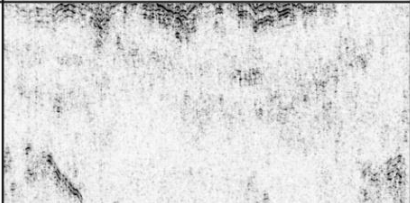
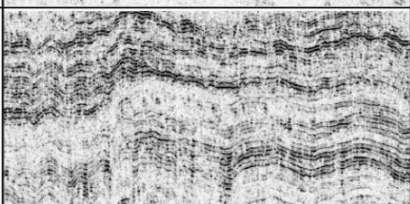

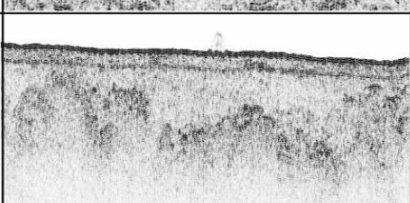

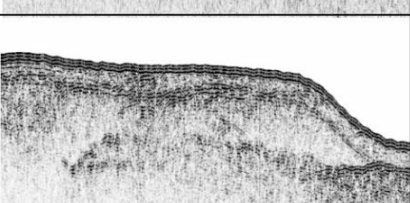
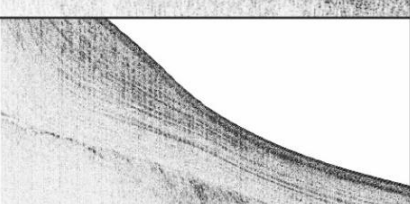
	Seismic image	Facies description
Acoustic basement (SF AB)		High amplitude irregular reflectors (relief) Reflection free to noisy chaotic facies
Fluvial (SF F)		Transparent to chaotic facies, preserved in the lowest parts of the incised Krka River valley Fluvial deposits
Fluvial/brackish (SF F/B)		High to low amplitude, medium continuity, wavy to chaotic subparallel reflectors Late Pleistocene and the Holocene fluvial to brackish deposits
Estuarine/marine (SF E/M)		Transparent facies to low amplitude, low continuity parallel reflectors Holocene estuarine/marine deposits
Channel fill (SF CH)		Transparent seismic horizons infilling incised paleo-channels Delta top distributary channels
Sand sheet? (SF SS)		Chaotic noisy seismic horizons Present at the both sides of channel infills Coarse-grained deposits (sand sheet?)
Terrestrial deposits? (SF TD)		Transparent to chaotic seismic facies Present in the westernmost part of the studied shallow shelf area Pleistocene terrestrial deposits
Clinoforms (SF CL)		Low to high-amplitude, high continuity and frequency seaward dipping continuous reflectors Oblique to sigmoid clinoforms Prograding to aggrading prodelta Soft sediment deformations are present

Figure 5.22 Description of seismic facies identified in the seismic profiles recorded within the submerged Krka River channel located between the mainland and the island of Zlarin, and the shallow shelf area.

Seismic facies F/B (Fluvial/brackish deposits)

Seismic facies F/B forms a highly variable body of sediment overlying the SF F or AB. SF F/B is characterized by laterally irregular wavy parallel to subparallel or chaotic reflectors of low to high amplitude and frequency. Within this sediment body an erosional surface can be recognized (Fig. 5.23) marking a probably short terrestrial phase of deposition. These deposits are truncated by an erosional surface of higher amplitude reflector. The thickness of these sediments is variable, varying between 4 m and approx. 10 m.

Seismic facies E/M (Estuarine/marine deposits)

SF E/M is the thin uppermost sedimentary body in the incised palaeochannel with thickness varying up to 2 m. This facies is marked by a reflection free to chaotic reflectors (Fig. 5.22) and is deposited above the SF F/B and is bounded by a seafloor reflector (Figs. 5.23 and 5.24). The seabed erosion of this facies is shown in Fig. 5.23.

Seismic facies CH (Delta top distributary channels)

Seismic facies CH is characterized by a lack of prominent internal seismic reflectors or low amplitude and low-frequency discontinuous reflectors (Fig. 5.22). This facies exhibits a cut-and-fill structure with an erosional surface. The architecture of channel fill is simple with thicknesses ranging from 2 to 13 m (Figs. 5.25–5.27) and occurs in the shelf area, from the south of the island of Zlarin and almost up to the shelf slope. The incision of palaeochannels can be traced at depths from 55 m bsl to approximately 75 m bsl in the NE-SW direction. The palaeochannels width ranges from 150 m to over 1.5 km. The SF CH is incised into the acoustic basement and it cuts almost the entire shelf and divides into two branches around the seamount presented in Figures 5.9 and 5.25. This seismic facies is truncated by a seafloor reflector (Figs. 5.25–5.27).

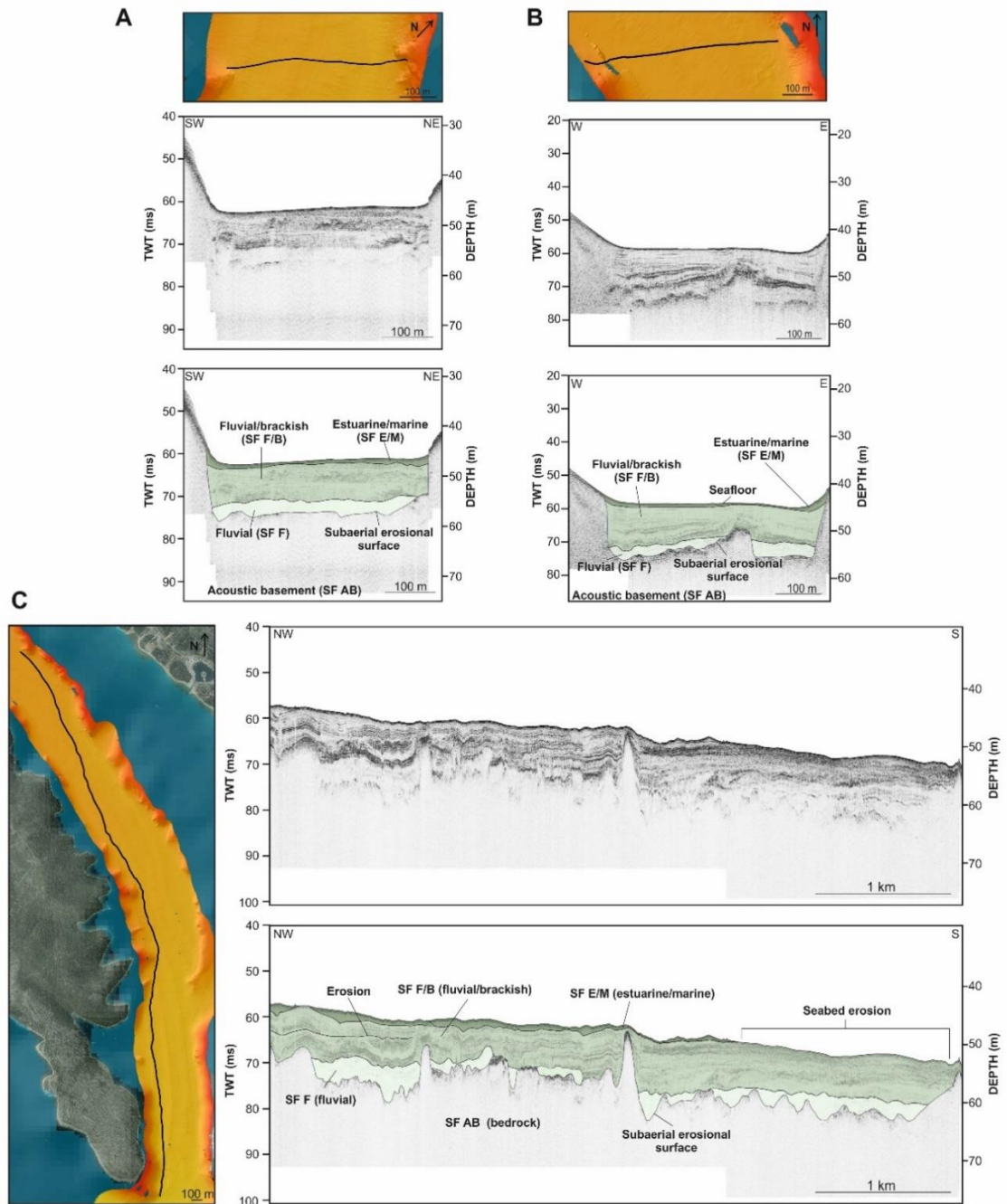


Figure 5.23 A, B, C. Bathymetry section with a position of seismic lines and processed seismic profiles and their corresponding stratigraphic interpretation of the submerged Krka River channel located between the mainland and the island of Zlarin.

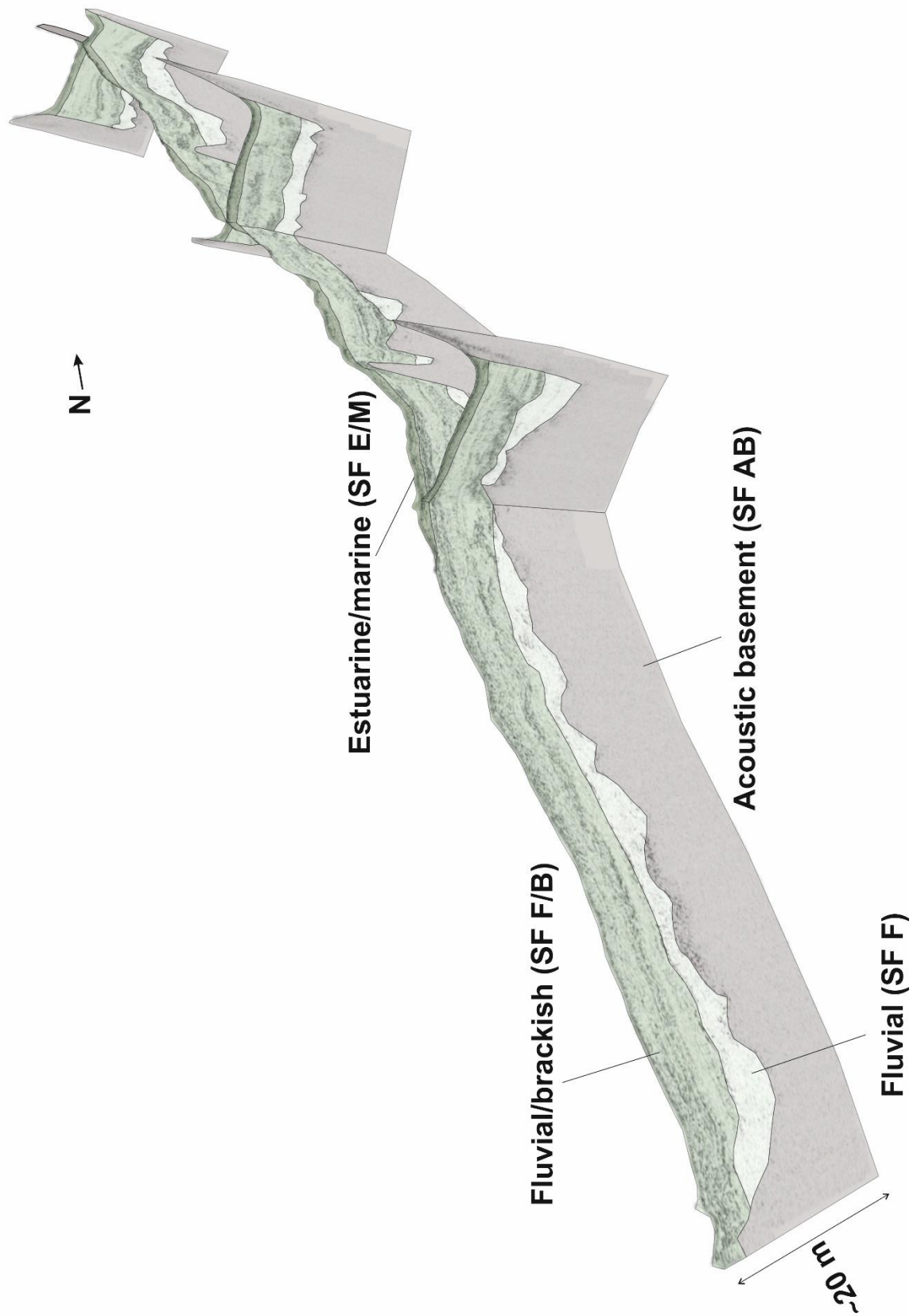


Figure 5.24 A fence diagram of 3D and interpreted seismic profiles, illustrates the distribution of seismic units of the submerged Krka River channel located between the mainland and the island of Zlarin.

Seismic facies CL (Clinoforms)

Seismic facies CL comprises continuous, sometimes locally discontinuous inclined reflectors (clinoforms) of low- to high-amplitude and frequency (Fig. 5.22). This facies is present on the shelf edge and the outer shelf overlapping the acoustic basement (Figs. 5.25 and 5.28). Different configuration patterns are present and those are sigmoid, oblique-sigmoid and hummocky. Clinoforms usually downlap at the basal surface and show a concordant or toplap geometry with respect to the upper unit (Fig. 5.28). The thickness of the clinoforms goes up to approx. 30 m. A parallel to subparallel, somewhere hummocky, clinoforms of low amplitude, frequency and continuity unconformably overlie the acoustic basement (Fig. 5.28). A progradational wedge-shaped facies can be observed on the shelf edge. It has a high angle seaward-dipping parallel to subparallel reflectors of medium to high amplitude and oblique-tangential seismic characteristics (Fig. 5.28). Its lower boundary is an erosional surface. Within this facies chaotic and discontinuous reflectors are present. Above the progradational wedge-shaped clinoforms, a parallel sigmoidal clinoforms are present of low to high amplitude and high frequency and continuity. Within this facies, strong erosional features can be observed (Fig. 5.28).

Seismic facies SS (Sand sheet)

The SF SS is characterized by a reflection free facies (Fig. 5.22) forming an extensive sediment drape that cover much of the shelf (Figs. 5.25–5.27) and is exposed at the seafloor. It is very thin (up to 1 m) and covers SF AB, SF Ch and SF Cl. This facies is characterized by a sheet-like shape in most of the study area or ridges. Based on its seismic characteristic and backscatter pattern, it can be interpreted as coarse-grained deposits (probably transgressive marine sheet or sand ridges).

Seismic facies TD (Terrestrial deposits)

SF TD is characterized by a reflection free facies or by a low amplitude to chaotic reflectors, sometimes prograding into SF CH. It can be observed at the westernmost side of the shelf area (Zlarinski Channel, Fig. 26A, B). A palaeoterrace is present at its boundary with the

palaeoalluvial plain of the Krka River (Fig. 26A, B). This facies can be interpreted as terrestrial Pleistocene deposits.

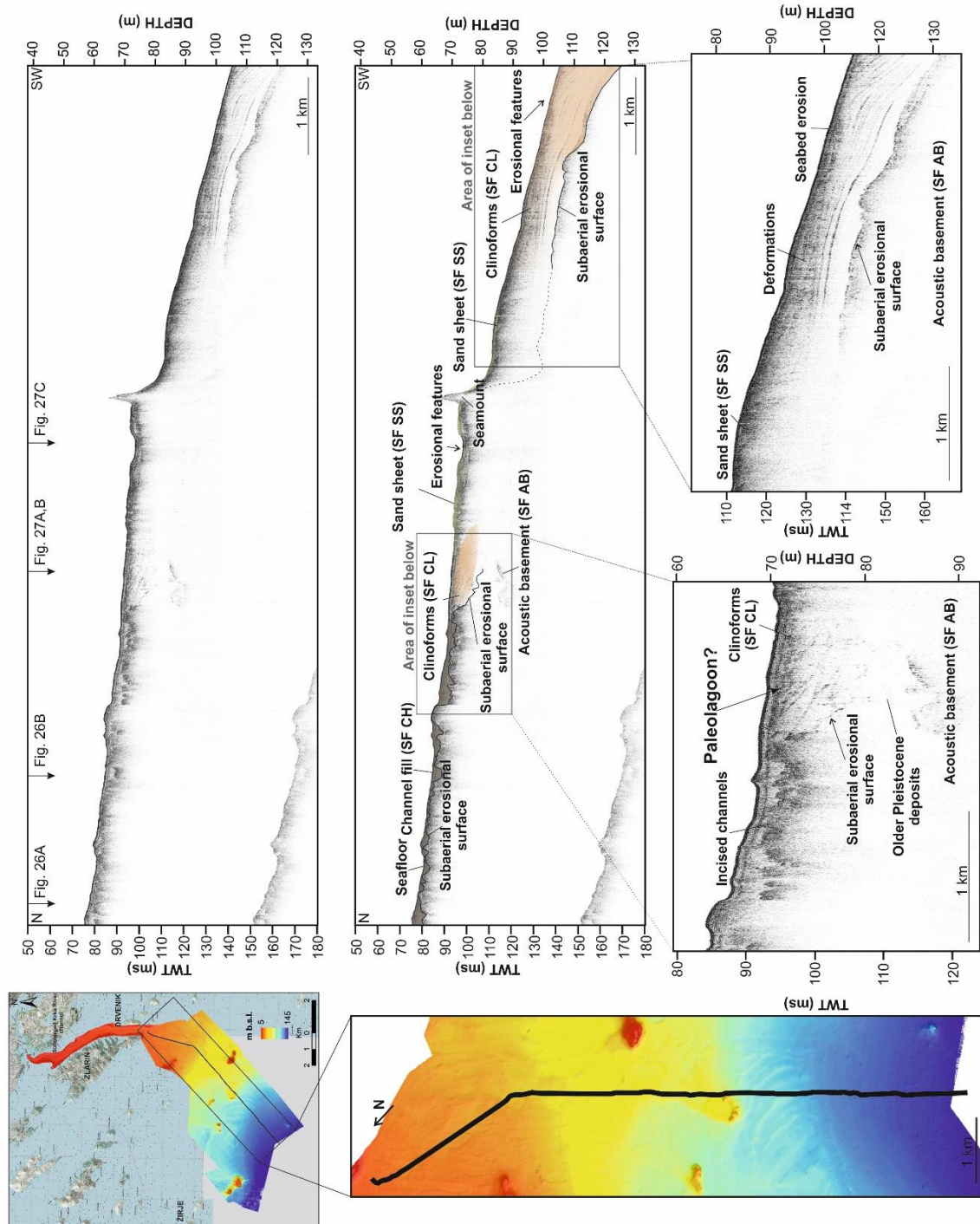


Figure 5.25 Processed longitudinal seismic profile and its corresponding stratigraphic interpretation from the central shelf region. See Figure 4.2B for seismic lines location.

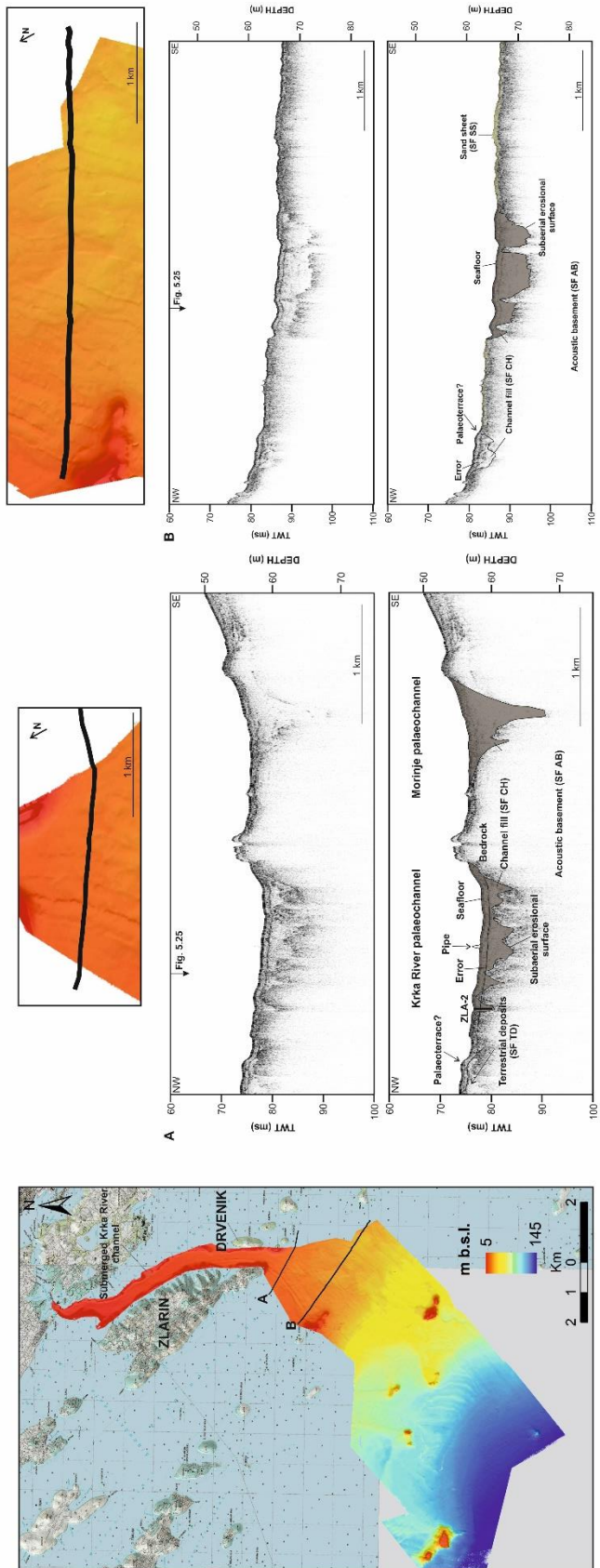


Figure 5.26 A, B. Processed seismic profile and its corresponding stratigraphic interpretation from the central shelf region. See Figure 4.2B for seismic lines location.

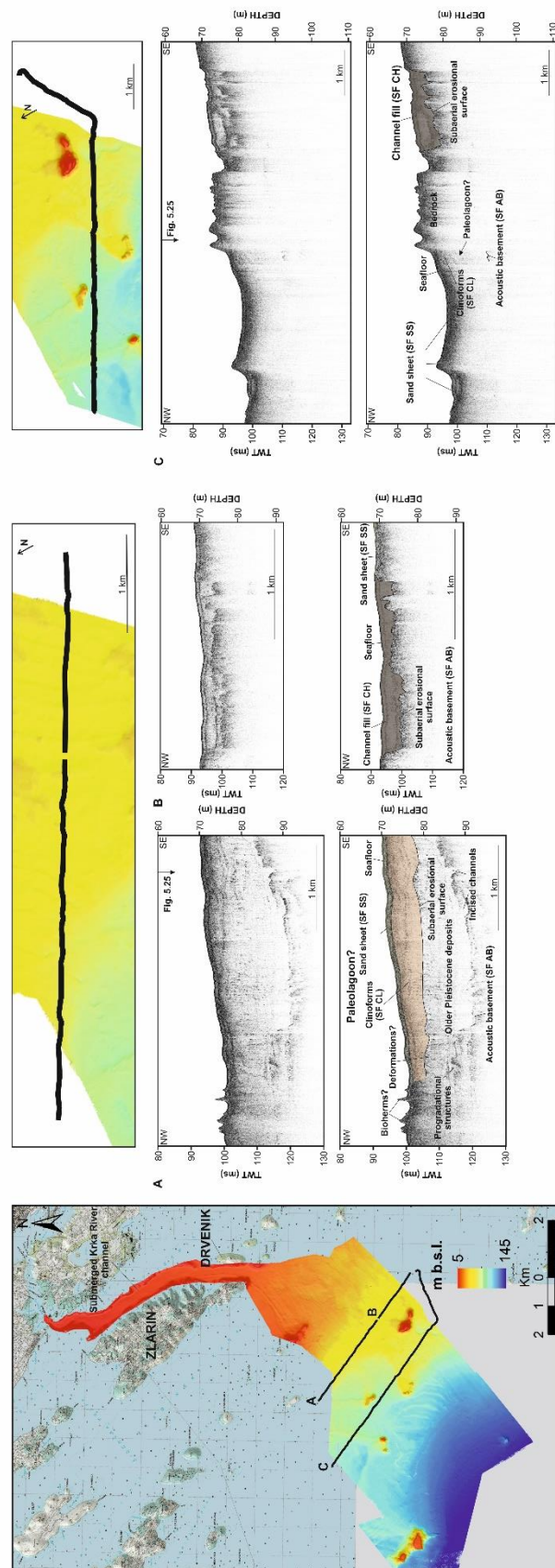


Figure 5.27 A, B, C. Processed seismic profile and its corresponding stratigraphic interpretation from the central shelf region. See Figure 4.2B for seismic lines location.

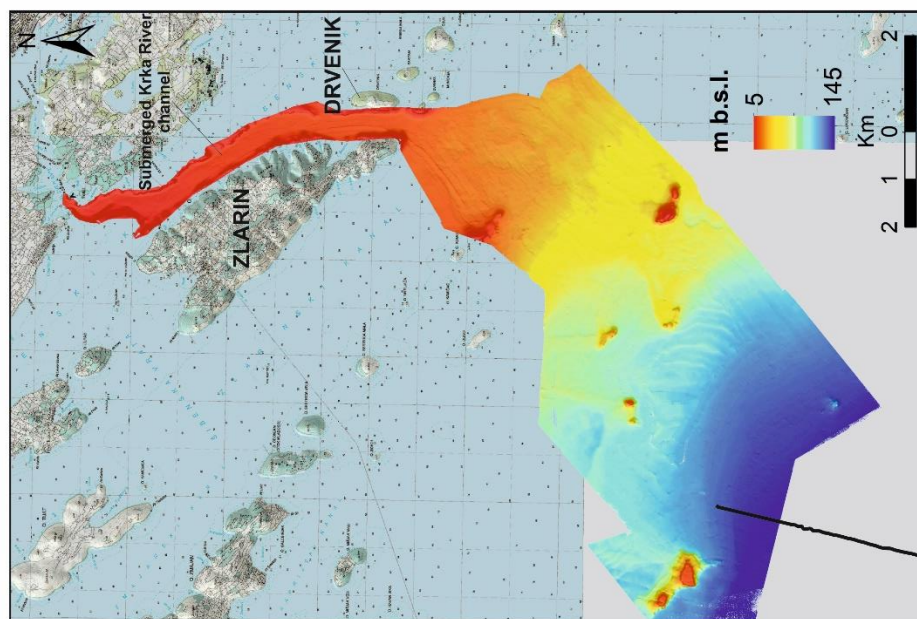
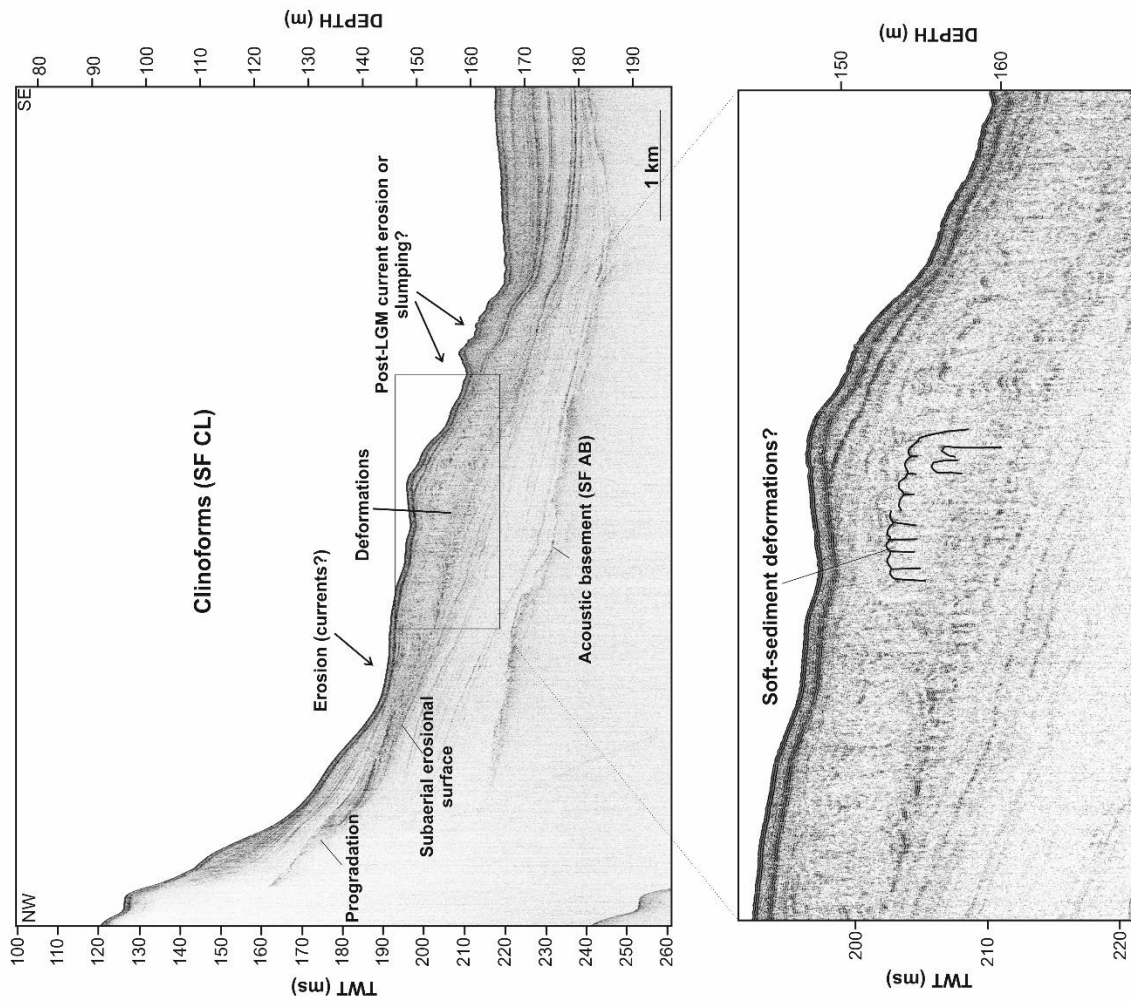


Figure 5.28 Processed seismic profile and its corresponding stratigraphic interpretation from the shelf slope. See Figure 4.2B for seismic line location.

5.3 Lithostratigraphy

Four sediment cores (PROK-1-4), retrieved in the Krka River estuary were positioned on interpreted seismic profiles to penetrate most of the seismic units. The cores were obtained from depths between 7.5 m and 17.9 m (Table 4.1). None of the cores reached the bedrock. The core PROK-4 was retrieved from the innermost part of the estuary (north of the town of Skradin, at the bridge that is the southern border of the NP Krka; Fig. 4.2A) to determine the highest riverine and anthropogenic influence on the estuarine system, while the cores PROK-1, PROK-2, and PROK-3 were recovered from the narrow part of the submerged Krka River canyon and the central part of Prokljan Lake (Fig. 4.2A) to evaluate the impact of barriers on sediment deposition and to establish the timing of marine flooding of barrier lakes and the installation of the present-day hydrodynamic conditions. The cores recovered the two youngest seismic units (SU3 and SU4) and were subjected to analyses to comply with the multiproxy approach of the PhD study. Based on these analyses, the sediment cores can be divided into five lithological units (LU) from the cores' bottom upwards, which represent distinct depositional systems (Table 5.1; Fig. 5.29). All five lithological units are observed only in the core PROK-3, while in the cores PROK-1 and PROK-2, four units are present (LU 2-5), and in the core PROK-4, two units are distinguished (LU 4 and 5).

All PROK cores show similar general sediment characteristics (Fig. 5.29) with the fining-upwards of sediment succession from coarse silt to medium and fine silt. Additionally, the colour of the sediment gradually changes from dark brown or reddish brown sediments at the bottoms of the cores to grey or beige sediments in the middle and beige or brown to reddish sediments at the tops of the cores. No bioturbation and animal burrows are present in the cores.

Sediment core ZLA-1 was retrieved in the submerged Krka River channel (Šibenik channel) east of the island of Zlarin at a depth of 48 m (Figure 4.2B; Table 4.1), while the sediment core ZLA-2 was collected at the exit of the submerged Krka River channel at the southern side of the island of Zlarin at a depth of 61 m (Figure 4.2B; Table 4.1). The cores were divided into several lithological units based on their physical and micropalaeontological characteristics (Table 5.2; Fig. 5.30). These lithological units present different environmental settings.

Table 5.1 Division of sediment cores into lithological units, their depth range, and age span.

Core	Units	Depth (cm)	Age
PROK-3	LU1	527.5–515	>10.1–9.9 cal kyr BP
	LU2	515–396	9.9–8.4 cal kyr BP
	LU3	396–270	8.4–6.2 cal kyr BP
	LU4a	270–120	6.2–3.0 cal kyr BP
	LU4b	120–40	3.0–0.4 cal kyr BP
	LU5	40–0	460 cal yr BP – present
PROK-1	LU2	847.5–808	>7.8–7.5 cal kyr BP
	LU3	808–600	7.5–6.1 cal kyr BP
	LU4a	600–220	6.1–2.0 cal kyr BP
	LU4b	220–60	2.0–0.3 cal kyr BP
	LU5	60–0	374 cal yr BP – present
PROK-2	LU2	446–365	>10.9–8.3 cal kyr BP
	LU3	365–320	8.3–6.2 cal kyr BP
	LU4a	320–165	6.2–1.9 cal kyr BP
	LU4b	165–45	1.9–0.3 cal kyr BP
	LU5	45–0	380 cal yr BP–present
PROK-4	LU4a	572–300	>4.2–1.5 cal kyr BP
	LU4b	300–140	1.5–0.5 cal kyr BP
	LU5	160–0	647 cal yr BP–present

Table 5.2 Division of ZLA-1 and ZLA-2 sediment cores into lithological units and their depth range.

Core	Units	Depth (cm)
ZLA-1	LU1-2	373–170
	LU1-1	170–0
ZLA-2	LU2-1	285–220
	LU2-2	220–50
	LU2-3	50–0

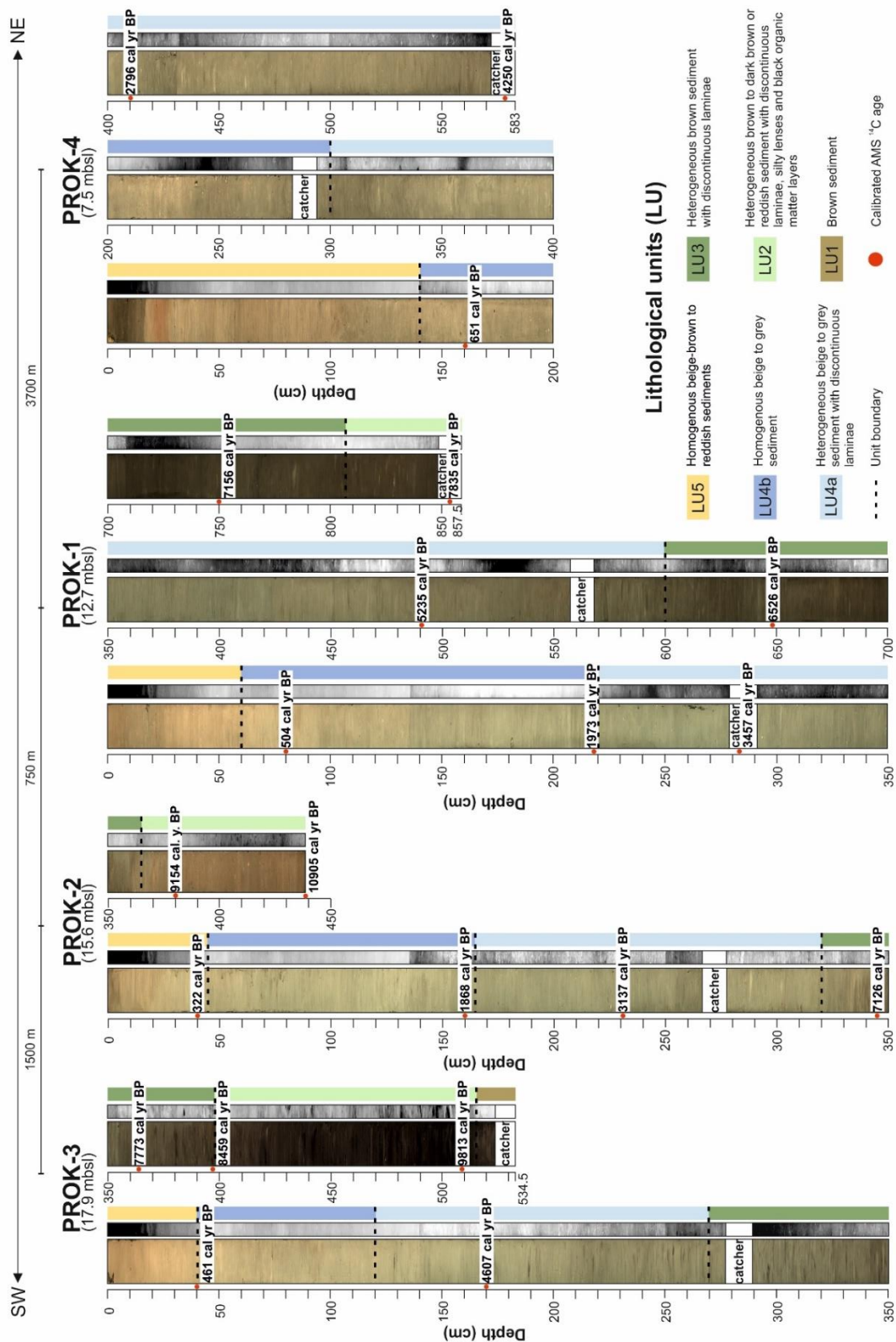


Figure 5.29 Lithological characteristics of studied PROK sediment cores, calibrated radiocarbon ages and the distinguished lithological units.

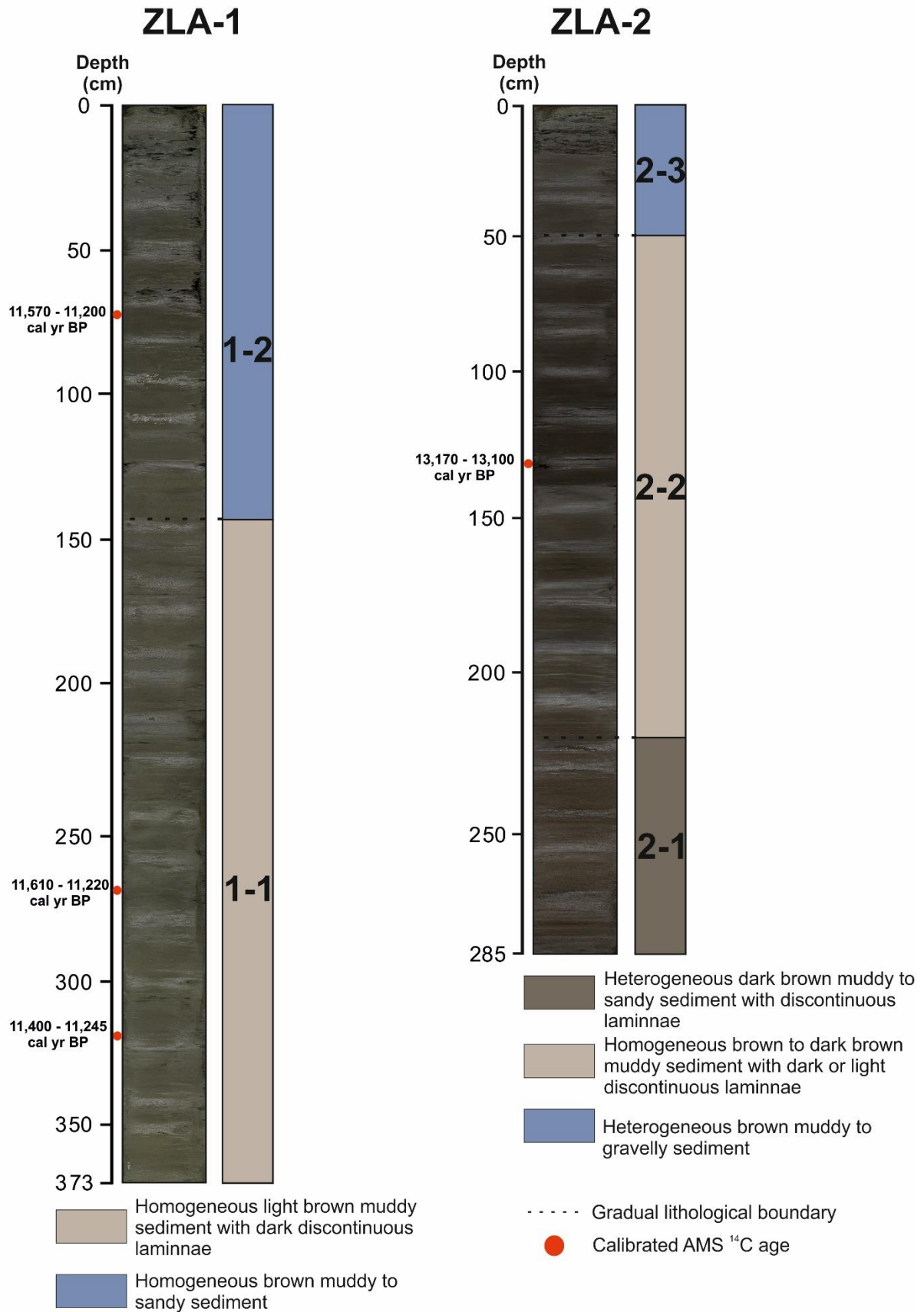


Figure 5.30 Lithological characteristics of studied ZLA sediment cores, calibrated radiocarbon ages and the distinguished lithological units.

5.3.1 Chronology

The radiocarbon dating results on a total of 22 molluscs shells, charcoal sample and bulk organic sediment of the PROK sediment cores indicated the Holocene age interval with the oldest age determined in the core PROK-2 (conventional age of 9600 BP) (Appendix 2–5; Table 5.3). Four radiocarbon dated samples (two molluscs, a charcoal and a plant fragment) from the sediment core ZLA-1 and ZLA-2 revealed the Pleistocene and Holocene ages (Appendix 6; Table 5.3). The oldest age was determined in the core ZLA-2 (conventional age of 11,240 BP). The three obtained ages in the core ZLA-1 gave age reversals. The stable carbon isotopes ($\delta^{13}\text{C}$) in all analyzed samples range from -2.9‰ to 5.4‰ (Table 5.3).

Age-depth models of studied PROK-1-4 sediment cores (Fig. 5.31; Appendix 2–5) are done in R environment using the rbacon package (Blaauw and Christen, 2011). All samples show consistent ages except for two gastropod shells from the core PROK-3 at depths of 240 cm and 490 cm which were excluded from the age-depth model. Sediment rates were calculated for all PROK cores (Fig. 5.31). The accumulation rates are mainly low (Fig. 5.31). The somewhat higher accumulation rates are present in the LU5 of the sediment cores, whereas the highest rates are present in the core PROK-4 and go up to 3 mm/yr (Fig. 5.3). Age depth models were made only for PROK sediment cores, since the age reversals are present in the core ZLA-1.

Table 5.3 Radiocarbon dates of samples from the studied sediment cores. Two dates highlighted in grey were excluded from further interpretation.

Core	Depth (cm)	Laboratory code	Material	Conventional radiocarbon age (BP)	$\delta^{13}\text{C}$	Probability (%)
PROK-1	80	Beta-599499	Bivalve shell	660 ± 30	1.1	94.8
PROK-1	218	Beta - 599500	Bivalve shell	2200 ± 30	1	94.4
PROK-1	283*	Beta - 573127	Bivalve shell	3290 ± 30	-0.1	94.9
PROK-1	491	Beta - 599501	Bivalve shell	5630 ± 30	1.8	94.3
PROK-1	648	Beta - 620526	Bivalve shell	6410 ± 30	-0.9	94.6
PROK-1	750	Beta - 599502	Bivalve shell	6630 ± 30	-2.6	94.8
PROK-1	852*	Beta - 573128	Charcoal	6940 ± 30	-26.2	94.7
PROK-1	852*	Beta - 573128	Bivalve shell	7820 ± 30	-3.6	94.8
PROK-2	40	Beta - 620527	Bivalve shell	550 ± 30	0.8	94.1
PROK-2	160	Beta - 99503	Gastropod shell	2170 ± 30	2.7	94.8
PROK-2	231	Beta - 620528	Bivalve shell	3170 ± 30	0.4	94.8
PROK-2	345	Beta - 599504	Bivalve shell	6620 ± 30	-0.1	94.8
PROK-2	380	Beta - 599505	Gastropod shell	9240 ± 30	-13.1	94.8
PROK-2	446*	Beta - 573130	Bivalve shell	9600 ± 30	-8.8	94.6
PROK-3	40	Beta - 599506	Bivalve shell	580 ± 30	2	94.6
PROK-3	170	Beta - 599507	Bivalve shell	4680 ± 30	1.6	94.7
PROK-3	240	Beta - 620529	Gastropod shell	3640 ± 30	2.9	95
PROK-3	363	Beta - 620530	Bivalve shell	7280 ± 30	-0.5	94.3
PROK-3	396.5	Beta - 599508	Bivalve shell	8170 ± 30	-1.2	94.7
PROK-3	490	Beta - 599509	Gastropod shell	7830 ± 30	2.1	94.9
PROK-3	508	Beta-649074	Bulk sediment	8610±30	-27.6	95.4
PROK-4	161	Beta - 620531	Bivalve shell	540 ± 30	-1.5	93.8
PROK-4	410	Beta - 620532	Bivalve shell	2160 ± 30	-0.3	94.4
PROK-4	572*	Beta - 573131	Bivalve shell	4090 ± 30	1.2	94.8
ZLA-1	71	Beta - 646496	Bivalve shell	10,200 ± 30	1.4	95.4
ZLA-1	268	Beta - 649075	Bivalve shell	10,230 ± 30	1.7	95.4
ZLA-1	317	Beta - 646498	Charcoal	9930 ± 30	-26.2	91.9
ZLA-2	130	Beta - 649066	Plant	11,240 ± 30	-28.8	95.4

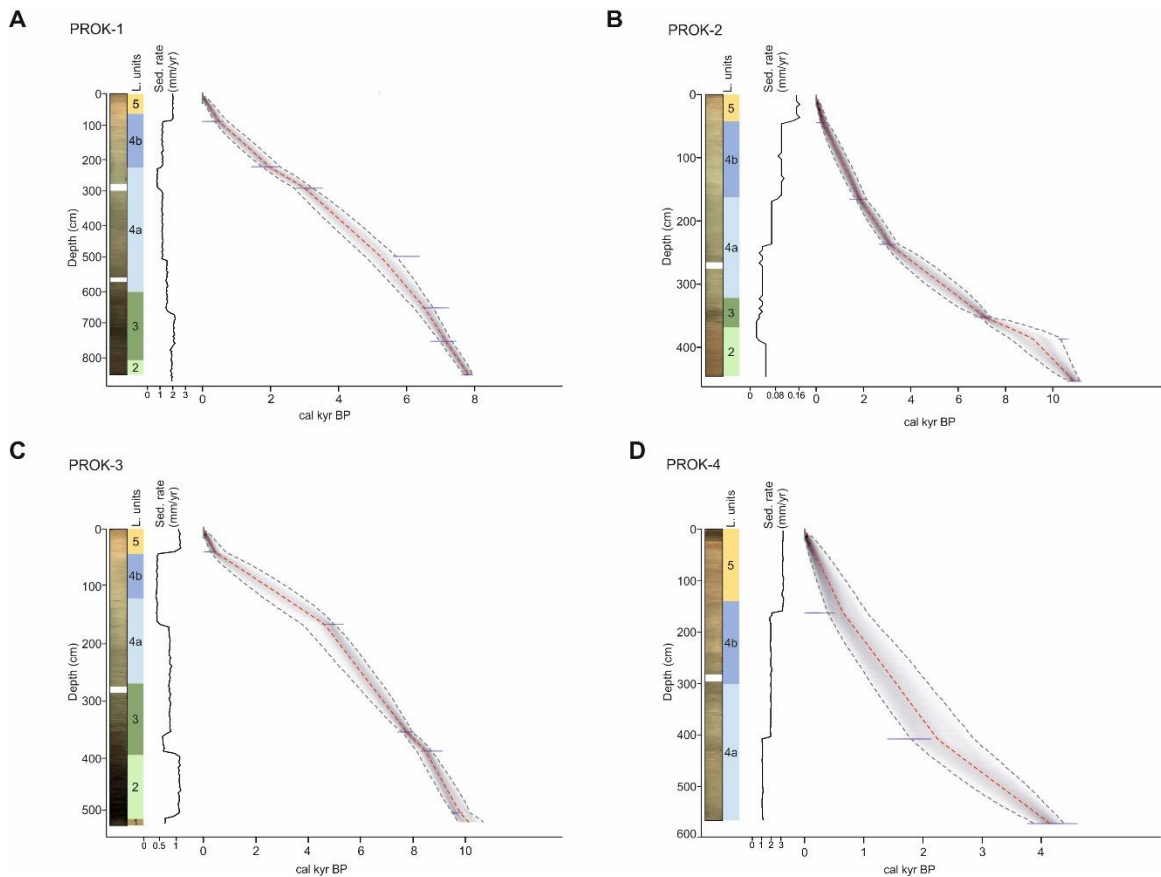


Figure 5.31 Bayesian age-depth models and sedimentation rates for PROK-1 to 4 sediment cores expressed in cal kyr BP.

5.3.2 Initial core description and physical properties

The sediment core PROK-1 is the longest of all cores (8.475 m; Table 4.1) collected in the submerged part of the Krka River canyon (Fig. 4.2A) at a depth of 12.7 m. The core PROK-1 correlates with seismic units 3b and 4 (Fig. 5.15). Based on the analyses (Appendix 2), the PROK-1 core has been subdivided into four lithostratigraphic units (Table 5.1, Fig. 5.29). The lower part of the core (LU2 and LU3) is composed of homogeneous dark brown sediment with sediment lenses and discontinuous laminae varying in color (Figs. 5.29 and 5.32). Both marine and freshwater mollusk shells were present in this unit. The middle part of the core (LU4a and LU4b) is composed of homogeneous beige to gray sediment (Figs. 5.29 and 5.32) with numerous mollusk shells and their debris. The uppermost part of the core (LU5) is characterized by beige to reddish homogeneous sediment (Figs. 5.29 and 5.32) and many marine mollusk shells. All boundaries between lithological units in the core PROK-1 are gradual (Fig. 5.29).

The density values of the analyzed sediments range between 1.3 and 1.8 g/cm³ (Fig. 5.32; Table 5.4). The values are generally high in the LU2 and LU3, while in the LU4a, the values are slightly decreasing upwards (Fig. 5.32). Then, LU4b is marked again by higher values at the beginning of the unit and decreases upwards towards LU5, which characterizes low-density values (Fig. 5.32). The MS is generally zigzag-shaped with increasing or decreasing trend upwards (Fig. 5.32, Table 5.5). The LU2 is characterized by a decreasing trend upward, whereas the values range from 1.58 to 4.49 SI (Fig. 5.32). Slightly higher and oscillating MS values (up to 5.56 SI) can be observed in LU3 (Fig. 5.32). A general trend of decreasing values can be observed upward for LU4a and LU4b (values range from 0.46 to 8.26 SI; Fig. 5.32). The last 60 cm of the PROK-1 (LU5) is characterized by an increasing trend upwards, up to 7.87 SI (Fig. 5.32).

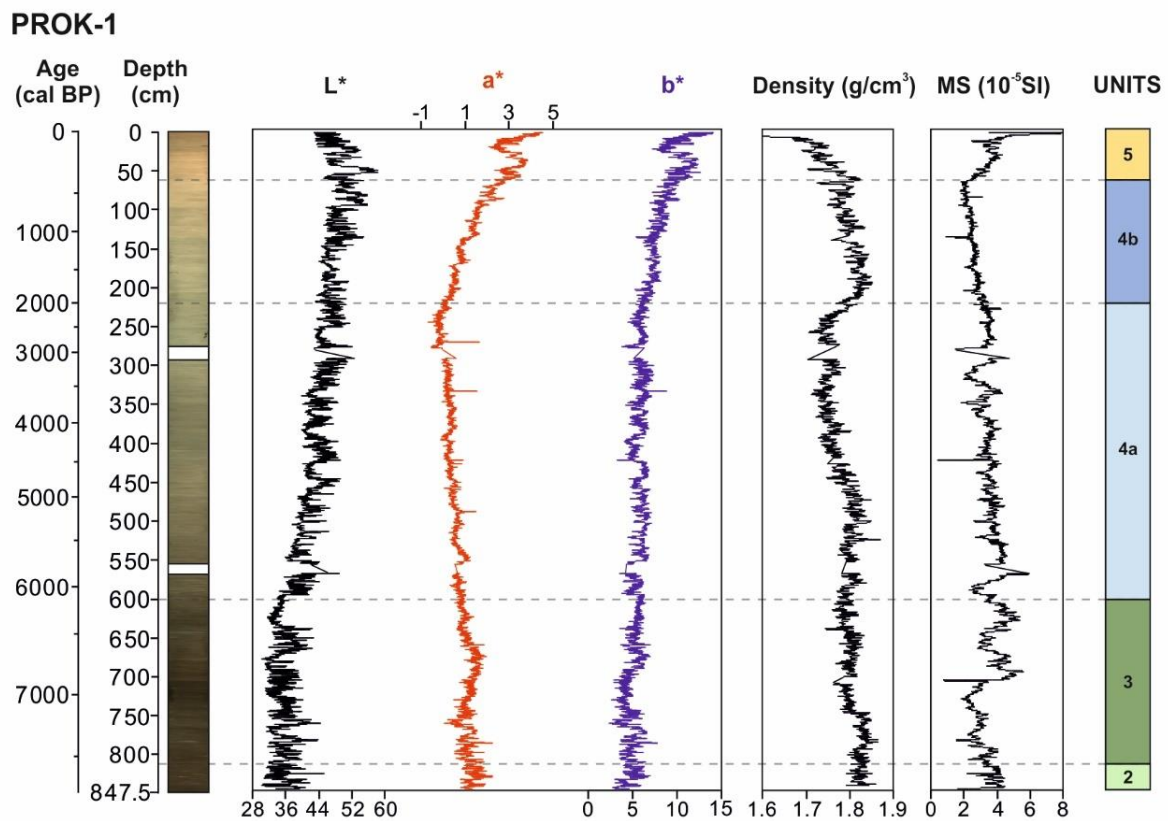


Figure 5.32 Physical properties of the sediment core PROK-1.

Table 5.4 Statistical parameters of bulk density values in sediments of the core PROK-1.

	PROK-1	LU2	LU3	LU4a	LU4b	LU5	TOTAL CORE
Bulk density (g/cm³)	Mean	1.82	1.80	1.76	1.80	1.72	1.79
	SD	0.01	0.02	0.03	0.02	0.08	0.04
	Min	1.79	1.74	1.70	1.73	1.37	1.37
	Max	1.86	1.86	1.87	1.85	1.82	1.88

Table 5.5 Statistical parameters of magnetic susceptibility values in sediments of the core PROK-1.

	PROK-1	LU2	LU3	LU4a	LU4b	LU5	TOTAL CORE
MS (10⁻⁵SI)	Mean	3.72	3.48	3.49	2.51	3.71	3.33
	SD	0.46	0.86	0.55	0.35	0.90	0.76
	Min	1.65	0.79	0.46	0.93	2.51	0.46
	Max	4.49	5.56	6.61	3.44	8.00	8.26

The sediment core PROK-2 (4.375 m; Table 4.1) was collected on the northern side of Prokljan Lake at a depth of 12.7 m (Fig. 4.2A). PROK-2 correlates with seismic units 3b and 4 (Fig. 5.17). Based on performed analyses (Appendix 3), PROK-2 consists of four lithostratigraphic units (Table 5.1, Fig. 5.29). The lower part of the core (LU2 and LU3), associated with SU3b (Fig. 5.17), is made of reddish brown sediment (Figs. 5.29 and 5.33), rich in freshwater gastropods and some marine shells. The middle part of the core (LU4a and LU4b) is composed of heterogeneous brown sediment recognized in the interval from 360 cm to 320 cm (Figs. 5.29 and 5.33), which gradually passes to homogeneous beige to grey sediment rich in marine shells (320–40 cm; Figs. 5.29 and 5.33). The upper 40 cm of the core (LU5) consists of beige to reddish sediment (Figs. 5.29 and 5.33). The middle and upper sections can be associated with SU4 (Fig. 5.17).

Density values for the PROK-2 are in the range between 1.68 and 1.90 g/cm³ (Table 5.6). A decreasing and oscillating trend of density occurs in LU2 and LU3 (Fig. 5.33). A rise in density values is present (up to 1.90 g/cm³) at 340 cm of the core, with a decreasing trend to the top of the core (Fig. 5.33). The MS is generally constant throughout the core, except for LU3 and LU5 where it shows an increasing trend upwards (Fig. 5.33). The MS values range from -0.6 to 10.05 SI (Table 5.7). The highest MS values are present in LU5 (Fig. 5.33).

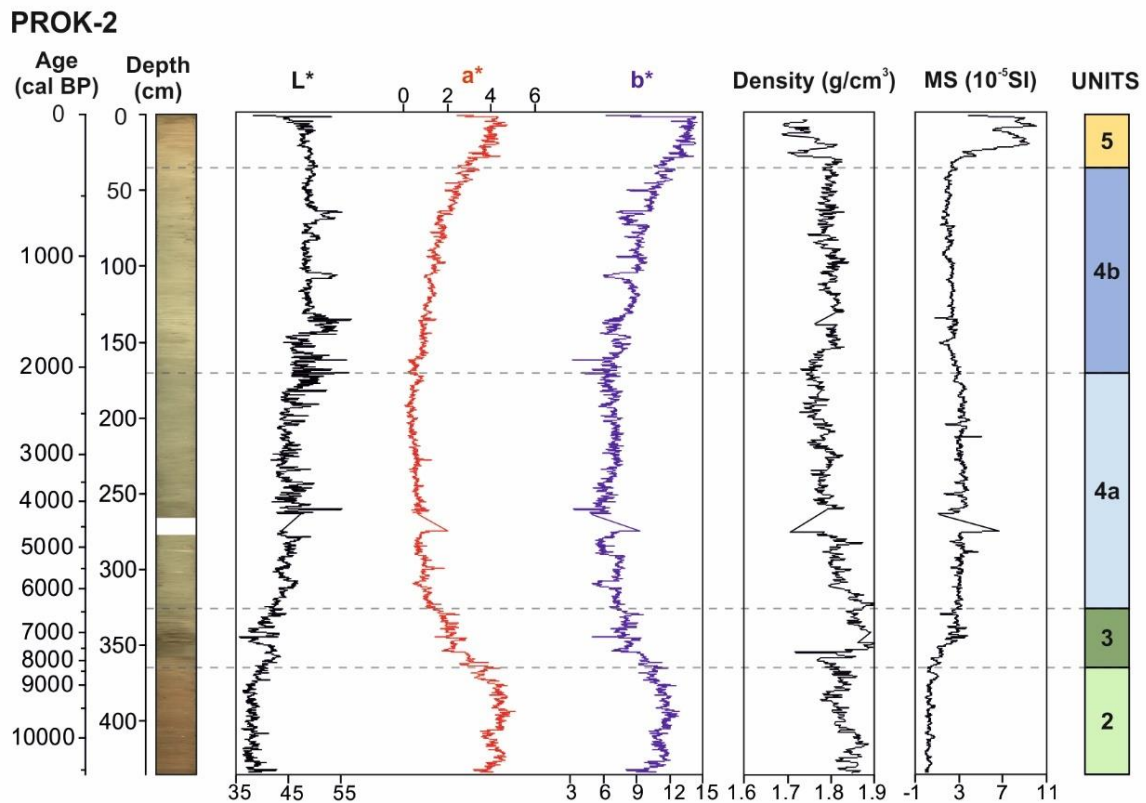


Figure 5.33 Physical properties of the sediment core PROK-2.

Table 5.6 Statistical parameters of bulk density values in sediments of the core PROK-2.

	PROK-2	LU2	LU3	LU4a	LU4b	LU5	TOTAL CORE
Bulk density (g/cm ³)	Mean	1.83	1.85	1.80	1.80	17.67	1.80
	SD	0.02	0.04	0.03	0.02	0.04	0.04
	Min	1.78	1.72	1.79	1.74	1.69	1.69
	Max	1.83	1.91	1.82	1.84	1.82	1.91

Table 5.7 Statistical parameters of magnetic susceptibility values in sediments of the core PROK-2.

	PROK-2	LU2	LU3	LU4a	LU4b	LU5	TOTAL CORE
MS (10 ⁻⁵ SI)	Mean	0.31	2.09	3.19	2.19	5.36	2.56
	SD	0.24	0.89	0.56	0.31	2.84	1.71
	Min	-0.06	0.20	1.12	0.80	1.66	-0.06
	Max	1.12	3.77	12.10	2.91	10.05	12.10

The sediment core PROK-3 (5.245 m; Table 4.1; Appendix 4) is located in the central part of Prokljan Lake (Fig. 4.2A) and contains an almost complete sedimentary infilling succession (Fig. 4.2A). The core consists of six lithological units (Table 5.1, Fig. 5.29). The bottom part of the core is composed of brown sediment (LU1, Figs. 5.29 and 5.34) and can be associated with SU3a (Fig. 5.18). The sharp boundary separates the lowermost section and the overlying heterogeneous dark brown sediment, with discontinuous laminae and dark

lenses that are probably rich in organic matter (LU2; SU3b; Figs. 5.18, 5.29 and 5.34). The middle part of the core (LU3 and LU4a; Fig. 5.18) is composed of the following: the lower part is heterogeneous beige to grey sediment with discontinuous laminae and shifts to a more homogeneous upper part (LU4b; Figs. 5.29 and 5.34). The upper 50 cm of the core is characterized by homogeneous brown to reddish deposits (LU5; Figs. 5.29 and 5.34). LU3–5 correspond to SU4 (Fig. 5.18).

In the core PROK-3, density values are in the range of 1.35 up to 2.12 g/cm³ (Fig. 5.34; Table 5.8). At the bottom of the core (LU1), density is high and then strongly decreases at the boundary with the LU2 (Fig. 5.34). The LU2 comprises increasing upward density values (Fig. 5.34). The values are constant up to the LU5, whereas a slightly decreasing trend can occur at the top of the core PROK-3 (Fig. 5.34). A similar curve trend to density is evident in the MS values (except for LU5) (Fig. 5.34) and ranges from -0.06 to 21.03 SI (Table 5.9).

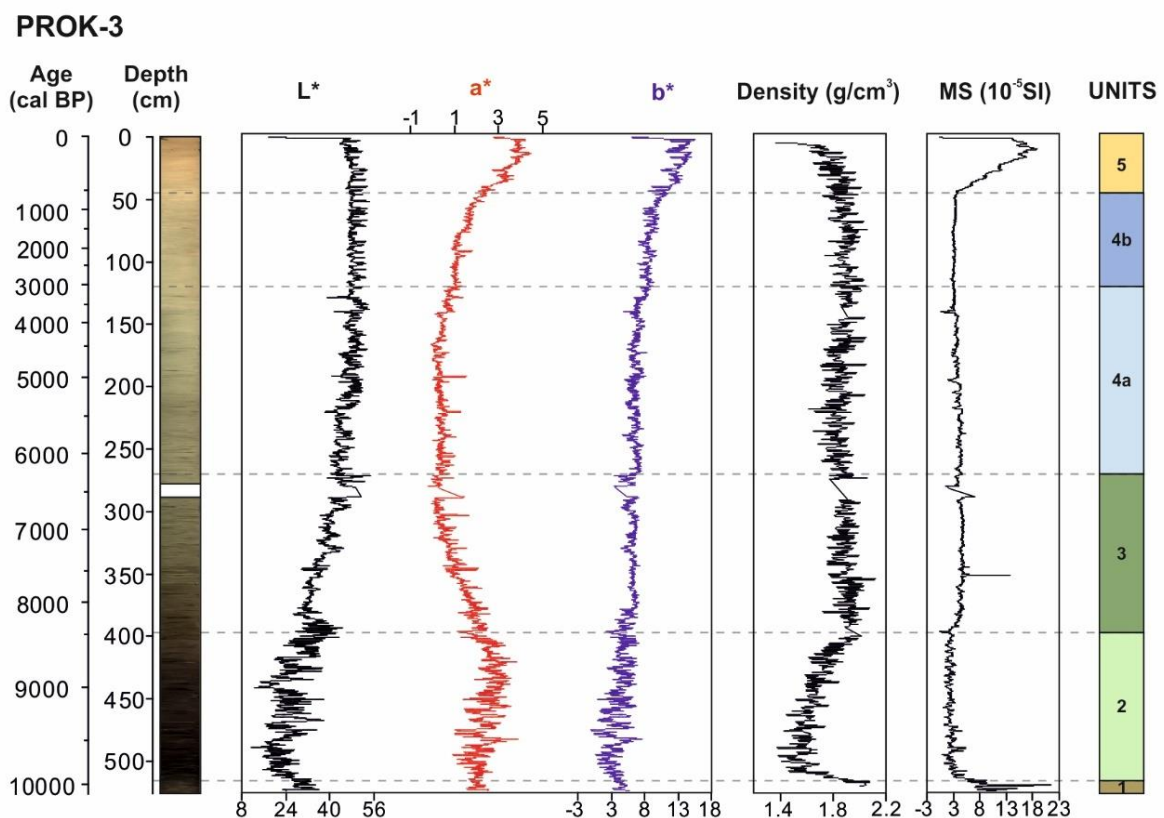


Figure 5.34 Physical properties of the sediment core PROK-3.

Table 5.8 Statistical parameters of bulk density values in sediments of the core PROK-3.

PROK-3		LU1	LU2	LU3	LU4a	LU4b	LU5	TOTAL CORE
Bulk density (g/cm³)	Mean	2.03	1.66	1.90	1.86	1.90	1.79	1.82
	SD	0.06	0.12	0.07	0.07	0.07	0.11	0.13
	Min	1.87	1.37	1.73	1.62	1.72	1.36	1.36
	Max	2.07	2.02	2.12	2.05	2.06	2.02	2.12

Table 5.9 Statistical parameters of magnetic susceptibility values in sediments of the core PROK-3.

PROK-3		LU1	LU2	LU3	LU4a	LU4b	LU5	TOTAL CORE
MS (10⁻⁵SI)	Mean	9.18	2.05	3.91	3.28	2.76	11.84	3.82
	SD	3.65	0.79	0.87	0.58	0.38	4.02	2.90
	Min	5.35	0.06	-0.06	0.13	1.92	0.00	-0.06
	Max	21.03	6.28	13.22	4.83	5.03	18.39	21.03

The core PROK-4 (5.7 m; Table 4.1; Appendix 5) is retrieved in the most proximal narrow part of the study area, near Skradin (Fig. 4.2A). The core consists of three lithological units corresponding to seismic unit 4 (Table 5.1; Figs. 5.13 and 5.29). Most of the core comprises homogeneous beige to grey sediment (LU4a and LU4b; Figs. 5.29 and 5.35), and the top of the core (LU5) is marked by brown to reddish sediment (Figs. 5.29 and 5.35). The density values are in the range 1.44 – 2.01 g/cm³ (Fig. 5.35; Table 5.10) and are constant from the bottom of the core up to 160 cm, where the values start to decrease upwards at the top of the core PROK-4 (Fig. 5.35). The MS values are in the range from -0.33 SI to 46.36 SI (Fig. 5.35; Table 5.11). The low MS values are present from the bottom of the core up to 140 cm, where the MS values increase and oscillate upwards (Fig. 5.35).

PROK-4

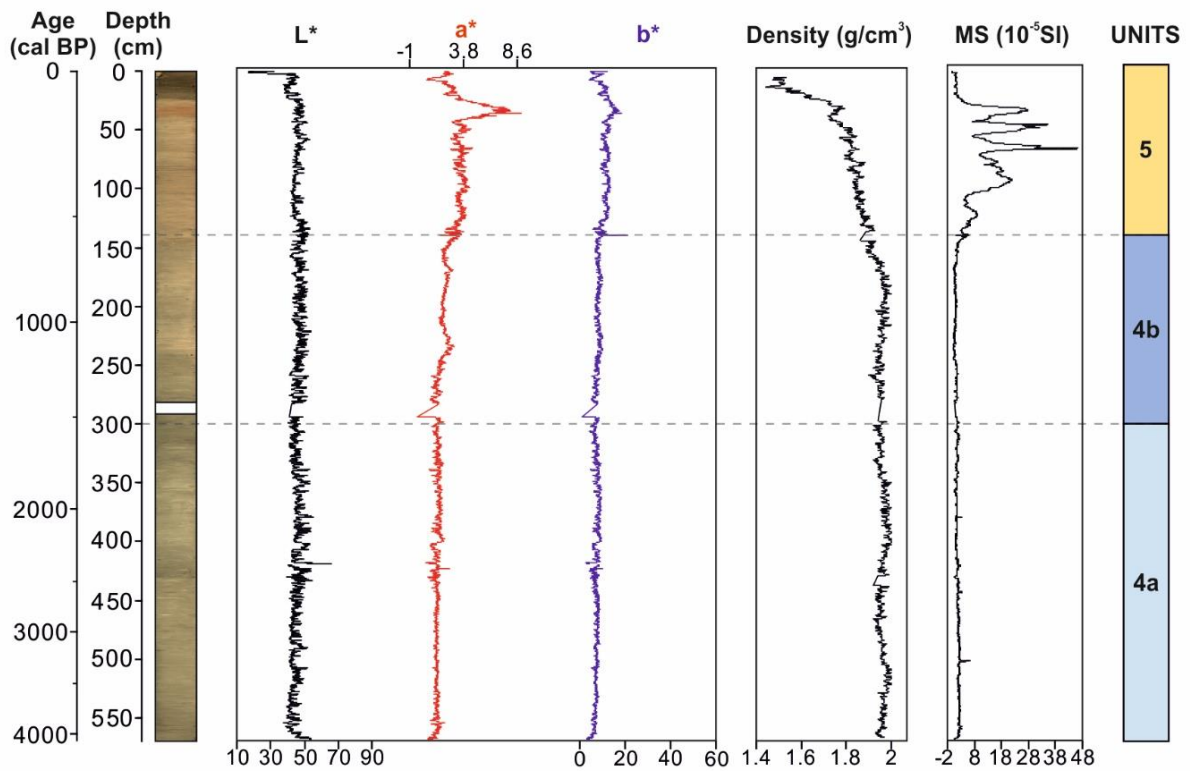


Figure 5.35 Physical properties of the sediment core PROK-4.

Table 5.10 Statistical parameters of bulk density values in sediments of the core PROK-4.

	PROK-4	LU4a	LU4b	LU5	TOTAL CORE
Bulk density (g/cm ³)	Mean	1.96	1.95	1.78	1.92
	SD	0.02	0.02	0.11	0.10
	Min	1.92	1.86	1.44	1.44
	Max	2.01	2.00	1.93	2.01

Table 5.11 Statistical parameters of magnetic susceptibility values in sediments of the core PROK-4.

	PROK-4	LU4a	LU4b	LU5	TOTAL CORE
MS (10 ⁻⁵ SI)	Mean	1.86	1.17	11.37	4.07
	SD	0.53	0.61	8.60	6.07
	Min	0.46	0.00	-0.33	-0.33
	Max	6.28	5.03	46.36	46.36

The sediment core ZLA-1 is 373 cm long (Table 4.1; Appendix 6) and was collected in the Šibenik channel, east of the island of Zlarin (Fig. 4.2B), at a depth of 49 m. A total of two

sediment cores were collected at this site, measuring 274 cm (0–274 cm) and 173 cm (200–373 cm) (Fig. 5.30). After overlapping these two cores, the total length amounts to 373 cm. The lithology of the sediment core ZLA-1 is generally homogeneous (Fig. 5.30). The first 140 cm of the core is composed of dark grey to dark greyish brown homogenous sediment (2.5Y 4/1–4/2), while the rest consists of dark greyish brown sediment (2.5Y 4/2) (Fig. 5.30). In the interval from 170 to 180 cm, the sediment is more sandy with muddy and dark organic matter layers and is less fossiliferous, unlike the upper part of the core. The sediment is somewhat coarser-grained in the interval from 200 cm to the end of the core. The core can be subdivided into two lithological units, LU-1-1 (373–145 cm) and LU-1-2 (170–0 cm), regarding its physical properties (Table 5.2; Fig. 5.36).

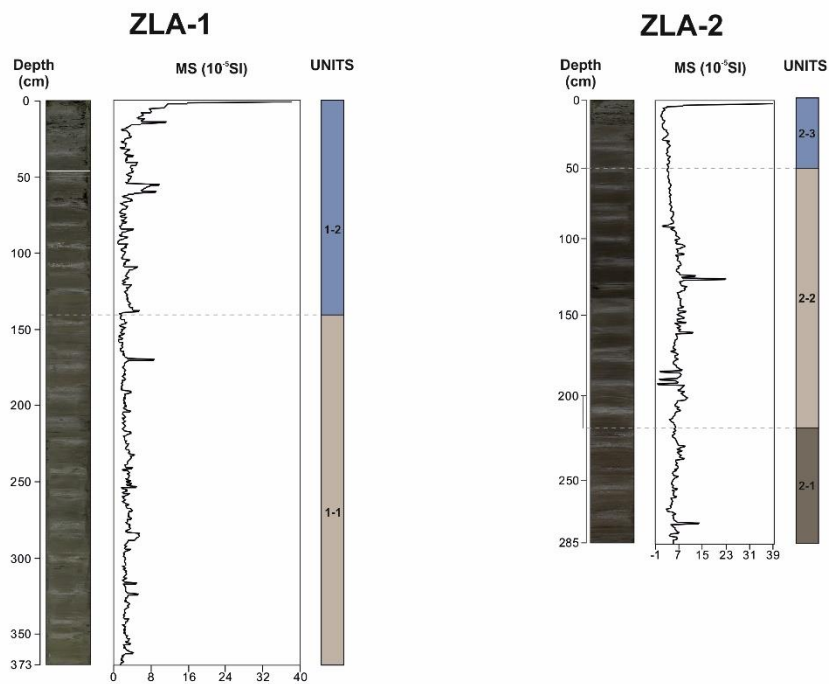


Figure 5.36 Physical properties of sediment cores ZLA-1 and ZLA-2.

The MS values are in the range from 0.8 SI to 38.3 SI (Fig. 5.36; Table 5.12). MS is generally uniform and constant throughout the core, whereas somewhat higher values are present for the first 15 cm of the core ZLA-1 (Fig. 5.36).

Table 5.12 Statistical parameters of magnetic susceptibility values in sediments of the core ZLA-1.

	ZLA-1	LU1-1	LU1-2	TOTAL CORE
MS (10⁻⁵SI)	Mean	2.74	3.46	3.09
	SD	0.75	3.43	2.47
	Min	1.4	0.8	0.8
	Max	5.6	38.3	38.3

The sediment core ZLA-2 is 285 cm long (Table 4.1; Appendix 6) and was recovered near the south side of the island of Zlarin at a depth of 61 m (Fig. 4.2B). The core consists of mostly homogenous dark grey to brown sediment (2.5Y 4/2) (Fig. 5.36). The first 20 cm of the core is composed of gravelly sediment, while in the interval from 20 to 190 cm, the sediment is homogenous and generally muddy up to 80 cm of the core. From 80 cm to 190 cm, the sediment is somewhat sandier, and then in the interval from 190 to 230 cm, the sediment is fine-grained and muddy. The bottom part of the core (230–285 cm) is characterized by muddy to somewhat sandy sediment. The core can be subdivided into three lithological units based on its physical and micropalaeontological properties and those are: LU-2-1 (285–220 cm), LU-2-2 (220–50 cm) and LU-2-3 (50–0 cm) (Table 5.2; Fig. 5.30).

The MS values range from -0.1 to 39.8 SI in the core ZLA-2 (Table 5.13; Fig. 5.36). MS is generally of a constant trend throughout the core, whereas the highest values measure at the top of the core, and somewhat higher values can occur in the interval from 112 to 114 cm (Fig. 5.36).

Table 5.13 Statistical parameters of magnetic susceptibility values in sediments of the core ZLA-2.

	ZLA-2	LU2-1	LU2-2	LU2-3	TOTAL CORE
MS (10⁻⁵SI)	Mean	5.69	6.28	4.22	5.78
	SD	1.59	2.21	7.07	3.58
	Min	2.8	-0.1	0.9	-0.1
	Max	13.9	22.8	39.8	39.8

5.3.3 Particle size analysis

Particle size analysis was performed on 87 samples from sediment core PROK-1 (Appendix 2). The results of PSA, i.e., volume percentages of sand, silt, and clay, are presented in Figure 5.37 and Table 5.14. All lithological units in the sediment core PROK-1 showed a clear predominance of the silt fraction (Fig. 5.37). The volume percentage of sand particles in PROK-

1 ranges from 0 to 33.8%, silt from 66.2 to 87.9%, and clay fraction varies between 0 and 19.3% (Table 5.14). A generally fining upward trend is observed (Fig. 5.37), except for the LU3, in which a higher content of sand particles occurs (Fig. 5.37). The mean particle size in the core PROK-1 ranges between 5.95 and 12.78 μm (Fig. 5.37). All samples are poorly to very poorly sorted (Appendix 2).

PSA was performed on 48 samples in the sediment core PROK-2 (Appendix 3), and the results are presented in Figure 5.38 and Table 5.15. A predominance of silt particles was observed throughout the core (Fig. 5.38) The volume percentage of sand particles in the PROK-2 ranges from 0 to 38.60%, the silty fraction from 57.60 to 86.80%, and the clay percentage from 3.70 to 20.81% (Table 5.15). The higher sand content occurs in the LU2, LU3, and LU4a of the core PROK-2 (Fig. 5.38). The mean particle size in core PROK-2 ranged from 5.29 to 44.15 μm (Fig 5.38). The fine silty sediment exhibits poor sorting, while the coarse silt is very poorly sorted (Appendix 3).

In the sediment core PROK-3, 62 samples were analyzed for particle size (Appendix 4). The PSA results are presented in Figure 5.39 and Table 5.16. The lower and central parts of the core PROK-3 are dominantly built of medium to coarse silt, while the upper part of the core is composed of fine silty sediment, i.e., a fining upward trend can be distinguished (Fig. 5.39). The sand component ranges from 0 to 41.48%, the silty fraction from 56.31 to 84.79%, and the percentage of clay from 0 to 24.32% (Table 5.16). The highest sand content can be observed at the bottom of the core and in intervals from 420 to 400 cm and between 370 and 340 cm (Fig. 5.39). The mean particle size ranges from 4.85 to 38.89 μm (Fig. 5.39). A generally fining upward trend can be observed (Fig. 5.39). The samples are poorly to very poorly sorted (Appendix 4).

PSA was performed on 66 sediment samples from the core PROK-4 (Appendix 5), and the results are presented in Figure 5.40 and Table 5.17. The sediment succession coarsens upward with a dominant silty fraction (Fig. 5.40). The sand content ranges from 0 to 33.80%, the silty fraction from 63.10 to 93.80%, and the percentage of clay from 0 to 23.43 % (Table 5.17). The mean particle sizes range from 4.71 to 42.41 μm (Fig. 5.40). The samples are mostly poorly sorted (Appendix 5).

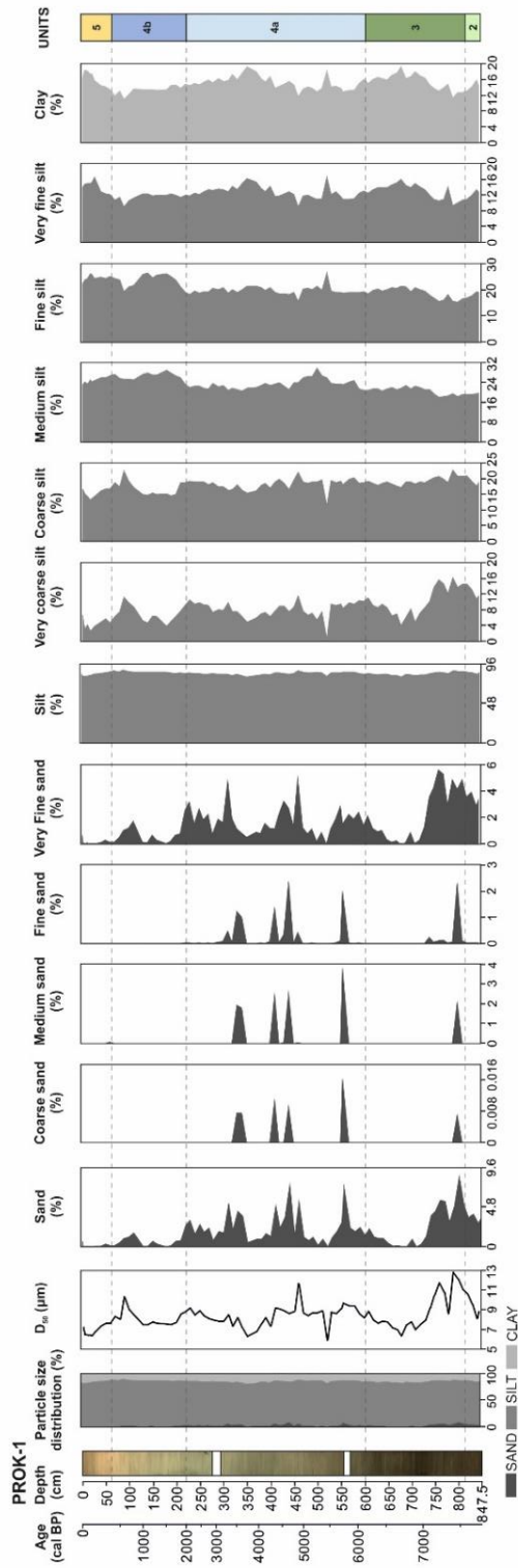


Figure 5.37 Particle size distribution in sediments of the core PROK-1.

Table 5.14 Statistical parameters for particle size distribution in sediments of the core PROK-1.

	PROK-1	LU2	LU3	LU4a	LU4b	LU5	TOTAL CORE
SAND (%)	Mean	3.76	2.19	2.37	0.69	0.16	1.89
	SD	0.80	2.40	1.80	0.71	0.21	1.95
	Min	2.9	0.00	0.00	0.00	0.00	0.00
	Max	5.00	8.6	7.6	2.6	0.7	8.6
COARSE SAND (%)	Mean	0.00	0.00	0.00	0.00	0.00	0.00
	SD	0.00	0.002	0.003	0.00	0.00	0.003
	Min	0.00	0.00	0.00	0.00	0.00	0.00
MEDIUM SAND (%)	Mean	0.00	0.10	0.34	0	0.01	0.17
	SD	0.00	0.46	0.90	0	0.02	0.65
	Min	0.00	0.00	0.00	0.00	0.00	0.00
FINE SAND (%)	Mean	0.04	0.15	0.27	0.00	0.00	0.15
	SD	0.03	0.51	0.58	0.007	0.004	0.46
	Min	0.00	0.00	0.00	0.00	0.00	0.00
VERY FINE SAND (%)	Mean	0.10	2.31	2.36	0.03	0.1	2.36
	SD	3.73	1.98	1.76	0.73	0.16	1.57
	Min	0.78	1.97	1.09	0.73	0.21	1.47
SILT (%)	Mean	2.87	0.01	0.00	0.03	0.01	0.00
	SD	4.92	5.63	4.99	2.58	0.68	5.63
	Min	82.16	82.08	82.46	85.88	83.50	83.03
VERY COARSE SILT (%)	Mean	0.77	1.20	2.08	1.39	1.68	2.13
	SD	81.17	78.51	76.84	82.55	81.57	76.84
	Min	83.27	82.73	86.84	87.91	86.24	87.91
COARSE SILT (%)	Mean	13.04	9.87	8.16	7.12	4.47	8.25
	SD	1.77	3.58	2.00	2.12	1.28	3.07
	Min	10.75	3.99	0.68	3.91	2.71	0.68
MEDIUM SILT (%)	Mean	14.77	16.37	11.70	11.27	6.72	16.37
	SD	19.52	19.18	18.29	18.37	15.42	18.03
	Min	1.38	1.27	1.75	1.89	1.36	2.07
FINE SILT (%)	Mean	17.76	17.23	11.59	14.51	13.32	11.59
	SD	21.04	22.80	22.19	22.60	16.91	22.80
	Min	19.55	20.88	23.47	26.64	24.85	23.31
VERY FINE SILT (%)	Mean	0.27	1.44	2.01	1.50	1.25	2.65
	SD	19.29	18.25	20.72	23.30	23.23	18.25
	Min	19.93	22.75	29.98	29.23	27.04	29.98
CLAY (%)	Mean	18.07	18.99	19.79	23.52	24.49	20.66
	SD	1.20	2.01	1.61	2.52	1.25	2.77
	Min	16.81	15.32	15.65	19.13	22.47	15.32
CLAY (%)	Mean	19.47	21.50	26.63	26.51	26.32	26.63
	SD	11.98	13.15	12.74	11.56	14.27	12.78
	Min	1.14	1.86	1.52	0.90	1.40	1.65
CLAY (%)	Mean	10.73	9.36	9.10	9.11	12.15	9.10
	SD	13.45	16.06	16.60	12.43	16.63	16.63
	Min	14.08	15.69	15.18	13.40	16.33	15.08
CLAY (%)	SD	1.24	1.95	1.63	1.05	1.75	1.83
	Min	12.75	11.37	11.83	11.08	13.56	11.08
	Max	15.92	19.29	19.34	14.85	18.37	19.34

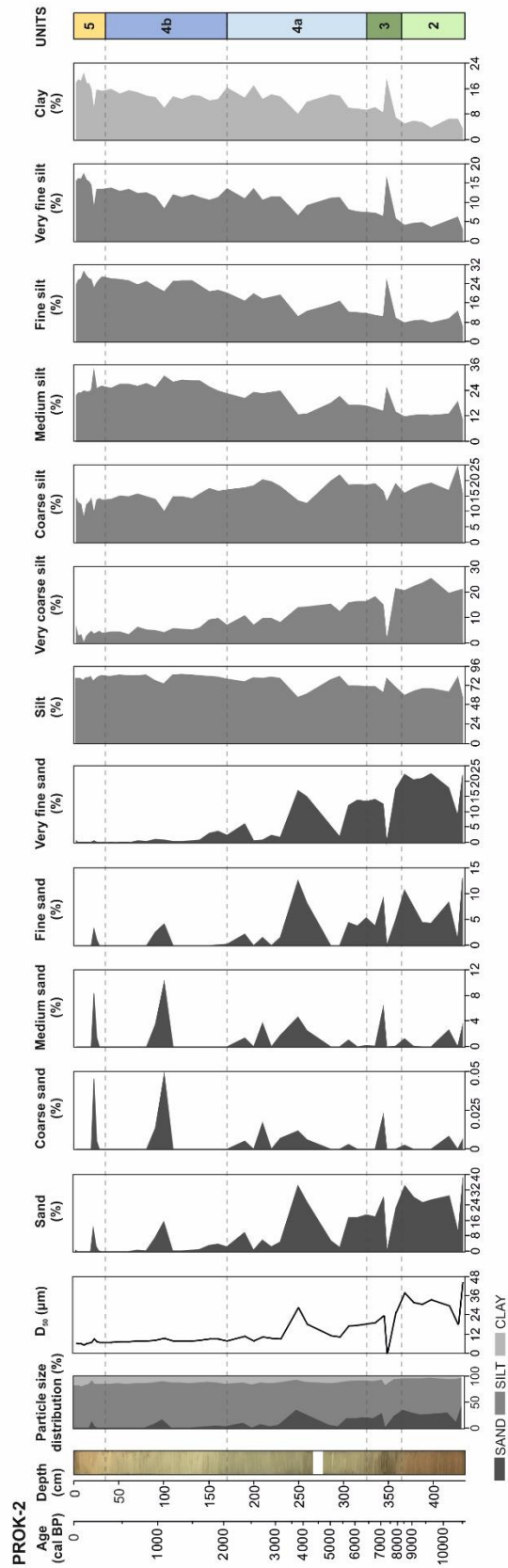


Figure 5.38 Particle size distribution in sediments of the core PROK-2.

Table 5.15 Statistical parameters for particle size distribution in sediments of the core PROK-2.

PROK-2		LU2	LU3	LU4a	LU4b	LU5	TOTAL CORE
SAND (%)	Mean	27.54	17.62	10.85	2.78	1.37	9.60
	SD	8.94	10.61	10.80	4.52	3.54	11.80
	Min	10.10	0.00	0.60	0.00	0.00	0.00
	Max	38.60	28.20	34.30	15.40	12.30	38.60
COARSE SAND (%)	Mean	0.00	0.00	0.00	0.01	0.00	0.00
	SD	0.003	0.01	0.006	0.01	0.01	0.01
	Min	0.00	0.00	0.00	0.00	0.00	0.00
	Max	0.01	0.02	0.01	0.05	0.05	0.05
MEDIUM SAND (%)	Mean	1.06	1.33	1.27	1.14	0.82	1.10
	SD	1.40	2.78	1.62	3.02	2.41	2.25
	Min	0.00	0.00	0.00	0.00	0.00	0.00
	Max	3.31	6.30	4.65	10.19	8.35	10.19
FINE SAND (%)	Mean	7.15	4.70	2.92	0.60	0.38	2.51
	SD	4.12	3.31	3.96	1.38	0.98	3.65
	Min	1.14	0.00	0.00	0.00	0.00	0.00
	Max	13.15	9.24	12.67	4.23	3.30	13.15
VERY FINE SAND (%)	Mean	19.33	11.59	6.65	1.03	0.17	5.99
	SD	4.84	6.74	6.15	1.19	0.21	7.80
	Min	8.96	0.00	0.58	0.01	0.01	0.00
	Max	22.50	17.55	16.95	3.81	0.60	22.50
SILT (%)	Mean	67.14	71.62	76.24	83.81	82.04	77.78
	SD	8.29	6.34	8.62	3.46	2.01	8.29
	Min	57.70	63.40	57.60	74.60	78.20	57.60
	Max	83.40	81.21	84.20	86.80	84.70	86.80
VERY COARSE SILT (%)	Mean	21.97	14.51	11.77	5.89	3.83	10.09
	SD	2.03	7.88	3.39	1.90	1.41	6.94
	Min	19.60	1.05	7.16	3.37	0.33	0.33
	Max	25.56	21.41	16.48	9.89	6.16	25.56
COARSE SILT (%)	Mean	18.48	17.35	18.09	14.92	12.73	15.94
	SD	2.99	2.55	2.66	1.83	1.98	3.21
	Min	16.04	13.16	12.65	10.05	8.02	8.02
	Max	24.66	19.16	21.99	17.58	14.26	24.66
MEDIUM SILT (%)	Mean	13.10	17.25	19.66	27.36	24.88	21.68
	SD	2.59	4.64	3.91	1.88	3.10	5.86
	Min	10.66	13.93	12.87	23.88	21.67	10.66
	Max	18.72	25.30	23.89	30.99	33.81	33.81
FINE SILT (%)	Mean	8.98	13.83	16.18	23.92	26.02	19.28
	SD	1.96	6.51	3.42	1.88	1.76	6.85
	Min	6.64	10.02	10.50	21.07	22.46	6.64
	Max	12.86	25.41	20.41	25.63	29.42	29.42
VERY FINE SILT (%)	Mean	4.62	8.69	10.56	11.73	14.57	10.80
	SD	1.06	4.30	2.19	1.30	2.31	3.81
	Min	3.11	5.88	6.61	8.40	8.56	3.11
	Max	6.31	16.29	13.67	13.57	17.55	17.55
CLAY (%)	Mean	5.31	10.76	12.91	13.42	16.59	12.62
	SD	1.15	4.65	2.65	1.38	2.78	4.29
	Min	3.70	7.00	8.10	10.00	9.50	3.70
	Max	6.50	18.79	17.00	15.40	20.81	20.81

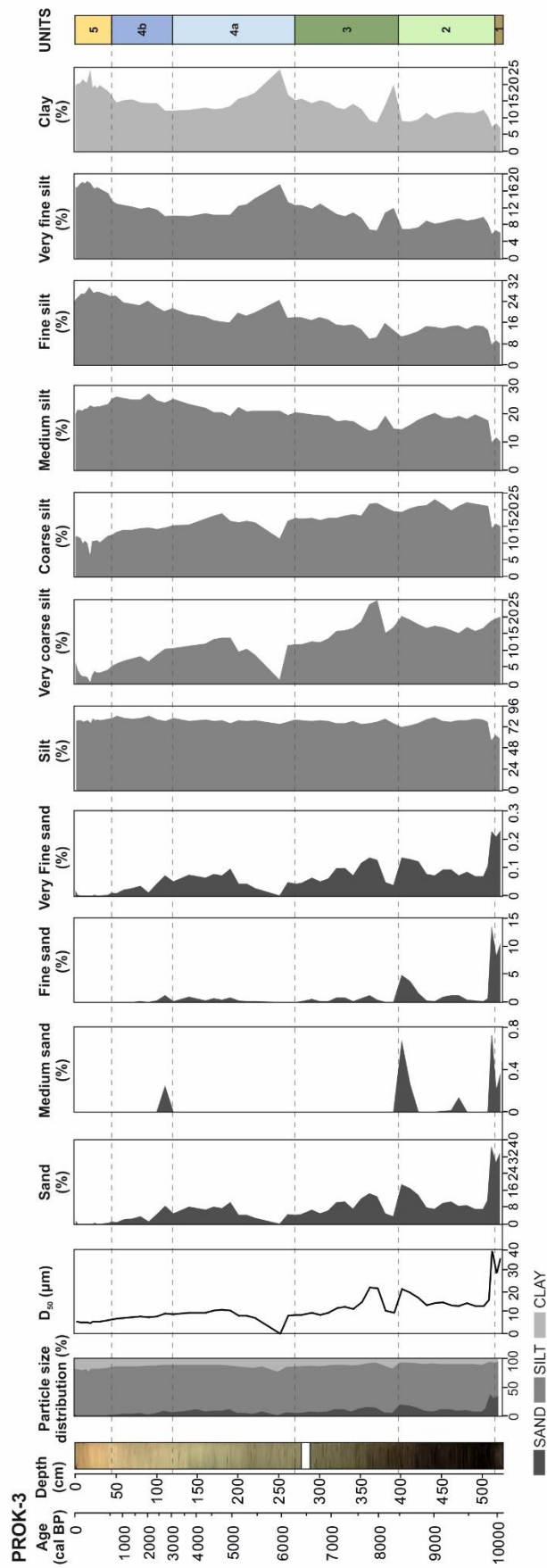


Figure 5.39 Particle size distribution in sediments of the core PROK-3.

Table 5.16 Statistical parameters for particle size distribution in sediments of the core PROK-3.

PROK-3		LU1	LU2	LU3	LU4a	LU4b	LU5	TOTAL CORE
SAND (%)	Mean	31.10	12.63	8.26	8.62	3.21	0.17	7.70
	SD	2.96	8.06	3.73	9.90	2.51	0.34	8.64
	Min	29.01	6.98	3.71	0.00	0.66	0.01	0.00
	Max	33.19	36.37	14.64	10.93	8.40	1.22	41.48
MEDIUM SAND (%)	Mean	0.27	0.14	0.00	2.37	0.03	0.00	0.58
	SD	0.09	0.26	0.00	8.16	0.08	0.00	3.89
	Min	0.20	0.00	0.00	0.00	0.00	0.00	0.00
	Max	0.33	0.72	0.00	30.67	0.24	0.00	30.67
FINE SAND (%)	Mean	9.10	2.18	0.39	1.25	0.19	0.00	1.14
	SD	1.45	3.56	0.37	2.76	0.38	0.002	2.65
	Min	8.08	0.12	0.01	0.00	0.00	0.00	0.00
	Max	10.13	13.04	1.13	10.65	1.19	0.01	13.04
VERY FINE SAND (%)	Mean	0.22	0.10	0.08	0.05	0.03	0.00	0.06
	SD	0.01	0.04	0.03	0.03	0.02	0.003	0.05
	Min	0.21	0.07	0.04	0.00	0.01	0.00	0.00
	Max	0.23	0.23	0.14	0.10	0.07	0.01	0.23
SILT (%)	Mean	61.17	76.92	78.10	77.20	82.45	79.70	78.04
	SD	2.10	6.86	1.87	5.61	1.65	1.51	5.53
	Min	59.71	56.31	75.19	58.50	79.42	76.08	56.31
	Max	62.63	82.99	81.43	80.51	84.79	82.69	84.79
VERY COARSE SILT (%)	Mean	19.64	17.27	16.43	10.00	7.81	3.03	11.41
	SD	0.39	1.44	4.16	4.04	1.85	1.41	6.20
	Min	19.37	15.05	11.66	1.06	5.29	0.21	0.21
	Max	19.92	20.24	24.68	13.79	10.56	5.78	24.68
COARSE SILT (%)	Mean	15.40	20.57	18.76	15.35	14.07	10.47	15.98
	SD	0.56	2.10	1.73	4.08	0.82	1.70	4.24
	Min	15.00	14.30	16.92	2.47	12.39	5.77	2.47
MEDIUM SILT (%)	Mean	10.96	17.54	17.42	22.25	25.32	21.99	20.36
	SD	0.87	2.76	2.25	5.07	0.85	0.92	4.40
	Min	10.34	9.79	13.95	19.26	24.07	20.12	9.79
FINE SILT (%)	Mean	11.57	20.18	20.33	39.45	27.06	23.47	39.45
	Mean	8.77	13.23	14.93	18.34	23.35	27.06	18.72
	SD	0.62	2.09	2.70	2.24	1.97	1.38	5.79
VERY FINE SILT (%)	Min	8.33	7.76	10.01	15.41	20.42	24.32	7.76
	Max	9.21	15.02	18.19	19.76	26.30	29.47	29.47
	Mean	6.40	8.30	10.56	11.25	11.91	17.15	11.58
CLAY (%)	SD	0.39	1.19	2.02	3.87	1.23	0.79	3.75
	Min	6.13	5.77	6.70	0.00	9.92	15.51	0.00
	Max	6.68	9.87	12.94	17.56	13.64	18.17	18.17
CLAY (%)	Mean	7.73	10.45	13.64	14.18	14.33	20.13	14.26
	SD	0.91	1.45	2.90	5.15	1.42	1.55	4.43
	Min	7.09	7.29	8.63	0.00	12.09	17.88	0.00
CLAY (%)	Max	8.37	12.33	19.77	24.32	16.41	23.92	24.32

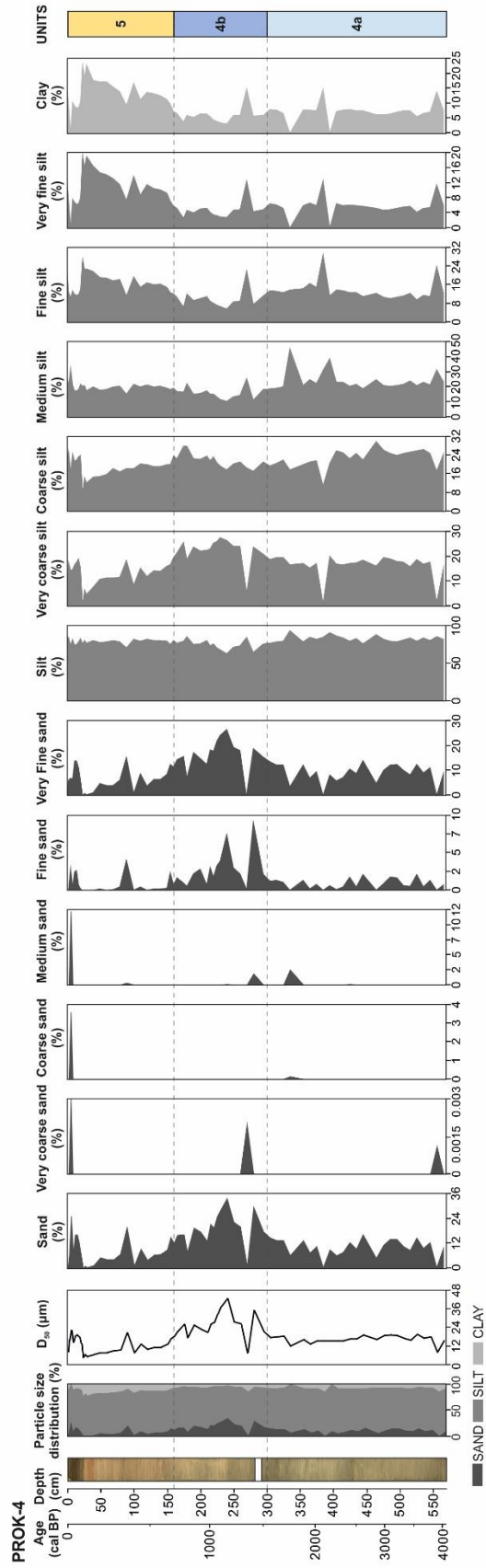


Figure 5.40 Particle size distribution in sediments of the core PROK-4.

Table 5.17 Statistical parameters for particle size distribution in sediments of the core PROK-4.

PROK-4		LU4a	LU4b	LU5	TOTAL CORE
SAND (%)	Mean	9.92	18.02	7.15	11.32
	SD	4.26	7.99	6.82	7.69
	Min	0.00	0.09	0.00	0.00
	Max	16.10	33.80	25.10	33.80
VERY COARSE SAND (%)	Mean	0.52	0.175	0.00	0.25
	SD	2.70	0.78	0.00	1.74
	Min	0.00	0.00	0.00	0.00
	Max	14.04	3.50	0.00	14.04
COARSE SAND (%)	Mean	2.90	1.16	0.16	1.52
	SD	12.99	5.19	0.77	8.58
	Min	0.00	0.00	0.00	0.00
	Max	67.04	23.20	3.61	67.04
MEDIUM SAND (%)	Mean	1.71	1.026	0.55	4.60
	SD	6.08	4.15	2.52	1.14
	Min	0.00	0.00	0.00	0.00
	Max	28.23	18.57	11.81	28.23
FINE SAND (%)	Mean	1.03	2.49	0.67	1.34
	SD	1.30	2.19	1.14	1.72
	Min	0.00	0.00	0.00	0.00
	Max	6.72	8.85	3.94	8.85
VERY FINE SAND (%)	Mean	8.47	15.08	5.77	9.52
	SD	4.13	6.18	4.60	6.15
	Min	0.00	0.09	0.00	10.00
	Max	14.01	26.51	15.47	26.51
SILT (%)	Mean	78.62	75.75	79.54	77.56
	SD	16.53	8.12	3.85	11.90
	Min	3.4	43.6	74.70	3.40
	Max	93.80	86.30	85.14	93.80
VERY COARSE SILT (%)	Mean	15.58	21.44	12.17	16.19
	SD	5.64	5.29	5.05	6.43
	Min	0.00	5.40	0.71	0.00
	Max	20.09	27.74	19.18	27.74
COARSE SILT (%)	Mean	21.55	21.34	18.70	20.58
	SD	6.12	3.47	4.31	5.01
	Min	0.04	12.87	8.19	0.04
	Max	30.00	28.14	26.17	30.00
MEDIUM SILT (%)	Mean	23.07	16.13	20.60	20.27
	SD	7.61	3.96	3.60	6.22
	Min	2.53	9.94	15.17	2.53
	Max	45.52	25.7	32.90	45.52
FINE SILT (%)	Mean	13.16	10.18	16.95	13.50
	SD	4.81	3.73	4.55	5.13
	Min	0.82	5.79	10.53	0.82
	Max	29.30	22.45	27.52	29.3
VERY FINE SILT (%)	Mean	5.34	4.89	11.02	7.02
	SD	2.86	2.59	4.72	4.42
	Min	0.00	0.18	0.00	0.00
	Max	12.59	12.64	19.63	19.63
CLAY (%)	Mean	6.68	6.10	13.42	8.66
	SD	3.47	3.15	5.28	5.18
	Min	0.00	0.00	0.00	0.00
	Max	14.91	15.02	23.43	22.43

PSA was performed on 38 sediment samples in the core ZLA-1 (Appendix 6), and the results are shown in Figure 5.41 and Table 5.18. A coarsening upward trend can be observed from the bottom of the core up to 220 cm of the core, but still with a dominant silty fraction (Fig. 5.41). A fining upwards occurs from 220 cm to the top of the core (Fig. 5.41). The sand content ranges from 0 to 7.94%, the silty fraction from 81.70 to 90.78%, and the percentage of clay from 8.58 to 17.19% (Table 5.18). The mean particle sizes range from 7.31 to 20.53 μm (Fig. 5.41). The samples are poorly sorted (Appendix 6).

In core ZLA-2, 28 samples were analyzed for PSA (Appendix 6). The results of PSA are presented in Figure 5.42 and statistical parameters in Table 5.19. From the bottom of the core to 235 cm, the sand fraction is dominant with up to 80%, then a fining upward trend can be observed up to 130 cm with the dominant silty fraction (with a higher content of sand at interval from 180 to 190 cm). From 130 cm to the top of the core, the sand fraction increased again (up to 30%) (Fig. 5.42). The sand content ranges from 3.10 to 80.40%, the silty fraction ranged from 19.50 to 85.00%, and the percentage of clay ranged from 0.10 to 11.90% (Table 5.19). The mean particle sizes range from 12.37 to 125.80 μm (Fig. 5.42). The samples are poorly to very poorly sorted (Appendix 6).

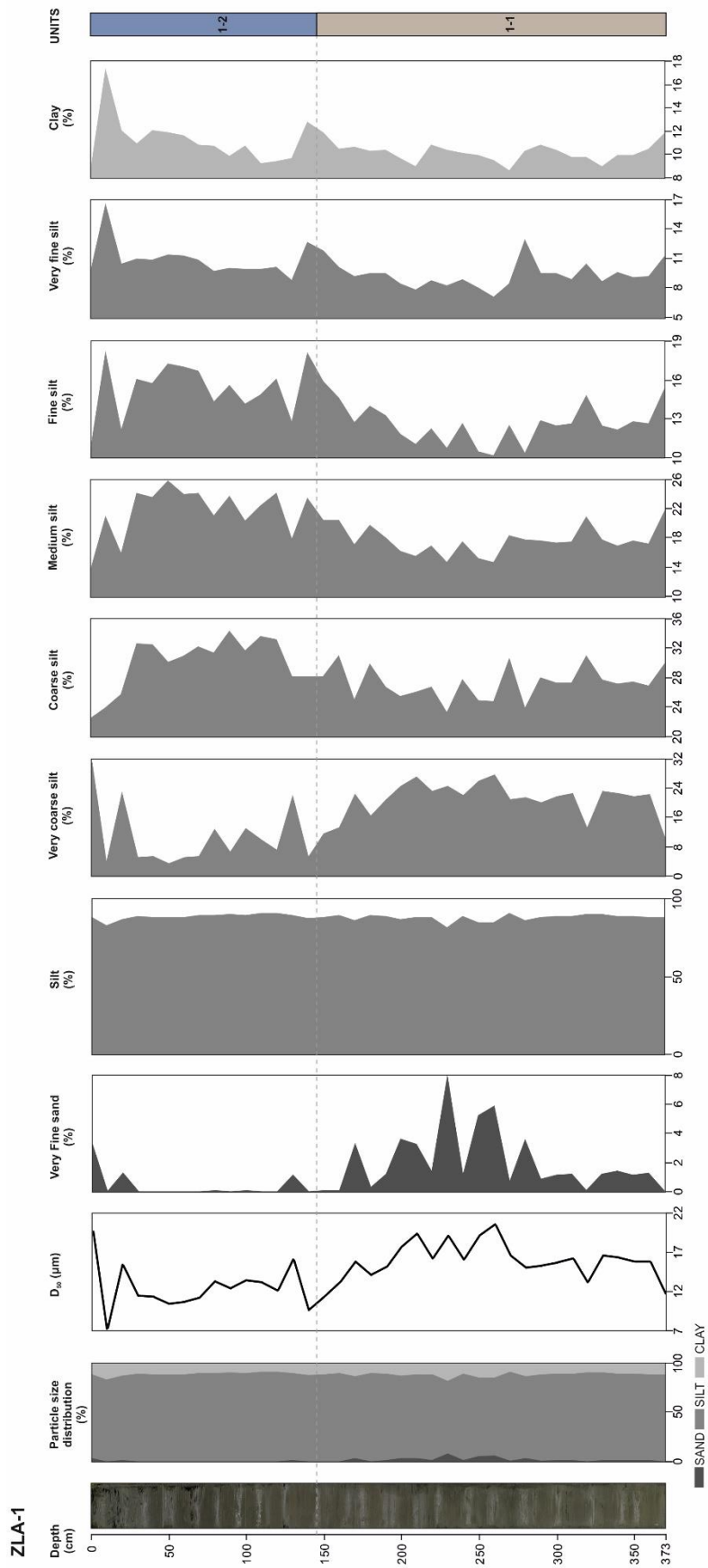


Figure 5.41 Particle size distribution in sediments of the core ZLA-1.

Table 5.18 Statistical parameters for particle size distribution in sediments of the core ZLA-1.

	ZLA-1	LU1-1	LU1-2	TOTAL CORE
SAND (%)	Mean	2.12	0.5	1.35
	SD	2.13	1.04	1.87
	Min	0.04	0.00	0.00
	Max	7.94	3.25	7.94
VERY FINE SAND (%)	Mean	2.12	0.5	1.35
	SD	2.12	1.04	1.87
	Min	0.04	0.00	0.00
	Max	7.88	3.25	7.88
SILT (%)	Mean	87.43	88.34	88.08
	SD	2.14	1.86	2.00
	Min	81.70	82.81	81.70
	Max	90.75	90.78	90.78
VERY COARSE SILT (%)	Mean	21.67	11.37	16.79
	SD	4.32	8.08	8.17
	Min	10.10	3.4	3.4
	Max	27.88	31.03	31.03
COARSE SILT (%)	Mean	27.13	29.72	28.36
	SD	2.09	3.52	3.11
	Min	23.27	22.59	22.59
	Max	30.96	34.29	34.29
MEDIUM SILT (%)	Mean	17.48	21.28	19.28
	SD	1.81	3.33	3.24
	Min	14.7	13.82	13.82
	Max	21.66	25.85	25.85
FINE SILT (%)	Mean	12.36	15.13	13.67
	SD	1.37	2.06	2.21
	Min	10.16	10.79	10.16
	Max	15.25	18.05	18.05
VERY FINE SILT (%)	Mean	9.21	10.29	9.98
	SD	1.27	1.70	1.68
	Min	7.07	8.82	7.07
	Max	12.94	16.52	16.52
CLAY (%)	Mean	10.04	11.16	10.57
	SD	0.72	1.86	1.48
	Min	8.58	8.83	8.58
	Max	11.82	17.19	17.19

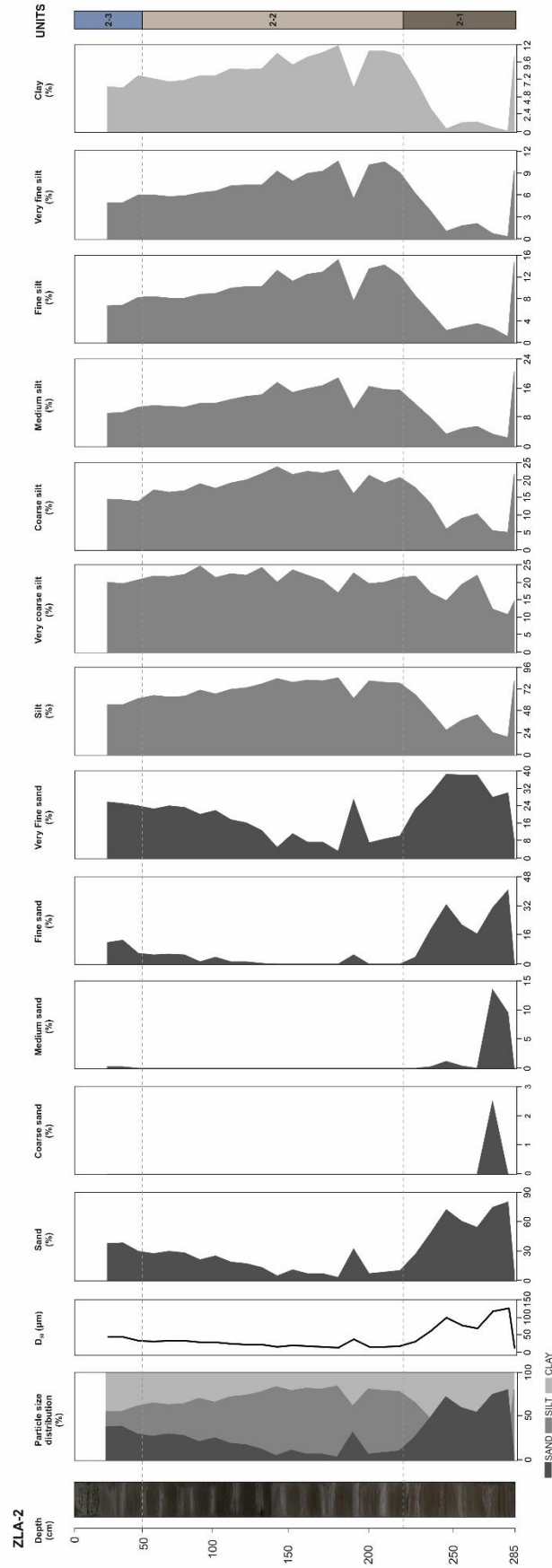


Figure 5.42 Particle size distribution in sediments of the core ZLA-2.

Table 5.19 Statistical parameters for particle size distribution in sediments of the core ZLA-2.

ZLA-2		LU2-1	LU2-2	LU2-3	TOTAL CORE
SAND (%)	Mean	57.20	16.12	33.5	28.87
	SD	24.30	9.61	5.62	22.43
	Min	8.40	3.10	27.60	3.10
	Max	80.40	32.10	38.50	80.4
COARSE SAND (%)	Mean	0.36	0.00	0.00	0.09
	SD	0.94	0.00	0.00	0.47
	Min	0.00	0.00	0.00	0.00
	Max	2.50	0.00	0.00	2.50
MEDIUM SAND (%)	Mean	3.56	0.00	0.10	0.90
	SD	5.56	0.00	0.12	3.05
	Min	0.00	0.00	0.00	0.00
	Max	13.50	0.00	0.20	13.50
FINE SAND (%)	Mean	23.14	1.65	9.00	8.08
	SD	13.24	2.11	4.13	11.33
	Min	0.30	0.00	5.00	0.00
	Max	40.90	5.60	13.00	40.90
VERY FINE SAND (%)	Mean	30.13	14.47	24.40	19.80
	SD	10.81	7.64	1.41	10.46
	Min	8.00	3.10	22.60	3.10
	Max	38.50	26.90	25.80	38.50
SILT (%)	Mean	40.31	74.80	59.60	64.01
	SD	20.80	7.87	2.44	18.90
	Min	19.50	61.90	55.40	19.50
	Max	81.20	85.00	65.10	85.00
VERY COARSE SILT (%)	Mean	15.90	21.69	20.68	20.10
	SD	4.00	1.84	0.50	3.45
	Min	10.80	17.10	19.70	10.80
	Max	22.20	24.80	22.00	24.80
COARSE SILT (%)	Mean	10.19	20.05	15.03	16.86
	SD	5.93	2.39	0.77	5.47
	Min	5.00	16.10	14.00	5.00
	Max	21.80	24.00	17.30	24.00
MEDIUM SILT (%)	Mean	6.81	14.14	10.18	11.74
	SD	6.31	2.62	1.09	4.83
	Min	2.30	10.10	9.10	2.30
	Max	20.50	18.90	11.30	20.50
FINE SILT (%)	Mean	4.69	11.02	7.68	8.96
	SD	4.66	2.40	0.90	4.00
	Min	1.10	7.60	6.80	1.10
	Max	14.80	15.30	8.50	15.30
VERY FINE SILT (%)	Mean	2.76	8.06	5.55	6.30
	SD	3.19	1.71	0.64	3.02
	Min	0.30	5.50	5.00	0.30
	Max	9.50	10.70	6.10	10.70
CLAY (%)	Mean	2.49	9.23	6.88	7.13
	SD	3.64	1.77	0.81	3.60
	Min	0.10	6.00	6.10	0.10
	Max	10.40	11.90	7.80	11.90

5.3.4 Mineralogical analysis

XRD mineralogical composition analysis was performed on 15 samples from the core PROK-1, and the results are given in Table 5.20. Sediments of the core PROK-1 are dominantly built of calcite, while the minor component consists of quartz, halite, illite, kaolinite, aragonite, and dolomite. The halite formed in the core by seawater crystallization after core extraction. The samples at 690 to 691 cm and 630 to 631 cm, obtained pyrite.

Table 5.20 Mineral composition of the sediment core PROK-1. Symbols (Kretz, 1983): Cal-calcite, Qtz-quartz, Hl-halite, Ms/I-muscovite/illite, Arg-aragonite, Dol-dolomite, Kln-kaolinite and Py-pyrite.

PROK-1	Main minerals	Accessory minerals
0-1	Cal	Qtz, Hl, Ms/I
30-31	Cal	Qtz, Hl, Ms/I, Kln
70-71	Cal	Qtz, Hl, Ms/I, Arg
130-131	Cal	Qtz, Hl, Ms/I, Arg
190-191	Cal	Qtz, Hl, Arg
240-241	Cal	Qtz, Hl, Ms/I, Arg
350-351	Cal	Qtz, Hl, Ms/I, Arg, Dol
451-452	Cal	Qtz, Hl, Ms/I, Arg, Dol
521-522	Cal	Qtz, Hl, Ms/I, Arg, Dol
630-631	Cal	Qtz, Hl, Ms/I, Py
690-691	Cal	Qtz, Hl, Ms/I, Py
750-751	Cal	Qtz, Hl, Ms/I, Arg, Dol
810-811	Cal	Qtz, Hl, Ms/I, Arg, Dol
830-831	Cal	Qtz, Hl, Ms/I, Arg, Dol
840-841	Cal	Qtz, Hl, Ms/I, Arg, Dol

In the sediment core PROK-2, a bulk mineral content was analyzed on 15 samples, and the results are present in Table 5.21. PROK-2 is dominantly composed of calcite, with the presence of quartz, halite, and aragonite, and minerals muscovite/illite occur from 360 cm to the top of the core. Only in the core PROK-2, dolomite is not present.

Table 5.21 Mineral composition of the sediment core PROK-2. Symbols (Kretz, 1983): Cal-calcite, Qtz-quartz, Hl-halite, Arg-aragonite and Ms/I-muscovite/illite.

PROK-2	Main minerals	Accessory minerals
6-7	Cal	Qtz, Hl, Arg, Ms/I
18-19	Cal	Qtz, Hl, Arg, Ms/I
30-31	Cal	Qtz, Hl, Arg, Ms/I
70-71	Cal	Qtz, Hl, Arg, Ms/I
140-141	Cal	Qtz, Hl, Arg, Ms/I
160-161	Cal	Qtz, Hl, Arg, Ms/I
190-191	Cal	Qtz, Hl, Arg, Ms/I
230-231	Cal	Qtz, Hl, Arg, Ms/I
287-288	Cal	Qtz, Hl, Arg, Ms/I
337-338	Cal	Qtz, Hl, Arg, Ms/I
360-361	Cal	Qtz, Hl, Arg, Ms/I
380-381	Cal	Qtz, Hl, Arg
400-401	Cal	Qtz, Hl, Arg
420-421	Cal	Qtz, Hl, Arg
435-436	Cal	Qtz, Hl, Arg

A total of 15 samples were analyzed for bulk mineralogy in the sediment core PROK-3 (Table 5.22). The sediment from the bottom of the core (521 cm) up to 510 cm is composed dominantly of dolomite, quartz, and calcite, whereas, from 510 cm up to the top of the core, the calcite is the main mineralogical phase. Additionally, muscovite/illite, kaolinite, plagioclase, halite, aragonite, Mg-calcite, and pyrite are present throughout the core. The pyrite is present only at the bottom part of the core.

Table 5.22 Mineral composition of the sediment core PROK-3. Symbols (Kretz, 1983): Cal-calcite, Qtz-quartz, Mg-Cal-Mg calcite, HI-halite, Arg-aragonite, Dol-dolomite, Ms/I-muscovite/illite, Kln-kaolinite, Py-pyrite and Sm/V/Chl-smectite/vermiculite/chlorite.

PROK-3	Main minerals	Accessory minerals
12-13	Cal	Qtz, HI, Arg, Ms/I
24-25	Cal	Qtz, HI, Arg, Ms/I
50-51	Cal	Qtz, HI, Dol, Arg, Ms/I, Sm/V/Chl
90-91	Cal	Qtz, HI, Arg, Dol, Ms/I, Kln
170-171	Cal	Mg-Cal, Qtz, Dol, Arg, HI, Ms/I, Kln
200-201	Cal	Qtz, Dol, Arg, HI, Ms/I, Kln
250-251	Cal	Qtz, Dol, Arg, HI, Ms/I, Kln
300-301	Cal	Mg-Cal, Qtz, Dol, Arg, HI, Ms/I, Kln
350-351	Cal	Qtz, Dol, Arg, HI, Ms/I, Kln
410-411	Cal	Qtz, Dol, HI, Ms/I, Kln, Py
430-431	Cal	Qtz, Dol, HI, Ms/I, Kln, Arg, Pl
460-461	Cal	Qtz, Dol, HI, Ms/I, Kln, Py
500-501	Cal	Dol, Qtz, HI, Ms/I, Pl, Amph, Py, Kln
510-511	Dol	Cal, Qtz, HI, Ms/I, Pl, Kln, Py
520-521	Dol, Qtz, Cal	Ms/I, Kln, HI, Pl

In the sediment core PROK-4, 15 samples were analyzed for bulk mineralogy, and the results are presented in Table. The core is dominantly composed of calcite, while quartz, halite, aragonite, and muscovite/illite occur as minor phases.

Table 5.23 Mineral composition of the sediment core PROK-4. Symbols (Kretz, 1983): Cal-calcite, Qtz-quartz, HI-halite, Arg-aragonite and Ms/I-muscovite/illite.

PROK-4	Main minerals	Accessory minerals
6-7	Cal	Qtz, HI, Arg
30-31	Cal	Qtz, HI, Arg
40-41	Cal	Qtz, HI, Ms/I, Arg
60-61	Cal	Qtz, HI, Ms/I, Arg
100-101	Cal	Qtz, HI, Ms/I, Arg
140-141	Cal	Qtz, HI, Ms/I, Arg
170-171	Cal	Qtz, HI, Arg
210-211	Cal	Qtz, HI, Arg
230-231	Cal	Qtz, HI, Arg
270-271	Cal	Qtz, HI, Arg
304-305	Cal	Qtz, HI, Ms/I, Arg
364-365	Cal	Qtz, HI, Arg
425-426	Cal	Qtz, HI, Ms/I, Arg
524-525	Cal	Qtz, HI, Arg
564-565	Cal	Qtz, HI, Ms/I, Arg

5.3.5 Geochemical analysis

5.4.5.1 μ -XRF core scanning

Inorganic elemental analysis using μ -XRF scanning was conducted on all four PROK cores at a 1 mm resolution. The results are semiquantitative and were obtained for the following elements: Al, Si, S, Cl, Ar, K, Ca, Ti, Mn, Fe, Ni, Cu, Zn, As, Br, Rb, Sr, Zr, Sb, Pb, Mo_{inc} and Mo_{coh} . On the basis of the quality check of the bulk data, only the elements that showed a high coefficient of determination ($R^2 > 0.7$) values between duplicate runs were considered reliable for scientific research, namely, K, Ca, Ti, Fe, Br, Rb, Sr and Mo_{inc}/Coh . In Appendices 2–5, all measured elements and their intensities are listed, while in Figures 5.43–5.46, numerical results of measured selected elements (Ca, Ti, and Sr) and log element ratios (Ca/Ti, Ti/Ca, Sr/Ca) are presented. Fe (cps) and K (cps) exhibit a similar trend across the cores as Ti (cps). Therefore, Ti (cps) will be used for further interpretations. Ti (cps) and $\log(Ti/Ca)$ are used as indicators of terrigenous input, while the carbonate content indicators are Ca (cps) and $\log(Ca/Ti)$, and for the aragonitic content and marine influence Sr (cps) and $\log(Sr/Ca)$ are used.

The lower part of core PROK-1 (LU2) shows higher Ca (cps) and $\log(Ca/Ti)$, with an upward increasing trend (Fig. 5.43). In LU3, a rapid decrease of Ca (cps) and $\log(Ca/Ti)$ occurs from 750 to 700 cm, followed by a slight increase in these chemical components in the upper part of LU3 (Fig. 5.43). An increase in Ca (cps) and $\log(Ca/Ti)$ in the lower part of LU4a occurs, where a slight decrease from 450 cm and 400 cm is present with the generally uniform trend to the upper part of LU4a (Fig. 5.43). An increase in Ca (cps) and $\log(Ca/Ti)$ occurs in the lower part of LU4b, while they decrease to the top of the core (LU5; Fig. 5.43). A generally constant trend of Sr (cps) and $\log(Sr/Ca)$ is present throughout the core PROK-1, whereas these chemical components decrease in LU3 (Fig. 5.43). Ti (cps) and $\log(Ti/Ca)$ have the highest values in LU3 and LU5 and the lowest in LU2 and LU4b (Fig. 5.43). In LU4a, Ti (cps) and $\log(Ti/Ca)$ have generally uniform and constant trends (Fig. 5.43).

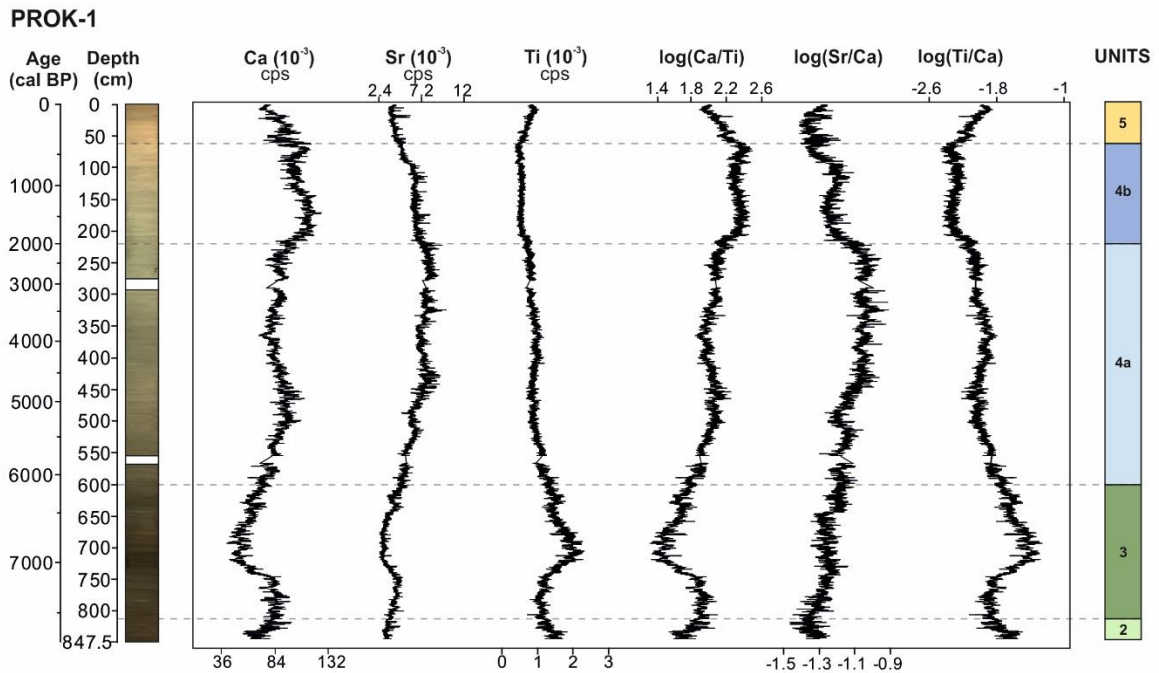


Figure 5.43 Variations of selected XRF elements and ratios with depth in the sediment core PROK-1.

The carbonate content proxies (Ca (cps) and log(Ca/Ti)) are the highest in LU2 and LU4b of the core PROK-2, while the lowest are in the LU3 and LU5 (Fig. 5.44). In LU4a of the core PROK-2, Ca (cps) and log(Ca/Ti) are constant throughout the unit and slightly lower compared to LU2 and LU4b (Fig. 5.44). Sr (cps) and log(Sr/Ca) are low in the lower part of the core in LU2, whereas a slightly increasing trend is present in the LU3 and the first part of the LU4a (until 270 cm; Fig. 5.44). Afterward, a generally constant trend throughout the LU4a is present, with a slight decrease in the first part of the LU4b (160–125 cm) with an increase to the top of the LU4b (Fig. 5.44). The intensity of Sr (cps) decreases in LU5, while the log(Sr/Ca) has a slightly increasing trend in this unit (Fig. 5.44). The terrigenous proxies (Ti (cps) and log(Ti/Ca)) are the highest in LU3, whereas, in the rest of the core, Ti (cps) and log(Ti/Ca) exhibit low and generally uniform values (Fig. 5.44).

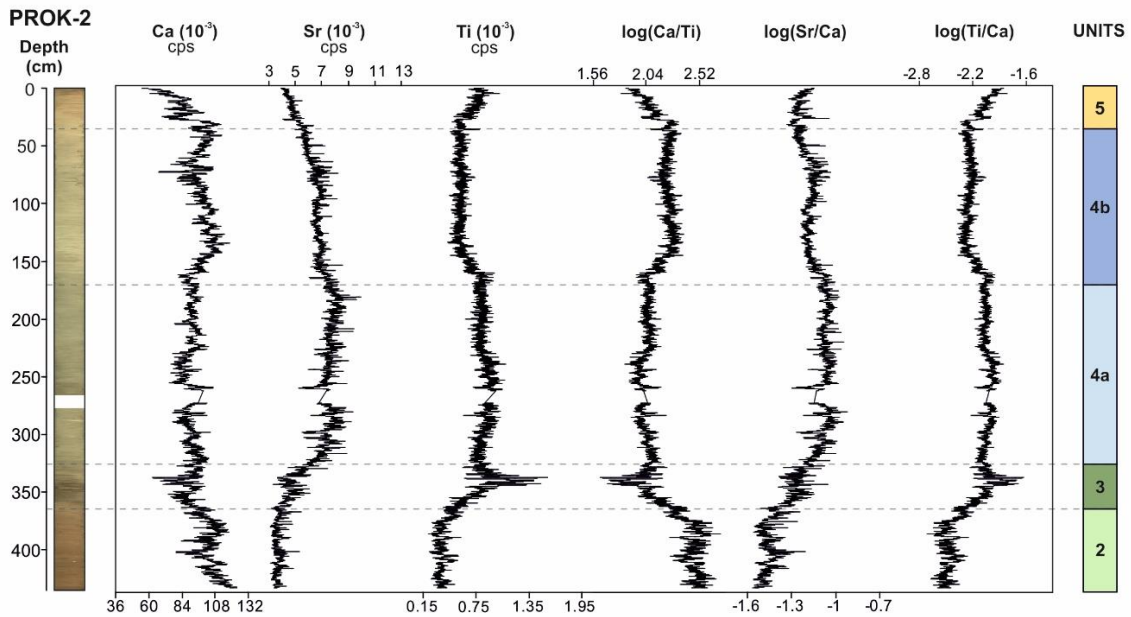


Figure 5.44 Variations of selected XRF elements and ratios with depth in the sediment core PROK-2.

Ca (cps) and $\log(\text{Ca}/\text{Ti})$ are the lowest in sediments from the units LU1 and LU5 of the core PROK-3, but have opposite trends (Fig. 5.45). An increase in these components occurs in LU2, while a generally uniform or slight decrease is present in LU3 and LU4a (Fig. 5.45). In LU4b, a slight increase of Ca (cps) and $\log(\text{Ca}/\text{Ti})$ occurs (Fig. 5.45). Sr (cps) and $\log(\text{Sr}/\text{Ca})$ are very low in the sediments of the LU1 (Fig. 5.45). A high increase in $\log(\text{Sr}/\text{Ca})$ is present for the first part of LU2, then a decrease and constant trend upwards occurs to the end of LU2 and increases in LU3 (Fig. 5.45). Sr (cps) shows a slightly increased trend in LU2 and LU3, similar to the $\log(\text{Sr}/\text{Ca})$. A generally constant trend of Sr (cps) and $\log(\text{Sr}/\text{Ca})$ is present in the LU4a, while in the LU4b, Sr (cps) slightly decreases in the upper part, and $\log(\text{Sr}/\text{Ca})$ is uniform (Fig. 5.45). In the LU5, Sr (cps) slightly decreases to the top of the core, whereas $\log(\text{Sr}/\text{Ca})$ is constant for the first part of the LU5 and then increases to the top of the core (Fig. 5.45). Ti (cps) and $\log(\text{Ti}/\text{Ca})$ exhibit an opposite trend compared to the previously described Ca (cps) and $\log(\text{Ca}/\text{Ti})$ (Fig. 5.45).

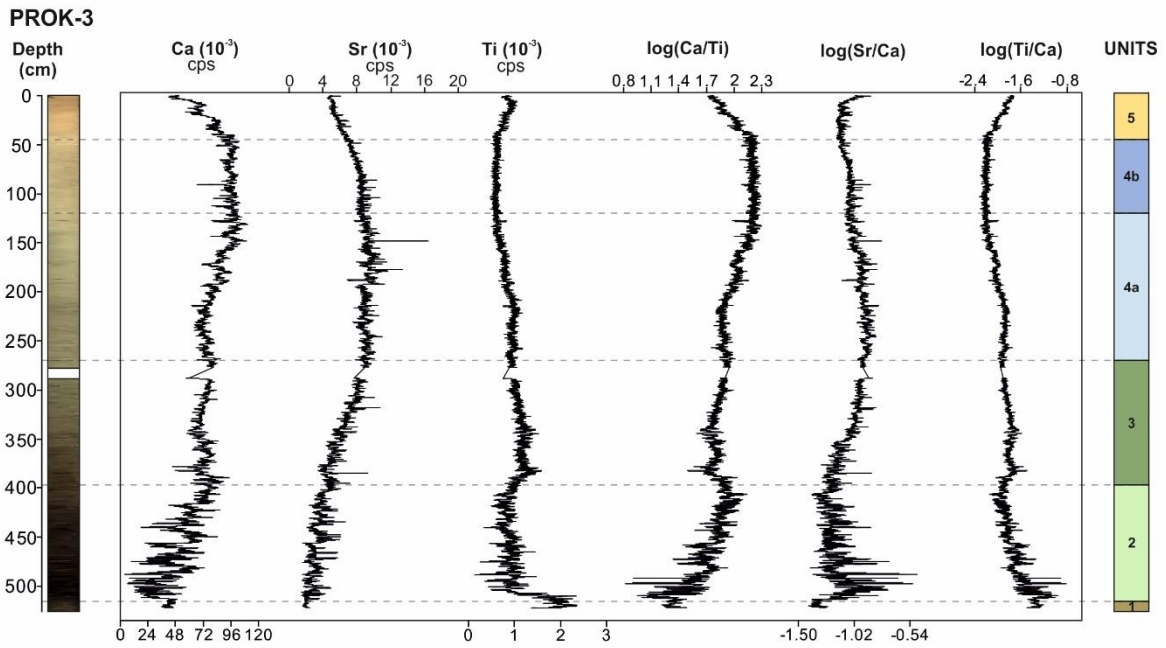


Figure 5.45 Variations of selected XRF elements and ratios with depth in the sediment core PROK-3.

In the core PROK-4, Ca (cps) and log(Ca/Ti) slightly increase in LU4a, then a decrease of these elements can be observed in the intervals from 360 to 250 cm (Fig. 5.46). Ca (cps) increases to the end of the LU4b, while log(Ca/Ti) decreases in the intervals between 230 and 210 cm and from 175 to the top of the LU4b, while an increase occurs in the intervals from 250 and 230 cm and between 210 and 175 cm of LU4b (Fig. 5.46). A decrease upwards of these chemical components is present in LU5 (Fig. 5.45). Sr (cps) and log(Sr/Ca) show a generally decreasing trend until LU5, where this component slightly increases to the top of the core (Fig. 5.46). Ti (cps) and log(Ti/Ca) show an opposite trend to Ca (cps) and log(Ca/Ti) (Fig. 5.46).

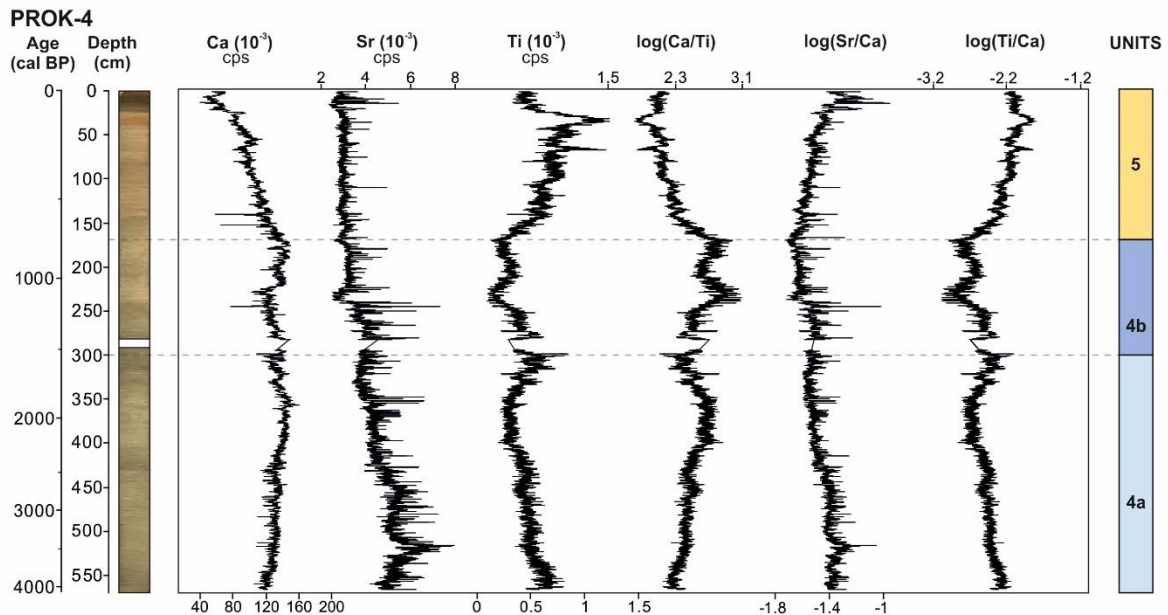


Figure 5.46 Variations of selected XRF elements and ratios with depth in the sediment core PROK-4.

5.3.5.2 Geochemical analysis of discrete core samples

The geochemical analysis was conducted on 93 discrete samples from the core PROK-1, 64 samples from the core PROK-3, and 65 samples from the core PROK-4 (Appendix 2,4 and 5; Figs. 5.47–5.55; Tables 5.24–5.26). The results of the analysis are shown as chosen elemental distribution by depth, separated as macro (%; Figs. 5.47, 5.50 and 5.53), micro and heavy elements (mg/kg; Figs. 5.48, 5.51 and 5.54), and elemental ratios (Figs. 5.49, 5.52 and 5.55).

In the core PROK-1 (Table 5.24), the macro elements Na, Mg, Al, P, S, K, Ti, and Fe generally have similar trends throughout the core (Fig. 5.47). Their concentrations are the highest in the LU3 and LU5, whereas the lowest concentrations occur at the bottom of the core. In the first part of LU4a (600–450 cm), a decreasing trend of these elements occurs with a slight increase in the interval from 450 to 350 cm, and then values decrease again to the top of LU4a (Fig. 5.47). In LU4b, a generally uniform trend can be observed, except for Na (%) and Mg (%), with higher concentrations from 150 cm to 100 cm (Fig. 5.47). The micro and heavy elements, Mn, Cu, Pb, Cr and Ni, have a similar distribution throughout the core as the macroelements (Fig. 5.48). Calcium and strontium have opposite trends to the previously

described macroelements, except for the Sr concentrations in LU4b, which also have a decreasing trend (Fig. 5.48). Their lowest concentrations occur in LU3 and LU5 and the highest in LU2 and LU4a. An increase in concentrations of these elements occurs in LU4a, with an abrupt rise in Sr values. Molybdenum concentrations differ from all the previously described elemental concentrations (Fig. 5.48). A decreasing and oscillating trend of Mo concentrations occurs in LU2 with an abrupt increase at the boundary of LU2 and LU3 (fig. 5.48). Afterward, the Mo concentrations decrease to the end of LU3, and a uniform trend occurs in LU4a, LU4b, and the first part of LU5 (Fig. 5.48). A slight rise in Mo concentrations occurs from 25 cm to the top of the core (Fig. 5.48). Elemental ratios, Cu/Al, Pb/Al, Ni/Al, have generally similar trends and are low and decreasing up to LU4b, where they start to increase to the top of the core (Fig. 5.49). Cr/Al and Cr/Ni have similar trends with very oscillating values through out the core (Fig. 5.49). In the lower units, LU2 and LU3, the Cr/Al and Cr/Ni are generally low and increase in LU4a, while a decrease can be observed at the 280 cm with a generally uniform and oscillating trend to the top of the core (Fig. 5.49). Ca/Al and Sr/Ca have similiar trends through out the core with higher values in LU2, then a decrease of these ratios can be observed in LU3 (Fig. 5.49). Afterward, a slowly increasing trend occurs in LU4a, whereas from the 220 cm of the core, these ratios start to decrease upwards to the top of the core (Fig. 5.49). Fe/Al and Ti/Al have similar trends through out the core, where the highest ratios are present in LU3 and LU5, and in the remaining units these ratios are low or have decreasing trends (Fig. 5.49).

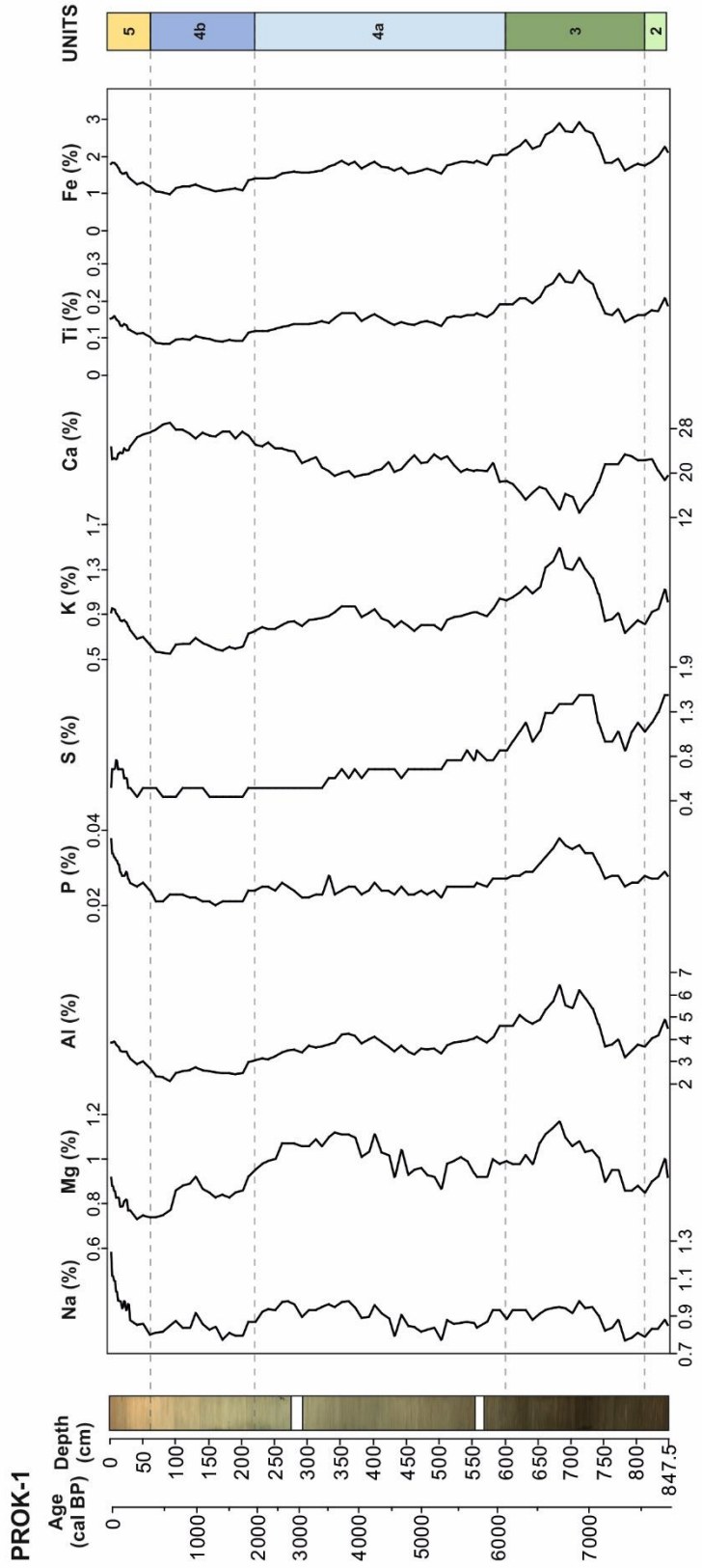


Figure 5.47 Variations in concentrations of selected major elements with depth in the sediment core PROK-1.

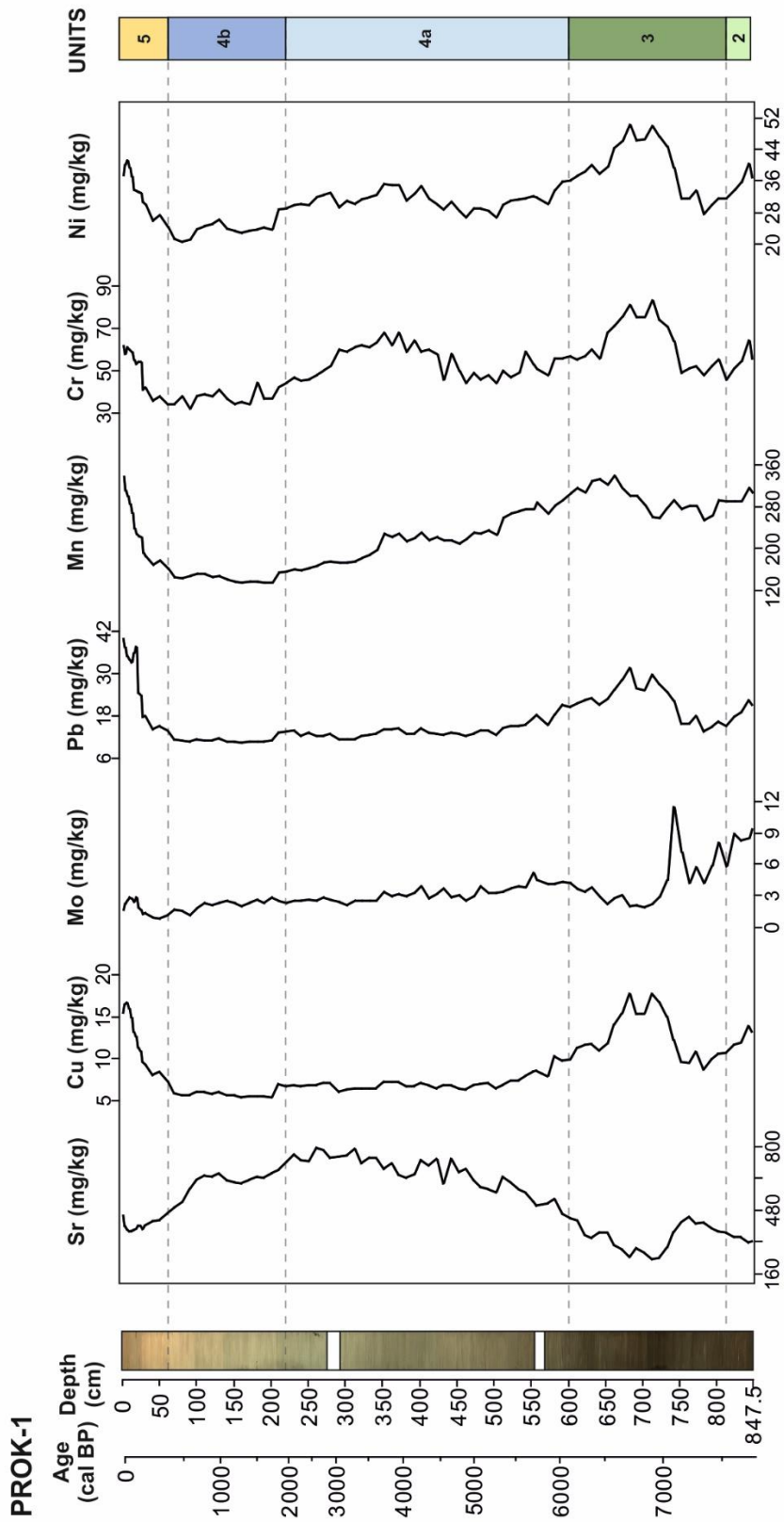


Figure 5.48 Variations in concentrations of selected trace and heavy elements with depth in the sediment core PROK-1.

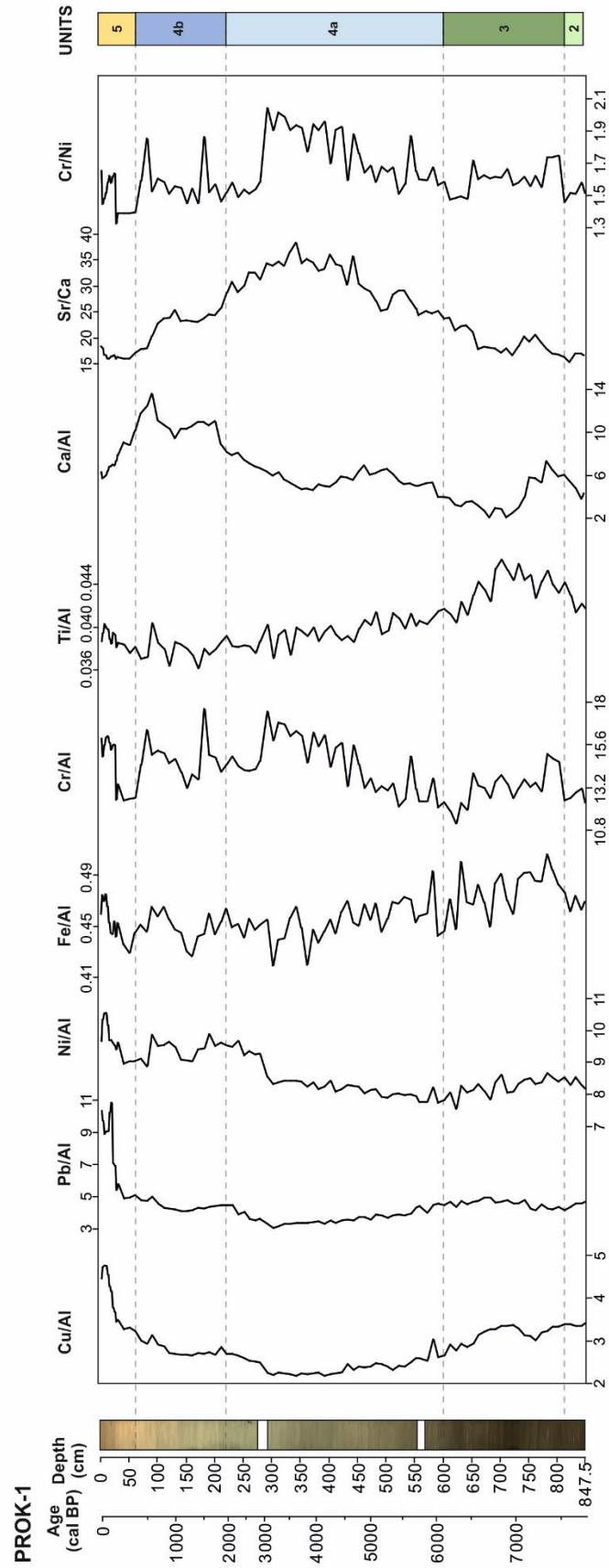


Figure 5.49 Variations in selected elemental ratios with depth in the sediment core PROK-1.

Table 5.24 Statistical parameters of selected major, trace and heavy elements in sediments of the core PROK-1.

	PROK-1	LU2	LU3	LU4a	LU4b	LU5	TOTAL CORE
Na (%)	Mean	0.84	0.90	0.90	0.84	0.98	0.89
	SD	0.03	0.06	0.05	0.04	0.12	0.07
	Min	0.79	0.77	0.77	0.77	0.80	0.77
	Max	0.88	0.98	0.98	0.92	1.24	1.11
Mg (%)	Mean	0.92	1.01	1.01	0.85	0.81	0.95
	SD	0.05	0.09	0.07	0.06	0.05	0.11
	Min	0.85	0.86	0.87	0.74	0.73	0.73
	Max	1.00	1.17	1.12	0.95	0.92	1.17
Al (%)	Mean	4.26	4.83	3.76	2.56	3.43	3.76
	SD	0.45	0.93	0.36	0.23	0.38	0.90
	Min	3.69	3.18	3.12	2.13	2.70	2.13
	Max	4.88	6.43	4.63	3.04	3.92	6.43
P (%)	Mean	0.03	0.03	0.02	0.02	0.03	0.03
	SD	0.00	0.00	0.00	0.00	0.00	0.00
	Min	0.03	0.03	0.02	0.02	0.02	0.02
	Max	0.03	0.04	0.03	0.02	0.04	0.04
S (%)	Mean	1.32	1.21	0.67	0.44	0.60	0.78
	SD	0.18	0.19	0.13	0.05	0.12	0.32
	Min	1.10	0.90	0.50	0.40	0.40	0.40
	Max	1.50	1.50	0.90	0.50	0.80	1.50
K (%)	Mean	0.97	1.12	0.87	0.63	0.83	0.88
	SD	0.11	0.22	0.07	0.06	0.10	0.20
	Min	0.82	0.74	0.75	0.55	0.63	0.55
	Max	1.12	1.49	1.04	0.75	0.96	1.49
Ca (%)	Mean	20.67	17.81	21.48	27.17	24.34	22.03
	SD	1.66	3.25	1.78	0.97	1.54	3.69
	Min	18.74	12.89	18.40	25.03	22.37	12.89
	Max	22.37	23.34	25.40	29.00	27.30	29.00
Ti (%)	Mean	0.18	0.21	0.15	0.10	0.13	0.15
	SD	0.02	0.04	0.02	0.01	0.02	0.04
	Min	0.16	0.14	0.12	0.09	0.10	0.09
	Max	0.21	0.28	0.19	0.12	0.16	0.28
Fe (%)	Mean	2.00	2.31	1.71	1.15	1.56	1.73
	SD	0.20	0.41	0.17	0.11	0.21	0.44
	Min	1.76	1.61	1.41	0.99	1.20	0.99
	Max	2.26	2.91	2.05	1.41	1.84	2.91
Sr (mg/kg)	Mean	339.40	341.95	659.74	628.88	404.50	531.24
	SD	19.11	68.30	95.85	57.01	28.85	162.05
	Min	318.00	232.00	439.00	494.00	374.00	232.00
	Max	365.00	446.00	792.00	719.00	463.00	792.00
Cu (mg/kg)	Mean	12.28	12.83	7.20	5.84	12.19	9.13
	SD	1.27	2.87	1.00	0.46	3.29	3.44
	Min	10.70	8.70	6.00	5.40	7.40	5.40
	Max	13.90	17.80	10.30	7.00	16.70	17.80
Mo (mg/kg)	Mean	8.16	4.22	3.25	2.19	1.91	3.36
	SD	1.37	2.43	0.71	0.44	0.72	1.90
	Min	5.80	1.90	2.10	1.20	0.90	0.90
	Max	9.30	11.50	5.20	2.90	2.90	11.50
Pb (mg/kg)	Mean	19.10	22.25	14.04	11.26	27.20	17.33
	SD	2.81	5.19	2.33	0.93	9.97	6.95
	Min	15.30	13.60	11.30	10.40	13.80	10.40
	Max	22.40	31.70	21.10	13.60	40.20	37.70

Mn (mg/kg)	Mean	298.20	294.05	221.58	143.69	236.21	228.91
	SD	12.56	26.02	41.10	7.53	56.79	60.65
	Min	289.00	253.00	159.00	134.00	163.00	134.00
	Max	316.00	339.00	305.00	156.00	338.00	339.00
Cr (mg/kg)	Mean	54.20	63.60	54.29	37.75	50.50	52.77
	SD	6.65	11.36	6.99	3.59	10.05	11.48
	Min	46.00	48.00	44.00	32.00	34.00	32.00
	Max	64.00	83.00	68.00	44.00	62.00	83.00
Ni (mg/kg)	Mean	35.66	39.72	31.33	24.08	33.46	32.39
	SD	3.42	7.08	2.33	2.38	5.32	6.56
	Min	31.50	27.60	26.70	20.50	24.40	20.50
	Max	40.50	50.40	36.00	29.00	41.30	50.40

In the core PROK-3 (Table 5.25), Na, S, and Mo concentrations have generally similar distribution with low concentrations in LU1, while the highest concentrations occur in the following LU2 (Fig. 5.50). In LU3, Na has an oscillating and slightly increasing trend upwards up to the 250 cm of LU4a, and then its concentrations slightly decrease to LU5, where again an increase in concentration occurs to the top of the core (Fig. 5.50). Sulphur has slightly decreasing values in LU3 and LU4a, with a uniform trend at the top of the core (Fig. 5.50). Molybdenum has uniform constant values to the top of the core after LU2 (Fig. 5.51). Generally, Al, P, K, Ti, Fe, and Cu concentrations have similar distributions throughout the core (Fig. 5.51). The lowest values of these elements can be observed in LU2 and LU4b, whereas slightly increased concentrations occur in LU1, LU3, and the first part of LU4a (up to 220 cm), where the concentrations start to decrease upwards (Fig. 5.51). Concentrations of Mn, Pb, Cr and Ni have similar distribution with generally uniform and constant concentrations throughout the core for the Mn and Pb, except for elevated concentrations in LU5, while the Cr and Ni have similar trends throughout the core but with more oscillating values (Fig. 5.51). Calcium and Strontium have similar distributions with increasing trend of concentrations from the bottom of the core to the LU4b, whereas in LU4b and LU5, a slightly decreasing trend of their concentrations can be observed (Figs. 5.50 and 5.51). The distribution of magnesium concentrations differs from all previously described elements and is constant and has a uniform trend, except at the transition from LU1 to LU2, where a rise in Mg concentrations occurs (Fig. 5.50). Elemental ratios Cu/Al, Cr/Al, Ca/Al and Ti/Al have a generally similar trend, except in the LU2 where at the beginning of this unit Cu/Al increases to LU2 and Cr/Al, Ca/Al and Ti/Al decreases (Fig. 5.52). Low and decreasing ratios of these elements are present from the LU3 to the LU5, where an increase in ratios can be observed

in the LU5 (Fig. 5.52). Ni/Al and Fe/Al have an overall similar distribution, with low ratios in LU1 and a constant uniform trend in LU2, LU3 and LU4a (Fig. 5.52). Fe/Al have somewhat more oscillating ratios in these units. A generally decrease in LU5 can be observed for these ratios (Fig. 5.52). Pb/Al ratio is very uniform from the bottom of the core up to LU5, where it increases to the top of the core (Fig. 5.52). Sr/Ca ratio is generally increasing from the bottom of the core up to LU4b, where it starts to decrease upwards. The last 20 cm of the core has a slightly increasing trend of Sr/Ca (Fig. 5.52). Cr/Ni ratio is very low in LU1, then higher ratio occurs in LU2, where as a decrease is present in the interval from 420 cm to 400 cm (Fig. 5.52). In LU3, LU4a and LU4b this ratio starts to increase, where it decreases in the first part of LU5 and again increases from 25 cm to the top of the core (Fig. 5.52).

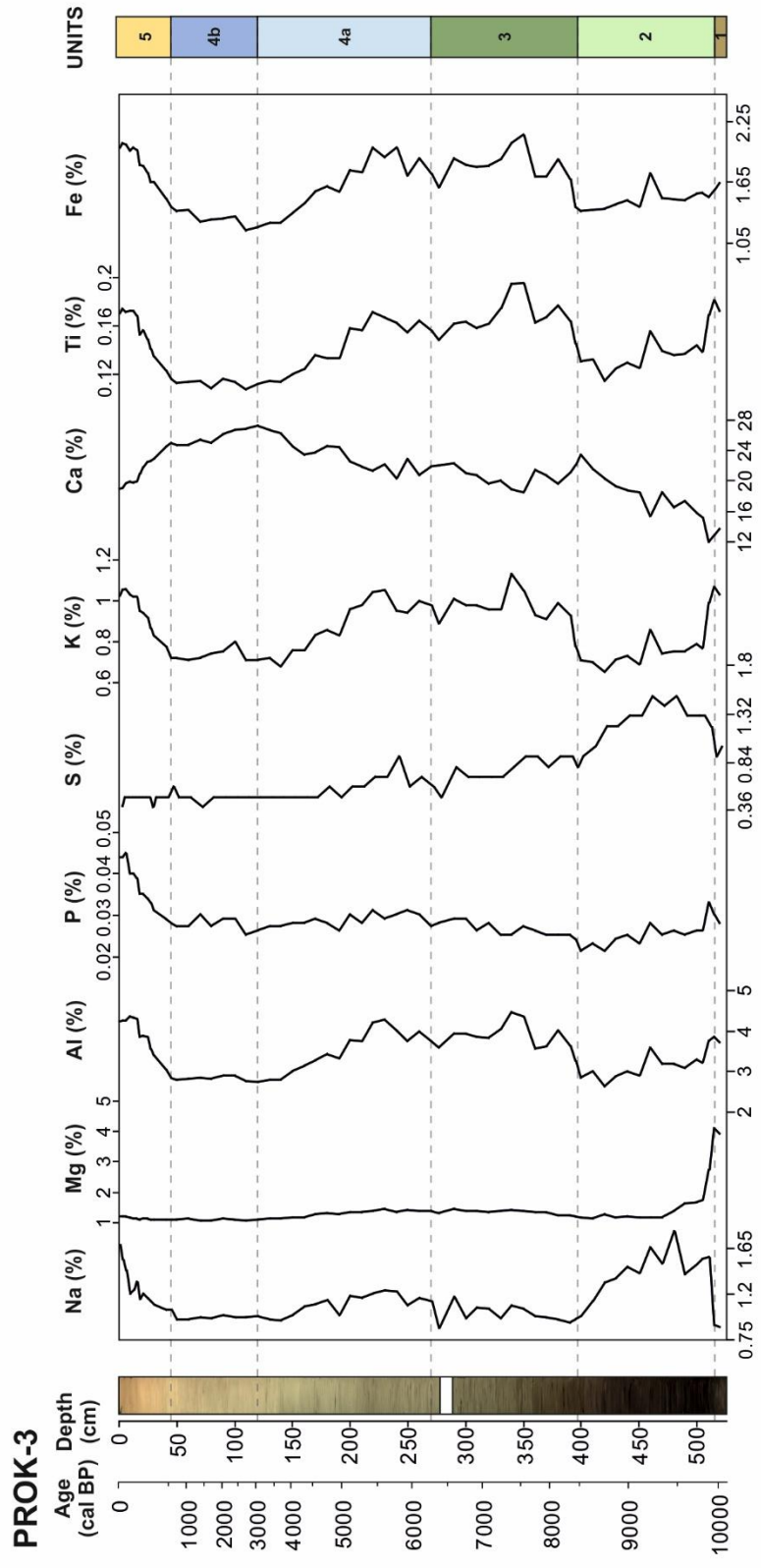


Figure 5.50 Variations in concentrations of selected major elements with depth in the sediment core PROK-3.

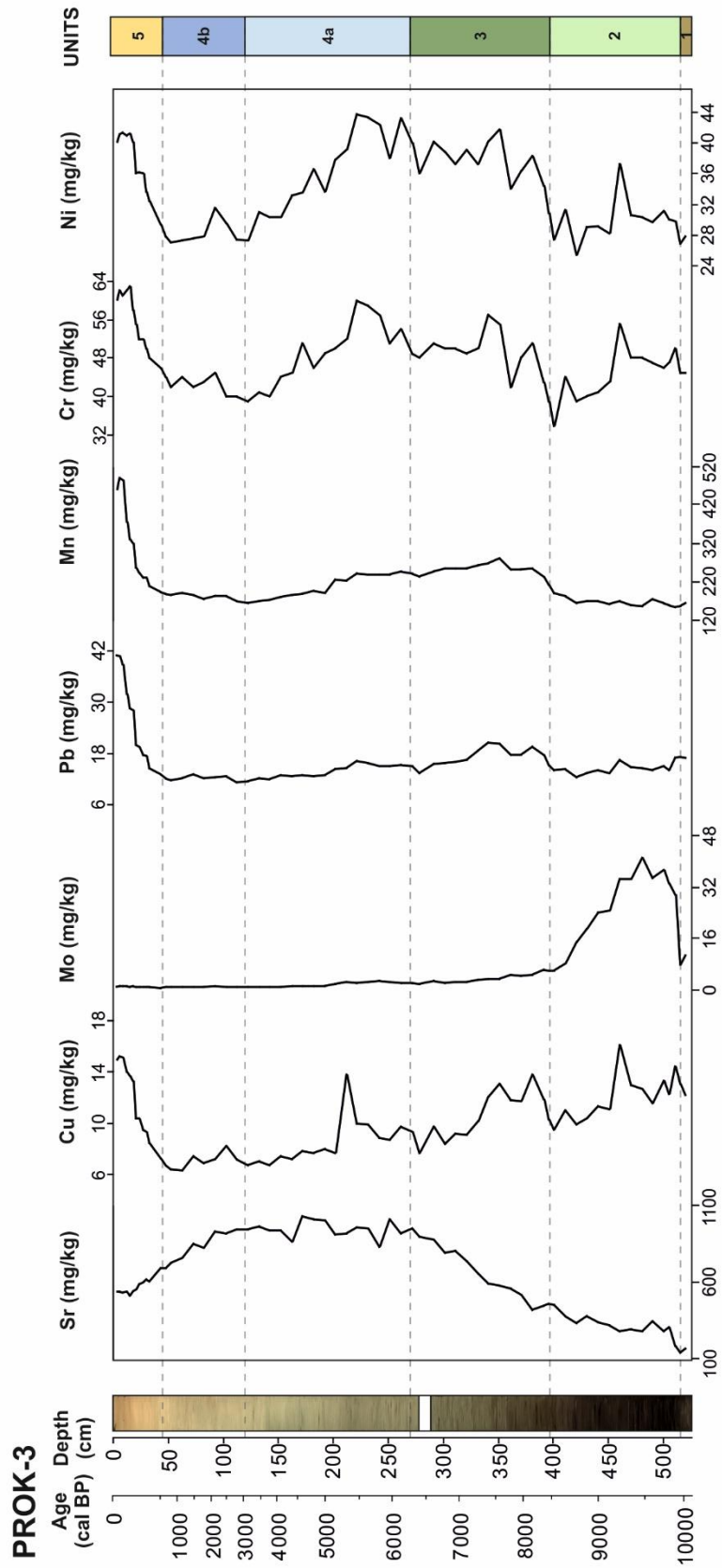


Figure 5.51 Variations in concentrations of selected trace and heavy elements with depth in the sediment core PROK-3.

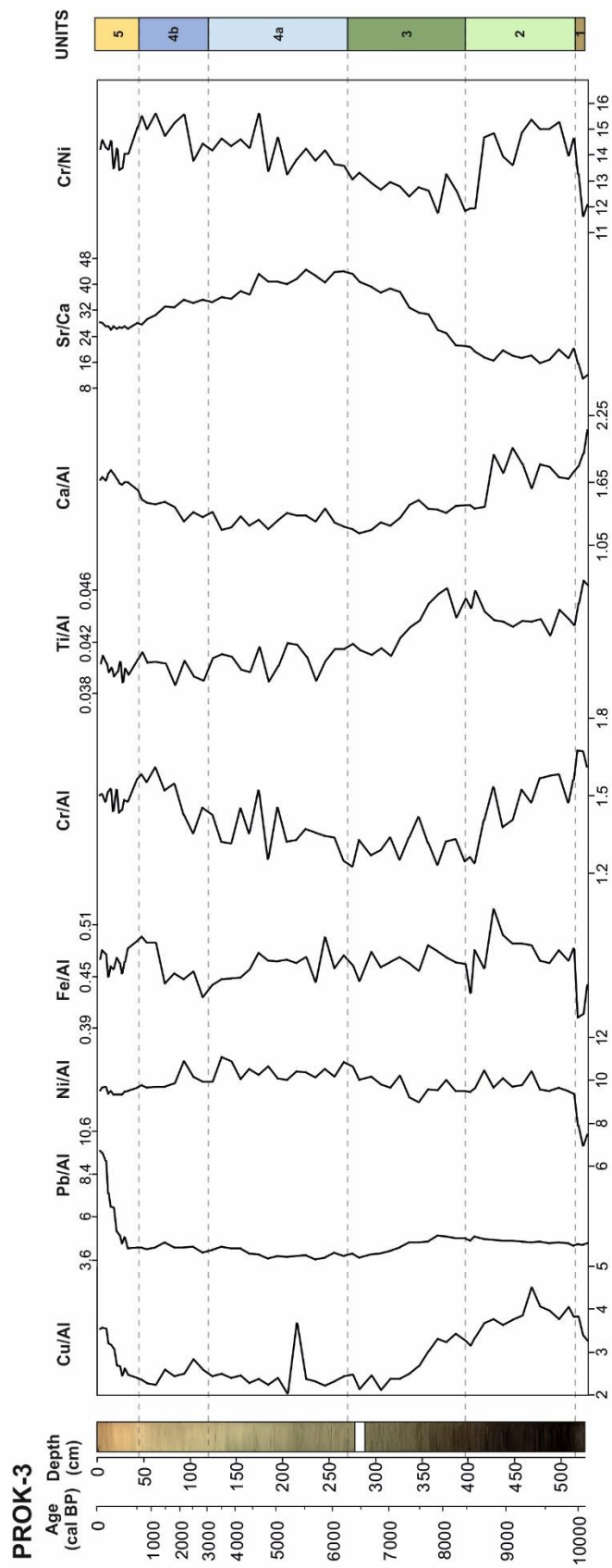


Figure 5.52 Variations in selected elemental ratios with depth in the sediment core PROK-3.

Table 5.25 Statistical parameters of selected major, trace and heavy elements in sediments of the core PROK-3.

	PROK-3	LU1	LU2	LU3	LU4a	LU4b	LU5	TOTAL CORE
Na (%)	Mean	0.89	0.98	1.00	1.11	0.98	1.27	1.16
	SD	0.01	1.83	0.08	0.10	0.03	0.20	0.22
	Min	0.88	1.44	0.87	0.95	0.95	1.05	0.87
	Max	0.90	0.22	1.17	1.24	1.05	1.70	1.83
Mg (%)	Mean	4.03	1.14	1.35	1.31	1.10	1.15	1.37
	SD	0.14	2.72	0.08	0.11	0.03	0.04	0.54
	Min	3.93	1.44	1.22	1.13	1.07	1.10	1.07
	Max	4.13	0.44	1.46	1.47	1.15	1.22	4.13
Al (%)	Mean	3.80	2.63	3.86	3.55	2.83	3.95	3.51
	SD	0.10	3.76	0.33	0.48	0.05	0.42	0.53
	Min	3.73	3.12	3.27	2.79	2.75	3.05	2.63
	Max	3.87	0.31	4.47	4.28	2.90	4.36	4.47
P (%)	Mean	0.03	0.02	0.03	0.03	0.03	0.04	0.03
	SD	0.00	0.03	0.00	0.00	0.00	0.01	0.005
	Min	0.03	0.03	0.02	0.03	0.03	0.03	0.02
	Max	0.03	0.00	0.03	0.03	0.03	0.05	0.05
S (%)	Mean	0.95	0.90	0.78	0.60	0.50	0.48	0.75
	SD	0.07	1.50	0.12	0.11	0.05	0.04	0.31
	Min	0.90	1.26	0.50	0.50	0.40	0.40	0.40
	Max	1.00	0.17	0.90	0.90	0.60	0.50	1.50
K (%)	Mean	1.05	0.65	0.96	0.89	0.73	0.96	0.87
	SD	0.03	0.99	0.08	0.12	0.03	0.09	0.13
	Min	1.03	0.76	0.78	0.68	0.71	0.78	0.65
	Max	1.07	0.09	1.13	1.05	0.80	1.06	1.13
Ca (%)	Mean	13.28	12.06	20.64	23.20	25.79	21.05	21.26
	SD	0.54	23.40	1.22	1.89	0.99	1.78	3.42
	Min	12.90	17.93	18.57	20.42	24.71	18.97	12.06
	Max	13.66	2.99	22.38	26.71	27.33	24.52	27.33
Ti (%)	Mean	0.18	0.12	0.17	0.14	0.11	0.16	0.15
	SD	0.01	0.17	0.01	0.02	0.00	0.02	0.02
	Min	0.17	0.14	0.15	0.11	0.11	0.12	0.11
	Max	0.18	0.01	0.20	0.17	0.12	0.17	0.20
Fe (%)	Mean	1.61	1.37	1.80	1.65	1.30	1.85	1.63
	SD	0.05	1.74	0.18	0.25	0.08	0.18	0.25
	Min	1.57	1.48	1.41	1.25	1.18	1.50	1.18
	Max	1.64	0.10	2.12	1.99	1.41	2.04	2.12
Sr (mg/kg)	Mean	152.50	330.57	655.42	942.87	840.11	570.42	646.05
	SD	17.68	71.74	163.79	53.72	99.65	49.93	255.74
	Min	140.00	189.00	416.00	830.00	689.00	513.00	140.00
	Max	165.00	456.00	896.00	1026.00	943.00	690.00	1026.00
Cu (mg/kg)	Mean	12.65	11.92	10.71	8.65	7.00	11.80	10.24
	SD	0.64	1.85	1.93	1.79	0.58	2.85	2.64
	Min	12.20	9.50	7.70	6.70	6.30	7.30	6.30
	Max	13.10	16.10	13.80	13.80	8.20	15.20	16.10
Mo (mg/kg)	Mean	9.25	24.72	3.52	1.78	1.00	1.06	7.11
	SD	1.91	12.13	1.28	0.64	0.16	0.20	11.02
	Min	7.90	5.90	1.80	1.00	0.80	0.70	0.70
	Max	10.60	40.90	6.30	2.80	1.30	1.40	40.90
Pb (mg/kg)	Mean	17.10	14.52	17.43	13.94	12.13	25.98	16.82
	SD	0.28	1.17	2.10	1.43	0.61	10.34	6.52
	Min	16.90	12.40	13.50	11.90	11.20	13.10	11.20
	Max	17.30	16.90	20.50	16.30	13.10	41.00	41.00

Mn (mg/kg)	Mean	161.00	171.36	254.33	212.67	181.22	319.25	225.39
	SD	5.66	15.89	12.98	29.07	9.39	109.87	72.97
	Min	157.00	154.00	235.00	171.00	164.00	195.00	154.00
	Max	165.00	213.00	282.00	248.00	191.00	491.00	491.00
Cr (mg/kg)	Mean	45.00	44.36	49.50	49.87	42.11	55.75	48.45
	SD	0.00	5.44	4.21	6.05	2.09	6.02	6.70
	Min	45.00	34.00	42.00	40.00	39.00	46.00	34.00
	Max	45.00	55.00	57.00	60.00	45.00	63.00	63.00
Ni (mg/kg)	Mean	27.40	30.04	37.83	37.09	28.14	37.38	34.18
	SD	0.71	2.64	2.33	4.86	1.45	4.01	5.26
	Min	26.90	25.40	34.10	30.30	27.00	29.40	25.40
	Max	27.90	37.30	41.70	43.70	31.50	41.30	43.70

In the core PROK-4 (Table 5.26), the macroelements Mg, Al, P, K, Ti and Fe, have a similar trend of their values with generally uniform or slightly decreasing values in LU4a and LU4b, while their values increase in LU5 (Fig. 5.53). Sulphur and sodium have similar low and constant values from the bottom of the core to LU5, where a slightly increasing trend for Na can be observed and oscillating values of S (Fig. 5.53). In the last 50 cm, values of these elements increase to the top of the core (Fig. 5.53). Calcium has an opposite trend from all described macro elements, with generally increasing values from the bottom of the core to LU5 (Fig. 5.53). In LU5 a decrease of Ca is present to the 40 cm of the unit and then it starts to increase again to the top of the core (Fig. 5.53). Micro and heavy elements, Cu, Mo and Pb, have generally similar trends of their values with uniform and constant values in LU4a and LU4b, and slightly increasing values of Cu and Pb, and uniform trend of Mo are present for the first 50 cm of LU5 (Fig. 5.54). A high increase occurs in LU5 in the interval from 50 cm to 25 cm of these elements, then they have a zig-zag pattern to the top of the core (Fig. 5.54). Concentrations of Mn, Cr and Ni have similar trends in LU4a and LU4b, as previously described element, but an increase in their values is present from the beginning of LU5 to the 25 cm of LU5, where they decrease to the top of the core (Fig. 5.54). Strontium has the opposite trend from all described micro elements and decreases from the bottom of the core to 550 cm, and a slight increase in the interval from 550 to 525 cm is present, then an overall decrease in values is present to the 80 cm of LU5 and a uniform and constant trend occurs to the top of the core (Fig. 5.54). Elemental ratios Cu/Al, Pb/Al, Ni/Al, Fe/Al, Cr/Al and Ti/Al, generally have similar trends throughout the core, where most of them have uniform constant trends in LU4a and LU4b, although the ratios Fe/Al and Cr/Al and Ti/Al in these lithological units have

somewhat more oscillating values (Fig. 5.55). All of these ratios start to increase in LU5 up to 50 cm and then have zig-zag and oscillating ratios to the top of the core (Fig. 5.55). The Ca/Al ratio is uniform and constant from the bottom of the core to 425 cm, where it starts to increase slightly in the interval from 425 to 400 cm, and then it decreases to the top of LU4b (Fig. 5.55). In LU4b, Ca/Al oscillates strongly with higher ratios in the intervals from 275 cm and 250 cm, and from 220 and 175 cm (Fig. 5.55). In LU5 a decrease of Ca/Al is present up to 30 cm, where again it increases slightly to the top of the core. The Sr/Ca ratio has an overall decreasing trend in LU4a and LU4b and a slight increase can be observed in LU5 (Fig. 5.55). The Cr/Ni ratio has very oscillating values through out the core, with a generally uniform trend in LU4 and LU4b, and from the bottom of LU5 up to 100 cm, where an increase of this ratio occurs from the 100 cm to the top of the core (Fig. 5.55).

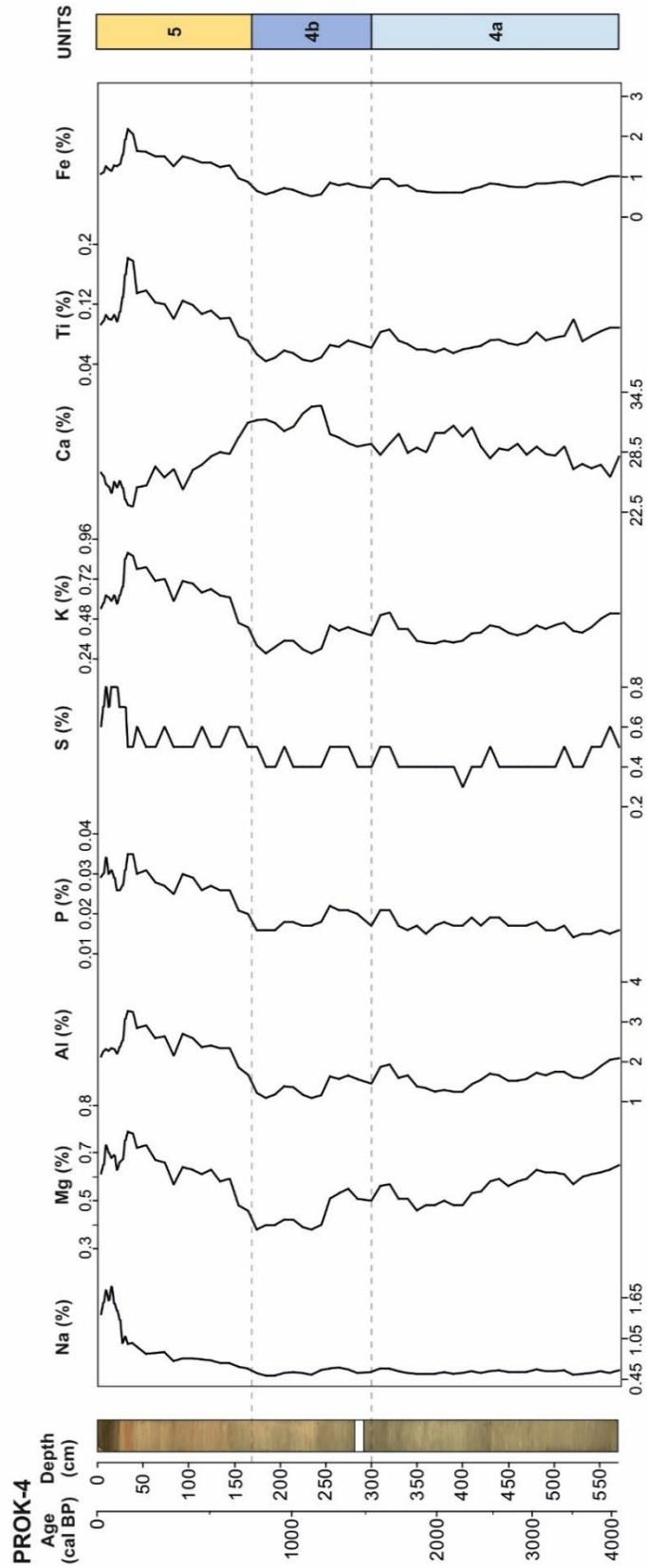


Figure 5.53 Variations in concentrations of selected major elements with depth in the sediment core PROK-4.

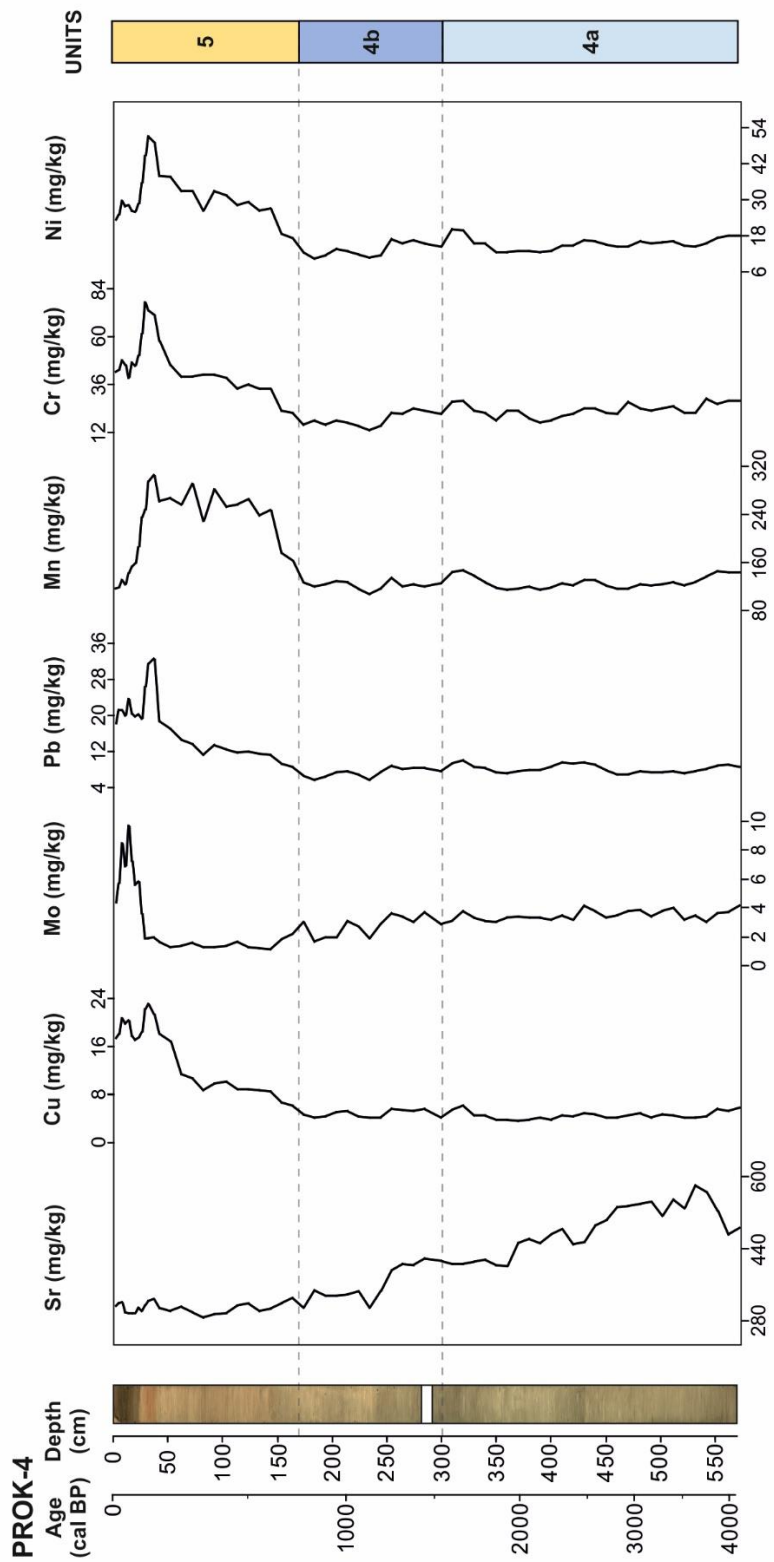


Figure 5.54 Variations in concentrations of selected trace and heavy elements with depth in the sediment core PROK-4.

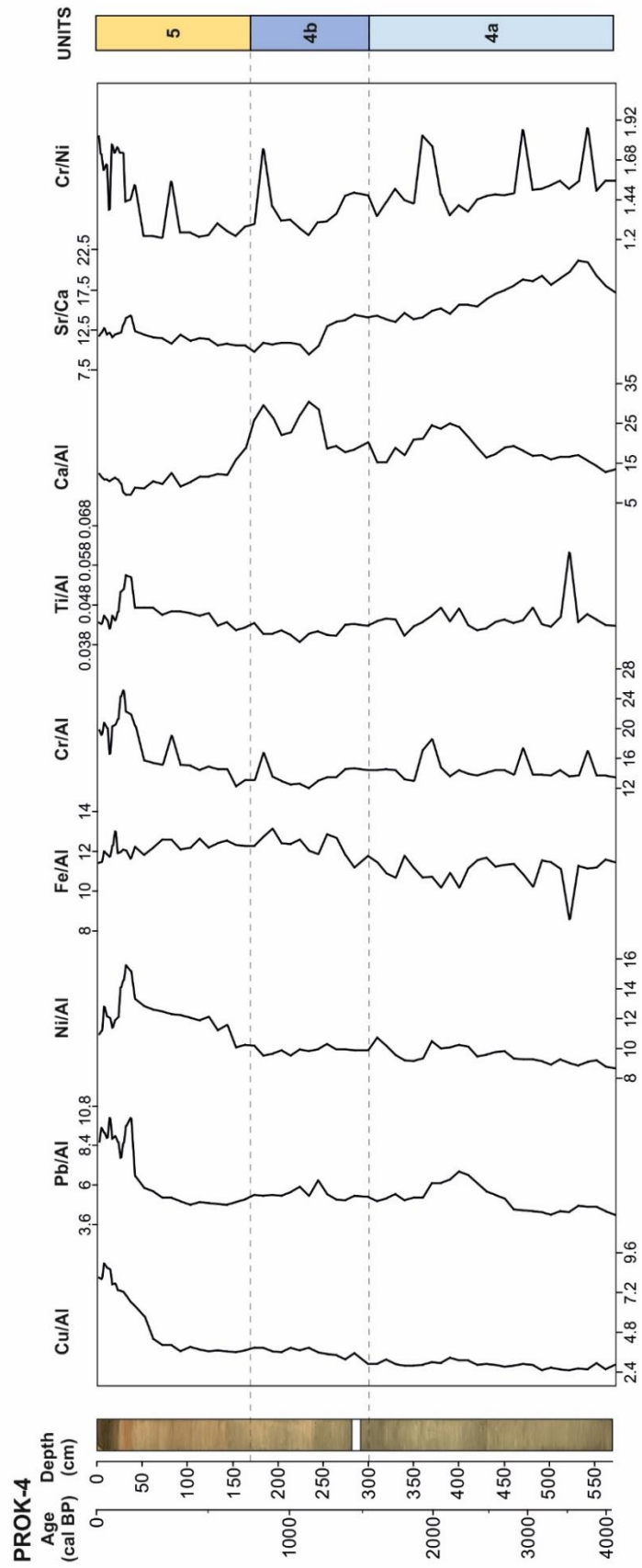


Figure 5.55 Variations in selected elemental ratios with depth in the sediment core PROK-4.

Table 5.26 Statistical parameters of selected major, trace and heavy elements in sediments of the core PROK-4.

	PROK-4	LU4a	LU4b	LU5	TOTAL CORE
Na (%)	Mean	0.52	0.50	1.09	0.75
	SD	0.61	0.62	0.38	0.34
	Min	0.56	0.56	0.68	0.50
	Max	0.03	0.04	1.80	1.80
Mg (%)	Mean	0.46	0.38	0.67	0.57
	SD	0.65	0.55	0.06	0.10
	Min	0.56	0.45	0.57	0.38
	Max	0.06	0.06	0.79	0.79
Al (%)	Mean	1.24	1.08	2.53	1.89
	SD	2.08	1.68	0.34	0.56
	Min	1.62	1.37	2.11	1.08
	Max	0.23	0.22	3.28	3.28
P (%)	Mean	0.01	0.02	0.03	0.02
	SD	0.02	0.02	0.00	0.01
	Min	0.02	0.02	0.03	0.01
	Max	0.00	0.00	0.04	0.04
S (%)	Mean	0.30	0.40	0.62	0.50
	SD	0.60	0.50	0.12	0.12
	Min	0.43	0.44	0.50	0.30
	Max	0.06	0.05	0.80	0.80
K (%)	Mean	0.33	0.27	0.67	0.50
	SD	0.52	0.44	0.10	0.15
	Min	0.42	0.36	0.54	0.27
	Max	0.06	0.06	0.88	0.88
Ca (%)	Mean	26.09	29.05	25.73	28.18
	SD	31.15	33.10	1.50	2.43
	Min	28.73	31.03	23.01	23.01
	Max	1.28	1.32	28.46	33.10
Ti (%)	Mean	0.06	0.04	0.12	0.09
	SD	0.10	0.07	0.03	0.03
	Min	0.07	0.06	0.09	0.04
	Max	0.01	0.01	0.18	0.18
Fe (%)	Mean	0.60	0.53	1.44	1.00
	SD	1.02	0.87	0.29	0.38
	Min	0.79	0.70	1.05	0.53
	Max	0.12	0.12	2.19	2.19
Sr (mg/kg)	Mean	402.00	310.00	307.04	391.43
	SD	581.00	418.00	10.65	89.05
	Min	482.70	359.29	288.00	288.00
	Max	54.47	38.56	329.00	581.00
Cu (mg/kg)	Mean	3.70	4.20	15.41	8.50
	SD	6.10	6.20	5.10	5.98
	Min	4.56	4.90	8.50	3.70
	Max	0.64	0.68	23.00	23.00
Mo (mg/kg)	Mean	3.00	1.70	3.41	3.27
	SD	4.20	3.70	2.71	1.67
	Min	3.50	2.72	1.10	1.10
	Max	0.35	0.66	9.70	9.70
Pb (mg/kg)	Mean	6.90	5.80	18.33	11.64
	SD	10.00	8.90	6.09	6.19
	Min	8.20	7.42	11.20	5.80
	Max	0.92	1.00	32.50	32.50

Mn (mg/kg)	Mean	115.00	108.00	219.83	160.42
	SD	147.00	163.00	63.22	58.75
	Min	127.30	125.50	116.00	108.00
	Max	10.24	12.61	306.00	306.00
Cr (mg/kg)	Mean	17.00	13.00	47.17	30.72
	SD	29.00	24.00	12.53	14.64
	Min	23.26	18.64	34.00	13.00
	Max	3.29	3.48	77.00	77.00
Ni (mg/kg)	Mean	12.60	10.30	32.09	20.93
	SD	20.10	17.20	7.58	9.62
	Min	15.31	13.59	23.00	10.30
	Max	2.04	2.37	51.10	51.10

5.3.6 Organic elemental analysis and stable isotope geochemistry

5.3.6.1 Organic carbon (TOC), nitrogen (TN) and inorganic carbon (TIC) analysis

Organic elemental analysis was made on samples from the sediment cores PROK-1, PROK-2, PROK-3, PROK-4, ZLA-1, and ZLA-2 (Appendix 2–7; Figs. 5.56–5.61; Tables 5.27–5.32). In the core PROK-1, 93 samples were analyzed for TN, TOC, TIC, and TOC/TN. TN content in the core PROK-1 ranges from 0.079 to 0.19%, with a mean value of 0.10% (Fig. 5.56; Table 5.27). TN content is generally constant throughout the core, while the higher values are present in the upper part of the core (LU5; Fig. 5.56). TOC content in the core PROK-1 ranges between 0.69 and 1.46%, with a mean of 0.96% (Fig. 5.56; Table 5.27). At the bottom part of the core, the TOC values are higher and fluctuate, whereas a decreasing trend can be observed in the middle part of the core (600–450 cm), while the constant values are present at the top of the core PROK-1 (Fig. 5.57). TIC content ranges from 3.94 to 9.99%, with a mean value of 7.15% (Fig. 5.56; Table 5.27). TIC content is constant from the bottom part of the core up to 750 cm, while a decrease in TIC values occurs up to 675 cm (Fig. 5.56). Afterward, the TIC values show a generally increasing trend upwards, up to 100 cm, where the values start to decrease up to the top of the core (Fig. 5.56). The percentage of insoluble residue in the core PROK-1 varies from 18.91 to 57.28%, with a mean value of 32.49% (Fig. 5.56; Table 5.27). From the bottom of the core up to 750 cm, the percentage of insoluble residue is constant, whereas it starts to increase up to 650 cm of the core (Fig. 5.56). A decreasing trend is present in the interval from 650 to 500 cm (Fig. 5.56). A generally constant trend occurs up to 100 cm of the core when the values increase to the top of the core (Fig. 5.56). The TOC/TN ratio is in the range between

5.94 and 16.63 (Fig. 5.56; Table 5.27). The highest TOC/TN values are determined in LU2 and LU3, then a decreasing trend in TOC/TN ratio can be observed up to LU5, where a slight increase in TOC/TN occurs (Fig. 5.56).

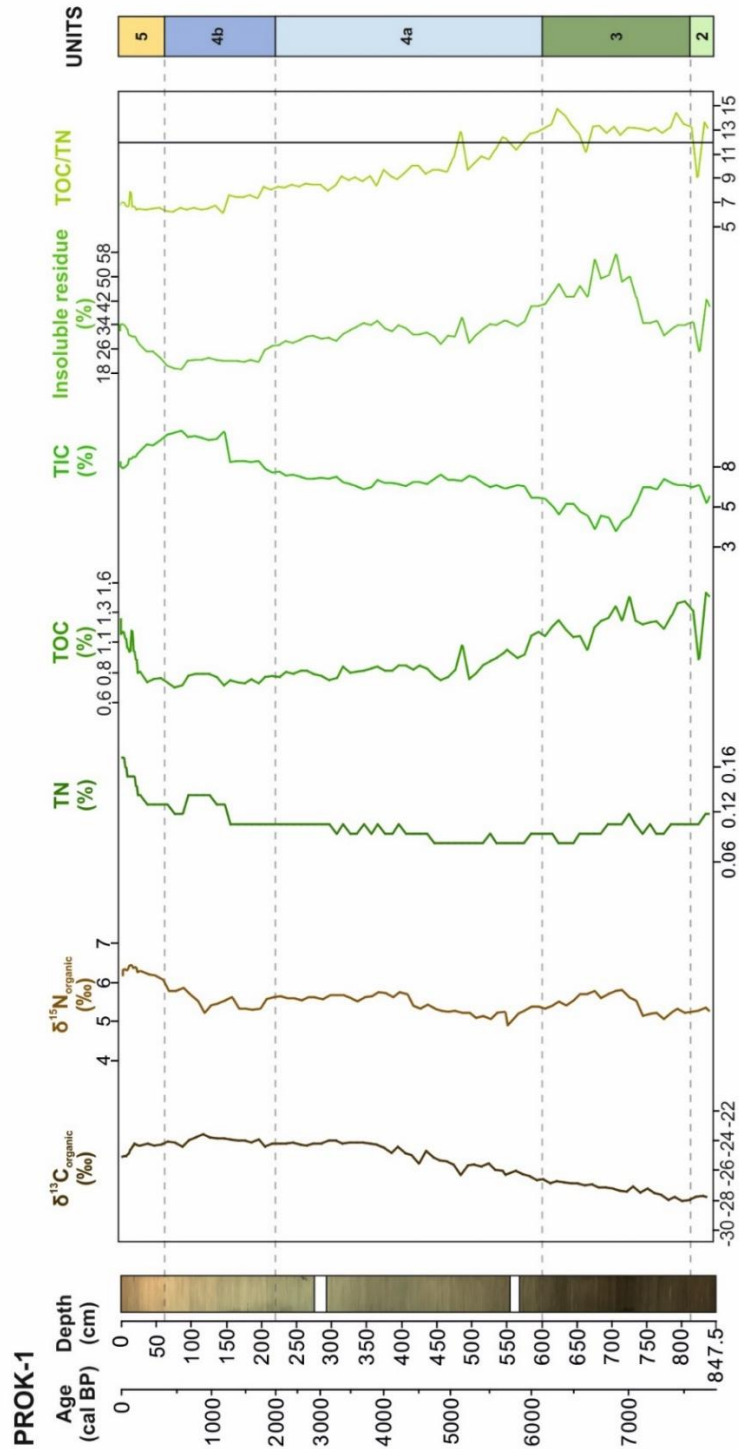


Figure 5.56 Distribution of $\delta^{13}C_{org}$, $\delta^{15}N_{org}$, TN, TOC, TIC, Insoluble residue and TOC/TN in sediments from the sediment core PROK-1.

Table 5.27 Statistical parameters of $\delta^{13}\text{C}_{\text{org}}$, $\delta^{15}\text{N}_{\text{org}}$, TN, TOC, TIC, Insoluble residue and TOC/TN in sediments from the sediment core PROK-1.

	PROK-1	LU2	LU3	LU4a	LU4b	LU5	TOTAL CORE
$\delta^{13}\text{C}_{\text{org}}$ (‰)	Mean	-27.90	-27.21	-25.00	-23.99	-24.59	-25.40
	ST	0.16	0.38	0.85	0.23	0.38	1.38
	Min	-28.12	-28.01	-26.65	-24.43	-25.13	-28.12
	Max	-27.71	-26.60	-23.95	-23.56	-24.21	-23.56
$\delta^{15}\text{N}_{\text{org}}$ (‰)	Mean	5.28	5.48	5.44	5.52	6.31	5.58
	ST	0.05	0.24	0.22	0.19	0.08	0.36
	Min	5.21	5.13	4.89	5.23	6.16	4.89
	Max	5.36	5.80	5.75	5.86	6.45	6.45
TN (%)	Mean	0.10	0.09	0.09	0.11	0.15	0.10
	ST	0.003	0.007	0.007	0.01	0.02	0.02
	Min	0.10	0.08	0.08	0.09	0.12	0.08
	Max	0.11	0.10	0.10	0.13	0.19	0.19
TOC (%)	Mean	1.30	1.21	0.86	0.76	1.00	0.96
	ST	0.22	0.10	0.09	0.04	0.16	0.21
	Min	0.92	0.99	0.75	0.69	0.74	0.69
	Max	1.46	1.41	1.14	0.80	1.15	1.46
TIC (%)	Mean	6.35	5.52	6.90	8.97	8.43	7.15
	ST	0.49	0.94	0.34	0.91	0.54	1.37
	Min	5.64	3.94	5.97	7.49	7.71	3.94
	Max	6.74	7.09	7.36	9.99	9.42	9.99
Insoluble residue (%)	Mean	35.18	43.18	31.94	22.07	29.70	32.49
	ST	6.76	7.71	3.13	1.91	3.58	8.12
	Min	24.86	30.44	27.63	18.91	22.75	18.91
	Max	42.31	57.28	40.08	26.92	34.25	57.28
TOC/TN	Mean	12.41	13.10	9.70	6.82	6.58	9.61
	ST	1.96	0.73	1.46	0.72	0.37	2.66
	Min	8.93	11.05	7.77	5.95	6.23	5.95
	Max	13.52	14.64	12.76	8.19	7.68	14.64

A total of 53 sediment samples in the core PROK-2 were analyzed for organic elemental analysis. TN content ranges between 0.06 to 0.15% with a mean value of 0.091% (Fig. 5.57; Table 5.28). It shows a generally uniform trend with slightly increasing values upwards to the top of the core (Fig. 5.57). TOC content range from 0.72 up to 1.20 % with a mean value of 0.85% (Fig. 5.57; Table 5.28). TOC content is generally uniform throughout the core, while the higher values are present in LU4a and LU5 (Fig. 5.57). TIC content ranges between 7.03 and 10.66% with a mean value of 8.43% (Fig. 5.57; Table 5.28). Higher TIC values occur at the bottom of the core until 360 cm (LU2; Fig. 5.57). Then, the TIC content shows a decreasing trend until LU4b, when the values start to increase upwards until LU5 (Fig. 5.57). In LU5, TIC values are decreasing again (Fig. 5.57). The percentage of insoluble residue ranges from 9.00 to 34.48%, with a mean value of 24.27% (Fig. 5.57; Table 5.28). The lowest values occur at the bottom of the core, and a generally increasing trend upwards can be observed

(Fig. 5.57). The TOC/TN ratio is in the range of 7.25 up to 14.79, with the highest values in LU2 and LU3, then it decreases until LU5 (Fig. 5.57; Table 5.28). Elevated values and an increasing trend upwards can be observed in the LU5 (Fig. 5.57).

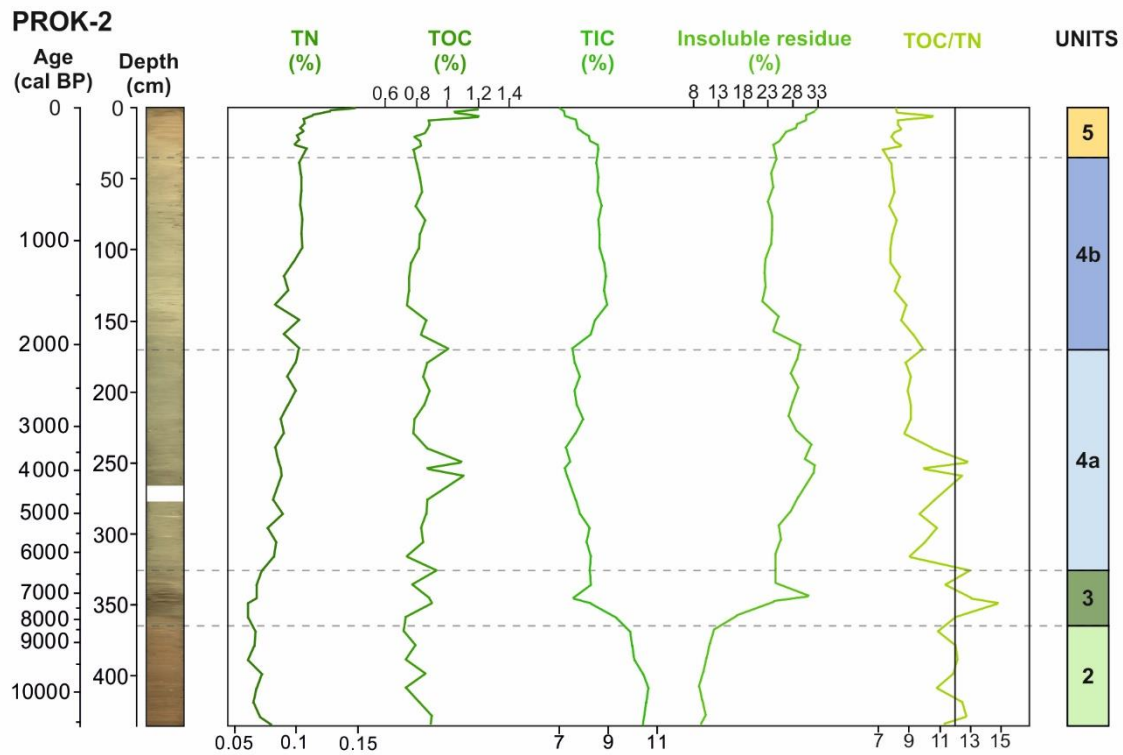


Figure 5.57 Distribution of TN, TOC, TIC, Insoluble residue and TOC/TN in sediments from the sediment core PROK-2.

Table 5.28 Statistical parameters of TN, TOC, TIC, Insoluble residue and TOC/TN in sediments from the sediment core PROK-2.

	PROK-2	LU2	LU3	LU4a	LU4b	LU5	TOTAL CORE
TN (%)	Mean	0.07	0.07	0.09	0.09	0.11	0.09
	ST	0.006	0.005	0.008	0.008	0.01	0.02
	Min	0.06	0.06	0.08	0.08	0.09	0.06
	Max	0.08	0.07	0.102	0.105	0.14	0.14
TOC (%)	Mean	0.81	0.84	0.88	0.81	0.92	0.86
	ST	0.07	0.08	0.10	0.04	0.15	0.11
	Min	0.72	0.73	0.74	0.74	0.79	0.72
	Max	0.90	0.93	1.10	0.86	1.2	1.2
TIC (%)	Mean	10.31	8.35	7.73	8.68	7.90	8.43
	ST	0.29	0.63	0.33	0.20	0.55	0.96
	Min	9.88	7.58	7.23	8.31	7.03	7.03
	Max	10.67	9.33	8.31	8.96	8.61	10.67
Insoluble residue (%)	Mean	10.33	24.17	28.56	23.35	28.82	24.27
	ST	1.03	5.05	2.38	0.91	3.55	6.86
	Min	9.01	16.67	24.48	21.92	24.04	9.01
	Max	12.23	24.54	32.30	25.14	34.48	34.48
TOC/TN	Mean	11.80	12.84	9.98	8.21	8.29	9.74
	ST	0.71	1.28	1.24	0.48	0.79	1.85
	Min	10.85	11.39	8.69	7.78	7.25	7.25
	Max	12.76	14.79	12.80	9.27	10.56	14.79

In the core PROK-3, 64 sediment samples were analyzed for TN, TOC, TIC, percentage of insoluble residue, and TOC/TN ratio. TN content varies between 0.07 and 0.38%, with a mean value of 0.14% (Fig. 5.58; Table 5.29). Generally, low TN values are present throughout the core, with the lowest values in the interval from 360 and 100 cm of the core (Fig. 5.58). TOC content ranges from 0.53 to 8.20%, with a mean value of 2.05% (Fig. 5.58; Table 5.29). The highest TOC values are measured in LU2, while other lithological units exhibit low and constant TOC values (Fig. 5.58). TIC content ranges between 5.21 and 9.42%, with a mean value of 7.47% (Fig. 5.58; Table 5.29). Generally, the TIC content shows an increasing upward trend, with higher values from 150 to 50 cm (Fig. 5.59). In LU5, TOC content is decreasing to the top of the core (Fig. 5.58). The percentage of insoluble residue ranges from 22.70 to 48.60%, with a mean value of 34.04% (Fig. 5.58; Table 5.29). It decreases from the bottom of the core upwards until 45 cm, whereas higher values occur from 45 cm to the top of the core (Fig. 5.58). TOC/TN ratio ranges from 5.81 up to 24.63 (Fig. 5.58; Table 5.29). The highest TOC/TN ratios are present in LU2, while in the other lithological units, the TOC/TN ratio is constant or slightly decreases upwards (Fig. 5.58).

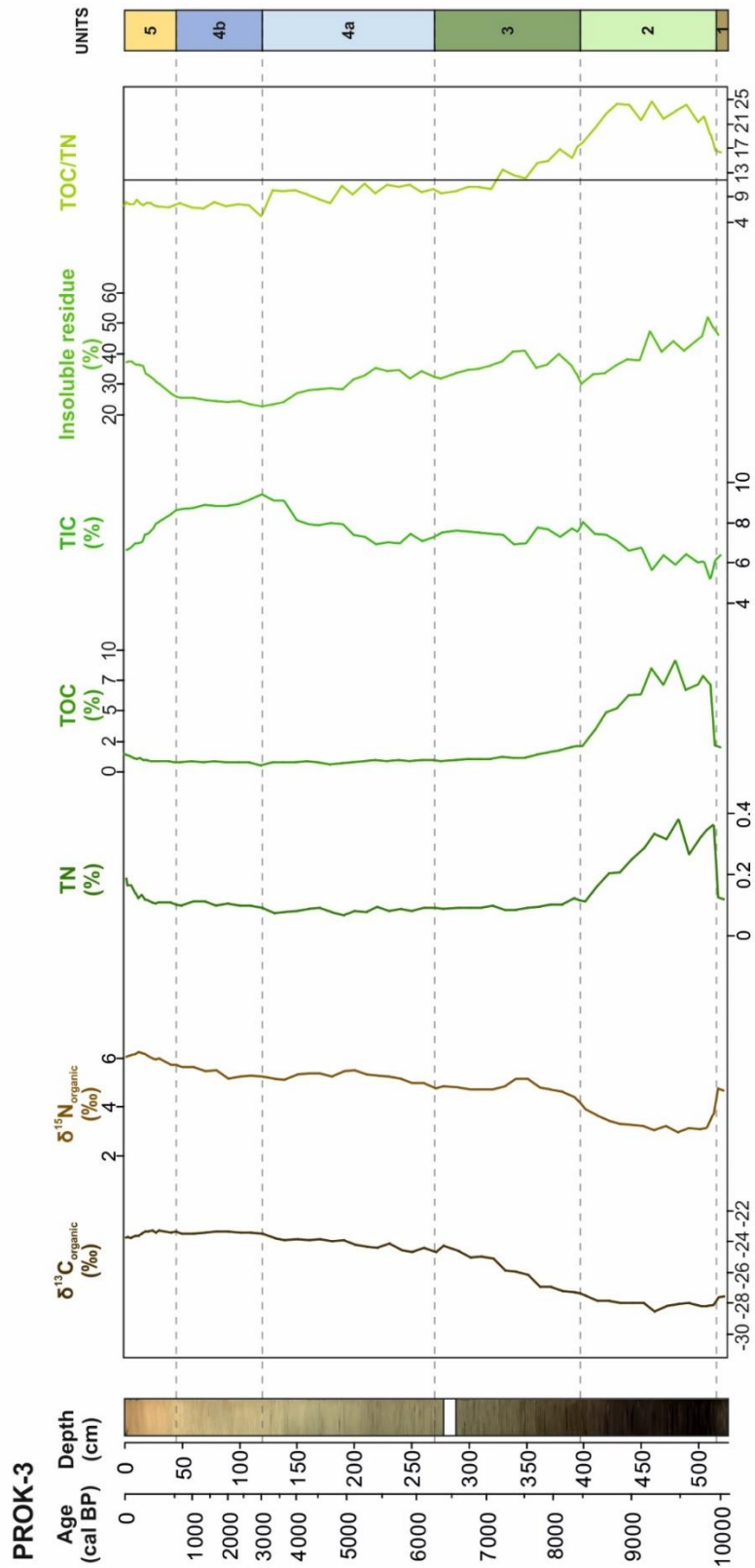


Figure 5.58 Distribution of $\delta^{13}C_{org}$, $\delta^{15}N_{org}$, TN, TOC, TIC, Insoluble residue and TOC/TN in sediments from the sediment core PROK-3.

Table 5.29 Statistical parameters of $\delta^{13}\text{C}_{\text{org}}$, $\delta^{15}\text{N}_{\text{org}}$, TN, TOC, TIC, Insoluble residue and TOC/TN in sediments from the sediment core PROK-3.

	PROK-3	LU1	LU2	LU3	LU4a	LU4b	LU5	TOTAL CORE
$\delta^{13}\text{C}_{\text{org}}$ (‰)	Mean	-27.56	-28.01	-25.97	-24.16	-23.40	-23.50	-25.18
	ST	0.05	0.25	1.09	0.32	0.07	0.18	1.86
	Min	-27.60	-28.54	-27.35	-24.69	-23.50	-23.77	-28.54
	Max	-27.53	-27.47	-24.24	-23.79	-23.32	-23.28	-23.80
$\delta^{15}\text{N}_{\text{org}}$ (‰)	Mean	4.70	3.32	4.74	5.22	5.44	6.07	4.91
	ST	0.06	0.29	0.26	0.20	0.20	0.15	0.94
	Min	4.66	2.95	4.18	4.74	5.17	5.71	2.95
	Max	4.75	3.95	5.17	5.49	5.72	6.27	6.27
TN (%)	Mean	0.12	0.27	0.097	0.08	0.10	0.13	0.14
	ST	0.004	0.08	0.01	0.008	0.007	0.03	0.08
	Min	0.12	0.11	0.09	0.07	0.09	0.11	0.07
	Max	0.13	0.38	0.12	0.09	0.11	0.19	0.38
TOC (%)	Mean	2.055	6.07	1.28	0.82	0.76	1.03	2.051
	ST	0.11	1.90	0.40	0.10	0.09	0.22	2.23
	Min	1.98	2.04	0.83	0.61	0.53	0.81	0.53
	Max	2.13	8.73	2.02	0.95	0.82	1.43	8.73
TIC (%)	Mean	6.26	6.54	7.45	7.70	8.90	7.33	7.47
	ST	0.22	0.79	0.26	0.70	0.25	0.58	0.92
	Min	6.11	5.21	6.94	6.92	8.64	6.63	5.21
	Max	6.42	8.01	7.72	9.12	9.42	8.42	9.42
Insoluble residue (%)	Mean	47.50	40.37	36.37	30.40	24.62	34.05	34.04
	ST	1.56	6.23	2.84	3.83	1.02	3.50	6.74
	Min	46.39	30.26	31.78	23.64	22.70	27.04	22.70
	Max	48.60	52.03	41.03	35.27	25.84	37.72	52.03
TOC/TN	Mean	16.55	22.08	12.99	10.00	7.46	7.83	12.50
	ST	0.28	2.05	2.66	0.87	0.69	0.33	5.59
	Min	16.36	17.95	9.61	8.06	5.81	7.35	5.81
	Max	16.75	24.64	17.30	10.98	8.14	8.45	24.64

In the core PROK-4, 68 sediment samples were analyzed for TN, TOC, TIC, percentage of insoluble residue, and TOC/TN ratio. TN content ranges from 0.06 to 0.30%, with a mean value of 0.10% (Fig. 5.59; Table 5.30). The lowest TN values occur at the bottom of the core with an increasing value upwards (Fig. 5.59). TOC content ranges from 0.49 to 2.49%, with a mean value of 0.92% (Fig. 5.59; Table 5.30). The uniform trend is present throughout the core except for LU5, which is characterized by somewhat higher values (Fig. 5.59). TIC values range between 7.22 and 10.78%, with a mean value of 9.38% (Fig. 5.59; Table 5.30). A slight increase in TIC values occurs from the bottom of the core until 360 cm, while the TIC content strongly decreases until 300 cm (Fig. 5.59). In the interval from 300 to 160 cm, higher TIC values occur, and then the TIC content decreases again up to the top of the core (Fig. 5.59). The percentage of insoluble residue ranges between 9.69 and 33.20%, with a mean value of 18.52% (Fig. 5.59; Table 5.30). Insoluble residue shows a generally constant trend until 160 cm of the core, with

an increasing trend upwards to the top of the core (Fig. 5.59). The TOC/TN ratio varies between 7.58 and 12.70 (Fig. 5.59; Table 5.30). A slight decrease in TOC/TN occurs up to 360 cm of the core. Then, the ratio increases until 300 cm of the core and decreases again until 140 cm (Fig. 5.59). The ratio is constant or slightly increases from 140 cm to the top of the core (Fig. 5.59).

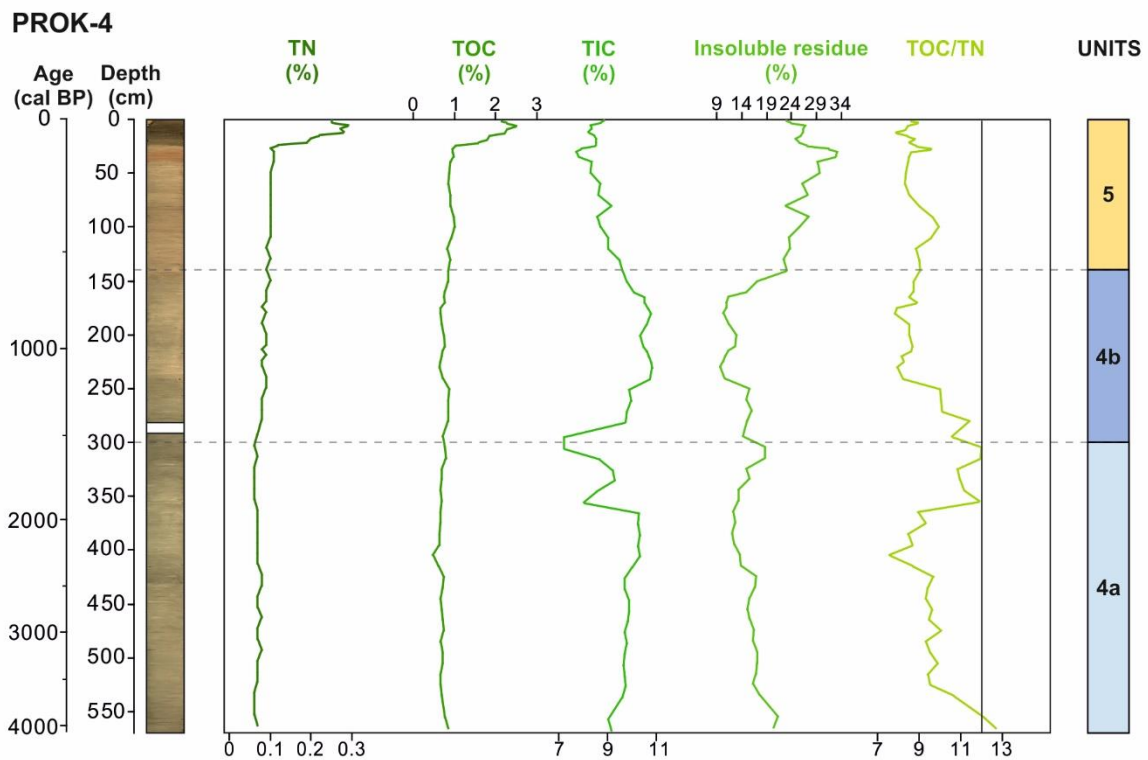


Figure 5.59 Distribution of TN, TOC, TIC, Insoluble residue and TOC/TN in sediments from the sediment core PROK-4.

Table 5.30 Statistical parameters of TN, TOC, TIC, Insoluble residue and TOC/TN in sediments from the sediment core PROK-4.

	PROK-4	LU4a	LU4b	LU5	TOTAL CORE
TN (%)	Mean	0.07	0.08	0.15	0.10
	ST	0.01	0.01	0.07	0.06
	Min	0.06	0.07	0.09	0.06
	Max	0.08	0.10	0.30	0.30
TOC (%)	Mean	0.69	0.75	1.32	0.92
	ST	0.07	0.07	0.59	0.45
	Min	0.49	0.63	0.82	0.49
	Max	0.84	0.88	2.49	2.49
TIC (%)	Mean	9.50	10.17	8.58	9.38
	ST	0.72	0.80	0.47	0.92
	Min	7.23	7.25	7.72	7.23
	Max	10.30	10.78	9.60	10.78
Insoluble residue (%)	Mean	15.79	12.71	26.40	18.52
	ST	2.42	2.31	3.10	6.37
	Min	12.14	9.69	22.46	9.69
	Max	21.39	17.06	33.20	33.20
TOC/TN	Mean	10.05	8.94	8.79	9.31
	ST	1.30	1.00	0.50	1.15
	Min	7.58	7.84	7.91	7.58
	Max	12.70	11.41	9.97	12.70

In the core ZLA-1, 38 sediment samples were analyzed for TN, TOC, TIC, percentage of insoluble residue, and TOC/TN ratio. TN content ranges from 0.02 to 0.05%, with a mean value of 0.03% (Fig. 5.60; Table 5.31). The lowest TN values occur at the bottom of the core, with an increasing value up to 90 cm (Fig. 5.60). The values decrease again to the top of the core (Fig. 5.60). TOC content ranges from 0.37 to 1.05%, with a mean value of 0.52% (Fig. 5.60; Table 5.31). An oscillating trend of values occurs from the bottom to 50 cm of the core, while a decrease occurs at the top (Fig. 5.60). TIC values range between 8.85 and 10.71%, with a mean value of 9.76% (Fig. 5.60; Table 5.31). From the bottom of the core until 220 cm, a slightly decreasing trend occurs, whereas an increase of values occurs from 220 cm to 190 cm of the core (Fig. 5.60). A decrease in TIC values occurs from 190 to 90 cm of the core, while the TIC content increases to the top of the core (Fig. 5.60). Insoluble residue varies between 13.57 and 27.12%, with a mean value of 21.55% (Fig. 5.60; Table 5.31). Its values oscillate until 100 cm, where they start to increase for 10 cm and then decrease to the top of the core (Fig. 5.60). TOC/TN ratio ranges from 9.83 up to 20.05 (Fig. 5.60; Table 5.31). A generally constant TOC/TN ratios occur up to 60 cm of the core (Fig. 5.60). Then, the ratio increases abruptly for 10 cm and decreases until the top of the core (Fig. 5.60).

In the sediment core ZLA-2, 33 samples were analyzed for organic elements. TN content was below the limit detection limit for most of the samples (<0.01%) (Fig. 5.61; Table 5.32). TOC content ranges from 0.26 to 1.02%, with a mean value of 0.93% (Fig. 5.61; Table 5.32). TOC content ranges from 0.26 to 1.02%, with a mean value of 0.93% (Fig. 5.61; Table 5.32). The lowest TOC values occur at the bottom of the core (Fig. 5.61). An increasing trend of values occurs from 250 cm to 200 cm of the core, whereas a constant trend is present from 200 cm to 130 cm (Fig. 5.61). From 130 cm to the top of the core, TOC content has a decreasing trend (Fig. 5.61). TIC content ranges from 7.88 to 10.93%, with a mean value of 9.39% (Fig. 5.61; Table 5.32). It has an opposite trend of values in comparison to TOC content (Fig. 5.61). The percentage of insoluble residue ranges from 11.87 to 36.03%, with a mean value of 24.76% (Fig. 5.61; Table 5.32). The insoluble residue has a very similar trend to TOC (Fig. 5.61).

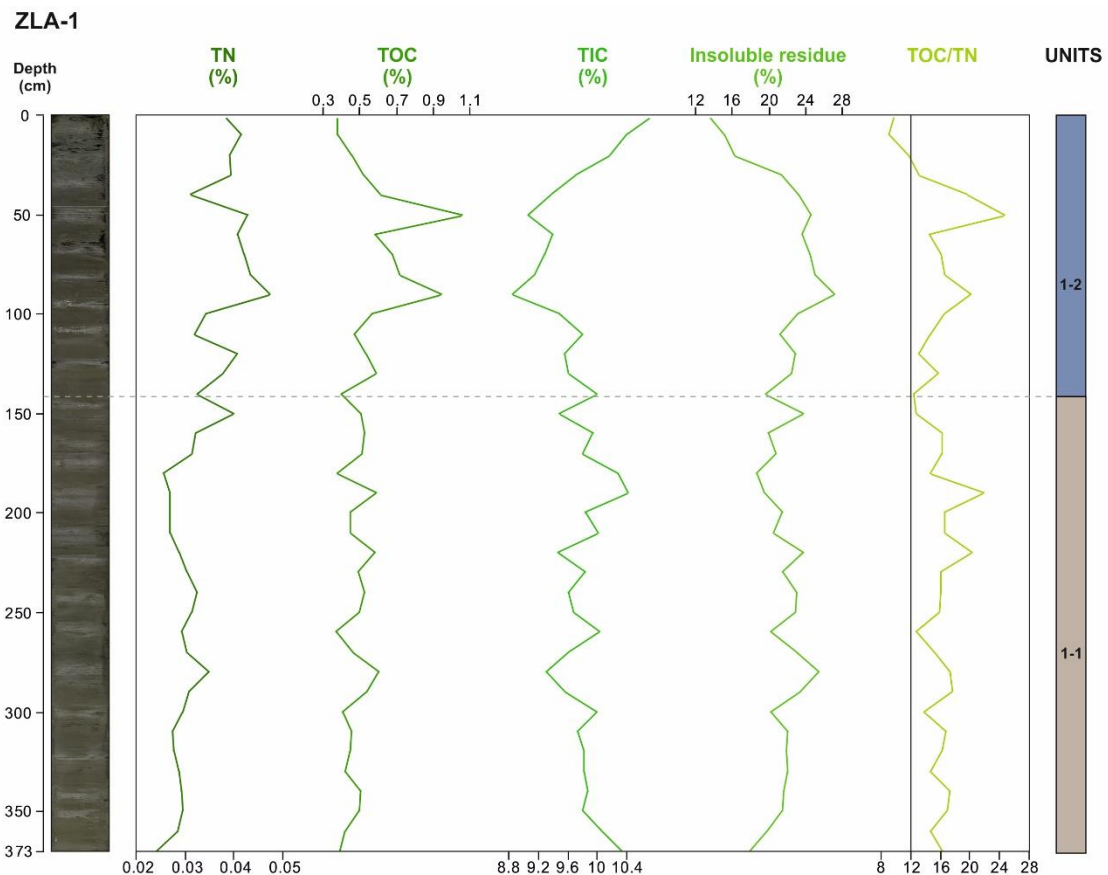


Figure 5.60 Distribution of TN, TOC, TIC, Insoluble residue and TOC/TN in sediments from the sediment core ZLA-1.

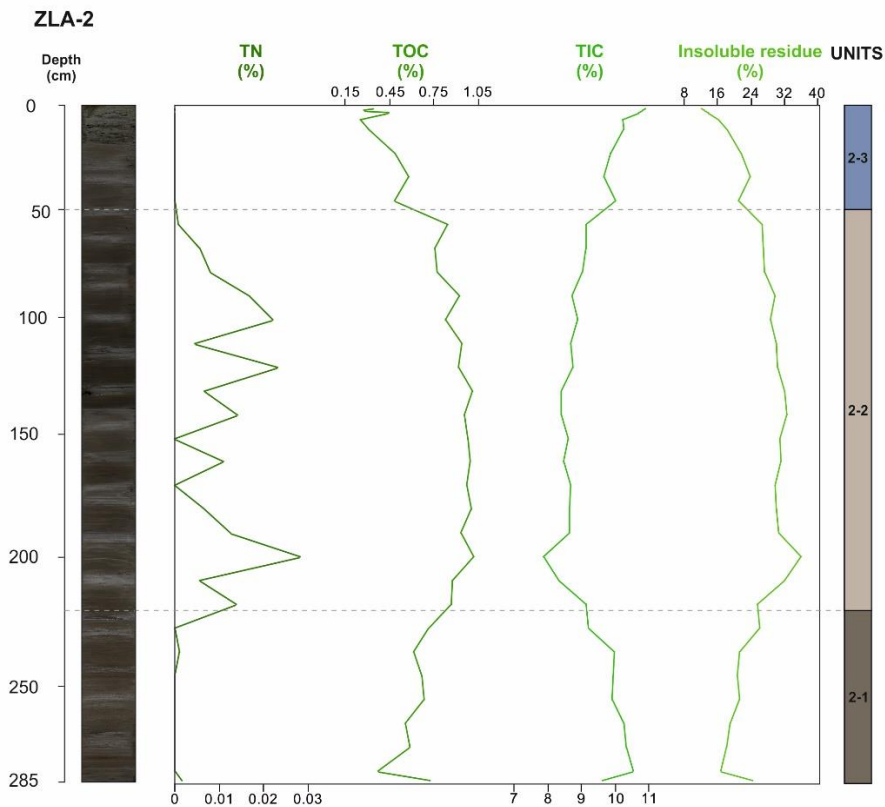


Figure 5.61 Distribution of TN, TOC, TIC and insoluble residue in sediments from the sediment core ZLA-2.

Table 5.31 Statistical parameters of TN, TOC, TIC, Insoluble residue and TOC/TN in sediments from the sediment core ZLA-1.

	ZLA-1	LU1-1	LU1-2	TOTAL CORE
TN (%)	Mean	0.03	0.04	0.03
	ST	0.00	0.01	0.01
	Min	0.02	0.03	0.02
	Max	0.03	0.05	0.05
TOC (%)	Mean	0.47	0.58	0.52
	ST	0.07	0.18	0.14
	Min	0.37	0.38	0.37
	Max	0.61	1.05	1.05
TIC (%)	Mean	9.85	9.65	9.76
	ST	0.28	0.47	0.39
	Min	9.31	8.85	8.85
	Max	10.41	10.71	10.71
Insoluble residue (%)	Mean	21.52	21.57	21.55
	ST	1.84	3.59	2.77
	Min	17.92	13.57	13.57
	Max	25.44	27.12	27.12
TOC/TN	Mean	16.38	15.14	15.80
	ST	2.03	3.75	3.00
	Min	12.80	9.14	9.14
	Max	21.90	24.58	24.58

Table 5.32 Statistical parameters of TN, TOC, TIC and insoluble residue in sediments from the sediment core ZLA-2.

	ZLA-2	LU2-1	LU2-2	LU2-3	TOTAL CORE
TN (%)	Mean	0.00	0.01	0.00	0.01
	ST	0.00	0.01	0.00	0.01
	Min	0.00	0.00	0.00	0.00
	Max	0.00	0.03	0.00	0.03
TOC (%)	Mean	0.60	0.91	0.45	0.72
	ST	0.12	0.10	0.18	0.24
	Min	0.37	0.71	0.26	0.26
	Max	0.72	1.02	0.84	1.02
TIC (%)	Mean	10.09	8.69	10.19	9.39
	ST	0.31	0.34	0.58	0.84
	Min	9.63	7.88	9.16	7.88
	Max	10.54	9.22	10.93	10.93
Insoluble residue (%)	Mean	20.17	30.00	18.45	24.76
	ST	2.51	2.59	5.24	6.47
	Min	16.65	25.69	11.87	11.87
	Max	24.29	36.03	26.80	36.03

5.3.6.2 Stable oxygen ($\delta^{18}\text{O}_{\text{cal}}$) and carbon ($\delta^{13}\text{C}_{\text{cal}}$) isotope analysis of carbonates

Stable oxygen ($\delta^{18}\text{O}_{\text{cal}}$) and carbon ($\delta^{13}\text{C}_{\text{cal}}$) isotope analysis of carbonates was made on 45 samples from the core PROK-1 (Appendix 2; Fig. 5.62; Table 5.33). The $\delta^{18}\text{O}_{\text{cal}}$ results range from -7.82 to -5.69‰ with a mean value of -6.61‰ (Table 5.33). The $\delta^{13}\text{C}_{\text{cal}}$ results range from -8.36 to -6.39‰ with a mean value of -7.33‰ (Table 5.33).

In LU2, five samples were analyzed for $\delta^{18}\text{O}_{\text{cal}}$ and $\delta^{13}\text{C}_{\text{cal}}$, and the results of $\delta^{18}\text{O}_{\text{cal}}$ ranged from -7.82 to -6.45‰, and $\delta^{13}\text{C}_{\text{cal}}$ values ranged from -7.81 to -6.79‰ (Fig. 5.62; Table 5.33). A fluctuation of both stable isotope values occurs with a general increase upward. Seven samples were analyzed for $\delta^{18}\text{O}_{\text{cal}}$ and $\delta^{13}\text{C}_{\text{cal}}$ in LU3. The $\delta^{18}\text{O}_{\text{cal}}$ values range from -7.58 to -6.30‰, and $\delta^{13}\text{C}_{\text{cal}}$ values from -7.81 to -6.79‰ (Fig. 5.62; Table 5.33). For the first part of LU3 (750–700 cm), a decrease in $\delta^{18}\text{O}_{\text{cal}}$ and $\delta^{13}\text{C}_{\text{cal}}$ values occurs, and then a slight increase upwards of $\delta^{18}\text{O}_{\text{cal}}$ and $\delta^{13}\text{C}_{\text{cal}}$ values is present (Fig. 5.62). In LU4a, 19 samples were analyzed for $\delta^{18}\text{O}_{\text{cal}}$ and $\delta^{13}\text{C}_{\text{cal}}$, where $\delta^{18}\text{O}_{\text{cal}}$ values range from -7.04 up to -5.69‰, and $\delta^{13}\text{C}_{\text{cal}}$ values from -7.61 up to -6.39‰ (Fig. 5.62; Table 5.33). For LU4a, a general increase of $\delta^{18}\text{O}_{\text{cal}}$ and $\delta^{13}\text{C}_{\text{cal}}$ values occurs up to 460 cm and then a slight decrease up to the end of the LU4 (Fig. 5.62). In LU4b, ten samples were analyzed for the $\delta^{18}\text{O}_{\text{cal}}$ and $\delta^{13}\text{C}_{\text{cal}}$, where $\delta^{18}\text{O}_{\text{cal}}$ values range from -6.98 up to -6.32‰, and $\delta^{13}\text{C}_{\text{cal}}$ values from -8.30 to -7.59‰ (Fig. 5.62; Table 5.33). Throughout LU4b, a general decrease of $\delta^{18}\text{O}_{\text{cal}}$ and $\delta^{13}\text{C}_{\text{cal}}$ values occurs (Fig. 5.62).

Four samples were analyzed for $\delta^{18}\text{O}_{\text{cal}}$ and $\delta^{13}\text{C}_{\text{cal}}$ in the uppermost LU5. $\delta^{18}\text{O}_{\text{cal}}$ values range from -7.05 to -6.67‰, and $\delta^{13}\text{C}_{\text{cal}}$ values from -8.36 up to -7.52‰ (Fig. 5.62; Table 5.33). In LU5, an opposite trend of $\delta^{18}\text{O}_{\text{cal}}$ and $\delta^{13}\text{C}_{\text{cal}}$ values is present, where the values of $\delta^{13}\text{C}_{\text{cal}}$ increase upward (Fig. 5.62).

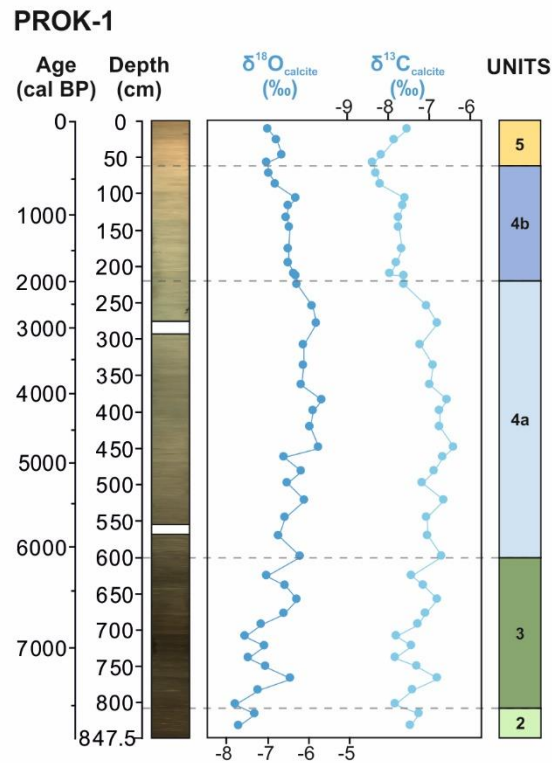


Figure 5.62. $\delta^{18}\text{O}_{\text{cal}}$ and $\delta^{13}\text{C}_{\text{cal}}$ results in the core PROK-1.

Table 5.33 Statistical parameters of $\delta^{18}\text{O}_{\text{cal}}$ and $\delta^{13}\text{C}_{\text{cal}}$ in sediments from the core PROK-1.

	PROK-1	LU2	LU3	LU4a	LU4b	LU5	TOTAL CORE
$\delta^{18}\text{O}_{\text{cal}}$ (‰)	Mean	-7.53	-7.04	-6.17	-6.54	-6.88	-5.87
	SD	0.29	0.47	0.31	0.21	0.18	1.97
	Min	-7.74	-7.82	-6.76	-6.98	-7.05	-7.82
	Max	-7.33	-6.30	-5.69	-6.32	-6.67	-5.69
$\delta^{13}\text{C}_{\text{cal}}$ (‰)	Mean	-7.49	-7.29	-6.89	-7.82	-7.97	-7.33
	SD	0.29	0.34	0.29	0.25	0.37	0.50
	Min	-7.81	-7.80	-7.61	-8.30	-8.36	-8.36
	Max	-7.24	-6.79	-6.64	-7.59	-7.52	-6.39

5.3.6.3 Stable carbon ($\delta^{13}\text{C}_{\text{org}}$) and nitrogen ($\delta^{15}\text{N}_{\text{org}}$) isotope analysis of organic matter

Stable carbon ($\delta^{13}\text{C}_{\text{org}}$) and nitrogen ($\delta^{15}\text{N}_{\text{org}}$) isotope analysis of organic matter was performed on 93 samples in the sediment core PROK-1 (Appendix 2; Fig. 5.56; Table 5.27) and 64 samples in the core PROK-3 (Appendix 4; Fig. 5.58; Table 5.29). In the core PROK-1, $\delta^{13}\text{C}_{\text{org}}$ values range from -28.12 up to -23.56‰ with a mean value of -25.40‰, while the $\delta^{15}\text{N}_{\text{org}}$ range from 4.89 up to 6.45‰ with a mean value of 5.58‰ (Fig. 5.56; Table 5.27). In the core PROK-3, $\delta^{13}\text{C}_{\text{org}}$ values range from -28.54 up to -23.28‰ with a mean value of -25.18‰ (Fig. 5.58; Table 5.29). The $\delta^{15}\text{N}_{\text{org}}$ values in the core PROK-3 range from 2.95 up to 6.27‰ with a mean value of 4.91‰ (Fig. 5.58; Table 5.29).

Eleven samples were analyzed for $\delta^{13}\text{C}_{\text{org}}$ and $\delta^{15}\text{N}_{\text{org}}$ in LU2 of the PROK-1 (Figure 5.56; Table 5.27). The values are low and negative and range from -28.12 to -27.27‰ for $\delta^{13}\text{C}_{\text{org}}$ and from 5.06 to 5.36‰ for $\delta^{15}\text{N}_{\text{org}}$ (Fig. 5.56; Table 5.27). In LU3 of the core PROK-1, fifteen samples were analyzed for $\delta^{13}\text{C}_{\text{org}}$ and $\delta^{15}\text{N}_{\text{org}}$, where the $\delta^{13}\text{C}_{\text{org}}$ values range from -27.43 to -26.60‰, and $\delta^{15}\text{N}_{\text{org}}$ are from 5.34 up to 5.80‰ (Fig. 5.56; Table 5.27). A slightly upward increasing trend is present for $\delta^{13}\text{C}_{\text{org}}$ and a constant trend of $\delta^{15}\text{N}_{\text{org}}$ values in LU3 (Fig. 5.56). In LU4a, fifty-four samples were analyzed for $\delta^{13}\text{C}_{\text{org}}$ and $\delta^{15}\text{N}_{\text{org}}$. The $\delta^{13}\text{C}_{\text{org}}$ values range from -26.36 up to -23.95‰ and $\delta^{15}\text{N}_{\text{org}}$ from 4.89 to 5.75‰ (Fig. 5.56; Table 5.27). An increasing upward trend occurs for $\delta^{13}\text{C}_{\text{org}}$ in LU4a. Sixteen samples were analyzed in LU4b for $\delta^{13}\text{C}_{\text{org}}$ and $\delta^{15}\text{N}_{\text{org}}$. The $\delta^{13}\text{C}_{\text{org}}$ values are in the range from -24.43 to -23.56‰, and the $\delta^{15}\text{N}_{\text{org}}$ from 5.23 to 6.06‰ (Fig. 5.56; Table 5.27). An increase in the $\delta^{13}\text{C}_{\text{org}}$ can occur up to 120 cm, and then a slight decrease upwards is present, while the $\delta^{15}\text{N}_{\text{org}}$ values show a constant trend throughout LU4b of the core PROK-1 (Fig. 5.56). In LU5, thirteen samples were analyzed for $\delta^{13}\text{C}_{\text{org}}$ and $\delta^{15}\text{N}_{\text{org}}$. $\delta^{13}\text{C}_{\text{org}}$ values range from -25.13 to -24.21‰, while the $\delta^{15}\text{N}_{\text{org}}$ from 6.16 to 6.45‰ (Fig. 5.56; Table 5.27). $\delta^{13}\text{C}_{\text{org}}$ and $\delta^{15}\text{N}_{\text{org}}$ values show generally constant trend in LU5, except for the last 20 cm, where the $\delta^{13}\text{C}_{\text{org}}$ values slightly decrease (Fig. 5.56).

In LU1 of the core PROK-3, two samples were analyzed for $\delta^{13}\text{C}_{\text{org}}$ and $\delta^{15}\text{N}_{\text{org}}$, with the $\delta^{13}\text{C}_{\text{org}}$ values of -27.60 and -27.53‰, and the $\delta^{15}\text{N}_{\text{org}}$ values of 4.66 and 4.75‰ (Fig. 5.58; Table 5.29). Fourteen samples were analyzed in LU2, where $\delta^{13}\text{C}_{\text{org}}$ values range from -28.54 up to -27.35‰, and $\delta^{15}\text{N}_{\text{org}}$ from 3.04 up to 4.18‰. (Fig. 5.58; Table 5.29) In LU3, a slightly increasing upward trend for $\delta^{13}\text{C}_{\text{org}}$ and a constant trend for $\delta^{15}\text{N}_{\text{org}}$ occur (Fig. 5.58). A total

of 13 samples were analyzed with $\delta^{13}\text{C}_{\text{org}}$ values in the range from -27.27 up to -24.24‰, while $\delta^{15}\text{N}_{\text{org}}$ values range from 4.39 up to 5.17‰ (Fig. 5.58; Table 5.29). Fifteen samples were analyzed in LU4a, where the $\delta^{13}\text{C}_{\text{org}}$ values show a constant trend through this unit and range from -24.69 to -23.46‰ (Fig. 5.58; Table 5.29). The $\delta^{15}\text{N}_{\text{org}}$ values range between 4.99‰ and 5.49‰, displaying a general increasing trend upward (Fig. 5.58; Table 5.29). A similar trend is present in LU4b, where eight samples were analyzed for $\delta^{13}\text{C}_{\text{org}}$ and $\delta^{15}\text{N}_{\text{org}}$. $\delta^{13}\text{C}_{\text{org}}$ values range from -23.50 to -23.32‰, while $\delta^{15}\text{N}_{\text{org}}$ values range from 5.17 to 5.72‰ (Fig. 5.58; Table 5.29). In LU5, twelve samples were analyzed with $\delta^{13}\text{C}_{\text{org}}$ values ranging from -23.77 up to -23.28‰, while $\delta^{15}\text{N}_{\text{org}}$ range from 5.71 up to 6.27‰ (Fig. 5.58; Table 5.29).

5.3.7 Micropalaeontological analysis

The microfossil analysis of foraminifera was made on 20 samples from the sediment core PROK-1 (Figure 5.63). Throughout the core, a total of 90 foraminifera species were determined from 48 different genera. The suborder Rotaliina is characterized by 48 foraminifera species, the suborder Miliolina by 35, and in the suborder Textulariina, 6 foraminifera species were identified (Fig. 5.63B). The list of genera and species of foraminifera is included in the Appendix 2.

In the lithological unit LU2 of the core PROK-1, 4 sediment samples were analyzed for foraminifera assemblage (837–838 cm, 807–808 cm, 771–772 cm, and 755–756 cm). In the sediment sample PROK-1 837–838, 19 foraminifera species were determined. The most abundant are the species that belong to the suborder Rotaliina (89.9%), whereas the suborder Miliolina is present with 10.1%. The most dominant species in the sediment sample are *Ammonia tepida* (Cushman, 1926) (67.06%), *Quinqueloculina seminulum* (Linnaeus, 1758) (5.49%) and *Aubignyna perlucida* (Heron-Allen and Earland, 1913) (5.88%) (Fig. 5.63A). In the sediment sample PROK-1 807–808, 20 foraminifera species were determined. The most abundant foraminifera species are from the suborder Rotaliina (87.72%), whereas 12.28% are foraminifera species from the suborder Miliolina. The most dominant species are as followed: *Ammonia tepida* (Cushman, 1926) (61.75%), *Haynesina germanica* (Ehrenberg, 1840) (8.77%) and *Miliolinella subrotunda* (Montagu, 1803) (4.21%) (Fig. 5.63A). The sediment sample in the interval from 771–772 cm is characterized by 17 identified

foraminifera genera and 23 species. Of the identified foraminifera species, 68.25% belong to the suborder Rotaliina, while 31.75% are classified under the suborder Miliolina. The dominant species are *Ammonia tepida* (Cushman, 1926) (40.48%), *Quinqueloculina schlumbergeri* (Wiesner, 1923) (14.29%), *Aubignyna perlucida* (Heron-Allen & Earland, 1913) (8.33%) and *Haynesina germanica* (Ehrenberg, 1840) (7.94%) (Fig. 5.63A). The sediment sample PROK-1 755–756 is characterized by a total of 19 identified foraminifera genera and 26 foraminifera species. Most foraminifera species belong to the suborder Rotallina (64.05%), whereas 35.95% are part of the suborder Miliolina. The dominant species are *Ammonia tepida* (Cushman, 1926) (38.67%), *Quinqueloculina schlumbergeri* (Wiesner, 1923) (21.15%), *Miliolinella subrotunda* (Montagu, 1803) (8.46%) and *Haynesina germanica* (Ehrenberg, 1840) (6.34%) (Fig. 5.63A).

Foraminifera analysis was performed on four sediment samples from the LU3 of the core PROK-1 (742–745 cm, 661–662 cm, 641–642 cm, 601–602 cm). In the interval from 742 to 745 cm, a total of 19 foraminifera genera and 23 foraminifera species were identified. Most foraminifera genera correspond to the suborder Rotaliina (73.53%), while 25.82% belong to the suborder Miliolina, and only 0.65% are the genera in the suborder Textulariina. The most dominant species in this interval are *Ammonia tepida* (Cushman, 1926) (39.22%), *Quinqueloculina schlumbergeri* (Wiesner, 1923) (10.78%), *Haynesina germanica* (Ehrenberg, 1840) (6.86%), *Aubignyna perlucida* (Heron-Allen & Earland, 1913) (5.88%) and *Porosonion subgranosus* (Egger, 1857) (5.56%) (Fig. 5.63A). In the sediment sample PROK-1 661–662, 16 foraminifera genera and 24 foraminifera species are identified. The identified species belong to the suborder Rotaliina (78.22%) and Miliolina (21.78%). The most dominant species are *Ammonia tepida* (Cushman, 1926) (42.90%), *Haynesina germanica* (Ehrenberg, 1840) (8.91%), *Quinqueloculina schlumbergeri* (Wiesner, 1923) (7.26%) and *Aubignyna perlucida* (Heron-Allen & Earland, 1913) (6.60%) (Fig. 5.63A). A total of 20 foraminifera genera and 24 species were identified in the sediment sample PROK-1 641–642. Most genera belong to the suborder Rotallina (70.11%), while the rest correspond to the suborder Miliolina (29.89%). The most dominant species in this interval are: *Ammonia tepida* (Cushman, 1926) (39.46%), *Quinqueloculina schlumbergeri* (Wiesner, 1923) (11.11%), *Haynesina germanica* (Ehrenberg, 1840) (8.05%), *Aubignyna perlucida* (Heron-Allen & Earland, 1913) (7.28%) and *Miliolinella subrotunda* (Montagu, 1803) (6.51%) (Fig.

5.63A). In the sediment sample PROK-1 601–602, 21 genera and 31 species were identified. Most of the foraminifera are of the suborder Rotaliina (64.47%), while 33.88% belong to Miliolina, and only 1.64% correspond to the suborder Textulariina. The most dominant species in this sediment sample are *Ammonia tepida* (Cushman, 1926) (24.01%), *Quinqueloculina schlumbergeri* (Wiesner, 1923) (12.83%), *Haynesina germanica* (Ehrenberg, 1840) (9.21%), *Aubignyna perlucida* (Heron-Allen & Earland, 1913) (7.24%) and *Porosonion subgranosus* (Egger, 1857) (7.24%) (Fig. 5.63A).

Foraminifera analysis was conducted on three sediment samples from LU4a of the PROK-1 core, specifically at depths of 448–449 cm, 335–336 cm, and 221–222 cm. In the interval from 448 to 449 cm, a total of 21 foraminifera genera and 28 species were identified. Most of the foraminifera species belong to the suborder Rotaliina (59.69%), 34.50% to the suborder Miliolina and 5.81% to the suborder Textulariina. Dominant species in this sample are *Ammonia tepida* (Cushman, 1926) (14.73%), *Haynesina germanica* (Ehrenberg, 1840) (13.18%), *Elphidium translucens* Natland, 1938 (10.08%), *Quinqueloculina schlumbergeri* (Wiesner, 1923) (6.98%), *Porosonion subgranosus* (Egger, 1857) (6.98%) and *Quinqueloculina laevigata* d'Orbigny, 1839 (6.59%) (Fig. 5.63A). In the sediment sample PROK-1 335–336, a total of 24 foraminifera genera and 32 species were identified. 66.53% of genera belong to the suborder Rotaliina, 28.29% to the suborder Miliolina, and 5.18% to the suborder Textulariina. The dominant species in this sediment sample are *Ammonia tepida* (Cushman, 1926) (11.55%), *Elphidium translucens* Natland, 1938 (9.96%), *Haynesina germanica* (Ehrenberg, 1840) (9.56%), *Asterigerinata mamilla* (Williamson, 1858) (9.16%), *Rosalina macropora* (Hofker, 1951) (6.37%) and *Porosonion subgranosus* (Egger, 1857) (6.37%) (Fig. 5.63A). A total of 24 foraminifera genera and 32 species were identified in the sample PROK-1 221–222. Most of the genera correspond to the suborder Rotaliina (68.75%), while 28.91% belong to the suborder Miliolina and 2.34% to the suborder Textulariina. The dominant species in this sample are *Ammonia tepida* (Cushman, 1926) (14.06%), *Elphidium translucens* Natland, 1938 (14.06%), *Porosonion subgranosus* (Egger, 1857) (10.55%), *Asterigerinata mamilla* (Williamson, 1858) (7.03%), *Haynesina germanica* (Ehrenberg, 1840) (6.64%) and *Miliolinella subrotunda* (Montagu, 1803) (6.64%) (Fig. 5.63A).

In the LU4b of the core PROK-1, 4 samples were analyzed for foraminifera assemblages (206–207 cm, 101–102, 80–81 cm, 67–68). In the sediment sample PROK-1 206–207, a total of 25 foraminifera genera and 34 species were identified. The most dominant species in this interval are *Asterigerinata mamilla* (Williamson, 1858) (10.20%), *Elphidium translucens* Natland, 1938 (10.20%), *Ammonia tepida* (Cushman, 1926) (9.41%), *Porosonion subgranosus* (Egger, 1857) (9.41%), *Haynesina germanica* (Ehrenberg, 1840) (9.02%) and *Miliolinella subrotunda* (Montagu, 1803) (5.49%) (Fig. 5.63A). In the sediment sample PROK-1 101–102, a total of 22 foraminifera genera and 31 species were identified. The most dominant species are *Elphidium translucens* (Natland, 1938) (16.38%), *Asterigerinata mamilla* (Williamson, 1858) (12.89%), *Ammonia tepida* (Cushman, 1926) (11.50%) and *Porosonion subgranosus* (Egger, 1857) (8.01%). A total of 26 foraminifera genera and 36 species were identified in the sediment sample PROK-1 80–81. The most dominant species in this interval are *Elphidium translucens* Natland, 1938 (15.44%), *Miliolinella subrotunda* (Montagu, 1803) (11.93%), and *Aubignyna perlucida* (Heron-Allen & Earland, 1913) (5.96%) (Fig. 5.63A). In the sediment sample PROK-1 67–68, 23 foraminifera genera and 31 species were identified. The most dominant species in this interval are *Elphidium translucens* Natland, 1938 (16.91%), *Haynesina germanica* (Ehrenberg, 1840) (9.71%), *Asterigerinata mamilla* (Williamson, 1858) (8.99%), *Aubignyna perlucida* (Heron-Allen & Earland, 1913) (6.83%), *Miliolinella subrotunda* (Montagu, 1803) (6.47%), *Ammonia tepida* (Cushman, 1926) (6.12%), and *Quinqueloculina laevigata* d'Orbigny, 1839 (5.04%) (Fig. 5.63A).

In the LU5 of the sediment core PROK-1, 5 sediment samples were analyzed for foraminifera assemblages (28–30 cm, 19–21 cm, 10–12 cm, 4–6 cm, 1–3 cm). In the sediment sample PROK-1 28–30 cm, 35 foraminifera species were identified. Out of the total number of species, 67.40% belong to the suborder Rotaliina, 31.14% to the suborder Miliolina, and 1.47% to the suborder Textulariina. The most dominant species in this interval are *Elphidium translucens* (Natland, 1938) (10.62%), *Porosonion subgranosus* (Egger, 1857) (8.79%), *Ammonia tepida* (Cushman, 1926) (8.42%), *Bulimina aculeata* (d'Orbigny, 1826) (6.59%), and *Miliolinella subrotunda* (Montagu, 1803) (5.86%) (Fig. 63A). In the sediment sample PROK-1 19–21, a total of 46 foraminifera species were determined, of which 60% belong to the suborder Rotaliina, 37% to the suborder Miliolina, and 3% to the suborder

Textulariina. The dominant species in this sample are *Miliolinella subrotunda* (Montagu, 1803) (13.2%), *Porosononion subgranosus* (Egger, 1857) (7.6%), *Bulimina aculeata* d'Orbigny, 1826 (5.9%) and *Bolivina dilatata* Reuss, 1850 (5.3%) (Fig. 5.63A). In the sediment sample PROK-1 10–12, a total of 40 foraminifera species were identified of which 77.68% of foraminifera species belong to the suborder Rotaliina, 19.13% to the suborder Miliolina, and 3.19% to the suborder Textulariina. The most dominant species are *Bulimina aculeata* d'Orbigny, 1826 (10.14%), *Neoconorbina terquemi* (Rzehak, 1888) (8.99%), *Asterigerinata mamilla* (Williamson, 1858) (8.12%), *Rosalina macropora* (Hofker, 1951) (7.54%) and *Miliolinella subrotunda* (Montagu, 1803) (6.96%) (Fig. 5.63A). In the sediment sample PROK-1 4–6, 38 foraminifera species were identified, where 69.3% belong to the suborder Rotaliina, 30% to the suborder Miliolina, and 0.7% to the suborder Textulariina. The dominant species are *Asterigerinata mamilla* (Williamson, 1858) (10.6%), *Miliolinella subrotunda* (Montagu, 1803) (8.1%), *Neoconorbina terquemi* (Rzehak, 1888) (8.1%), *Haynesina germanica* (Ehrenberg, 1840) (8.1%), *Bulimina aculeata* d'Orbigny, 1826 (7.1%) and *Bolivina spathulata* (Williamson, 1858) (7.1%) (Fig. 5.63A). In the interval from 1 to 3 cm, 37 foraminifera species were identified, of which 65.34% belong to the suborder Rotaliina, 33.07% to the suborder Miliolina, and 1.59% to the suborder Textulariina. The dominant species in this interval are *Haynesina germanica* (Ehrenberg, 1840) (12.7%), *Asterigerinata mamilla* (Williamson, 1858) (12%), *Miliolinella subrotunda* (Montagu, 1803) (10%), *Bulimina aculeata* d'Orbigny, 1826 (7.6%), *Porosononion subgranosus* (Egger, 1857) (7.2%), *Quinqueloculina schlumbergeri* (Wiesner, 1923) (6.8%) and *Elphidium translucens* Natland, 1938 (5.6%) (Fig. 5.63A).

The microfossil foraminifera analysis was made on 17 samples from the sediment core PROK-3 (Fig. 5.64). Throughout the core, a total of 99 foraminifera species were determined from 47 different genera. The suborder Rotaliina is characterized by the 48 foraminifera species, the suborder Miliolina by 35, and in the suborder Textulariina 6 foraminifera species are identified (Fig. 5.64B). The list of genera and species of foraminifera is included in Appendix 4, while selected specimens of representative foraminifera were photographed using SEM microscope and are presented in Plate 1 and Plate 2.

In the lithological unit LU1 of the core PROK-3, two sediment samples were analyzed for foraminifera (527–537 cm and 521–522 cm). In the sediment sample PROK-3 527–537 cm,

a total of 12 foraminifera species were determined. The most abundant are the species that belong to the suborder Rotaliina (89.9%), whereas the suborder Miliolina is present with 10.1%. The most dominant species in the sediment sample is *Ammonia tepida* (Cushman, 1926) (73.58%) (Fig. 5.64A). In the sediment sample PROK-3 521–522 cm, 18 foraminifera species were determined, of which 92.7% belong to the suborder Rotaliina and 7.3% to the suborder Miliolina. The most dominant species are *Ammonia tepida* (Cushman, 1926) (59.32%) and *Haynesina* sp. sensu Cimerman and Langer (1991) (11.30%) (Fig. 5.64A).

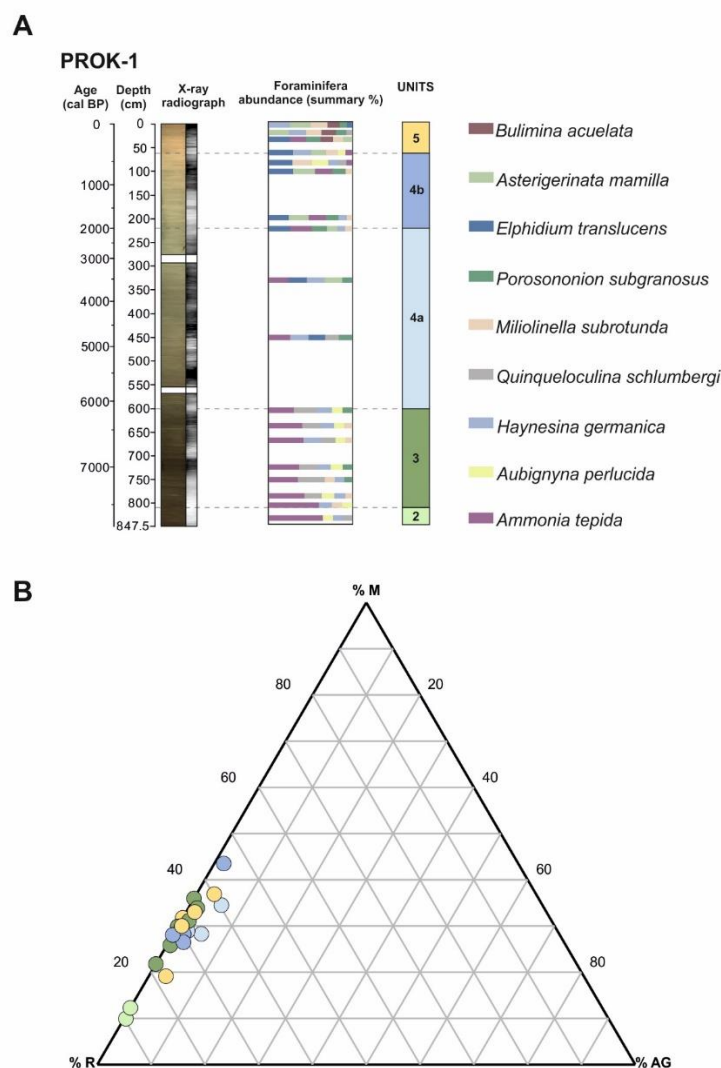


Figure 5.63 A. A summary of the most abundant foraminifera species (>4%) and lithological units (LU2= light green, LU3= dark green, LU4a= light blue, LU4b= dark blue, LU5= yellow) in the sediment core PROK-1 are shown. B. Ternary diagram showing percent abundances of wall structural types of foraminifera (miliolid (%M), rotalid (%R) and agglutinated (&AG) foraminifera) detected in lithological units from sediment core PROK-1.

In LU2 of the core PROK-3, seven sediment samples were analyzed (512–513 cm, 502–503 cm, 496–497 cm, 482–483 cm, 433–434 cm, 418–420 cm, 404–405 cm). In the sediment sample PROK-3 512–513, a total of 22 foraminifera species were identified, of which 93.3% belong to the suborder Rotaliina, 6.3% to the suborder Miliolina and 0.4% to the suborder Textulariina. The most dominant species are *Ammonia tepida* (Cushman, 1926) (62.30%) and *Haynesina* sp. sensu Cimerman and Langer (1991) (13.89%) (Fig. 5.64A). A total of 31 foraminifera species were identified in the sediment sample PROK-3 502–503. Out of the total number of identified species, 89.4% belong to the suborder Rotaliina, 8.9% to the suborder Miliolina and 1.7% to the suborder Textulariina. The dominant species in this interval are *Ammonia tepida* (Cushman, 1926) (51.19%) and *Haynesina* sp. sensu Cimerman and Langer (1991) (12.97%) (Fig. 5.64A). The sediment sample PROK-3 496–497 is characterized by 21 identified foraminifera species. 98.1% of all species belong to the suborder Rotaliina and 1.9% to the suborder Miliolina. The dominant species in this sample are *Ammonia tepida* (Cushman, 1926) (58.70%) and *Aubignyna perlucida* (Heron-Allen and Earland, 1913) (11.49%) (Fig. 5.64A). In the sediment sample 482–483, a total of 21 foraminifera species were determined, of which 92.6% belong to the suborder Rotaliina and 7.4% to the suborder Miliolina. *Ammonia tepida* (Cushman, 1926) (56.35%) is the most dominant species in this sample, while the share of the rest species are <10% (Fig. 5.64A). The sediment sample PROK-3 433–434 is characterized by a total of 23 foraminifera species, of which 92.3% belong to the suborder Rotaliina, 7.7% to the suborder Miliolina. *Ammonia tepida* (Cushman, 1926) (53.23%) and *Haynesina* sp. sensu Cimerman and Langer (1991) (10.65%) are the most dominant species in this interval (Fig. 5.64A). A total of 17 foraminifera species were identified in the sediment sample PROK-3 418–420. 94.7% of identified species belong to the suborder Rotaliina, 5.3% to the suborder Miliolina. The most dominant species in this sample are *Ammonia tepida* (Cushman, 1926) (58.65%) and *Haynesina* sp. sensu Cimerman and Langer (1991) (19.17%) (Fig. 5.64). In the sediment sample 404–405, a total of 29 foraminifera species were determined. Most of the species belong to the suborder Rotaliina (81.9%), while 18.1% of species belong to the suborder Miliolina. The most dominant species in this sediment sample are *Ammonia tepida* (Cushman, 1926) (42.47%) and *Haynesina* sp. sensu Cimerman and Langer (1991) (15.44%) (Fig. 5.64A).

In LU3 of the core PROK-3, three sediment samples were analyzed for foraminifera assemblages (372–373 cm, 351–353 cm and 293–294 cm). In the sediment sample PROK-3 372–373, a total of 30 foraminifera species were identified, of which 76% belong to the suborder Rotaliina, 23.7% to the suborder Miliolina and 0.3% to the suborder Textulariina. The most dominant species in this interval is *Ammonia tepida* (Cushman, 1926) (35.11%) (Fig. 5.64A). A total of 30 foraminifera species were determined in the sample PROK-3 351–353. Most of the identified species belong to the suborder Rotaliina (71.4%), 26.2% to the suborder Miliolina and 2.4% to the suborder Textulariina. The most dominant species in this sample are *Haynesina* sp. sensu Cimerman and Langer (1991) (18.67%) and *Ammonia tepida* (Cushman, 1926) (16.27%) (Fig. 5.64A). In the sediment sample PROK-3 293–294, a total of 31 foraminifera species were identified, of which 64.3% belong to the suborder Rotaliina, 26.8% to the suborder Miliolina and 8.9% to the suborder Textulariina. In this sample the most dominant species are *Haynesina* sp.1 sensu Cimerman i Langer (1991) (13.69%), *Ammonia tepida* (Cushman, 1926) (12.10%) and *Elphidium translucens* Natland, 1938 (10.19%) (Fig. 5.64A).

In the LU4a of the core PROK-3, two samples, in the intervals from 253 to 254 cm and from 178 to 179 cm, were analyzed for foraminifera assemblages. In the sediment sample PROK-3 253–254, a total of 28 foraminifera species were identified, of which 62.7% belong to the suborder Rotaliina, 29.1% to the suborder Miliolina and 8.2% to the suborder Textulariina. The most dominant species in this sample are *Haynesina* sp.1 sensu Cimerman i Langer (1991) (14.18%), *Elphidium translucens* Natland, 1938 (10.07%) and *Miliolinella subrotunda* (Montagu, 1803) (10.07%) (Fig. 5.64A). A total of 33 foraminifera species were identified in the sediment sample PROK-3 178–179. Out of all determined species, 65.1% belong to the suborder Rotaliina, 28% to the suborder Miliolina and 6.8% to the suborder Textulariina. The dominant species in this interval is *Haynesina* sp.1 sensu Cimerman i Langer (1991) (14.39%) (Fig. 5.64A).

One sample, in the interval from 93 to 94 cm, was analyzed in LU4b of the core PROK-3 for the foraminifera assemblages. In this sample 46 foraminifera species were identified, of which 74.3% belong to the suborder Rotaliina, 21.5% to the suborder Miliolina and 4.2% to

the suborder Textulariina. The most dominant species in this sample is *Elphidium translucens* Natland, 1938 (15.85%) (Fig. 5.64A).

In LU5 of the core PROK-3, two samples were analyzed in intervals from 52 to 54 cm and from 7 to 9 cm. In the sediment sample PROK-3 52–54, a total of 27 foraminifera species were identified with the dominance of species that belong to the suborder Rotaliina (75.6%), while 23.1% of species belong to the suborder Miliolina and 1.3% to the suborder Textulariina. The most dominant species in this interval are *Haynesina* sp.1 sensu Cimerman i Langer (1991) (24.10%) and *Elphidium translucens* Natland, 1938 (13.68%). A total of 31 foraminifera species were identified in this interval, of which 75.4% belong to the suborder Rotaliina, 21.7% to the suborder Miliolina and 2.9% to the suborder Textulariina. The most dominant species in this sample are *Haynesina* sp.1 sensu Cimerman i Langer (1991) (15.16%), *Bulimina aculeata* d'Orbigny, 1826 (13.72%) and *Elphidium translucens* Natland, 1938 (10.83%) (Fig. 5.64A).

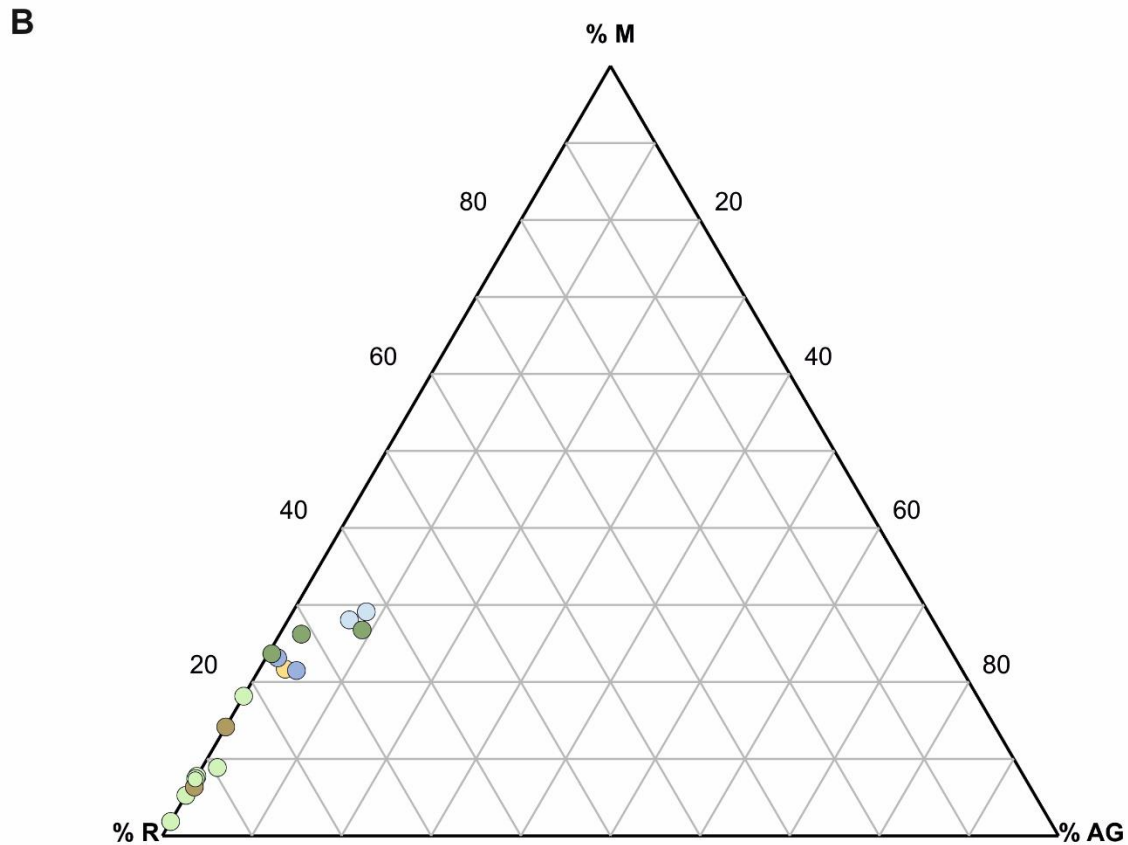
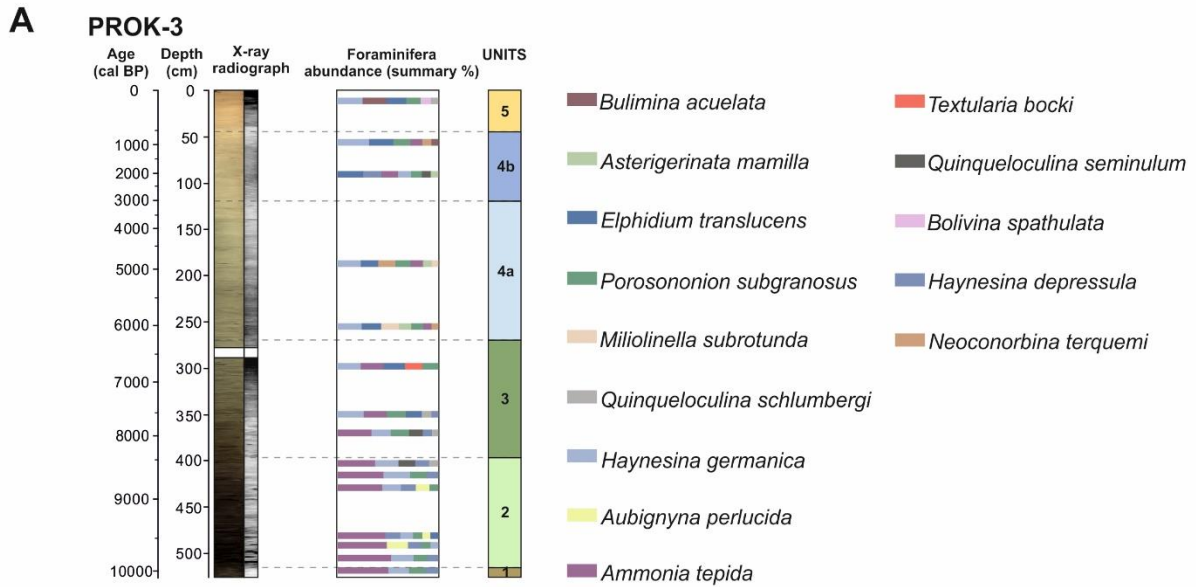


Figure 5.64 A. A summary of the most abundant foraminifera species (>4%) and lithological units (LU1= brown, LU2= light green, LU3= dark green, LU4a= light blue, LU4b= dark blue, LU5= yellow) in the sediment core PROK-3 are shown. B. Ternary diagram showing percent abundances of wall structural types of foraminifera (miliolid (%M), rotalid (%R) and agglutinated (%AG) foraminifera) detected in lithological units from sediment core PROK-3.

In the sediment core ZLA-2, 8 sediment samples (51–52 cm, 71–72 cm, 101–102 cm, 151–152 cm, 201–202 cm, 221–223 cm, 226–227 cm, 281–282 cm) were analyzed for the content of the ostracod assemblage. In the analyzed sediment samples freshwater, brackish, and marine ostracod species were identified: *Candona* sp., *Candona angulata* Müller, *Candona neglecta* Sars, *Prionocypris zenkeri* (Chyzer & Toth), *Ilyocypris* cf. *bradyi* Sars, *Ilyocypris* sp., *Cyclocypris* sp., *Pseudocandona* sp., *Potamocypris* sp., *Schellencandona triquetra* (Klie), *Herpetocypris* sp., *Cypria* sp., *Mixtacandona* sp., *Cyprideis torosa* (Jones), *Leptocythere* cf. *rara* (Müller), *Carinocythereis carinata* (Rooemer), *Aurila punctata* (Münster), *Aurila* sp., *Cushmanidea turbida* (Müller), *Loxoconcha* sp., *Pterygocythereis ceratoptera* (Bosquet), *Cytherella alvearium* Bonaduce, Ciampo & Masoli, *Callistocythere* cf. *adriatica* Masoli, *Hiltermannicythere turbida* (Müller), *Xestoleberis* cf. *communis* Müller, *Cytheroptheron* sp., *Parakrithe* sp., *Semicytherura* sp., *Cytheromorpha* cf. *fuscata* Brady, *Loxoconcha exagona* Bonaduce, Ciampo & Masoli, *Loxoconcha* cf. *tumida* Brady. The juvenile species were not determined in the samples. The most abundant and preserved ostracod fauna was identified in the sample ZLA-2 151–152, while in the last three samples at the bottom of the core, poor ostracod assemblage was identified. In the remaining samples, the ostracods are numerous and well-preserved. In most of the samples, mixed marine/brackish and freshwater microfauna was determined. In the sediment sample ZLA-2 281–282, freshwater and brackish ostracod species were identified. The freshwater ostracod species are *Prionocypris zenkeri*, *Candona neglecta* Sars, *Pseudocandona?* sp., *Potamocypris* sp., while the identified brackish species is *Cyprideis torosa*. Plant fragments, gastropod debris and *Elpidium* foraminifera species were additionally determined.

In the sediment sample ZLA-2 226–227, freshwater ostracod assemblage with rare marine and brackish forms were identified. The determined freshwater ostracod species are *Prionocypris zenkeri*, *Mixtacandona* sp., *Candona* sp., and *Potamocypris* sp., while the marine/brackish species are *Cyprideis torosa*, *Cytheromorpha* cf. *fuscata*, *Leptocythere* sp. *Semicytherura* sp. Additionally, in this sample, numerous plant fragments were found, as well as a few benthic foraminifera (*Ammonia* sp.).

In the sample ZLA-2 221–222, a few ostracod individuals were found, of which the most abundant are freshwater and a few marine/brackish ostracod species. The identified freshwater species are *Prionocypris zenkeri*, *Schellencandona triquetra*, *Candona* cf. *candida*, *Candona* sp., *Pseudocandona* sp., and *Potamocypris* sp., while the marine/brackish species are *Leptocythere* cf. *ramosa* and *Cyprideis torosa*. Furthermore, carbonized plant fragments and seeds were found, as well as *Chara* oogonium and a few damaged shallow-water benthic foraminifera.

In the sediment sample ZLA-2 201–202, mixed shallow marine and freshwater fauna was determined. The identified marine/brackish ostracod species are *Loxoconcha* cf. *stellifera*, *Carinocythereis antiquata*, *Cyprideis torosa*, and *Cytheromorpha* cf. *fuscata*, while the freshwater species are *Prionocypris zenkeri*, *Candona angulata*, *Ilyocypris* sp., and *Pseudocandona* sp. Algae talus, gastropods and bivalve shells, benthic foraminiferas (*Ammonia* sp. and *Elphidium* sp.), and pyrite aggregates were found as well.

The sediment sample ZLA-2 151–152 was the most fossiliferous in the whole sediment core. Mixed freshwater/brackish and shallow marine ostracod fauna were determined with the most diverse freshwater species in all the analyzed sediment samples. The identified freshwater species are *Prionocypris zenkeri*, *Candona angulata*, *Potamocypris* sp., *Ilyocypris* sp., *Herpetocypris* sp., *Cycloocypris* sp., and *Cypria* sp., while the marine/brackish species are *Loxoconcha* cf. *stellifera*, *Cushmanidea turbida*, and *Cyprideis torosa*. The most dominant ostracod species is *Prionocypris zenkeri* which represents autohtoneous taphocenosis due to the identification of all juvenile stadiums and adult individuals. Additionally in this sample benthic foraminiferas, *Chara* oogonium, gastropod, bivalved, and plant fragments were found.

In the sediment sample ZLA-2 101–102, mixed shallow marine, brackish, and freshwater ostracod fauna were determined. The identified marine species are as follows: *Carinocythereis carinata*, *Aurila punctata*, *Cushmanidea turbida*, *Loxoconcha exagona*, *Loxoconcha* cf. *tumida*, *Hiltermannicythere turbida*, *Xestoleberis* cf. *communis*, *Calistocythere* sp., *Cytherella* sp., *Aurila* sp., *Semicytherura* sp. The determined brackish species is *Cyprideis torosa*, and the freshwater species are *Candona angulata*, *Prionocypris zenkeri*, and *Cypria* sp.

Furthermore, gastropod shell debris and bivalve shells, benthic foraminiferas, bryozoans, Chara oogoniums, carbonized plant fragments, and pyrite aggregates were found.

In the sediment sample ZLA-2 71–72, mixed shallow marine, brackish, and freshwater ostracod fauna were determined. The identified marine species are *Pontocythere turbida*, *Loxoconcha* sp., *Xestoleberis* cf. *communis*, *Loxoconcha exagona*, *Loxoconcha* cf. *tumida* and *Aurila punctata*, while the brackish species is *Cyprideis torosa* (the most abundant species with juvenile and adult forms) and the freshwater species are *Candona angulata* and *Prionocypris zenkeri*. Additionally, in this sample, gastropods, bivalves, benthic foraminiferas, and Chara oogoniums were found.

In the topmost analyzed sample (ZLA-2 51–52), the marine and freshwater/brackish ostracod fauna was determined. The most dominant ostracod species are marine and the identified species are *Leptocythere* cf. *rara*, *Carinocythereis carinata*, *Cushmanidea turbida*, *Pterygocythereis ceratoptera*, *Cytherella alvearium*, *Callistocythere* cf. *adriatica*, *Hiltermannicythere turbida*, *Xestoleberis* cf. *communis*, *Cytheroptheron* sp., *Loxoconcha* sp., *Parakrithe* sp., *Aurila* sp. The identified brackish species is *Cyprideis torosa* (with numerous juvenile forms), and the freshwater species are *Candona angulata* and *Prionocypris zenkeri*.

6. DISCUSSION

In the discussion chapter, the results from the previous chapter will be compiled and divided into several subchapters to reconstruct the sedimentary palaeoenvironments of the studied areas since the Last Glacial. The acoustic data (comprising MBES, SSS, and seismic profiles) coupled with the lithostratigraphy will be discussed to interpret the morphology and origin of the submarine landforms within studied areas and to reconstruct the palaeoenvironments of the Krka River mouth area since the Last Glacial. The sedimentary processes that influenced the palaeoenvironments will be emphasized. The obtained results will be compared with relative sea-level changes during that period in the Adriatic Sea and with the eustatic sea-level data.

6.1 Acoustic and core data interpretation of the Pleistocene Krka River incised valley and deltaic deposits

The late Quaternary depositional history of the Krka River incised valley and the shelf area can be reconstructed based on the seismic facies, lithology, and radiocarbon ages concerning sea-level and climate changes, hydrodynamic conditions, sediment supply, and bottom morphology.

Multibeam, backscatter, and seismic data reveal a generally simple shelf area characterized by a patchy geomorphological pattern (Figs. 5. 9–5.11). The lateral variations in geomorphological features are likely due to the presence of materials with different erodibility, as well as the palaeogeographical configuration formed during the postglacial flooding. The shelf area appears predominantly rocky, with observed incised channels and seamounts, and is covered by a generally thin layer of sediments (Figs. 5. 11, 5.25–5.27).

The application of geophysical methods and the examination of legacy and shallow seismic profiles of the Pleistocene palaeo-estuary of the Krka River (5.23–5.28), as well as shallow, high-resolution seismic data of the present-day estuary (Figs. 5.13–5.21), have indicated the existence of an incised Krka River valley into the substrate (most likely limestone). First, the seismic interpretation of deep and shallow profiles in the shelf area is

discussed, followed by the area of incised canyon between the mainland and the island of Zlarin and, finally, the area of the present-day estuary.

The legacy seismic profiles (Fig. 6.1) were provided by the Croatian Hydrocarbon Agency (CHA) and were used to interpret the morphology and sediment thickness above the „Top of carbonate platform (TCP)“ (Kamenski and Korbar, 2023; and references within). The interpreted profiles reveal the existence of a tectonically conditioned channel of the Krka River and a Pleistocene deltaic plain developed on the shallow shelf area with a maximum sediment thickness of approximately 100 meters, overlying the top of carbonate in depressions (Figs. 6.2–6.5). The shallow seismic data provided insight into the uppermost approximately 30 meters of the sedimentary sequence.

Currently, the timing of the Krka River incised valley formation can only be estimated by examining depositional units eroded by fluvial incision and the age of the sediments that infilled the channel at the base of the valley. The Krka River valley was for the last time incised into the carbonate bedrock most likely during the Last Glacial Period but probably started even during the Messinian salinity crisis (Miocene) due to eustatic sea-level changes. During this period, sea level in the Mediterranean dropped by approximately 1500 meters compared to the Atlantic (Mocochain et al., 2009). In addition, the Messinian crisis reflector was identified on deep seismic profiles by Vaniček (2013) and Volpi et al. (2015).

Based on deep seismic profiles, it was possible to interpret the seabed surface and the top of the carbonate rocks (Durn, 2020). The seabed is represented by the first visible seismic arrival on the seismic lines, while the top carbonate horizon (a discordance) represents the top of the carbonate sequence (platform; Kamenski and Korbar, 2023). The exposed surface of carbonates forms the base of younger sediments (Figs. 6.2–6.5). The top carbonate is most likely composed of carbonate deposits from the Cretaceous and Eocene periods (Durn, 2020).

It can be observed that the carbonate bedrock is located very close to the seabed surface, with a very thin layer of younger sediments deposited on top of carbonates, up to a maximum of 100 meters in depressions, and laterally thinning out, leaving the top of carbonates as islands, submerged islands or bedrock on the seafloor. Therefore, a shelf area

on the eastern Adriatic coast can be interpreted as a sediment-starved continental shelf (low sedimentation).

Sediment supply is limited due to the lack of other river systems in the study area. Consequently, the nature of stacked shoreline progradation sequences that form during low sea levels most probably depends on the duration of the lowstand. Erosion and/or lack of sediment deposition were most likely intensified in areas where high morphological features further limited available accommodation space. That led to local reductions in sediment thickness or the non-preservation of regressive sequences.

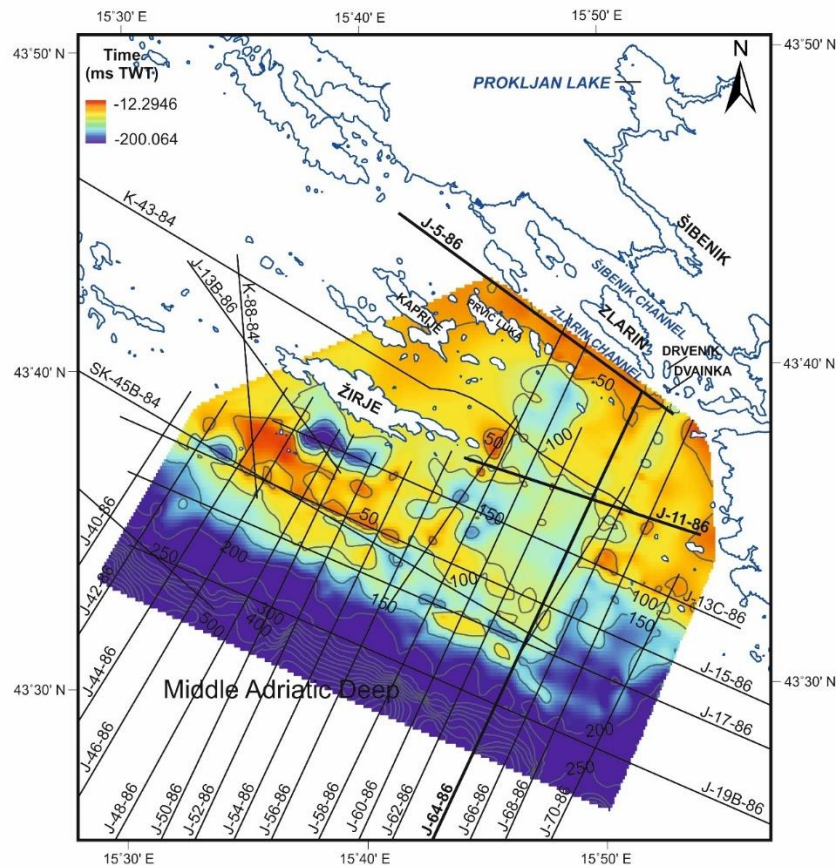


Figure 6.1 Sediment thickness map (ms TWT) (above the top of carbonate bedrock-interpreted by T. Durn from the Croatian Hydrocarbon Agency in frame of the QMAD project in 2020). The map shows the locations of all deep seismic profiles recorded in this area, with profiles interpreted in this study, highlighted in bold.

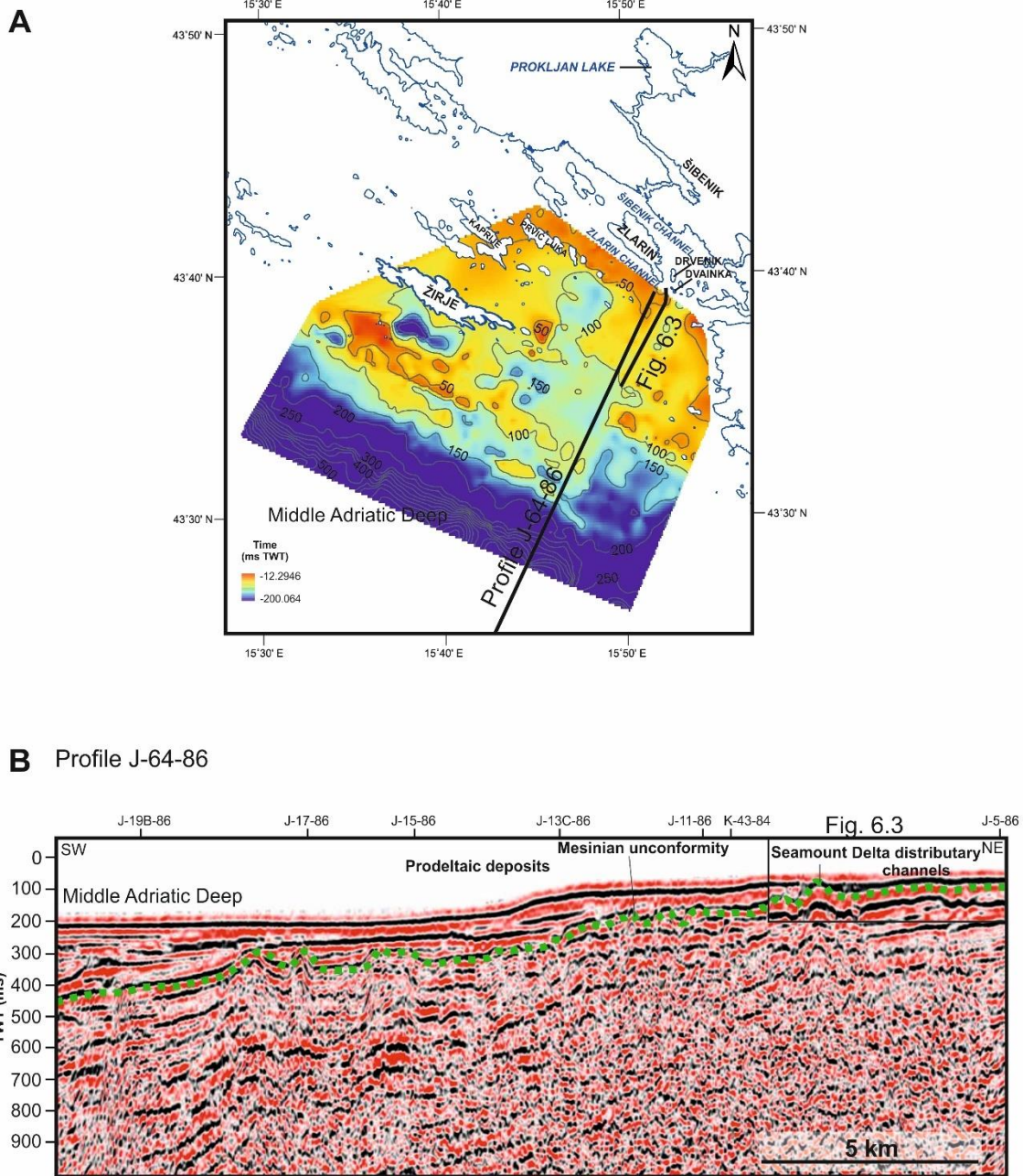


Figure 6.2 A Sediment thickness map overlying the top of carbonates (ms TWTT) with interpreted seismic profiles indicated. B Interpreted seismic profile J-64-86 (Croatian Hydrocarbon Agency).

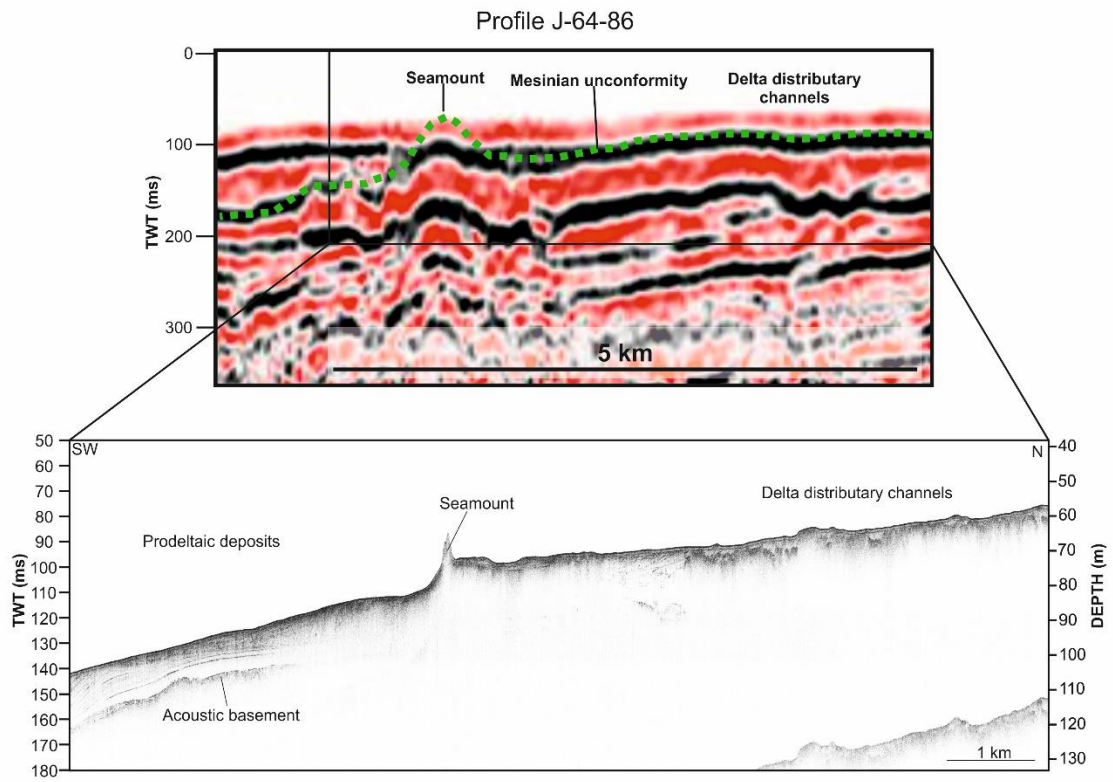
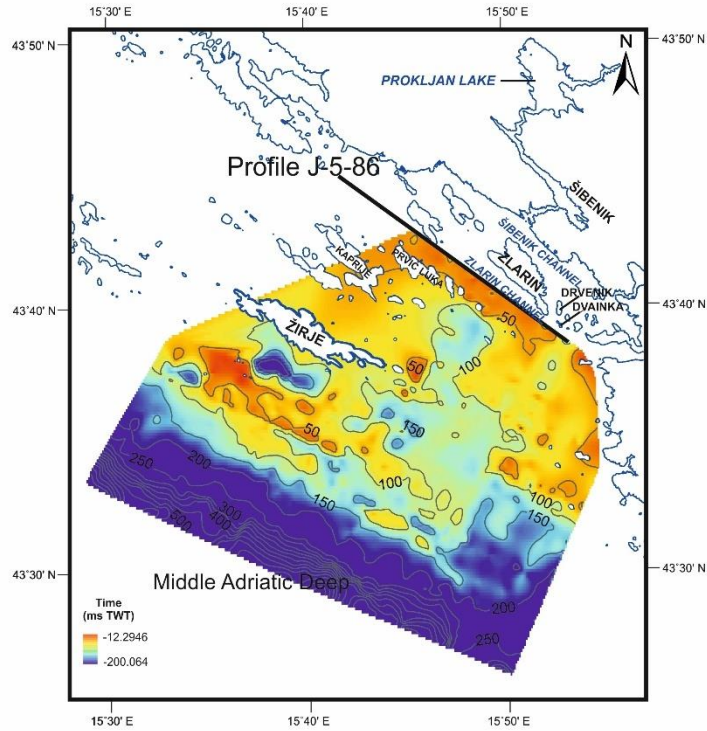


Figure 6.3 Enlarged section of the profile J-64-86 from Fig 6.2 and shallow seismic profile.

A

Profile J-5-86

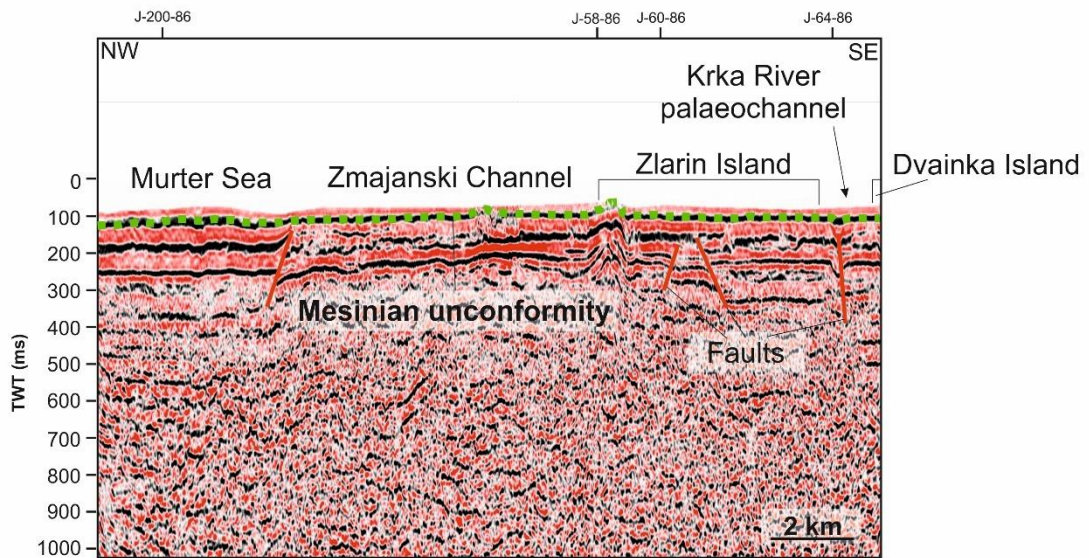
B

Figure 6.4 Sediment thickness map overlying the top of carbonates (ms TWT) with the location of interpreted seismic profile J-5-86 (B) indicated.

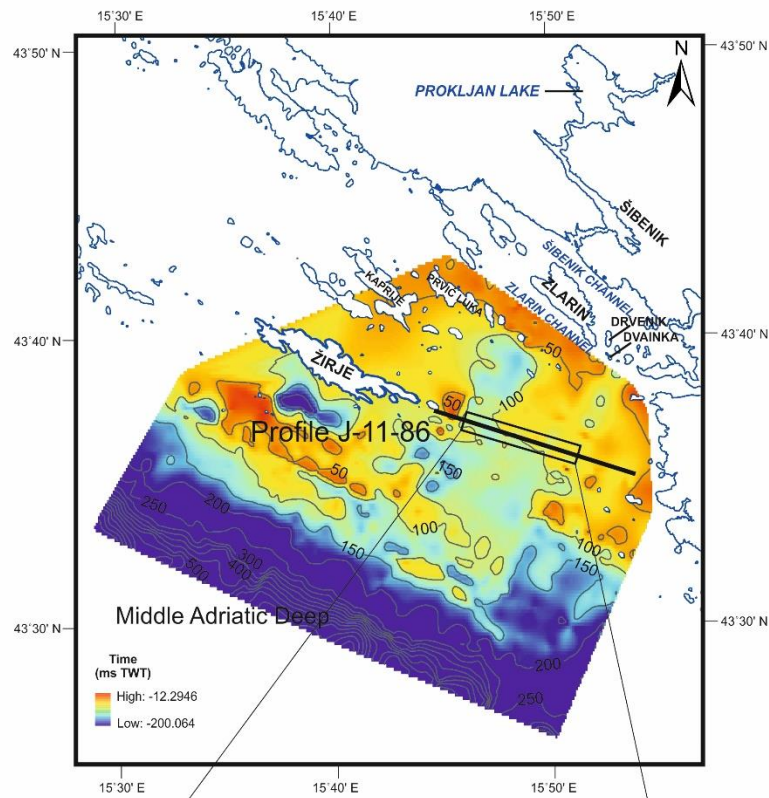
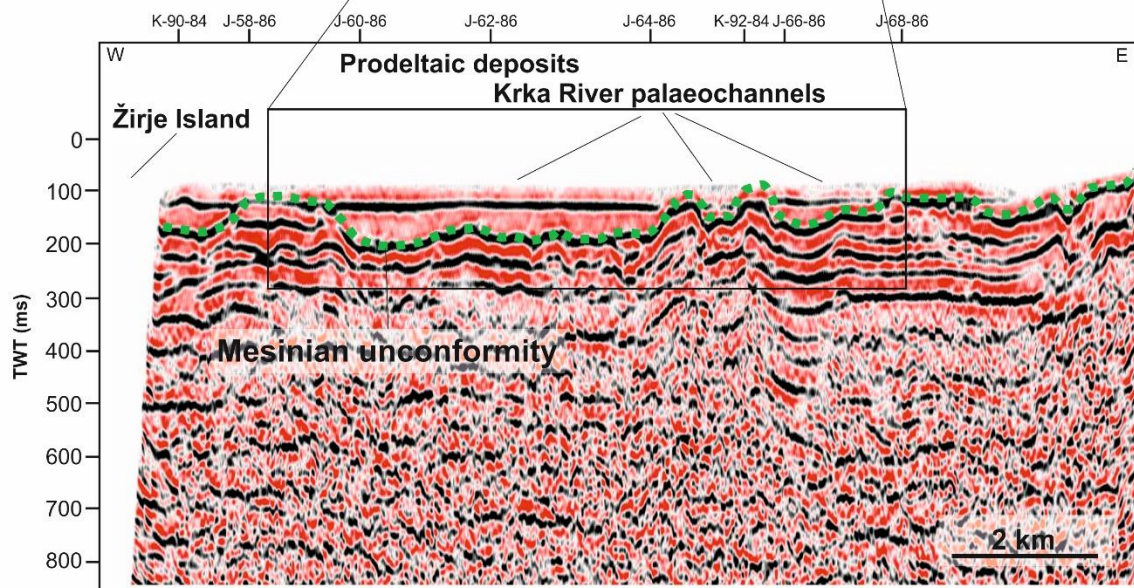
A**B** Profile J-11-86

Figure 6.5 Sediment thickness map overlying the top of carbonates (ms TWT) with the location of interpreted seismic profile J-11-86 (B) indicated.

Pleistocene deltaic deposits

Acoustic basement

Seismic facies AB is the oldest in the study area and presents the acoustic basement (Figs. 5.23–5.28). Regarding its overall stratigraphic position, the acoustic basement could correlate with the carbonate bedrock in the incised part of the valley (between the mainland and the island of Zlarin) and observed seamounts and rocky outcrops, or perhaps older Pleistocene deposits in the shelf area (the opaque character of the basement may be due to its relatively high degree of compaction and/or to the presence of coarse-grained deposits). Its surface strongly truncates the acoustic basement and may have been produced by subaerial erosion when the shelf was exposed during the late Pleistocene sea-level fall of MIS 2 (a sequence boundary, according to Mitchum et al., 1977). This surface can be tracked continuously until it reaches the shelf edge.

Incised channel fill and delta top distributary channels

Seismic facies F (Figs. 5.22 and 5.23) and CH (Figs. 5.25–5.27) can be associated with incised channel fill. The seismic facies F is deposited above the bedrock between the mainland and the island of Zlarin and correlate well with the acoustic characteristics of SU1 observed in the recent Krka River estuary (described below). This seismic facies could be interpreted as fluvial or brackish sediments deposited during periods of low sea level or post-LGM transgression.

The seismic facies CH exhibits a base characterized by highly irregular surfaces with incisions, upon which the channel fill is deposited. This facies resemble the cut-and-fill features observed by other researchers (e.g., Trincardi et al., 1994; Correggiari et al., 2005; Dyer et al., 2021), suggesting they formed during a rapid delta construction phase. The channels are interpreted as part of the lower delta plain, advancing over and cutting into the acoustic basement. The channel divides into two around the seamount observed in Figures 5.9 and 5.25 with deposition of clinoforms. The timing of the deposition of SF CH is uncertain, but it may simply represent the infilling during the lowstand period and/or post-glacial transgression.

In the incised channel near the southern part of the island of Zlarin (Fig. 4.2), a sediment core ZLA-2 was recovered, which consisted of freshwater to marine coarse silty sediment (Fig. 5.42; Table 5.19). The core was divided into three lithological units based on physical, geochemical, and micropalaeontological data (Fig. 5.30). The first lithological unit (LU2-1, the bottom part of the core) is characterized by heterogeneous sandy sediment (Fig. 5.42) with discontinuous laminae and generally uniform MS values (goes up to 13.9×10^{-5} SI; Fig. 5.36). A slightly increasing trend of insoluble residue could indicate increasing terrigenous components, including terrigenous organic matter (increase in TOC values and decrease in TIC values; Fig. 5.61). The ostracod analysis showed poor diversity of ostracod assemblages in the LU2-1, mainly freshwater ostracods associated with shallow and rapid streams connected with underground habitats. Additionally, a few brackish and marine ostracods were determined, as well as Charophyta oogoniums, many plant fragments, and some damaged benthic foraminifera (*Ammonia* sp.), suggesting a dominantly freshwater (fluvial) environment with the introduction of some marine fauna into the environment. Therefore, it can be concluded that the deposition of this unit occurred during the post-glacial transgression. However, the timing of deposition could only be assumed due to the lack of dating material in this unit. The overlying unit LU2-2 is characterized by homogeneous brown to dark brown sediment of dominantly muddy-sized particles (Figs. 5.30 and 5.42). An increasing trend of TOC and insoluble residue values are present for the first part of this unit, and they start to decrease to the top of LU2-2 (Fig. 5.61), which suggests a slight increase in terrigenous component and organic matter input, and then it lowers to the top of the unit. LU2-2 is the most fossiliferous unit characterized by mixed ostracod assemblages, i.e., present with shallow marine, brackish, and freshwater fauna. From the bottom of this unit up to 150 cm, a higher amount of marine and brackish species suggests a freshwater environment associated with streams, springs, and shallow lake environments rich in algae and aquatic plants (possibly floodplain), under the occasional short-term influence of the sea. Furthermore, from the 100 cm of the core up to the LU2-3, the marine fauna (ostracods and mollusks) is becoming dominant, but still with the presence of brackish and freshwater ostracods and Charophyta oogoniums. The ostracod assemblages suggest development of a marine to brackish restricted coastal environment, with the dominance of the *Cyprideis torosa* species and the introduction of freshwater fauna by flowing streams. The appearance of the nodules on the surface of *Cyprideis torosa* indicates a possible decrease in water

salinity. At 130 cm of the core, a plant fragment was dated to approximately 13,170–13,100 cal yr BP. Therefore, the results most probably imply the development of an estuarine environment during this phase, which could correlate with the ZLA-1 sediments described below. The uppermost part of the core (LU2-3) is characterized by homogeneous dark grey to brown sediment (Fig. 5.30). The sand size particles are increasing in this unit, while the topmost 20 cm of the core is built of gravelly sediment (Fig. 5.42; Table 5.19). The coarse-grained sediment could be related to the recent sediment input from the land since this core was located near the coast of the island of Zlarin. A decrease in TOC values and insoluble residue suggest a lowering in terrigenous components and organic matter, while an increase in TIC values is related to a rise in carbonate component (Fig. 5.62). In LU2-3, marine and freshwater-to-brackish ostracod fauna were determined, as well as benthic and a low number of planktonic foraminifera, marine mollusks, and Charophyta oogoniums. The detected fauna support the existence of marine in situ fauna, while the freshwater assemblages could be redeposited. Similar facies was observed in the sediment core ZLA-1 (described below).

Deltaic deposits

The seismic facies CL present a highly variable series of deposits consisting of sigmoidal to oblique-sigmoidal reflectors corresponding to the distal deltaic environment (Tesson et al., 2000; Perov and Bhattacharya, 2011; Dyer et al., 2021) or clinofolds. The higher amplitude sigmoidal clinofolds might reflect sandier deposits, while the lower amplitude and frequency clinofolds could indicate muddy deposits (Perov and Bhattacharya, 2011). However, the amplitude and frequency of these reflections depend on the frequency content of the high-resolution seismic profiler. The lowermost clinofolds deposited above the acoustic basement have a weakly defined continuous parallel to subparallel reflections with a transitional boundary (erosional surface formed during subaerial exposure, which becomes conformable seaward), with the overlying high amplitude reflections (Fig. 5.28). The shape of these clinofolds suggests their formation at the distal muddy prodelta of the shelf-margin deltas. The lack of steep clinofolds suggests a largely aggradational component.

The overlying clinofold reflectors recognizable between approximately 120 and 140 m water depth are steeper and of higher amplitude, suggesting progradation of sediment

during sea-level lowstand (Fig. 5.28). Within these facies, a clinoform inflection point at a depth of 130 m (LGM lowstand) can be observed and most probably corresponds to the wave base (Patrino and Helland-Hansen, 2018), indicating a palaeo-shoreline trajectory. Basinward, this progradational facies is truncated by chaotic wavy reflections suggesting deformational structures and soft sediment deformations. These deformations might be related to sediment instability due to rapidly deposited sediments contributing to slumping at the delta front, or the other possible explanations are the storms or earthquakes (Perov and Bhattacharya, 2011). In addition, deformations might be associated with the sediment drifts, i.e., because of recent erosion of sediment, transport, and accumulation basinward, which occurred by the sea bottom currents, since in this area, the seabed currents are intense (Marini et al., 2016).

Moreover, the overlying medium amplitude sigmoid clinoforms of the retrograding pattern are also deformed, with rounded slopes at depths between 140 and 150 m, supporting the explanation of seabed erosion by currents. At a depth of 160 m, a possible slump is detected, most probably related to post-LGM slope failure (Fig. 5.28). Due to the retrogradational pattern of the uppermost clinoforms and onlap on the underlying progradational reflectors, this facies suggests post-LGM transgression (Fig. 5.28).

Terrestrial and transgressive deposits

A low amplitude to chaotic seismic facies is present (SF TD; Fig. 5.26 A) at the western flanks (Zlarin and Žirje channels) of the deltaic plain and distributary channels. This facies could point to terrestrial Pleistocene sediments deposited during the period of subaerial conditions. Additionally, a palaeoterrace can be observed at the boundary of this seismic facies, which could be related to a period of sea-level stillstand or slow rise in sea level. The palaeoterrace is present at a depth of approximately 55 mbsl. The sea level was lower by about 50 m at the Younger Dryas stillstand (12,900 to 11,700). Therefore, this palaeoterrace could be related to this period. It can be concluded that during the YD period, most of the shallow shelf and lowstand deposits and channels were drowned with deposition of the thin sand sheet (SF CD), or perhaps sand ridges formed.

In the Krka River incised valley during the transgression, a deposition of seismic facies F/B and E/M occurred (Fig. 5.32). The seismic facies F/B could be interpreted as fluvial to brackish deposits based on its seismic characteristic and the sediment core ZLA-1. The core lithology is generally uniform and is divided into two lithological units (LU1-1 and LU1-2). In comparison to LU1-2, LU1-1 is somewhat sandier and consists of homogeneous sediment with dark organic matter layers (Figs. 5.30 and 5.41), while the overlying unit consists of muddy homogeneous sediment (Fig. 5.30). Three samples were radiocarbon-dated and gave an age reversal but were of Holocene age (Fig. 5.30; Table 5.3). It could suggest sediment reworking due to the intense course of the Krka River since this core was collected in the narrow palaeocanyon of the Krka River. The MS values are uniform in both lithological units, with higher values at the top of the core, indicating recent erosion and terrigenous input from the land (Fig. 5.36). The distribution of TN, TOC, TIC, insoluble residue, and TOC/TN is generally uniform in LU1-1 (Fig. 5.60). Some fluctuations can be observed in LU1-2, with an increase in TN, TOC, insoluble residue, TOC/TN, and a decrease in TIC values up to the 50 cm of the core, suggesting higher terrigenous and organic matter input most likely due to the proximity of the coast to the coring location (Fig. 5.60). Moreover, the TOC/TN ratio is >12 in both units, indicating terrestrially derived organic matter, except for the first 50 cm of the core, which could be related to the dominantly algal organic matter (Fig. 5.60). Based on the core data and the characteristics of the seismic facies, the LU1-1 could be formed in an estuarine environment with a strong fluvial influence. A similar facies to SF F/B was recognized in the recent part of the Krka River estuary. SF F/B overlies the acoustically transparent facies SF F, and its lower and upper boundaries are strong reflectors, probably marking erosional surfaces. Above the SF F/B, a reflection-free seismic facies E/M is deposited. It is the uppermost (the youngest) facies that fills the incised Krka River valley, which could be interpreted as estuarine to marine deposits. It is recovered in the sediment cores ZLA-1 and ZLA-2 and is characterized by silty homogeneous sediments (Figs. 5.30, 5.41, and 5.42). Within this facies, erosional features are observed, suggesting a present Krka River influence or perhaps strong seabed currents.

6.2 Acoustic and core data interpretation of the Krka River estuary

The studied section of the Krka River estuary comprises two distinct morphological regions: a narrow, submerged Krka River estuary canyon and the broader Prokljan Lake. Both areas feature unique geomorphological characteristics, including submerged calcareous tufa barriers and carbonate mounds, typical of the karst landscape. The most notable geomorphological elements in the investigated area are the well-preserved calcareous tufa barriers in the submerged Krka River canyon and Prokljan Lake. These distinctive karst formations, formed by algae and mosses encrusted with carbonate, are abundant in the upstream freshwater part of the Krka River (Frančišković-Bilinski et al., 2004). They function as sediment traps, retaining portions of sediment behind them. Integrating morpho-bathymetric surveys (MBES, BSE, and SSS), acoustic SBP profiling, ground-truthing, and extensive sediment sample analyses successfully enabled the creation of a precise OBIA, interpreted and classified data into reliable maps, which are explained below in the Subchapter 6.3.

By correlating the seismic stratigraphic analysis with sedimentological and radiocarbon data from the upper tract of the Krka River estuary, four seismostratigraphic units were identified above an unconformable palaeorelief surface. Units were deposited after the LGM and reflected major depositional and environmental changes during the Holocene. Furthermore, the depth of each detected calcareous tufa barrier in the Krka River estuary, along with the onset of marine sedimentation, could serve as an indicator of sea-level changes, as these barriers cease to grow once they are submerged.

The acoustic basement

The acoustic facies F0 of seismic unit SU0 are characterized by chaotic noisy reflectors at the top, which gradually transition to reflection-free facies with increasing depth. Although the sediment cores did not reach the acoustic basement, most probably, the basement consists of Cretaceous limestone based on the catchment geology and nearby onshore outcrops (Mamužić, 1975). The palaeorelief surface (p) is identified at the top of the acoustic basement,

indicating the river's erosion/incision phase during the sea-level lowstand (Fig. 5.13 to 5.21). The palaeorelief surface correlates with the erosional surface observed in the shelf area.

Fluvial deposits

SU1 consists of transparent seismic facies and is recognized between the acoustic basement and the SH1 horizon. This unit is thin and not uniformly distributed across the study area; it is only found in the central part of Prokljan Lake and within the palaeochannels of the Krka and Guduča Rivers (Figs. 5. 17–5.21). Its patchy distribution may be due to the partial erosion of sediment, or it could be obscured by multiples or poor penetration of the acoustic signal. Therefore, it can be assumed that SU1 represents fluvial sediments, likely deposited at a lowstand period. However, as this seismic unit was not sampled by the cores, its exact lithology and age can only be hypothesized. Similar seismic facies (SF F) have been identified in the Krka River valley between the mainland and the island of Zlarin, where they were interpreted as fluvial deposits. The upper boundary of SU1 is the SH1 horizon, which varies from an irregular continuous surface to a planar continuous horizon in different areas. SH1 is interpreted as an erosive unconformity surface or the initial transgressive surface, according to Allen and Posamentier (1993). In regions where SU1 is absent, the palaeorelief surface also aligns with the transgressive surface.

Freshwater calcareous tufa deposits and calcareous tufa mounds

SU2 is identified in the canyon of the Krka River estuary and the central and eastern parts of Prokljan Lake (Figs. 5.15–5.21). This unit extends from the basement and rises above the Cretaceous bedrock with steep side slopes. It is characterized by nontransparent or chaotic noisy reflectors (SF2; Fig. 5.12), suggesting the presence of homogeneous sediments or rock. Due to its nontransparent nature, the lower boundary of this unit could not be precisely determined and was only inferred. Based on recent unpublished seismic investigations in Visovac Lake (upstream Krka River) and this geomorphic research in Prokljan Lake (Hasan et al., 2023), this unit is interpreted as a system of submerged freshwater calcareous tufa

barriers. The formation of these barriers enabled the development of lakes between them (Pedley, 1990).

On the western side of the most seaward calcareous tufa barrier, extending into Prokljan Lake, SU2 has a lesser thickness and a circular form (Fig. 5.17C). These features were interpreted as calcareous tufa carbonate mounds (Fig. 5.1), with diameters ranging from 10 to 90 meters and heights between 2 and 5 meters above the lake floor. Many of these mounds, particularly those closer to the most seaward calcareous tufa barrier in Prokljan Lake, have been delineated (Hasan et al., 2023). They likely grew circular due to shallow, stagnant waters and a low-gradient relief. Tufa mounds exhibit the same seismic characteristics as calcareous tufa barriers and can be interpreted as phytoherm “reefs” (freshwater “reefs”) or barrage lake deposits (Pedley, 1990; Ford and Pedley, 1996). Similar structures have been found in Mono Lake (Dunn, 1953) and Lake Van (Cukur et al., 2015), where mound formation is associated with springs (Pentecost, 2005) or tectonics (Cukur et al., 2015). However, no submerged springs were observed in the study area, as mound formation requires pressurized water (Pentecost, 2005). Another possibility is that these features were initially calcareous tufa barriers that were eroded and reshaped during transgression. SU2 was not cored because it was impenetrable with the piston corer.

Fluvio-lacustrine to brackish deposits

SU3 was deposited directly above the basement or SU2 and is bounded at the base by the palaeorelief surface or SH1 or SH2 horizon (Figs. 5.13–5.21). The seismic unit could be interpreted as fluvio-lacustrine deposits. On the eastern side of Prokljan Lake, where the calcareous tufas are present, SU3 has a greater thickness (up to 15 m; Figs. 5.13–5.17), while in the palaeochannel of Guduča River and joint palaeochannel of Krka and Guduča Rivers (Figs. 5.20 and 5.21), the thickness of SU3 is low (less than 5 m). The reason for such sediment distribution is that there are no calcareous tufas in the palaeochannel of the Guduča River, which would have enabled sediment entrapment.

Seismic characteristics and core observations enabled the division of this unit into two subunits: SU3a and SU3b. However, these subunits were not recognized in all seismic profiles;

therefore, in some profiles, only the SU3 unit is indicated. SU3a comprises the extensive part of SU3 and consists of irregular wavy aggradational parallel to subparallel reflectors (F3a; Fig. 5.12). Reflectors are mainly laterally continuous, but in other areas, they show low continuity, indicating a more dynamic sedimentation of heterogeneous deposits. The reflectors are partially intercalated with acoustically semitransparent to nontransparent facies, probably indicating the presence of gas. SU3a was determined only in the lower part of core PROK-3 (LU1; Fig. 6.6). Foraminiferal count in these sediments is very low, with the domination of *Ammonia tepida* (Fig. 6.6), a typical species inhabiting marginal marine environments with high organic content and brackish water conditions (Debenay and Guillou, 2002; Murray, 2006). The low presence of foraminifera could indicate a dominantly fluvial environment with restricted marine influence due to marine ingression through calcareous tufa barriers or perhaps on storm events that could have led to occasional flooding of the barriers. The freshwater conditions are further supported by high detrital components (e.g., MS and $\log(\text{Ti}/\text{Ca})$) and organic matter with high TOC/TN values affected by higher erosional and fluvial activity (Figs. 6.6–6.8). The high-amplitude irregular wavy reflectors of SU3 correspond to the LU1 (Fig. 5.18), providing additional evidence for fluvial deposition.

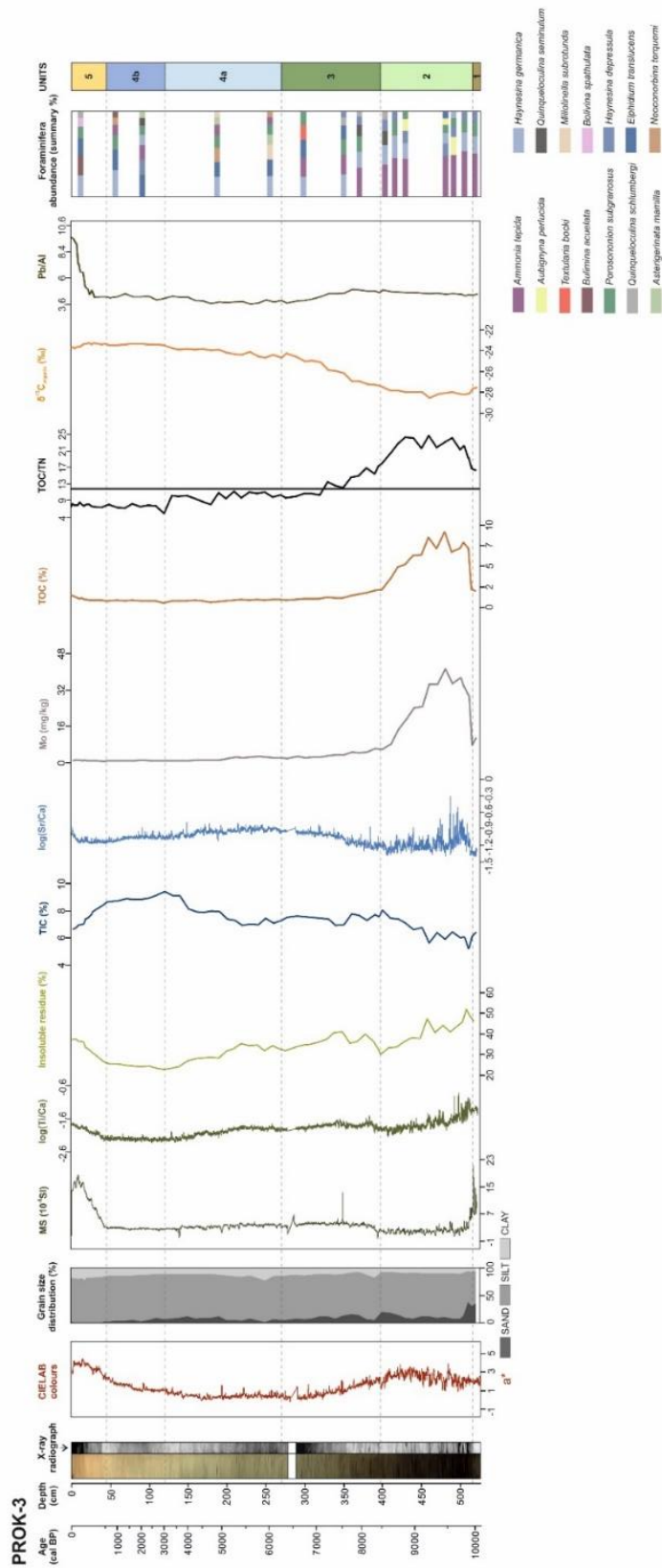


Figure 6.6 The distribution of selected geochemical and sedimentological indicators in sediment core PROK-3.

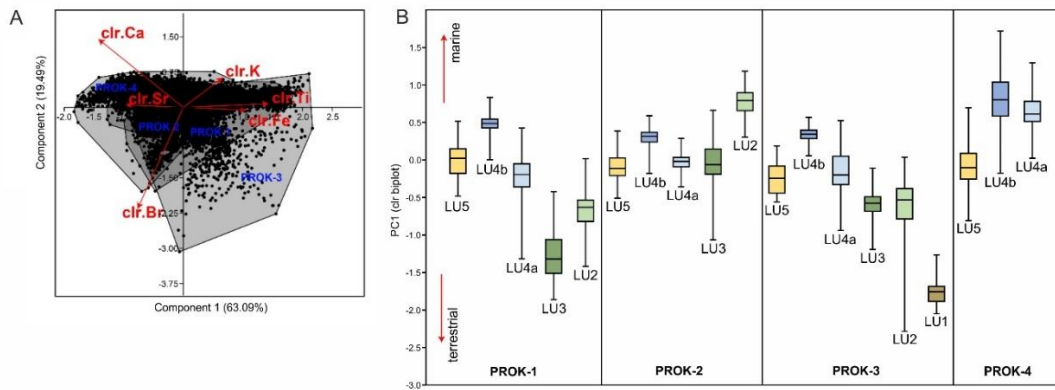


Figure 6.7 Change of terrigenous influence in relation to the core location and chronology. A) Compositional biplot showing that most variation in the data is explained by the first principal component (PC1). Elements associated with terrigenous influence have positive loading on PC1, while those associated with marine influence have negative loadings. Thus, most variation in the data is caused by changes in marine/terrigenous influence. B) Categorized box plot of PC1 for each core and sedimentation unit. The same trend is visible in all cores, except for the LU2 of the core PROK-2, which shows the highest marine influence. This deviation of LU2 can be explained by the large proportion of aragonitic shells in this unit, and therefore higher input of Sr.

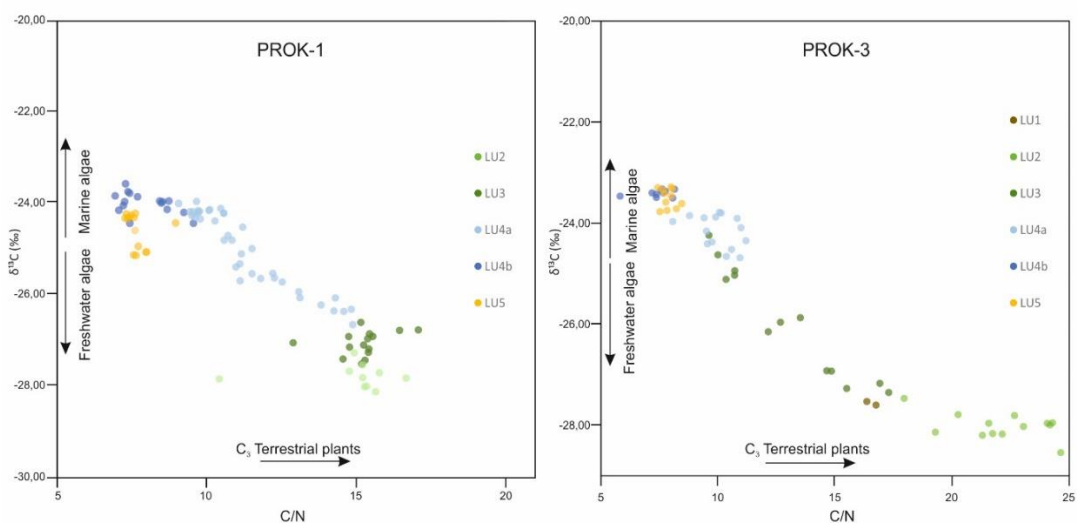


Figure 6.8 Cross-plots of TOC/TN ratio of the organic matter versus $\delta^{13}C_{org}$ of organic carbon from the cores PROK-1 and PROK-3. Typical $\delta^{13}C_{org}$ and TOC/TN ranges for organic inputs to coastal environments are based on Lamb et al. (2006). A transition from dominantly terrestrial to marine organic matter can be clearly distinguished.

The seismic pattern of the SU3b subunit is very similar to that of SU3a but has a lower amplitude (semitransparent; F3b; Fig. 5.12). This subunit is recorded in LU2 of the sediment cores PROK-1 (Fig. 6.9), PROK-2 (Fig. 6.10), and PROK-3 (Fig. 6.6). However, it is somewhat lithologically different due to core locations. PROK-2 is located in the basin upstream of the

most seaward calcareous tufa barrier under the influence of the stream of the Krka River, while cores PROK-1 and PROK-3 have a distal position of sampling location (small calcareous tufa lake upstream of core PROK-2 (PROK-1) or in the central part of Prokljan Lake (PROK-3)). The sediment in PROK-2 is more reddish to brown in colour (Fig. 6.10), indicating more terrigenous riverine input with numerous freshwater shells (probably *Bithynia* sp.), but some marine shells are also present. Furthermore, discontinuous laminae are present in the sediments, possibly indicating higher fluvial input related to high precipitation events. Similar characteristics were found in cores PROK-1 and PROK-3, but the colour of the sediment is dark brown with discontinuous laminae and dark brown organic laminae or lenses.

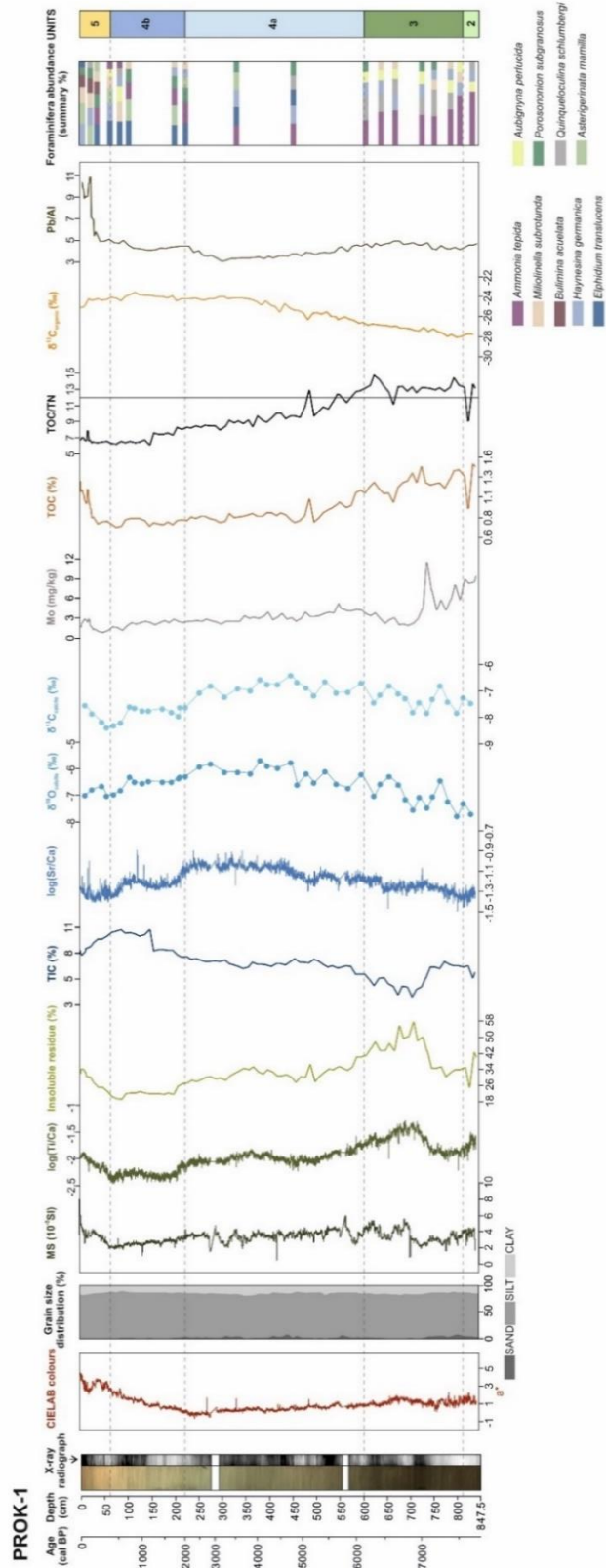


Figure 6.9 The distribution of selected geochemical and sedimentological indicators in sediment core PROK-1.

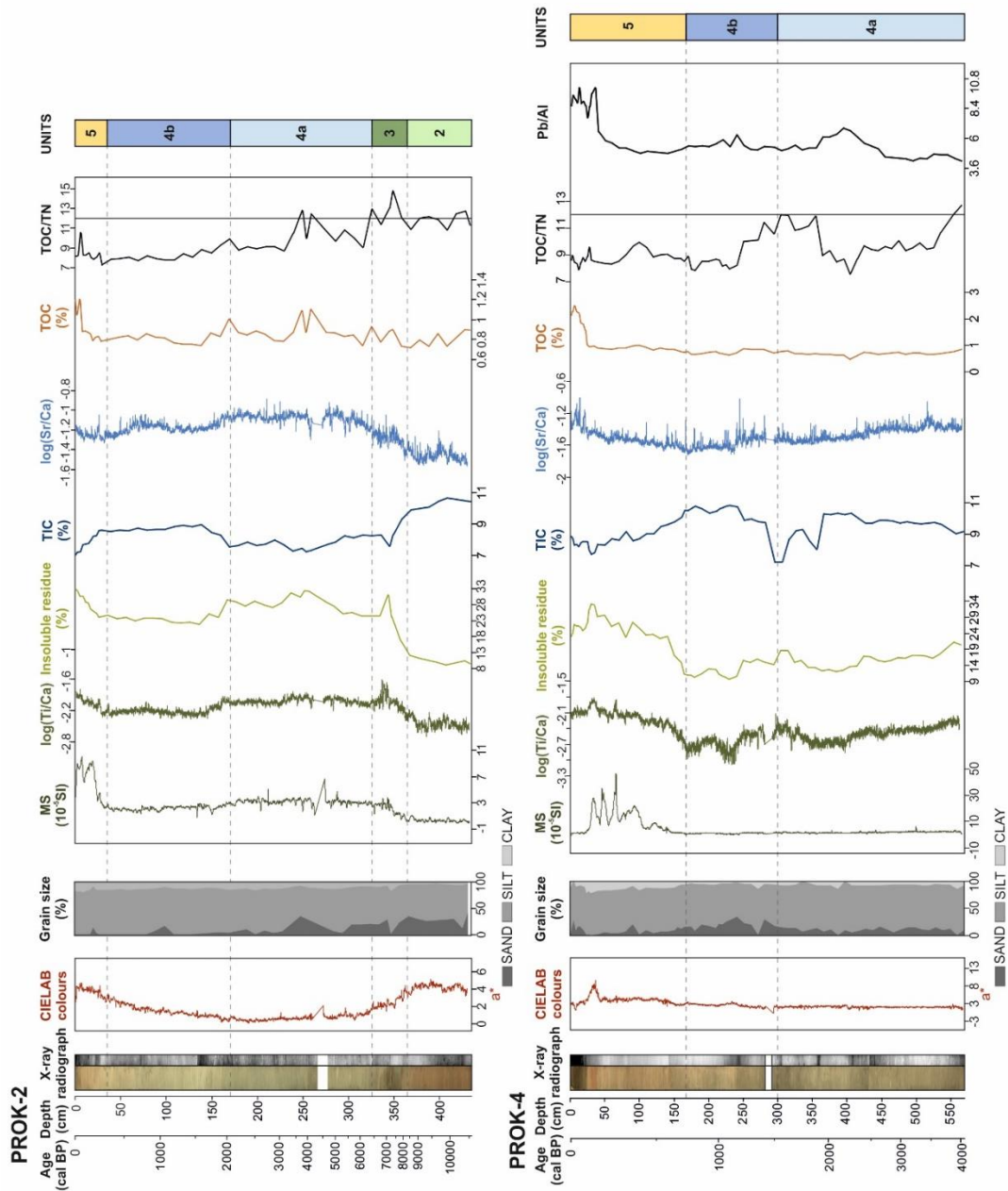


Figure 6.10 The distribution of selected geochemical and sedimentological indicators in sediment cores PROK-2 and PROK-4.

LU2 of the core PROK-3 is characterized by the rapid rise in $\log(\text{Sr}/\text{Ca})$ and its overall increasing trend (Fig. 6.6) that can be linked to increasing marine influence and aragonite precipitation. Furthermore, foraminifera species (high domination of *Ammonia tepida*; Fig. 6.6) suggest the existence of a marginal marine environment with limited marine influence and brackish-water conditions (Debenay & Guillou, 2002; Koukousioura et al., 2012; Murray,

2006). The presence of pyrite in the sediments of LU2 (Table 5.22) can be linked to short-term seawater incursions, since Fe-sulphides require a substantial amount of sulfide in pore water for their formation (Rickard and Luther, 2007). Pyrite is a common authigenic mineral found in brackish water sediments and is linked to sediments with a significant content of organic matter (Postma, 1982). The formation of pyrite aggregates could lead to a decline in MS (Riedinger et al., 2005), which can be observed in the LU2 (Fig. 6.6). The short-term seawater incursions and low-salinity brackish deposits can be explained by the progressive intrusion of marine water through the highly porous calcareous tufa barriers (cavities in the barriers can be cm or even up to m wide; García-del-Cura et al., 2012) and with the permeable karst, where the rise in sea level can significantly impact seawater intrusion in a coastal karst aquifer, and long-distance seawater intrusion can occur through the subsurface conduit system (Menning et al., 2015). Due to the marine intrusion through the karstified rocks and calcareous tufas, the marine ponds probably developed with the deposition of brackish sediments. This environment could have been similar to other marine ponds previously detected along the EAC (Brunović et al., 2019; Ilijanić et al., 2022). Within this interval, the organic carbon content is elevated, as are TOC/TN ratios and negative $\delta^{13}\text{C}_{\text{org}}$ values, suggesting an increased contribution of lacustrine organic matter, i.e., C3 terrestrial plants (Figs. 6.6 and 6.8).

High concentrations of Mo are present at the beginning of LU2 of the core PROK-3 and PROK-1 (Fig. 6.6 and 6.9), and at the top of LU2, the Mo is decreasing. Mo is considered a good proxy of palaeohydrographic conditions and for distinguishing oxic from anoxic environments (Algeo and Lyons, 2006; Crusius et al., 1996; Tribouillard et al., 2006). Some authors suggest that in some silled basins or lakes, high peaks of Mo concentrations were observed before these environments were flooded and oxidized by seawater (Algeo and Lyons, 2006; Razum et al., 2020). Therefore, it can be concluded that these tufa lakes were transitional environments (restricted brackish ponds and not an open marine environment) since the basin was Mo depleted, as suggested by Mo peaks, which occurred just before marine intrusion. In addition, it supports the hypothesis of short-term marine water intrusion through porous tufa barriers and karst. Therefore, the depth of the tufa barriers relative to the present sea level induced the time of the marine flooding.

The marine lake at the location of the PROK-1 sediment core developed between >7.8 and 7.5 cal kyr BP, with the barrier crest situated at a water depth of approximately 11.5 meters. Low negative $\delta^{18}\text{O}_{\text{cal}}$ values at the bottom of LU2 in the PROK-1 sediment core (Fig. 6.9) indicate a predominant freshwater influence (Fig. 6.7). The Krka River catchment is primarily recharged by groundwater and surface runoff from precipitation ((Bonacci et al., 2006). The $\delta^{18}\text{O}$ of Krka River water is generally consistent throughout the year, averaging -7.3‰ VSMOW in winter and -7.5‰ VSMOW in summer (Lojen et al., 2009), suggesting that local evaporation likely has a minor influence on the system due to the short residence time of the water, even during the summer period (Legović, 1991). The primary source of carbonate in the upstream freshwater part of the Krka River's fluvio-lacustrine sediments is in-situ carbonate precipitation, resulting from the constant supersaturation of river water with calcite (Cukrov et al., 2013). Detrital carbonate has a minor influence upstream and in the Krka River estuary (Cukrov et al., 2013). Therefore, the predominant factor affecting the carbonate $\delta^{18}\text{O}_{\text{cal}}$ and $\delta^{13}\text{C}_{\text{cal}}$ composition in the estuary during the Holocene sea-level rise is the mixing of freshwater and marine water. Additionally, $\delta^{18}\text{O}_{\text{cal}}$ values of serpulid tubes in the Krka River estuary reflect the stable oxygen isotope composition of the water, with more positive $\delta^{18}\text{O}_{\text{cal}}$ and $\delta^{13}\text{C}_{\text{cal}}$ values as the distance from the estuary head increases. In the freshwater part, values ranged from -14.4 to -8.4‰ , in the brackish part near the estuary mouth from -3.4 to -2.9‰ , and in the marine part from -1.5 to -1.3‰ (Lojen et al., 2014). The oscillating and gradually upward increasing $\delta^{18}\text{O}_{\text{cal}}$ values up to LU4a suggest short-term changes in salinity and surface water hydrography.

Core PROK-2 is situated in a depositional basin formed behind the most seaward calcareous tufa barrier (Fig. 5.1), allowing marine water to intrude through the porous tufa barrier. These calcareous tufas grow irregularly, with cavities produced by encrusting mosses and various microbiota. Consequently, they are highly permeable, with pores ranging from several centimeters wide to meter-sized cavities (Pavlović et al., 2002; Golubić et al., 2008; García-del-Cura et al., 2012), enabling marine water intrusion. The basin where PROK-3 was cored is enclosed to the south by karstified bedrock with a sill at 15 meters below sea level (b.s.l.), and to the west it is isolated by the calcareous tufa barrier. Due to marine intrusion through the karstified rocks and calcareous tufas, a marine pond likely developed, resulting in the deposition of brackish sediments of SU3b. Similar marine pond environments were

previously identified along the Eastern Adriatic Coast (Brunović et al., 2019; Ilijanić et al., 2022).

The upper boundary of SU3 is marked by seismic horizon SH2, a continuous boundary distinguishing lower heterogeneous deposits from upper homogeneous ones. In the palaeochannels, SH2 appears as a planar reflector, while in the basins formed between calcareous tufa barriers, it exhibits erosive characteristics. Scours, several meters wide and deep, are likely associated with waterfall erosion, previously described by Hasan et al. (2023) as the plunge pool effect. The SH2 unconformity could be interpreted as marine flooding surface, although the restricted marine influence was present earlier through the calcareous tufa barriers and karstified rocks.

Estuarine to marine deposits

Seismic unit SU4 is the thickest and most extensive unit and constitutes the bulk of the valley fill. Acoustic signals of this unit display aggradational parallel reflectors or, in other areas, transparent facies (F4a–c; Fig. 5.12) with very weak reflectors, indicating homogeneous sediment. These deposits also comprise the thickest unit in all sedimentary cores and consist of beige to grey, faintly laminated, or homogeneous silty sediments (Fig. 5.29). Furthermore, the presence of mixed freshwater and marine fauna, indicates a brackish environment with strong marine influence. The lower part of this section is characterized by some freshwater and marine shells (suggesting a freshwater influence), with a gradual transition into the sediment with more significant marine influence, comprising only marine shells with numerous *Turritella* sp.

Additionally, coarse silty and discontinuous laminae are present only in the lower part of this section, implying a stagnant low-energy environment with tidal influence (grey and reddish laminae). At a depth of approximately 3 m below SF, a reflector with numerous acoustic diffractions (F4d; Fig. 5.12; Schwarz, 2019) can be observed in the seismic profiles. The possible interpretation is that diffractions represent coarser-grained deposits, probably shell accumulations related to a maximum ingression surface. The uppermost interval in all cores, the top 50–160 cm (0.647 kyr BP to present), showed similar characteristics. Mainly, it

is marked by beige to reddish sediments, or in core PROK-4, it is characterized by reddish to brown sediment (Fig. 6.10). The red colour of the sediment can be attributed to the erosion of soils from the catchment due to increased agriculture, deforestation, and higher fluvial activity. Pronounced human activity is particularly evident in the uppermost part of the estuary, near the town of Skradin, where high accumulations of sediments are present (Figs. 5.13 and 5.14). The occurrence of gas (probable free methane in sediments) was also detected (Fig. 4b; Figs. 5.12–5.14 and 5.15B). The presence of gas can be explained as a consequence of the degradation of organic matter in the sediments, affecting the acoustic signal.

In the period of 8.4–6.1 cal kyr BP, a noticeable shift can be observed based on the LU3 sediments (Figs. 6.6, 6.9, and 6.10), with deposition of medium to coarse silty sediment and an increase in the detrital siliciclastic component suggesting intensive erosional processes within the catchment (Figs. 6.7 and 6.8). It can be concluded that increased precipitation and detrital input occurred, which coincided with a pluvial period. Pluvial phase and wet climate have been previously observed in the Adriatic and Mediterranean (Schmidt et al., 2000; Zhorniyak et al., 2011; Combourieu-Nebout et al., 2013; Brunović et al., 2020; Razum et al., 2021). The organic matter accumulation is still significant at the beginning of the LU3 (Fig. 6.8). It decreases at the end of the unit, with a mix of terrestrial plants, freshwater, and marine algae, which further supports this transition.

Additionally, foraminifera species are more abundant in comparison to older deposits, with the dominant species *Ammonia tepida* at the beginning of LU3, which is subsequently replaced with *Elphidium translucens* (Figs. 6.6 and 6.9). The abundance of other shallow-marine species suggests increasing marine influence in the study area (Figs. 6.6 and 6.9). Consequently, the input of freshwater organic matter during the pluvial period may have suppressed the marine signature in sediment cores (PROK-3, PROK-2, and PROK-1; Fig. 6.8), masking the initial marine deposition.

The decrease in the detrital component and increase in the marine component (Figs. 6.7 and 6.8) from 6.1 cal kyr BP marks the end of humid climate conditions and the onset of rising sea level, leading to the accumulation of estuarine sediments (LU4a; Figs. 6.6, 6.9, and 6.10). The continuous sea-level rise resulted in a dominance of marine macrofossils (shells

and gastropods) and foraminifera (Figs. 6.6 and 6.9), with a higher diversity of foraminiferal species compared to older deposits. The dominant species are *Elphidium translucens* and *Haynesina germanica*, which are typical species of shallow marine environments (Murray, 2006). Increased values of $\delta^{18}\text{O}_{\text{cal}}$ and $\delta^{13}\text{C}_{\text{cal}}$ reflect changes in hydrology and freshwater/marine mixing or possibly indicate a more arid climate, reducing freshwater influence and thus relatively increasing marine influence, which facilitated surface water mixing (Fig. 6.9). Additionally, low TOC and TOC/TN ratios, along with high $\delta^{13}\text{C}_{\text{org}}$ values, suggest a growing dominance of marine-origin organic matter (Fig. 6.8). Therefore, during this period, a partially mixed or slightly stratified estuary formed. Arid conditions during the mid-Holocene have also been reported in the Mediterranean Sea (e.g., Roberts et al., 2008; Wagner et al., 2009; Leng et al., 2010; Joannin et al., 2012) and Lake Dojran (Francke et al., 2013), further supporting this interpretation.

During the late Holocene, sea level fluctuations stabilized and reached their present position (Lambeck et al., 2014). From 3.0 cal kyr BP to 600 cal yr BP, homogeneous sediment (LU4b; Figs. 6.6, 6.9, and 6.10) rich in marine macrofossils, mainly *Turritella* sp. shells, was deposited. Foraminifera assemblages were dominated by *Elphidium translucens*, which replaced *Ammonia tepida*, the dominant species in older units (Figs. 6.6 and 6.9). This unit exhibited the highest diversity of foraminiferal assemblages, indicating shallow marine conditions (Murray, 2006). A decrease in siliciclastic proxies suggested minor detrital influence (Fig. 6.7), supported by low levels of terrigenous organic matter (Fig. 6.8). A shift in $\delta^{18}\text{O}_{\text{cal}}$ and $\delta^{13}\text{C}_{\text{cal}}$ values showed a declining negative trend (Fig. 6.9). By this time, the gradually rising sea level had inundated the calcareous tufa barriers, creating a predominantly marine environment while maintaining sufficient freshwater input to support a stratified water column (Pritchard, 1989). Consequently, the establishment of present-day salt-wedge estuarine conditions occurred at 3.0 cal kyr BP in core PROK-3 (Fig. 6.6), while in core PROK-2, the halocline formed at 2.1 cal kyr BP (Fig. 6.10), in core PROK-1 at 2.0 cal kyr BP (Fig. 6.9), and in core PROK-4 at 1.5 cal kyr BP (Fig. 6.10). The different timing of the establishment of stratified conditions in the cores at various locations within the investigated area may be due to the calcareous tufa barriers and the different elevations of the core sites, in combination with sea-level rise and the seawater intrusion through the barriers and karst.

LU5, the uppermost sediment layer spanning the last 600 calendar years BP, reflects significant changes in the catchment area characterized by higher detrital input of particles with the highest sand content and high organic matter content (Figs. 6.6–6.10). These changes indicate increased instability and erosion of the catchment, likely linked to anthropogenic activities such as agriculture and possibly deforestation. Human impact and erosion are particularly evident in sediment core PROK-4 (Fig. 6.10), retrieved from the upper estuary near the town of Skradin, where organic-rich sediment deposition and gas accumulations are more pronounced (Figs. 5.13, 6.7, 6.8, and 6.10). During this period, foraminiferal assemblages were diverse and abundant, with an increased presence of the infaunal species *Bulimina aculeata* (Figs. 6.6 and 6.9), commonly found in oxygen-depleted environments (Langlet et al., 2013; Murray, 2006), indicating more stressful bottom conditions. Previous studies have noted periods of hypoxic conditions in the Krka River estuary (Legović et al., 1991). Notably, $\delta^{18}\text{O}_{\text{cal}}$ and $\delta^{13}\text{C}_{\text{cal}}$ in this lithological unit do not show a positive correlation (Fig. 6.9), possibly due to bacterial degradation of organic matter. Bacterial methanogenesis in organic-rich sediments could result in enriched $\delta^{13}\text{C}_{\text{cal}}$ values (Kelts and Talbot, 1990).

6.3 Seabed sediment composition, dynamics and assessment of human impact

The Krka River estuary exhibits relatively low terrigenous sediment input due to its karstic watershed and tufa barriers upstream, which limit sediment transport (Legović et al., 1994). Marine sediment transport is also minimal due to the estuary's salt-wedge type, limited wave action, weak bottom currents, and tides (Moreira-Turcq et al., 1993; Korlević et al., 2016). Therefore, it is likely that the primary source of terrigenous material in the lower Krka River estuary is the Guduča River, which drains a catchment area dominated by flysch deposits (Mamužić, 1975). Unlike the Krka River, the Guduča River lacks tufa barriers, allowing sediment transport downstream.

Analysis of surface estuary sediment particle size distribution (Fig. 5.8) reveals a decrease in particle size with increase in water depth. The highest concentration of silty sediment occurs in the palaeochannel of the Guduča River on the western side of Prokljan Lake, near the mouth of the Guduča River, and at the southern outlet of Prokljan Lake (Fig. 6.11), where ancient channels of the Krka and Guduča rivers cut through the canyon towards

Šibenik. The upper part of the Krka River canyon seabed consists of sandy silt, while sediment on tufa barriers and carbonate mounds ranges from silty sand to coarse sand. Biogenic origins, such as shells and benthic organism fragments, dominate the sand particles. The bimodal or polymodal distribution and poor sorting of sediments suggest multiple sediment sources and a mixture of terrigenous and biogenic particles.

This is further supported by the mineral composition. Calcite is the predominant mineral in all surface sediments. In the fine-grained fraction, terrigenous quartz and clay minerals are also present, originating mainly from areas of the catchment with Eocene marls and, to a lesser extent, from erosion of the sparse soil cover overlying the karst. The sand fraction from tufa barriers and carbonate mounds is dominated by aragonite and calcite, indicating a biogenic origin. Insoluble residue and magnetic susceptibility exhibit a weak negative correlation with the backscatter intensity of silt samples (Fig. 6.11).

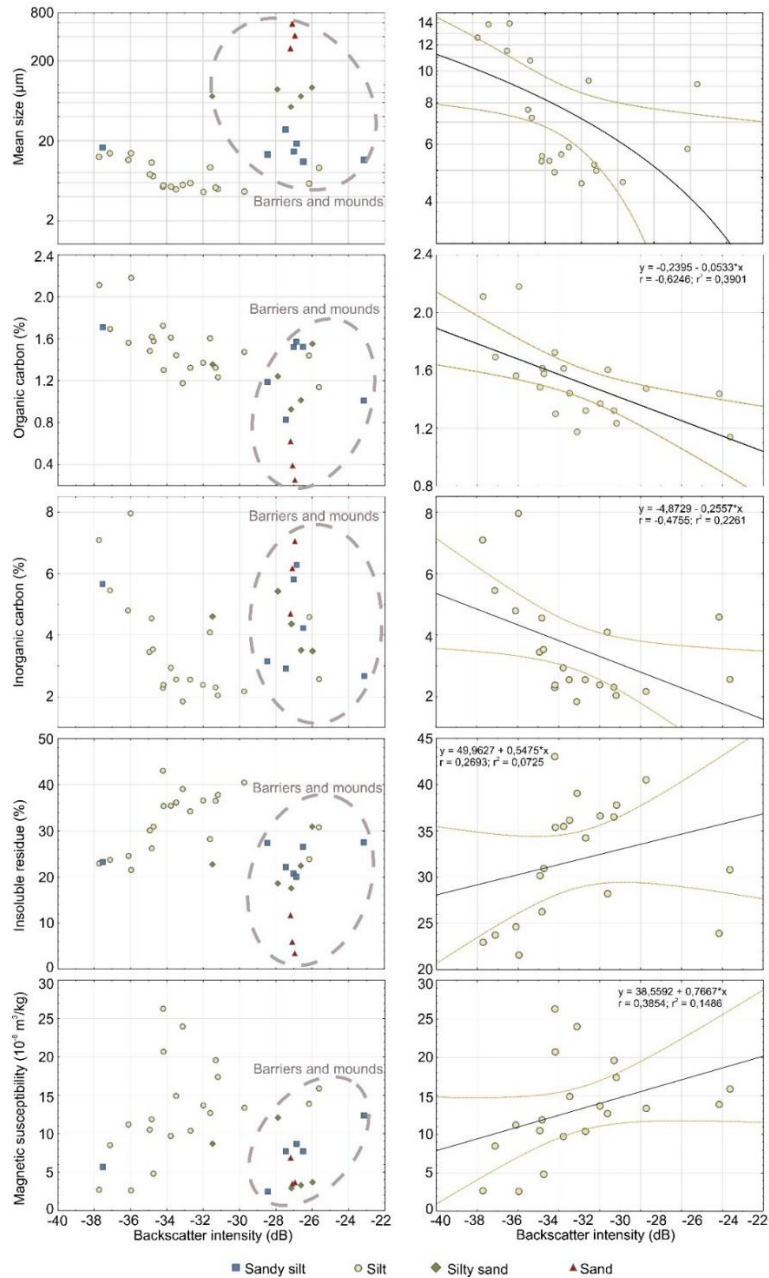


Figure 6.11 Values of backscatter intensity compared with mean grain size (μm), OC (%), IC (%), IR and magnetic susceptibility ($10^{-8} \text{ m}^3/\text{kg}$). Scatterplots in the left column are made for all grab samples grouped by the sediment type. Scatterplots in the right column represent silt-sized samples and their correlation with variables. Gray ellipses represent the distribution of samples mainly from barriers and mounds. Yellow dashed lines represent the 95% confidence interval.

MS values show a strong correlation with backscatter intensity (Figure 6.11). The highest MS values were observed in sediments below the highway bridge, likely due to anthropogenic influences from road runoff. Slightly elevated values were also detected on

the western side of Prokljan Lake near the Guduča River ($>20 \times 10^{-8} \text{ m}^3/\text{kg}$) and at the southern outlet of Prokljan Lake. These samples also exhibited a higher percentage of frequency-dependent magnetic susceptibility ($f_d > 8\%$), indicating the presence of ultrafine superparamagnetic magnetite minerals commonly found in soils (Dearing et al., 1996). This aligns with the terrigenous supply and higher siliciclastic content observed in these samples.

Numerous studies on organic matter distribution in surface sediments have demonstrated a direct relationship between TOC content, PSA, and mineral composition (e.g., Kemp, 1971; Meyers, 1994; Gao et al., 2012; Gu et al., 2017). Linear regression analysis between mean backscatter (dB) and TOC (Fig. 6.11) showed a significant linear model fit for mud sediments ($r=0.62$), but no correlation was found for coarse carbonate sediments originating from the disintegration of submerged tufa barriers and mounds (Fig. 6.11). A predicted TOC distribution map was generated for the estuary (Fig. 6.12) using correlation equation derived for the mud-sized fraction (Figure 6.11).

The distribution of TOC is influenced by the estuarine morphology of the Krka River, with the highest concentrations found in small basins between individual submerged tufa barriers in the canyon section. Despite low energy and hydrodynamics in the estuary (Legović et al., 1994), TOC concentrations in sediments are generally higher along the current of the Krka River and decrease towards the sea (Fig. 6.12). The highest TOC concentrations, ranging from 1.17 to 2.18%, were observed in silt samples (rich in clay content) from the Krka River canyon near Skradin and the mouth of the Guduča River. Both areas are characterized by catchments with highly erodible Eocene flysch deposits (marls) and agricultural lands, suggesting possible anthropogenic influences and/or higher sedimentation rates (Kemp, 1971; Cukrov and Barišić, 2006).

In the central part of Prokljan Lake, where sedimentation rates are lower, TOC concentrations are also reduced. Sandy samples composed of calcite, aragonite, and high-magnesium calcite (PJ-15, PJ-29, and PJ-30) exhibited the lowest TOC concentrations ($<1\%$). Conversely, silty samples with higher clay fractions generally displayed higher TOC concentrations ($>1\%$). The distribution of organic matter closely correlates with fine-grained sediments (Mayer, 1994; Tyson, 1995) and high sedimentation rates (Kemp, 1971). However,

factors such as bioturbation and bottom-water oxygen levels can also influence TOC distribution.

TN concentrations and their spatial distribution also exhibit a strong correlation with TOC values ($r=0.96$), indicating a common organic source (Faust and Knies, 2019).

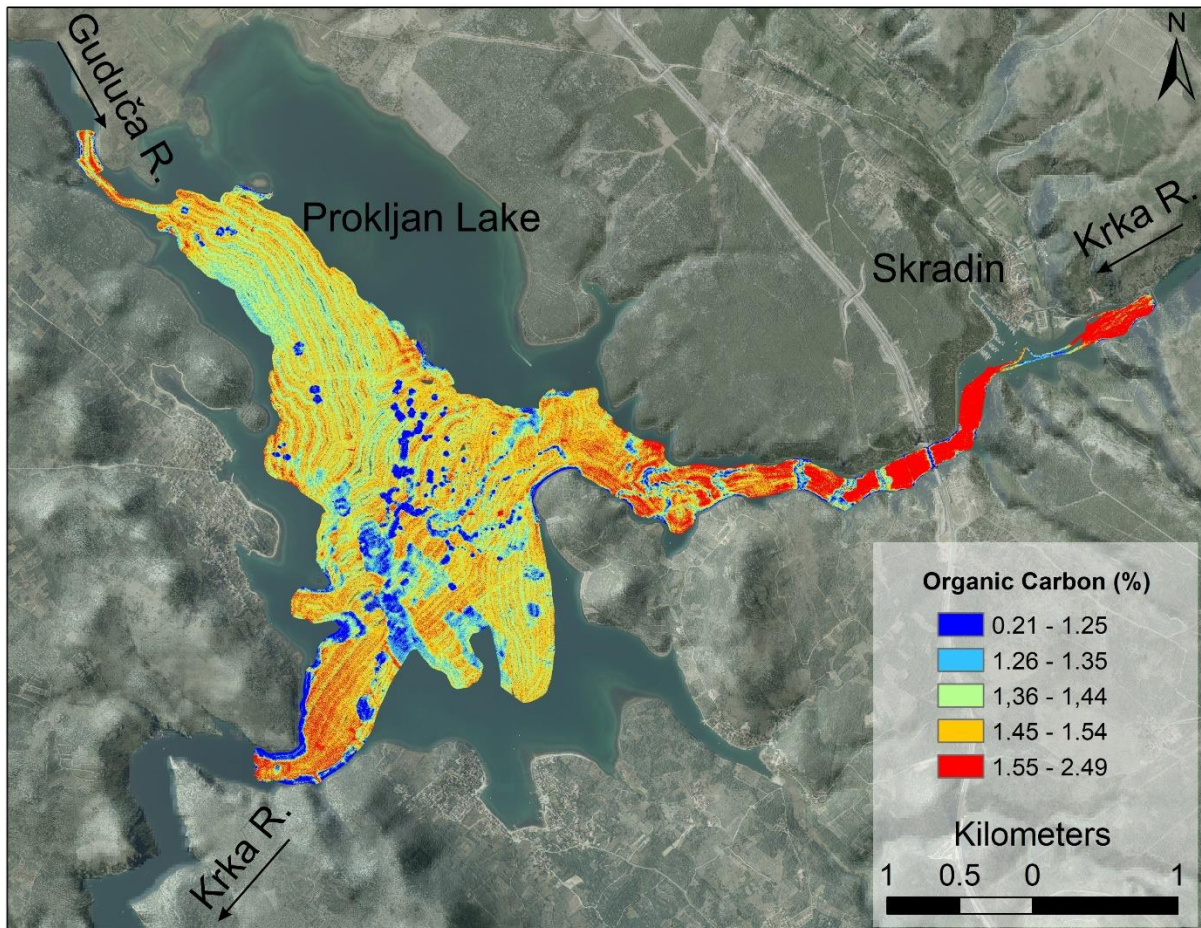


Figure 6.12 Predicted distribution of organic carbon (%) based on the correlation equation calculated for the silt-sized fraction.

The TOC/TN ratio serves as a key indicator of organic matter sources in marine and lacustrine environments (Meyers, 1994; Lamb et al., 2006), distinguishing between algal and higher-plant origins (Meyers, 1994). Estuaries, characterized by mixed riverine and marine influences, feature organic matter in surface sediments sourced from both realms (Gao et al., 2012). In the Krka River estuary, TOC/TN ratios range from 4.59 to 8.86, indicating predominantly marine origins, likely algal or pelagic (Svensen et al., 2007).

Analysis of sediment data reveals that estuarine sedimentation is largely influenced by catchment geology, geomorphology, river flow dynamics, and biogenic production. A positive correlation between OC and backscatter intensity ($r=0.62$) was observed in mud sediments (Fig. 6.11), consistent with findings by (Hunt et al., 2020). Correlations between TOC, magnetic susceptibility, TIC, and insoluble residue demonstrated varying degrees of influence on backscatter intensities in fine sediment fractions, whereas no such correlation was found in coarse carbonate sediments resulting from the physical breakdown of submerged tufa barriers.

Although the accuracy estimation of a classifier depends on the sample size and the accuracy of the ground truth (Carlotto, 2009), this study, along with several previous ones (Micallef et al., 2013; Janowski et al., 2018; Brown et al., 2019), classified results based on a relatively small yet carefully selected representative sample set. Overall accuracy assessments indicate 93.3% for a four-class classification map and 86.7% for a seven-class map, with corresponding Kappa coefficients of 0.9 and 0.83, respectively. The integration of backscatter data, sediment particle size data, and MBES data enabled the successful classification of the study area's seabed into either four or seven classes. The four-class map (Fig. 5.8A) categorizes sediment as silt, sandy silt, silty sand, and sand, while the seven-class map (Fig. 5.8B) distinguishes fine, medium, and coarse silt and fine, medium, and coarse sand. The relationship between sediment particle size and backscatter intensity confirms that coarser sediment produces stronger returns, consistent with previous findings (Zhi et al., 2014; Buhl-Mortensen et al., 2015; Montereale Gavazzi et al., 2016; Brown et al., 2019).

The OBIA-based maps clearly illustrate that coarse-grained sand sediments cover the barriers and mounds, while fine-grained sediments dominate the flatter and deeper areas. The barriers, which protrude from the flat bottom, are particularly vulnerable to erosion by estuarine bottom currents, leading to a scarcity of fine-grained sediments and an accumulation of coarser sediments along with shells and debris (Fig. 6.13). Upstream in the canyon, sediment analysis reveals somewhat coarser medium silt sediments compared to finer silt sediments downstream from Barrier 2 into Prokljan Lake (Figs. 5.8B and 6.13H). This disparity can be attributed to the influence of the Krka River, which transports larger particles that are blocked within the canyon by the barriers.

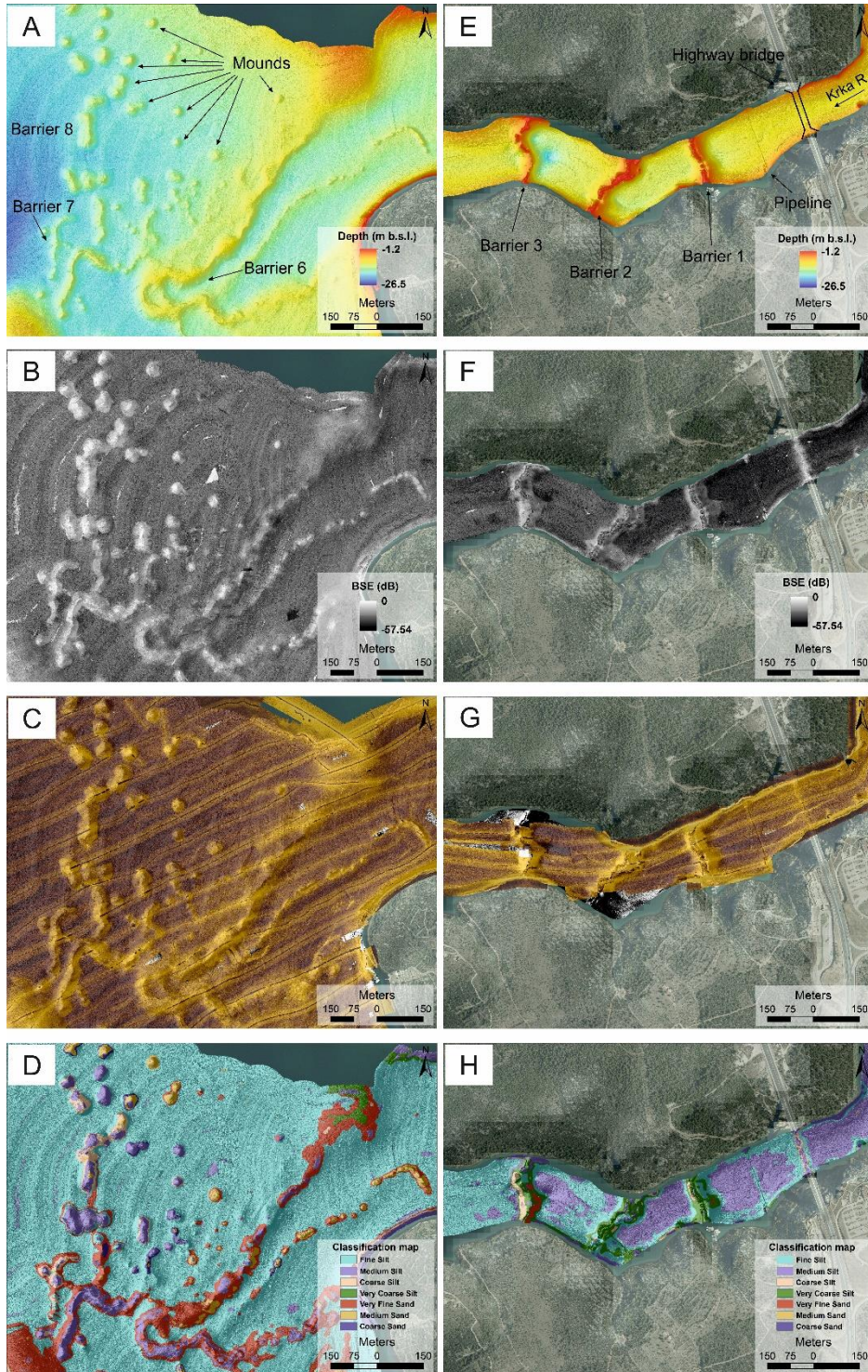


Figure 6.13 Barriers and mounds at the end of the canyon at the entrance to Prokljan Lake are detailed in maps (A–D). The maps include: (A, E) MBES map; (B, F) BSE map; (C, G) SSS map; (D, H) final classification map.

6.3.1 Geochemical record of environmental change during the past 600 years caused by human activities

Population increase, intensive farming, and consequent deforestation are predominant factors influencing the erosion rate (Lasanta et al., 2000), especially in coastal areas. Human influence on erosion/sedimentation has been increasingly important since the 19th century, but there is also evidence of similar effects in the past. Evidence of increased erosion in the Dalmatian region, attributed to human activities during the late Holocene, has been discussed in Hasan (2017).

Estuarine sediments are recognized as good deposit area for sediments that are generated in catchments, because the clastic fraction of freshwater riverine sediment generally derives from the drainage basin by erosion that may be the product of natural and/or anthropogenic forcing mechanisms (Kennish, 2016). Therefore, the composition of estuarine sediments can reflect watershed lithology, terrestrial characteristics, ecosystem development, climate change, mineralogy, and geochemical properties. Elements such as Al, Fe, and Ti are commonly used as proxies to define sediment sources and identify changes in clastic sediment supply (Gasparon et al., 2007; de Carvalho Gomes et al., 2009).

In the Krka River estuary, changes in sediment composition have been recognized in the last 600 years based on the multiproxy analyses (LU5 of the PROK sediment cores). A sediment colour change is present (reddish sediment), somewhat higher sedimentation rates are visible, as well as elevated MS values and geochemical components, such as an increase of most lithogenic elements (Fe, Al, Ti, K, Ti/Ca, insoluble residue) and TOC, and a reduction of Ca. All this data point to enhanced catchment erosion and transport of soil detrital material to the estuary. The enhanced erosion from the catchment could be associated with human settlements in this area (especially near the rivers) and, therefore, their usage of agricultural land and deforestation, which could cause soil erosion (mostly calcocambisol and terra rossa soils developed on carbonates, as well as soils developed on Eocene marls). The erosional characteristics can be observed in PROK sediment cores (LU5) at different time intervals. The earliest erosion can be identified in sediment core PROK-4 at 647 cal yr BP (Medieval warm period) near the town of Skradin. The Skradin area is characterized by flysch deposits, which are agriculturally arable, and thus, erosion occurs with the material transport by torrential

streams into the estuary. A higher accumulation of sediment and gas is present in this area, well visible on the seismic profiles (Figs. 5. 13 and 5.14). The gas accumulations occur due to the decomposition of sediment rich in organic matter.

In other three locations, erosion occurs approximately at the same time, during the Little Ice Age (LIA). In the core PROK-1 erosion is detected at 374 cal yr BP, in the core PROK-2 at 380 cal yr BP, and in the core PROK-3 at 460 cal yr BP. This could point to erosion caused by deforestation in the catchment during the LIA.. Evidence of late Holocene erosion processes caused by human activities along the EAC was determined in cores from Lake Vrana on Cres Island dated to the period between 600 and 400 years BP (Mesić 2004, Miko et al., 2008, Ilijanić, 2014), and the Zrmanja River estuary (Hasan, 2017),

6.3.2 Anthropogenic influence on heavy metal contents in the past 150 years

Additionally, sediments play a crucial role as carriers of pollutants in coastal environments. Estuarine embayments often serve as significant contaminant reservoirs, functioning as sinks for fine, contaminant-reactive sediments (e.g., Cundy, 2003; Morelli et al., 2012). The use of heavy metals in various industrial activities has recently increased metal inputs in coastal areas. Due to their inherent toxicity and non-degradability, these metals are monitored for their ecological impact (Lacerda et al., 1992). The reworking of old sediments through natural, physical, biological, and human activities can readily release anthropogenic metals associated with these sediments back into the environment, negatively impacting the ecosystem.

To reduce variability in metal concentration due to differences in grain size and clay content, heavy metal concentrations were normalized against Al (Figs. 5.59, 5.52, and 5.55). Aluminum was preferred to other elements because of its conservative nature in the marine environment. Aluminum is a good proxy for clay mineral content since it is associated with the alumino-silicate fraction (Loring and Rantala, 1992; Roychoudhury, 2007; Badr et al., 2009). Therefore, it differentiates natural concentrations in sediments from anthropogenic content.

Estimating the “Enrichment Factor” based on Al-normalized values allows for plotting geochemical trends, allowing comparison of metal enrichment in sediments at a spatial scale (Morelli et al., 2012). Therefore, an EF for sediment cores PROK-1, PROK-3, and PROK-4 was calculated. The calculation of EF has been previously explained in Subchapter 4.2.11. EF values indicate the level of enrichment: EF < 1 suggests no enrichment, EF= 1–3 indicates minor enrichment, EF= 3–5 suggests moderate to severe enrichment, EF= 10–25 signifies severe enrichment, EF= 25–50 indicates very severe enrichment, and EF >50 represents extremely severe enrichment (Vreca and Dolenc, 2005; Wang et al., 2007). The graphical plots of EFs for the three PROK sediment cores are shown in Figure 6.14.

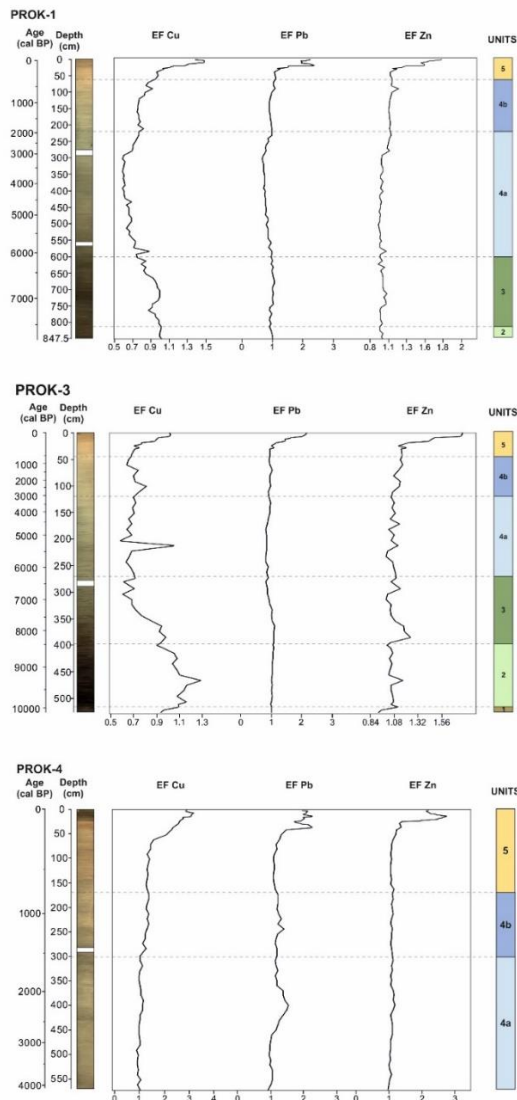


Figure 6.14 The graphical plots of Efs for the PROK-1, PROK-3, and PROK-4 sediment cores.

Since a large part of the Krka River freshwater area is under the Krka National Park authority (protection), one can assume that there is no contamination entering the estuarine part of the Krka River. Moreover, as previously noted, the terrigenous input in the estuary is generally low, with most of the sediment deposited in the active tufa lakes upstream. However, elevated anthropogenic influence, i.e., higher input of heavy metals concentration, was detected previously in the most seaward tract of the estuary at the Šibenik city harbor (Mikac et al., 1989; Kwokal and Lovrić, 2006; Cukrov et al., 2020, 2024).

It is evident that, after normalization, heavy metals such as Cr and Ni do not show an increase in the PROK-3 core, only natural variation in the sediment (Fig. 5.52). However, this increase is visible in the PROK-1 and PROK-4 cores after normalization (Figs. 5.49 and 5.55). These variations are likely because the PROK-1 and PROK-4 cores were sampled near the shore, while the PROK-3 core is located in the center of Prokljan Lake. The overall concentration of heavy metals is caused by the increased influx of siliciclastic components into the basin, most probably related to the deforestation and burning of forests, followed by the erosion of materials into the marine environment. Such conclusions are also suggested by research in the Krka River estuary (Prohić and Juračić, 1989), where the authors interpret increased concentrations of Ni and Zn in the sediments as natural due to the influence of basic and ultrabasic rocks on the composition of the flysch and limestone in the catchment area, which is then eroded into the basin.

An increase in Pb/Al and Cu/Al ratios is visible (Figs. 5.49, 5.52, and 5.55). While the rise in lead in the sediments is linked to anthropogenic impact and atmospheric deposition (e.g., Miko et al., 2008), the increase in copper is associated with agricultural activities, particularly viticulture (Miko et al., 2003). The increase in Cu and Pb in the sediment cores is evident from 650 BP and continues to rise to the present day. Since the rise in Pb and Cu in marine sediments coincides with the onset of erosion in the catchment area, it is possible that a portion of Pb and Cu in the sediment was precipitated from the surface layer of terrestrial sediments, where it was deposited due to human activity before the deforestation or burning of forests for clearing land for agriculture.

The variability of EFs in all three cores is shown in Figure 6.14. In the core PROK-1, the EF ranges of Cu, Pb, and Zn were 0.58–1.48, 0.66–2.36, and 0.94–1.79, while in the core PROK-3 they were 0.58–1.29, 0.81–2.16, and 0.92–1.77, and in the core PROK-4 they were 0.90–3.19, 0.94–2.26, and 0.97–2.73. When compared to natural values (background), the EFs of these elements are slightly higher for the first 30 cm (185 cal yr BP) of the sediment core PROK-1, 20 cm (220 cal yr BP) of the core PROK-3, and 60 cm (240 cal yr BP) of the core PROK-4. All this data indicates low pollution for Cu and Zn (except for moderate pollution of Cu in the core PROK-4), while Pb shows moderate pollution, enriched over background levels. The main anthropogenic source of Cu in the sediment probably originates from agricultural activities (vineyards; Miko et al., 2003), while Zn could be of geogene origin related to flysch marls since it is abundant in Eocene flysch deposits. Elevated values of Pb could point on anthropogenic source, i.e., it is most probably associated with the Roman period of lead enrichment. Additionally, lead pipelines could be a source of Pb enrichment (Prohić and Juračić, 1989), or the Pb enrichment could be linked to airborne pollution (Miko et al., 2003).

While Fe, Cr, and Co exhibited values exceeding 2 at only two (Fe, Co) or three (Cr) sampling sites, it can be inferred that these elements in the surface sediments of the Krka River estuary are primarily of natural origin. Overall, the surface sediment could be classified as nearly pristine. Down from Prokljan Lake in the area of Šibenik harbor, there was enrichment of heavy metals due to industry and nautical tourism (Cukrov et al., 2020).

6.4 Late Quaternary palaeoenvironmental history of the Krka River mouth area in response to sea-level fluctuations: From a river valley to a karst estuary

The late Quaternary evolutionary and depositional history of the Krka River mouth can be reconstructed based on the results of seismic stratigraphy, sedimentological analyses, and radiocarbon ages concerning sea-level changes. The sedimentary infill of the Krka River mouth consists of several stages of development since the Last Glacial (lowstand, transgressive, and highstand) and was principally controlled by relative sea-level and climate changes, inherited topography and basin morphology, sediment supply, and karst hydrodynamics.

Lowstand stage

Many rivers incised their valleys during the Pleistocene marine lowstands, when the relative sea level was significantly lower, up to 130 m (e.g., Lambeck & Chappell, 2001; Lambeck et al., 2002). During these phases, the present shelf areas (as well as the Adriatic Sea) were transformed into alluvial plains due to the fluvial river incision, acting as sediment bypassing zones. In the Adriatic Sea, the lowstand sediments were mainly deposited in the present MAD in the form of prograding wedges fed from the north by the Po River and its tributaries (Trincardi et al., 1994) but also from the east from karst rivers such as the Krka River.

Due to the eustatic sea-level fall, the Krka River incised its fluviokarstic valley across the continental shelf in the Pleistocene, with the most significant incision during the LGM (Fig. 6.15). Additionally, the Pleistocene fossil calcareous tufas in the upstream part of the valley of the Krka River and its tributaries are found up to 20 meters above the present-day riverbed, indicating the elevation at which the river flowed during the MIS 5 interglacial (Horvatinčić et al., 2000). During the LGM period, the palaeo-shoreline of the Adriatic Sea was located at approximately the present 120 m depth contour (Fig. 6.15; Pellegrini et al., 2017). Consequently, many shallow coastal areas were subaerially exposed, and erosion occurred, including the Krka River. The incised palaeochannel of the Krka River can be traced at a depth of approximately 80 m between the mainland and the island of Žirje. The lower boundary, the unconformable palaeorelief surface (p), and the erosional surface recognized in the shelf area are probably the result of intense subaerial erosion and are associated with fluvial incision during the lowstand period (Catuneanu and Zecchin, 2013).

The results suggest that during this period, the Krka River flowed through a narrow and relatively deep bedrock-controlled channel in the most proximal palaeo-valley (recent estuary), where most of the low-volume sediments probably bypassed the valley and were carried and deposited on the continental shelf edge. In addition, the deltaic deposits, as they were exposed on the emerged shelf, were eroded by fluvial processes and channel incision (Fig. 6.15). The outer shelf and slope wedges are common and typically linked to periods of forced regression, lowstand fluvial deposition, or the reworking of outer shelf sediments during transgressive phases (Green et al., 2013; Lobo et al., 2018).

The shallow shelf area exhibits cut and fill features (erosional channels) that most likely represent delta top distributary channels, which exist between the islands of Zlarin and Žirje. The incised channel splits into two branches in the south around the seamount observed in Figure 5.25, where a progradation of sediments occurs. The western and eastern parts of the studied shelf area were most likely intersected with more tributary palaeochannels, like the one that flowed from Morinje Bay (Fig. 5.26A) and joined the main palaeochannel of the Krka River. There are no definitive age constraints on valley formation or fill deposition. The shelf part of the valley could correspond to multiple lowstand-highstand cycles (Fig. 5.27A), where the subaerial erosional surface reflector represents the LGM subaerial unconformity.

These channels were possibly filled with the lowstand material under the high energy conditions or/and were most likely infilled during the subsequent transgression, under estuarine conditions. Most of the lowstand sediments accumulated around the mouth of the incised valley system at the shelf edge and Middle Adriatic Depression. The clinofolds deposited at the shelf edge were beyond the reach of fluvial erosion. However, within the progradational deposits, deformational structures are present (Fig. 5.28), which can be related to the sediment gravity flows acting on the continental slope and/or sediment reworking during sea-level rise. Some lowstand sediments were possibly deposited in the upper tract of the recent estuary, i.e., in the palaeochannels of the Guduča and Krka Rivers observed in Prokljan Lake.

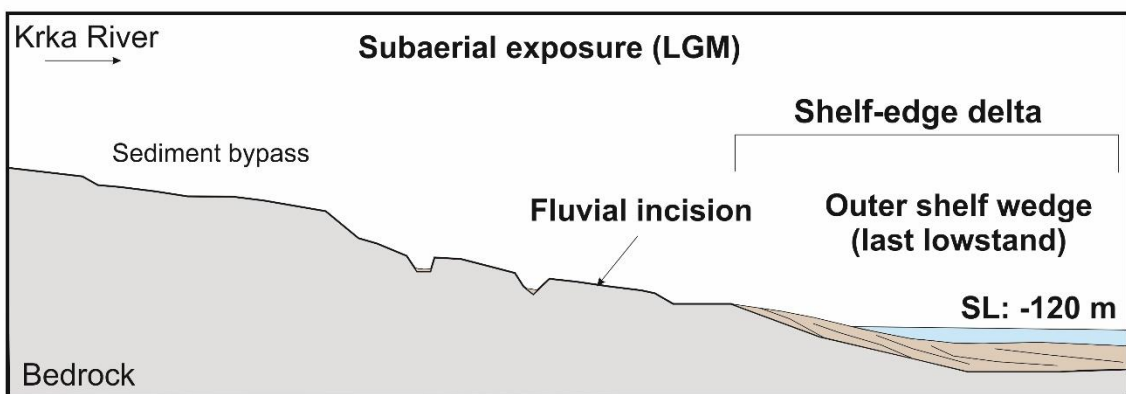
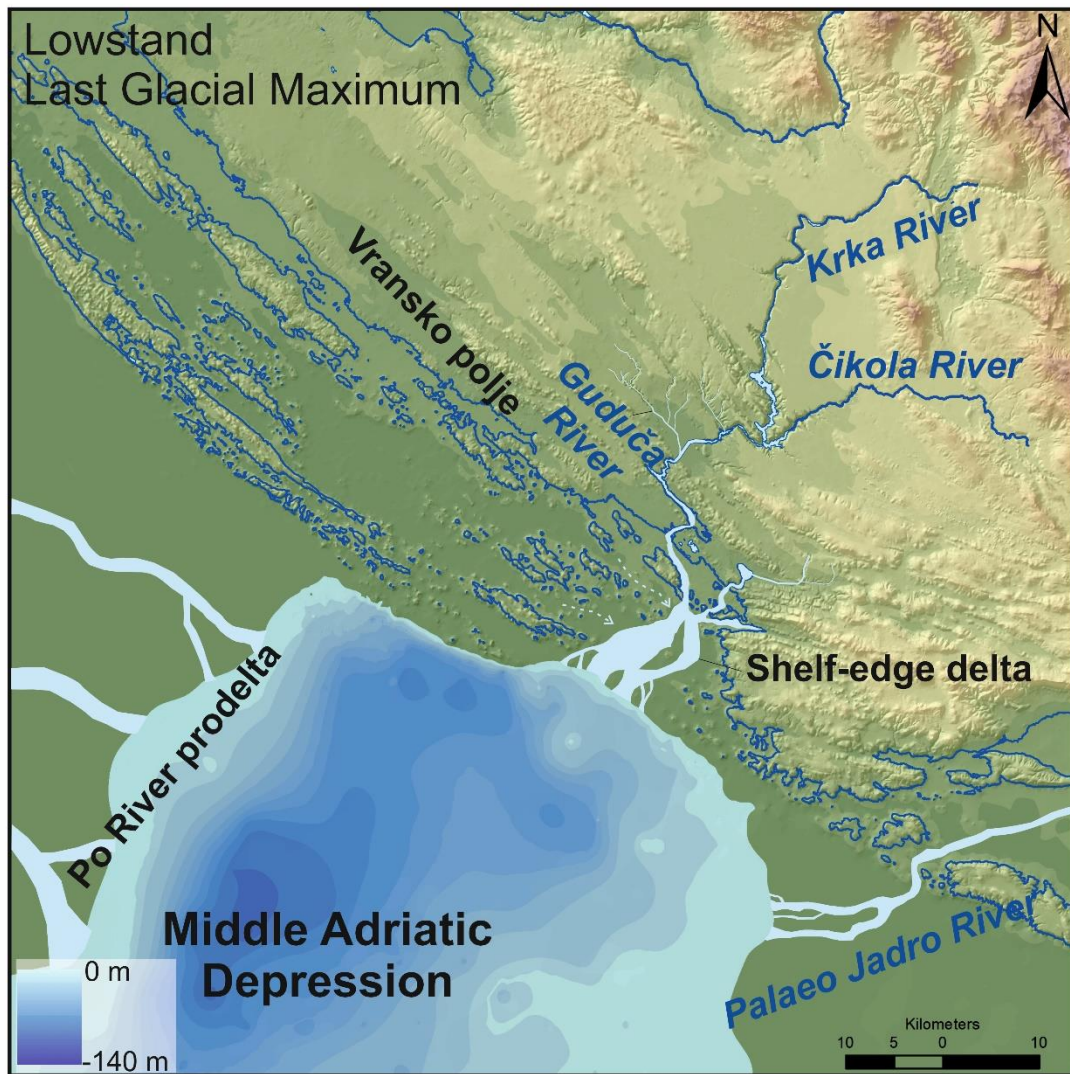


Figure 6.15 Palaeogeographic map, based on the obtained results, showing the Krka River mouth area and the evolutionary model during the lowstand period (SL-sea level). The present-day coastline is marked by a blue line.

Transgressive stage

At the end of the LGM, a rapid rise in sea level occurred between 19.0 and 7.0 kyr BP (Clark et al., 2004; Lambeck et al., 2014), changing the base levels of the rivers. Additionally, the climate had changed to a warmer climate with a rapidly rising CO₂ concentration (e.g., Clark et al., 2012), thus creating favorable conditions for the deposition of freshwater calcareous tufas (Goudie et al., 1993) since their growth is restricted to warm interglacial periods (Ford & Pedley, 1996; Horvatinčić et al., 2000; Golubić et al., 2008). A combination of several factors is necessary for calcareous tufa deposition. The water must be supersaturated with bicarbonate (HCO₃⁻), and physical and biochemical outgassing of CO₂ is necessary, but aquatic plants and microbes are also important in controlling and triggering the precipitation of CaCO₃ (Herman and Lorah, 1988; Golubić et al., 2008). The system of calcareous tufa barriers developed most probably during the postglacial transgression in the area of recent Prokljan Lake and existed for at least 8000 kyr before they were flooded in the Holocene (Fig. 6.16 and 6.17). These barriers reduced the erosional energy of the river and enabled the formation of a system of smaller-sized stagnant depositional basins (tufa lakes) between the calcareous tufa barriers with the accumulation of fluvio-lacustrine sediments (SU3), which then restricted already low sediment transport to the shelf area. Sediments of similar seismic characteristics as SU3 in Prokljan Lake were deposited in an incised channel between the mainland and the island of Zlarin.

The rapid sea-level rise caused rapid movement of the palaeo-coastline landward because of a relatively low gradient continental shelf (Fig. 5.9). The subaqueous accommodation increased faster than the compensation of low sediment accumulation during the post-glacial sea-level rise. At this time, the shelf area was characterized by flooding of incised channels and their further infilling with estuarine to marine sediment (Fig. 6.16). In addition, the rapid rise in sea level most probably reworked the surface sediments on the continental shelf and redistributed into the thin lag of the sand layer.

During the early stages of transgression, in the outer shelf area, the formerly active lowstand prograding complexes were rapidly drowned with the deposition of retrograding sigmoid clinoforms, which are most likely deposited during the transgression and highstand conditions (Fig. 6.16). Considering the lack of sediment cores and radiocarbon data in these

areas, the ages of deposition and palaeoenvironments of these deposits could only be hypothesized.

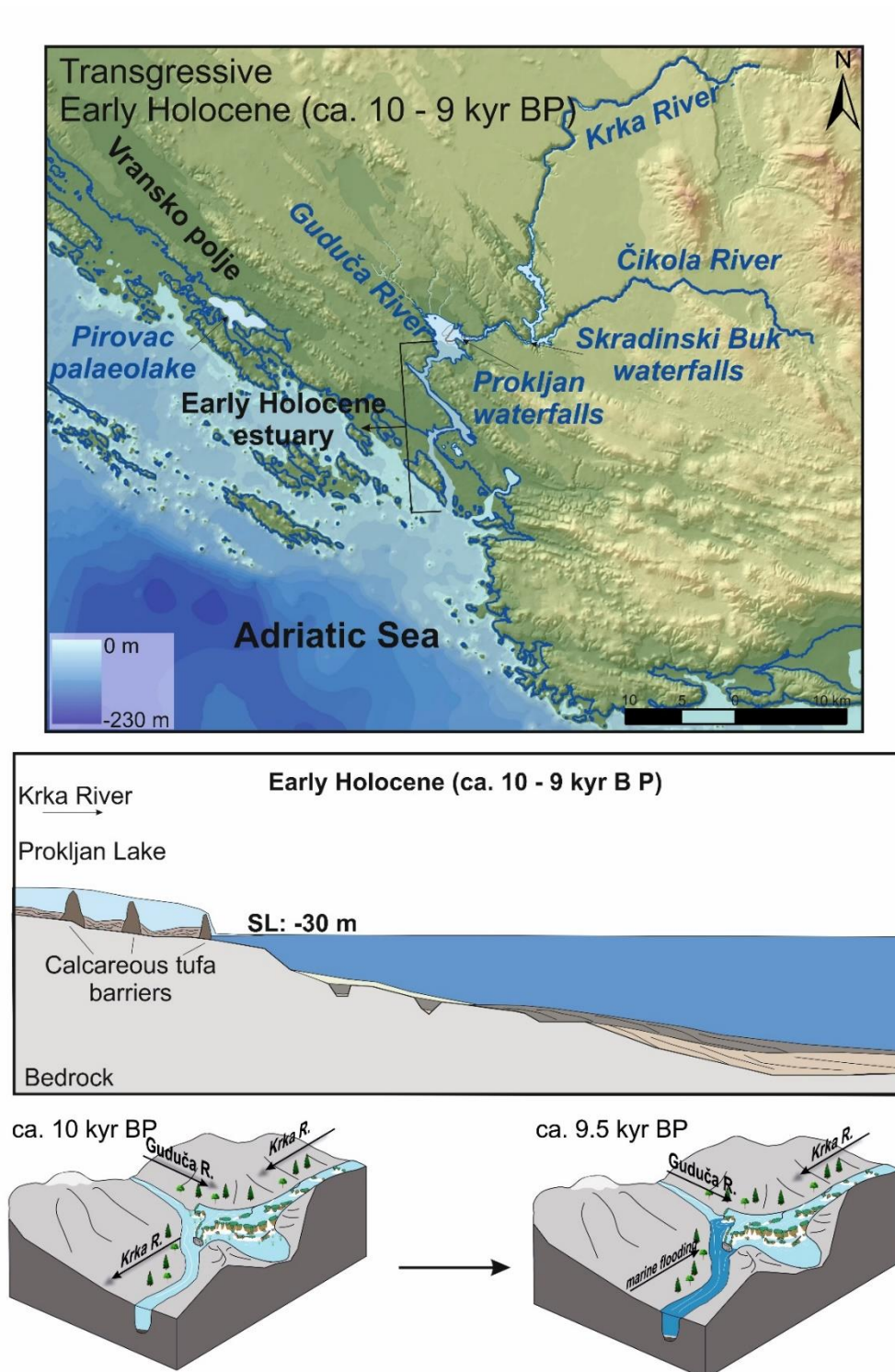


Figure 6.16. Palaeogeographic map, based on the obtained results, showing the Krka River mouth area and the evolutionary models during the transgressive period (SL-sea level). Around 9.5 kyr BP sea level gradually reaches the most southern calcareous tufa barriers. The present-day coastline is marked by a blue line.

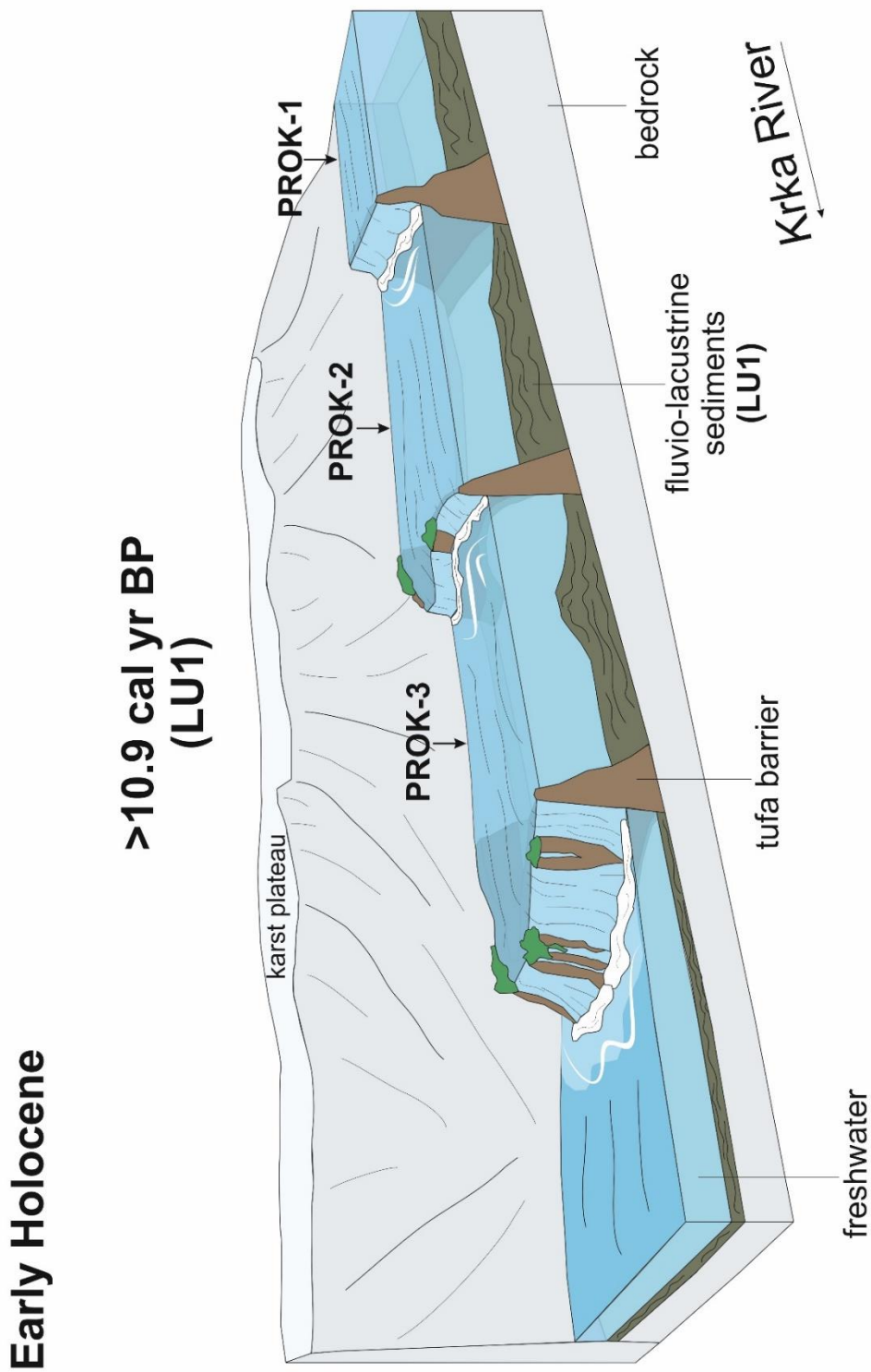


Figure 6.17 Block diagrams showing the development of the calcareous tufa barrier system during the postglacial period.

The boundary between the Pleistocene and the Holocene is the onset of the Younger Dryas (YD, 12.6–11.7 kyr BP) cold event, which was accompanied by a stillstand or even a minor fall in sea level within a general transgressive trend (Fairbanks, 1989). In the shelf area, at the valley flanks, palaeoterraces are present at approximately -55 m of depth (Fig. 5.26), which could be formed at the Younger Dryas stillstand. Additionally, within the fluvial to brackish deposits, an erosional surface can be observed in the incised valley between the mainland and the island of Zlarin (Fig. 5.23C) at the depth range of approximately 47 to 50 m bsl, which could also point to a YD period of minor regression. With further transgression, the sea flooded the areas where sediment cores ZLA-2 and ZLA-1 are located. These sediments record the transition from brackish to estuarine and marine conditions during the early Holocene. However, due to poor age constraints and age reversal, the exact timing of estuarine conditions formation remains unknown.

In the late phase of sea-level rise during the early Holocene, the sea transgressed farther landward and started to flood Prokljan Lake. The sediment core PROK-3, located in the central part of Prokljan Lake, is surrounded by a karst sill at its SE side at a depth of 15 m and a tufa barrier at its NW side at a depth of 13 m. The dark brown sediment of LU1 at the bottom of the sediment core PROK-3 (>9.8 cal kyr) was deposited in a freshwater fluviolacustrine environment (Fig. 6.17). In that period, the eustatic sea level was more than 35 m lower than the present (Lambeck et al., 2014), implying that the sea level remained below the karstified sill and calcareous tufa barrier at that time, preventing marine intrusion to the core location.

The core PROK-3 was influenced by sea-level transgression from 9.8 cal kyr BP to 8.4 cal kyr BP, with the formation of a restricted marine lake (pond; LU2; Fig. 6.18). According to the global eustatic sea-level curve and the sea-level curve for the Adriatic, the rise in sea level occurred from -37 m (9.8 kyr BP) and -17 m (8.4 kyr BP) and was below the present depth of karstified sill (-15 m) and calcareous tufa barrier (-13 m). The short-term seawater incursions and low-salinity brackish deposits can be explained by the progressive intrusion of marine water through the highly porous calcareous tufa barriers (cavities in the barriers can be cm or even up to m wide; García-del-Cura et al., 2012) and with the permeable karst, where the rise in sea level can significantly impact seawater intrusion in a coastal karst aquifer, and long-

distance seawater intrusion can occur through the subsurface conduit system as a source of groundwater contamination (Menning et al., 2015).

Similar brackish environments were recorded in the core PROK-2 from >10 cal kyr BP to 8.2 cal kyr BP (Fig. 6.18). This core is located approximately 1500 m landward from the core PROK-3 behind the calcareous tufa barrier whose crest is at a depth of approximately 13 m (Hasan et al., 2023). To explain such early marine intrusion and older brackish deposits in the core PROK-2, the presence of the freshwater reservoir effect could be considered. The terrestrial origin of the shell and the possible effect induced by older non-organic carbon, the age of the sample can be significantly overestimated. The freshwater reservoir effect can be significant in rivers and estuaries, especially in karst settings, giving much older dates (Philippsen, 2013). The marine lake was developed in the tufa lake of PROK-1 core from >7.8 to 7.5 cal kyr BP (the barrier crest is at approximately 11.5 m depth).

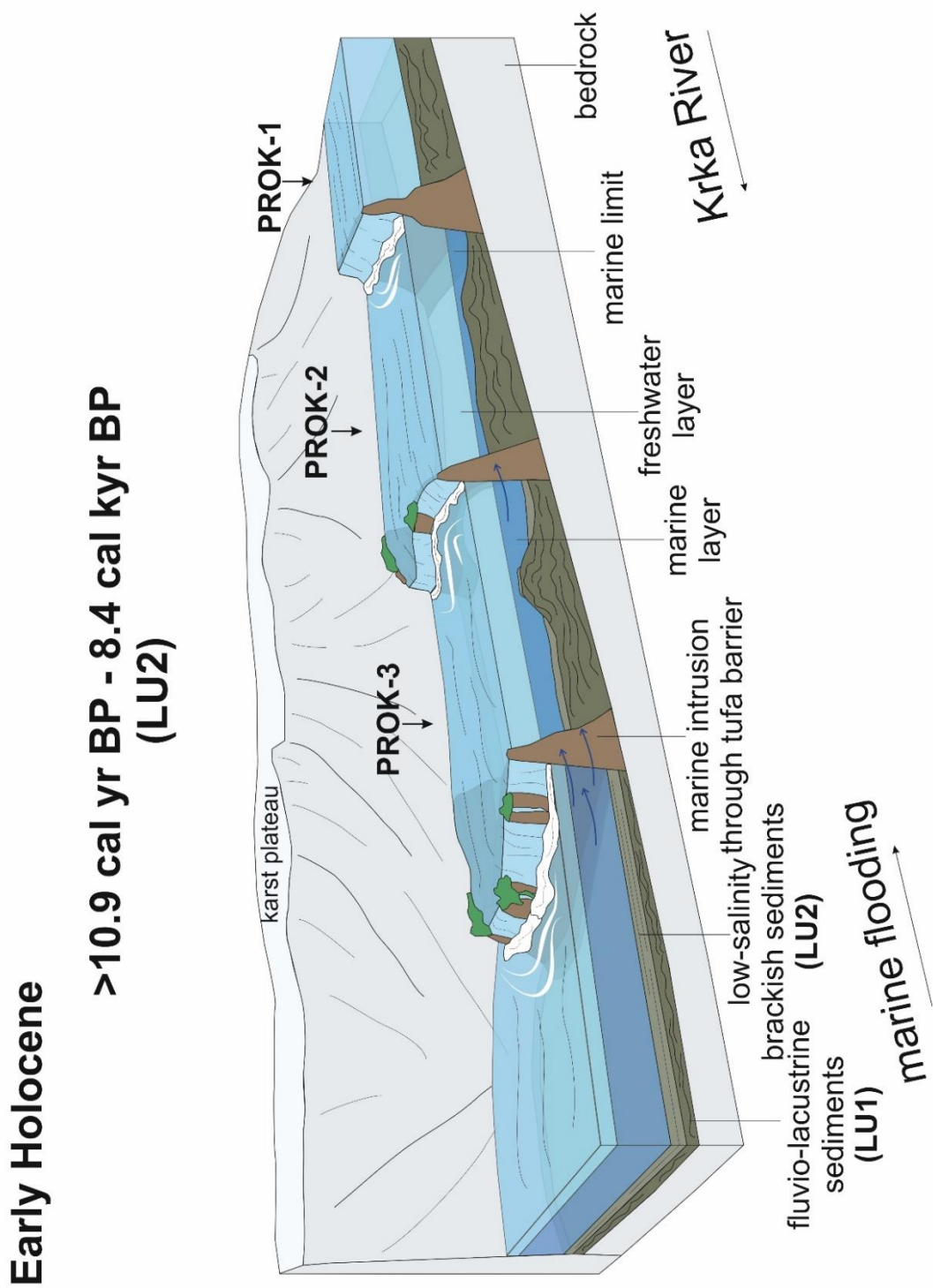


Figure 6.18 Marine intrusion through porous calcareous tufa barriers and formation of low-salinity brackish environments in the period >10.9–8.4 cal kyr BP.

A further rise in sea level during the early Holocene caused an increase in water depth and flooding of a karstified sill and calcareous tufa barriers, causing a transition in depositional environments from restricted marine ponds to the estuary (Fig. 6.19 and 6.20). The marine deposition was detected in the core PROK-3 when the karstified sill at a depth of 15 m was flooded at the age of approximately 8.4 cal kyr BP, the calcareous tufa barrier (at a depth of 13 m) surrounding the core PROK-2 began to flood at 8.2 cal kyr BP, while marine deposition in the PROK-1 core location started at 7.5 cal kyr BP (barrier at 11.5 m bsl), which agrees with the overall eustatic behavior and relative sea-level changes in the Adriatic (Antonioli et al., 2009; Lambeck et al., 2014). Based on the analyzed calcareous tufa barriers morphology and the depth of their crests, the crest of the most landward tufa barrier (B1) was found at a depth of approximately 5 m. However, two gaps have been recognized at the barrier crest at the depth of approximately 8 m, and, therefore, it could have been flooded at approximately 7.3 kyr BP.

During the middle Holocene, the rate of sea-level rise decreased (Lambeck et al., 2014). The Krka River canyon was flooded up to the Skradinski Buk waterfalls, assuming a formation of a partially mixed estuary based on multiproxy data (Fig. 6.21). The highstand conditions, which coincided with the development of salt-wedge estuarine conditions and accumulation of homogeneous estuarine to marine sediments, were developed during the late Holocene (Fig. 6.22). At the PROK-3 location, the present salt-wedge condition was formed at 3.0 cal kyr BP, whereas at the core PROK-2 location at 2.1 cal kyr BP, at the core PROK-1 location at 2.0 cal kyr BP and at the core PROK-4 location at 1.5 cal kyr BP.

A decrease in sea-level rise further reduced the sediment supply to the shelf area and the change of marine conditions that might have caused the erosion of the Pleistocene deltaic deposits at the shelf and shelf-edge (Fig. 6.20). Therefore, the shelf area can be considered an erosion-dominated shallow-marine region.

In the last 600 years, significant changes in the Krka River catchment have been observed, linked to anthropogenic activities such as the use of arable land, which caused pronounced soil erosion (terra rossa) and erosion of flysch deposits, as well as deforestation (Fig. 6.22). All these processes led to a slightly increased sediment discharge into the Krka River estuary. These processes have been previously described in Subchapter 6.3.

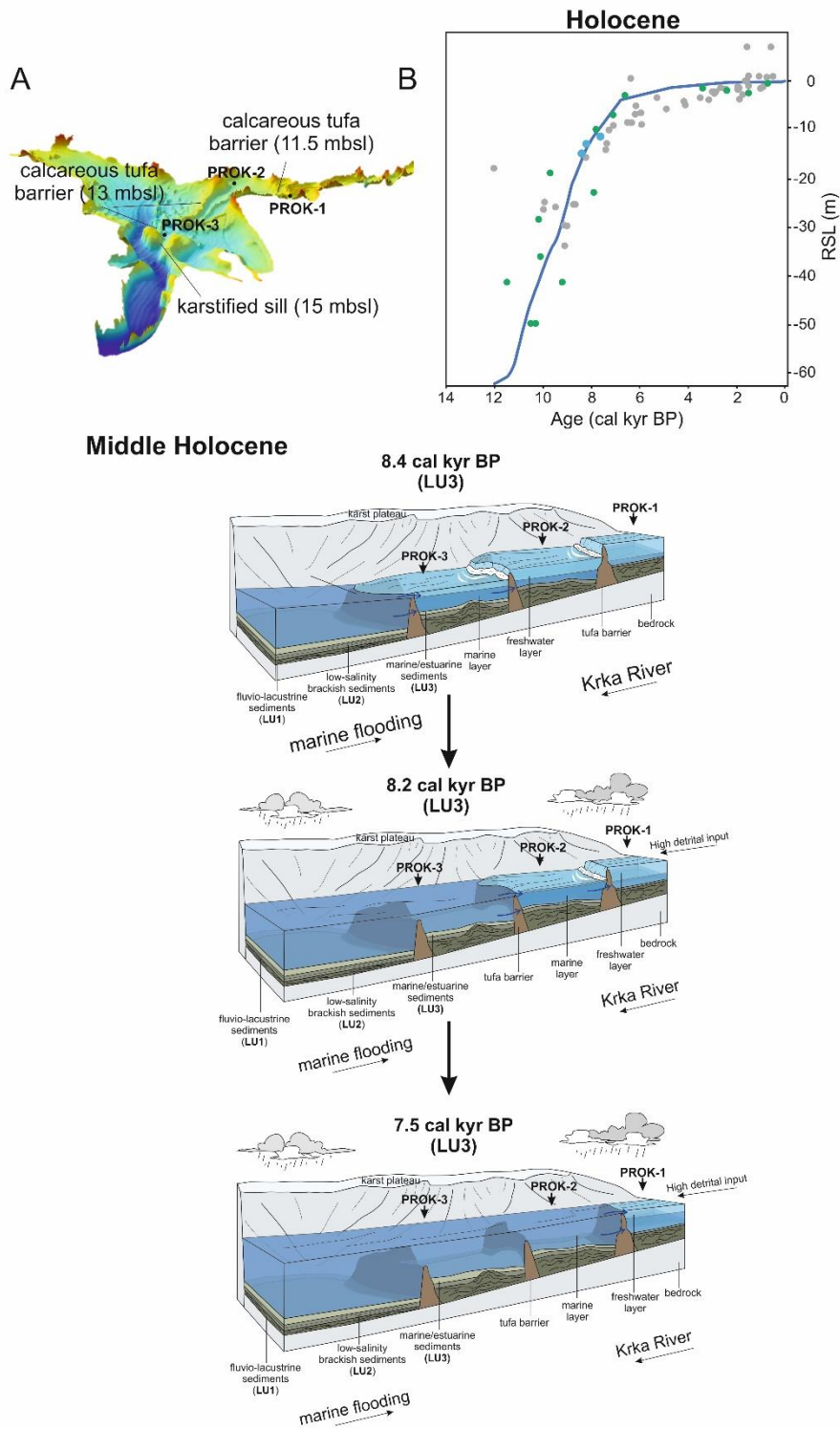


Figure 6.19 Block diagrams showing the palaeoenvironment evolution of the Krka River estuary during the middle Holocene (8.4–7.5 cal kyr BP). A Further flooding of the Krka River canyon during the pluvial period. B Relative sea-level rise during the Holocene in the Adriatic Sea (in grey; Antonioli et al., 2009) and index points from other studies along the EAC in green (Wunsam et al., 1999; Surić et al., 2005; Surić and Juračić, 2010; Faivre et al., 2013; Hasan, 2017; Razum, 2018; Brunović, 2020; Ilijanić et al., 2020) in relation to the global eustatic sea-level (esl) curve (blue; Lambeck et al., 2014), and index points from this study (light blue dots).

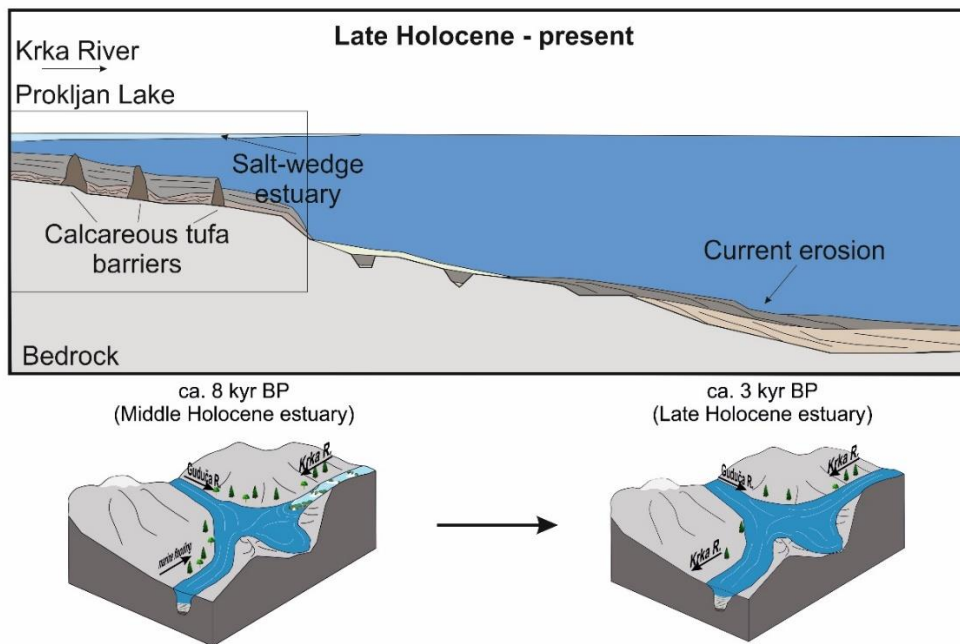


Figure 6.20 Palaeogeographic map, based on the obtained results, showing the Krka River mouth area and the evolutionary models during the highstand period.

Middle to late Holocene

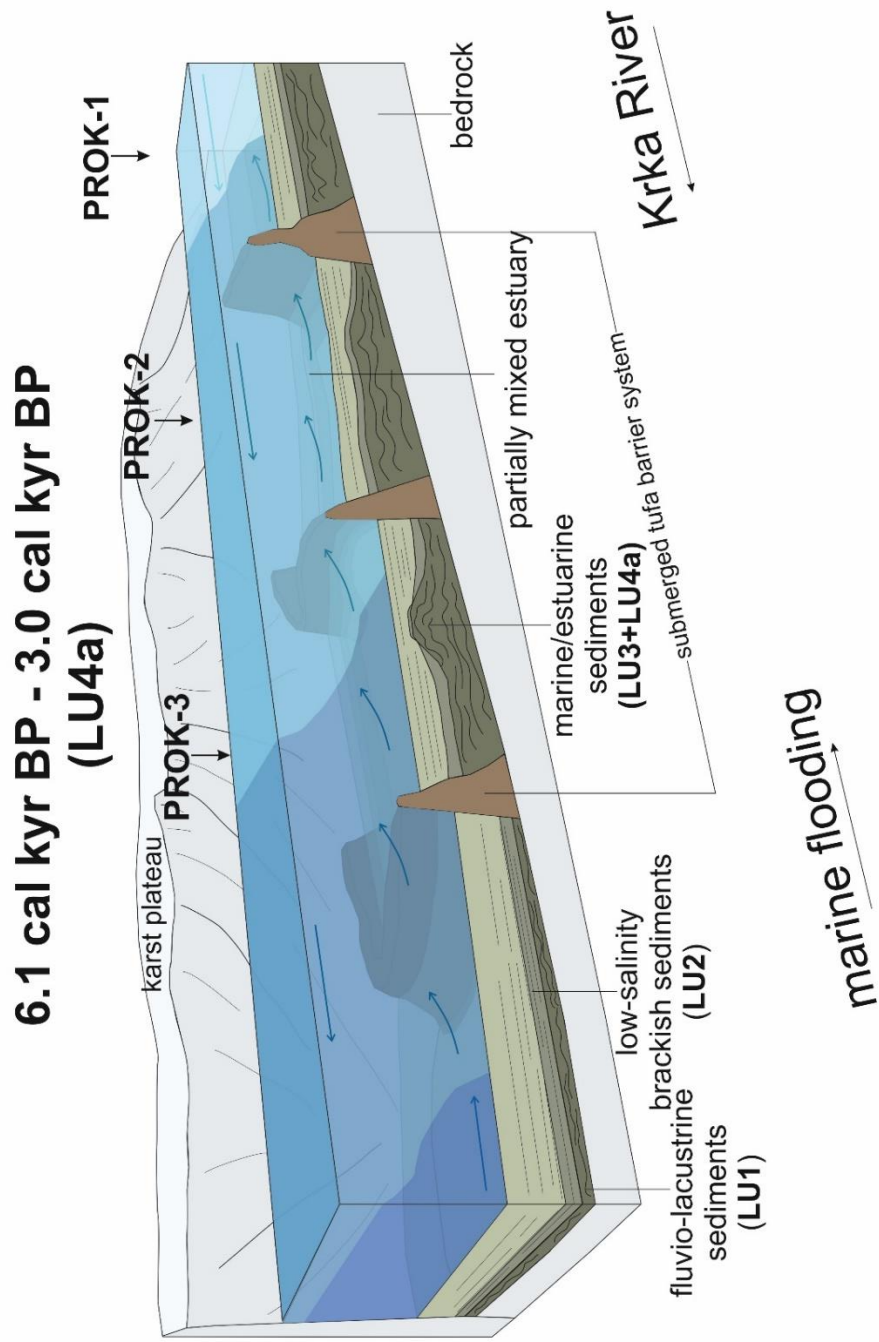


Figure 6.21 Block diagrams showing a formation of partially mixed estuary in the period 6.1 – 3.0 cal kyr BP.

Late Holocene

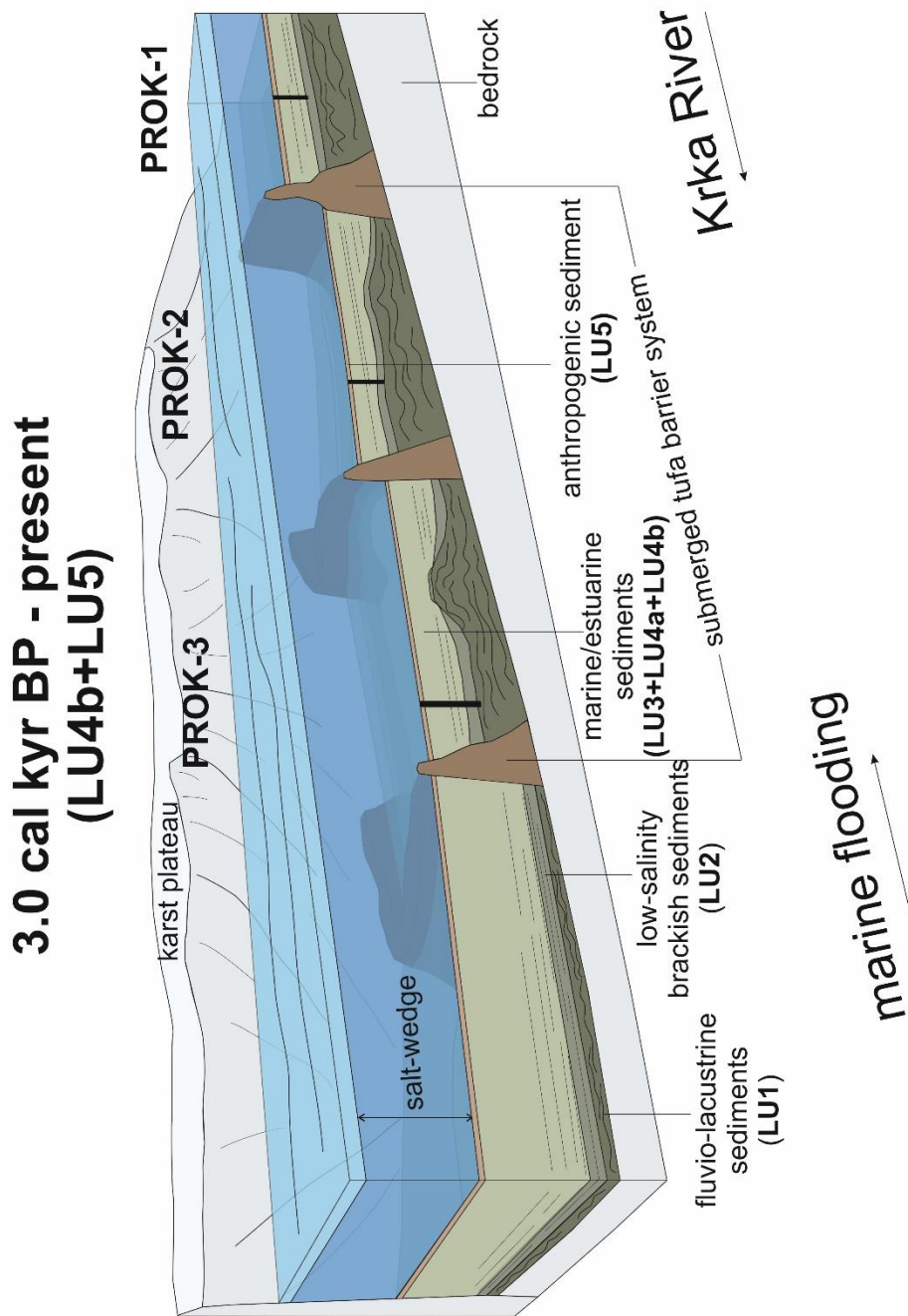


Figure 6.22 Block diagrams showing the palaeoenvironment evolution of the Krka River estuary during the late Holocene (3.0 cal kyr BP–present) and formation of present salt-wedge conditions with anthropogenic influence.

Studying the river mouths is of great importance since many processes have influenced its evolution and future changes. The Krka River drainage basin was under the influence of sea-level changes, climate, inherited (antecedent) topography, low sediment supply, and changes in hydrological regimes. It can be concluded that the sea-level variations had a first-order control on the evolution of the Krka River mouth area, where the river incision and erosion occurred during the glaciation, and low sea level removed part of previous deposits and generated new accommodation space for subsequent sea-level cycles. Whereas, during the transgressive and highstand period, vast areas were flooded with the development of larger accommodation space within the incised valley and shelf area, which led to the dominance of estuarine/marine processes.

The long-term tectonic movements (Late Cretaceous synsedimentary tectonics; Vlahović et al., 2005) in the study region have formed an area of unique geomorphology, which greatly influenced fluvial morphology and drainage pathways across the shelf and the mainland. Additionally, the mostly karst setting of the study area is a key factor controlling the stream power of the river, as well as the low sedimentary supply to the shelf area, therefore forming a sediment-starved continental shelf, which has an increased potential to preserve topographic features such as shelf valleys and canyons. No clear evidence of tectonic activity during the Quaternary has been found among the data from the Krka River mouth area. Moreover, climate changes and the karst geomorphology enabled the deposition of freshwater calcareous tufas in the form of barriers, which had a dominant influence on the sediment supply, i.e., they trapped most of the sediment in small tufa lakes, as well as they had a dominant influence on stepwise flooding of the Krka River canyon. Climatic changes also influenced higher incidences of storms and flooding, with a pluvial period recorded in estuarine sediments and a period of arid climatic conditions. Thus, the climate is also an important factor of control of the sedimentary evolution of the Krka River.

In addition to all the above-described processes that influenced the Krka River, another importance of identification of submerged terrestrial landforms and the evolution of continental Adriatic shelf could lie within the archaeological studies of human migration, which might have existed during times of lower sea level. Since coastal subaerial archaeological sites are often found along riverine terraces (Davis et al., 2004), submerged

palaeodrainages are key areas of interest for investigating early coastal migration. As such, their accurate identification and mapping are vital for improving predictive models and identifying target search areas. Understanding fluvial response to sea level fluctuations and the geologic controls on-site preservation are invaluable for these studies.

7. CONCLUSIONS

This chapter compiles the main conclusions drawn from the results and their interpretations throughout the research. Combining the geophysical and multiproxy sedimentological data coupled with radiocarbon dating data, provided the first insight into the seismic stratigraphy of the sedimentary infill and the reconstruction of geomorphological evolution and palaeoenvironments of the Krka River mouth area. The main conclusions are as follows:

The Krka River was interpreted as an incised valley with multiple incision cycles related to sea-level variations during the Pleistocene. The incision through various cycles of sea-level changes caused the erosion of older deposits and sediment bypass, transporting them to the Middle Adriatic Depression and further incision into bedrock. The bedrock is composed of Mesozoic carbonate rock (top of the carbonate platform) based on the legacy and high-resolution shallow seismics.

Deep seismic profiles gave an insight into the existence of (post Messinian) deltaic plain deposits of up to approximately 100 meters of thickness developed on a shallow shelf area during the lowstand period. The shallow seismic data provided insight into the uppermost 30 m of the sedimentary sequence in the shelf area, and the high-resolution seismic profiles recorded within the Krka River estuary up to 20 m of sedimentary infill.

LGM aluvial sediments are preserved in the deepest zone of incised channels inherited topography and the recent estuary. The postglacial infill is well preserved and displays a succession of facies recording a general transgression in the study area. Several seismic facies and units have been identified above the acoustic basement that recorded sea-level changes and allowed the palaeoenvironmental evolution during the Quaternary. Depositional environments within the incised Krka River valley system have distinct characteristics on the seismic data. It was possible to distinguish deltaic deposits (clinoforms and delta distributary channels), palaeoterraces, tufa barrier system, fluvial to fluvio-lacustrine, and estuarine to marine deposits.

The palaeoterraces recognized in the shelf area could represent a Younger Dryas period of short sea-level stillstand or slowly rising sea level.

Results from this study have also provided a conceptual model for the geomorphic evolution of an oligotrophic salt-wedge karst estuary on the EAC. This unique and geomorphologically complex karst setting and its sedimentary infill were affected by multiple factors, including postglacial sea-level rise and climate, the palaeo-morphology of the valley bedrock, the preservation and morphology of the postglacial tufa barriers, sediment supply from the Krka River and its tributaries, and changes in hydrodynamics.

During the lowstand erosive period, the study area was a river valley with two main fluvial channels incised into remnants of the antecedent land surface. The infilling of these channels most likely occurred during the postglacial transgression. The transgression in the late Pleistocene led to a change in the base level of rivers, forcing the conversion of river valleys into estuaries and, with further sea-level rise, into a dominantly marine environment. The sediment cores ZLA-1 and ZLA-2 allowed an interpretation of geophysical data on the shelf area.

The estuarine environments developed during the late Pleistocene and early Holocene between the island of Zlarin and the mainland and subsequently moved inland due to relative sea-level rise, whereas the flooding of Prokljan Lake occurred during the Holocene.

During the postglacial (warmer) climate change with a rapidly rising CO₂ concentration, favorable conditions developed for tufa deposition in the area of Prokljan Lake and the upstream tract of the river canyon up to the town of Skradin. Calcareous tufas developed into barrier formations, dividing the river canyon and allowing the formation of smaller-sized lake basins. These calcareous tufa lakes reduced the river stream power and enabled a higher deposition of fluvio-lacustrine sediment. The remnant tufa barrier system had a significant influence on the stepwise marine flooding of the estuary.

The depth of tufa barrier crests in connection to the marine sediments within the estuary could be used as an indicator of sea level since the calcareous tufa formation stopped due to marine flooding.

Multi-proxy analyses of four sediment cores collected in an upstream tract of the estuary allowed the reconstruction of its Holocene palaeoenvironmental evolution. The

fossils provided insight into the marine or brackish community, whereas sedimentology and geochemistry gave insight into estuarine hydrological changes related to sea-level and climatic conditions. The cores share generally similar features in terms of stratigraphic trends. Above bedrock in the estuarine area, the postglacial succession shows a depositional architecture of transgressive deposits of fluvio-lacustrine to estuarine facies. During the early Holocene, marine flooding occurred in the Krka River estuary. The tufa barriers restricted direct marine ingression with a formation of slightly brackish tufa lakes, which were developed between the tufa barriers. The sea flooded the calcareous tufa barriers during the middle Holocene (8.7–7 cal kyr BP) with a formation of a partially mixed estuary. Higher input of terrigenous component and negative low $\delta^{18}\text{O}_{\text{cal}}$ point to higher erosion and generally wetter climate (pluvial period) during the early and first part of the middle Holocene. After 6 ka BP and during the late Holocene, arid climatic conditions occurred. The present salt-wedge estuarine conditions emerged during sea-level stabilization in the late Holocene (3–1.5 cal kyr BP) in the uppermost tract of the estuary.

In the last 600 years, significant changes have been visible in the Krka River basin, with significant erosion from the catchment related to increased human population activities (deforestation and agriculture). Heavy metal (Cu, Zn and Pb) enrichment was observed in the most recent sediments (top 15-20 cm). Sediment geochemistry in the cores did not record earlier human activities in the catchment (Roman period, or Bronze and Neolithic periods).

This doctoral research study provides a geological framework for understanding karst subterranean estuaries by preserving proxies of biogeochemical reaction zones between land and sea.

8. EXTENDED ABSTRACT

Klimatske promjene te promjene morske razine tijekom kvartara znatno su utjecale na evoluciju obalnih okoliša. Riječna ušća, kao plitka obalna područja, pod utjecajem su stalnih izmjena kopnenih i marinskih uvjeta s obzirom da je njihov nastanak vezan za niz procesa koji uključuju usijecanje riječnog toka te stvaranje novog taložnog prostora i njihove ispune. Sedimentacija se odvija u vodama različitog saliniteta te je vezana za riječne procese, utjecaja plime i oseke i valova. Kao takva, smatraju se jednim od najkompleksnijih geomorfoloških obalnih okoliša te su vrlo značajni u paleookolišnim istraživanjima te istraživanjima relativnih promjena morske razine, a koje su vezane i za klimatske promjene. Posebno osjetljiva na ove promjene su krška područja, čiji je veliki dio danas potopljen zbog postglacijalnog porasta morske razine. Stjenovita istočna obala Jadranskog mora građena je predominantno od okršenih karbonata s brojnim potopljenim krškim oblicima, kao što su npr. potopljeni kanjoni krških rijeka, odnosno krški estuariji. Krški estuariji predstavljaju okoliše niske energije te su pod malim utjecajem plimnih oscilacija. Zbog toga njihova stratigrafija odstupa od klasičnih modela ispuna estuarija koji su pod dominantnim utjecajem plima ili valova. U ovoj disertaciji prikazana je paleookolišna evolucija područja krškog riječnog ušća Krke tijekom kasnog pleistocena i holocena. Paleookolišna rekonstrukcija istraživana je „multiproxy“ analizom sedimentnih jezgri i geofizičkim podacima.

Na području plitkog šelfnog mora te recentnog estuarija rijeke Krke provedena su geofizička istraživanja, koja su se sastojala od snimanja površine morskog dna višeslojnim te panoramskim dubinomjerom, a potpovršina, odnosno uvid u stratigrafski slijed dobiven je primjenom geoloških dubinomjera (seizmika). Batimetrijska istraživanja na području šelfa ukazala su na postojanje generalno zaravnjenog šelfnog morskog dna s različitim geomorfološkim strukturama, odnosno utvrđeni su usječeni paleo-kanali rijeke Krke tu su prisutna kamenita područja te sitnozrnati i krupnozrnati sediment. Na morskome dnu estuarija identificirane su različite geomorfološke strukture, a to su usječeni paleo-kanjoni rijeke Krke i Guduče te otprilike 3.5 km dug sustav potopljenih sedrenih barijera koje se nalaze na dubinama između 5 i 20 m. Ukupno je snimljeno 37 seizmičkih profila na šelfnom području, gdje se smatra da postoji pleistocenska deltna ravnica rijeke Krke te 119 seizmičkih profila u recentnom estuariju rijeke Krke i u potopljenom kanjonu koji se nalazi između kopna i otoka

Zlarina i Drvenika. Utvrđeno je postojanje sedimentnog slijeda debljine do otprilike 100 m u potpovršini deltnih naslaga, dok je visoko-rezolucijska plitka seizmika dala uvid u najgornjih 30 m sedimentata. Na području estuarija utvrđen je sedimentni slijed debljine do 20 m.

Na temelju seizmičkih podataka te geomorfološki kompleksnog područja, određeno je nekoliko lokacija na kojima su prikupljene sedimentne jezgre. Interpretacija 6 sedimentnih jezgri zasnivala se na „multiproxy“ analizi. Na šelfnom području te usječenom paleokanjonu između kopna i otoka Zlarina, prikupljene su 2 sedimentne jezgre (ZLA-1, ZLA-2), dok su preostale 4 jezgre (PROK-1, PROK-2, PROK-3, PROK-4) izbušene na području Prokljanskog jezera te potopljenog kanjona uzvodno od Prokljanskog jezera do Skradina. Jezgre su uzorkovane na ovim područjima s ciljem utvrđivanja različitih procesa koji su utjecali na paleookolišnu evoluciju istraživanog područja te utvrđivanja relativnih promjena morske razine. Na sedimentnim jezgrama napravljena su mjerenja boje sedimenta, magnetskog susceptibiliteta, ukupne gustoće sedimenta, određena je veličina čestica, mineralni sastav, geokemijski sastav (μ XRF, ICP-MS, organski i anorganski ugljik, izotopni sastav autigenih karbonata te organske tvari) te su provedene mikropaleontološke analize (zajednice foraminifera i ostrakoda). Kronologija sedimenta utvrđena je pomoću datiranja metodom radioaktivnog ugljika (AMS ^{14}C) te su napravljene kronološki modeli za jezgre PROK-1, PROK-2, PROK-3 i PROK-4.

Geofizički i sedimentološki podaci omogućili su rekonstrukciju paleookolišnog razvoja ušća rijeke Krke koji je povezan s oscilacijama morske razine od posljednje niske razine mora te su utvrđene dinamične paleohidrološke promjene u estuariju rijeke Krke tijekom holocena. Krški kanjon rijeke Krke najvjerojatnije je usijecan tijekom posljednje niske razine mora, erodirajući starije naslage do karbonatne podloge, dok se transport sedimenta i njegovo taloženje odvijao na deltnoj ravnici te rubu šelfa prema padini Srednjo-jadranske depresije. Na kraju posljednjeg glacijalnog maksimuma (prije otprilike 19000 godina) dolazi do globalne transgresije koja je uzorkovala potapanje deltne ravnice te estuarijsku sedimentaciju na području šelfa. Dok su se uzvodno na području današnjeg Prokljanskog jezera i uzvodno od jezera formirale sedrene barijere (i sedrena jezera) koje su smanjile erozivnu moć rijeke te omogućile taloženje fluvijalno-jezerskog sedimenta. Tijekom ranog holocena dolazi do potapanja dijela Prokljanskog jezera te taloženja brakičnih estuarijskih naslaga. Sedrene barijere onemogućile su direktno poplavlivanje paleo-kanjona te su se formirali slabo brakični

okoliši u sedrenim jezerima tijekom ranog i dijelom srednjeg holocena. Ingresija mora dogodila se kroz porozne sedrene barijere, ali i okršenu karbonatnu podlogu. Tijekom srednjeg holocena, u periodu od 8300 do 7300 kalendarskih godina prije sadašnjosti, dogodilo se poplavljanje sedrenih barijera te su se formirali djelomično miješani estuarijski uvjeti. Također, u periodu od otprilike 8300 do 6100 kalendarskih godina prije sadašnjosti utvrđen je pluvijalni period u PROK sedimentnim jezgrama. Tijekom kasnog holocena (3000–1500 kalendarskih godina prije sadašnjosti) dolazi do formiranja današnjih estuarijskih uvjeta, odnosno formiranja klina morske vode. U posljednjih 600 godina u estuarijskim sedimentima zabilježena je pojačana antropogena aktivnost i erozija sliva rijeke Krke.

9. REFERENCES

- Abraham, G.M.S. and Parker, R.J. (2007): Assessment of heavy metal enrichment factors and the degree of contamination in marine sediments from Tamaki Estuary, Auckland, New Zealand. *Environ. Monit. Assess.* 136, 227–238. <https://doi.org/10.1007/s10661-007-9678-2>
- Aitchison, J. (1986): *The Statistical Analysis of Compositional Data*. Springer Netherlands, Dordrecht. <https://doi.org/10.1007/978-94-009-4109-0>
- Aitchison, J. (1982): *The Statistical Analysis of Compositional Data*. *J. R. Stat. Soc. Ser. B Stat. Methodol.* 44, 139–160. <https://doi.org/10.1111/j.2517-6161.1982.tb01195.x>
- Aitchison, J. and Greenacre, M. (2002): Biplots of Compositional Data. *J. R. Stat. Soc. Ser. C Appl. Stat.* 51, 375–392. <https://doi.org/10.1111/1467-9876.00275>
- Alberico, I., Giliberti, I., Insinga, D.D., Petrosino, P., Vallefucio, M., Lirer, F., Bonomo, S., Cascella, A., Anzalone, E., Barra, R., Marsella, E. and Ferraro, L. (2017): Marine sediment cores database for the Mediterranean Basin: a tool for past climatic and environmental studies. *Open Geosci.* 9. <https://doi.org/10.1515/geo-2017-0019>
- Algeo, T.J. and Lyons, T.W. (2006): Mo–total organic carbon covariation in modern anoxic marine environments: Implications for analysis of paleoredox and paleohydrographic conditions. *Paleoceanography* 21. <https://doi.org/10.1029/2004PA001112>
- Allen, G.P. and Posamentier, H.W. (1993): Sequence stratigraphy and facies model of an incised valley fill: the Gironde Estuary, France. *J. Sediment. Petrol.* 63, 378–391. <https://doi.org/10.1306/D4267B09-2B26-11D7-8648000102C1865D>
- Amorosi, A., Fontana, A., Antonioli, F., Primon, S. and Bondesan, A. (2008): Post-LGM sedimentation and Holocene shoreline evolution in the NW Adriatic coastal area. *GeoActa* 7, 41–67.
- Amorosi, A., Colalongo, M., Fiorini, F., Fusco, F., Pasini, G., Vaiani, S. and Sarti, G. (2004): Palaeogeographic and palaeoclimatic evolution of the Po Plain from 150-ky core

records. *Glob. Planet. Change* 40, 55–78. [https://doi.org/10.1016/S0921-8181\(03\)00098-5](https://doi.org/10.1016/S0921-8181(03)00098-5)

Amorosi, A., Maselli, V. and Trincardi, F. (2016): Onshore to offshore anatomy of a late Quaternary source-to-sink system (Po Plain–Adriatic Sea, Italy). *Earth-Science Rev.* 153, 212–237. <https://doi.org/10.1016/j.earscirev.2015.10.010>

Anderson, H. and Jackson, J. (1987): Active tectonics of the Adriatic Region. *Geophys. J. Int.* 91, 937–983. <https://doi.org/10.1111/j.1365-246X.1987.tb01675.x>

Antonioli, F., Anzidei, M., Lambeck, K., Auriemma, R., Gaddi, D., Furlani, S., Orrù, P., Solinas, E., Gaspari, A., Karinja, S., Kovačić, V. and Surace, L. (2007): Sea-level change during the Holocene in Sardinia and in the northeastern Adriatic (central Mediterranean Sea) from archaeological and geomorphological data. *Quat. Sci. Rev.* 26, 2463–2486. <https://doi.org/10.1016/j.quascirev.2007.06.022>

Antonioli, F., Ferranti, L., Fontana, A., Amorosi, A., Bondesan, A., Braitenberg, C., Dutton, A., Fontolan, G., Furlani, S., Lambeck, K., Mastronuzzi, G., Monaco, C., Spada, G. and Stocchi, P. (2009): Holocene relative sea-level changes and vertical movements along the Italian and Istrian coastlines. *Quat. Int.* 206, 102–133. <https://doi.org/10.1016/j.quaint.2008.11.008>

Babić, L. and Zupanič, J. (2012): Laterally variable development of a basin-wide transgressive unit of the North Dalmatian foreland basin (Eocene, Dinarides, Croatia). *Geol. Croat.* 65, 1–27. <https://doi.org/10.4154/gc.2012.01>

Badr, N.B.E., El-Fiky, A.A., Mostafa, A.R. and Al-Mur, B.A. (2009): Metal pollution records in core sediments of some Red Sea coastal areas, Kingdom of Saudi Arabia. *Environ. Monit. Assess.* 155, 509–526. <https://doi.org/10.1007/s10661-008-0452-x>

Balsam, W.L., Deaton, B.C. and Damuth, J.E. (1999): Evaluating optical lightness as a proxy for carbonate content in marine sediment cores. *Mar. Geol.* 161, 141–153. [https://doi.org/10.1016/S0025-3227\(99\)00037-7](https://doi.org/10.1016/S0025-3227(99)00037-7)

- Bechor, B., Sivan, D., Miko, S., Hasan, O., Grisonic, M., Rossi, I.R., Lorentzen, B., Artioli, G., Ricci, G., Ivelja, T., Spada, G. and Brook, A. (2020): Salt pans as a new archaeological sea-level proxy: A test case from Dalmatia, Croatia. *Quat. Sci. Rev.* 250, 106680. <https://doi.org/10.1016/j.quascirev.2020.106680>
- Bechor, B., Avnaim-Katav, S., Mischke, S., Miko, S., Hasan, O., Grisonic, M., Radić Rossi, I., Herut, B., Taha, N., Porat, N. and Sivan, D. (2023): How can past sea level be evaluated from traces of anthropogenic layers in ancient salt pans. *PLoS ONE* 18(7), 23. <https://doi.org/10.1371/journal.pone.0287977>
- Bekić, L., Pešić, M., Scholz, R. and Meštrov, M. (2015): Podvodna arheološka istraživanja na prapovijesnom nalazištu Pakoštane – Janice. *Diadora Glas. Arheol. muzeja u Zadru* 29, 7–22.
- Benac, Č. and Juračić, M. (1998): Geomorphological indicators of sea level changes during upper pleistocene (Würm) and holocene in the Kvarner region (NE Adriatic Sea). *Acta Geogr. Croat.* 33, 27–45.
- Benjamin, J., Rovere, A., Fontana, A., Furlani, S., Vacchi, M., Inglis, R.H., Galili, E., Antonioli, F., Sivan, D., Miko, S., Mourtzas, N., Felja, I., Meredith-Williams, M., Goodman-Tchernov, B., Kolaiti, E., Anzidei, M. and Gehrels, R. (2017): Late Quaternary sea-level changes and early human societies in the central and eastern Mediterranean Basin: An interdisciplinary review. *Quat. Int.* 449, 29–57. <https://doi.org/10.1016/j.quaint.2017.06.025>
- Bianchi, T. S. and Canuel, E.A. (2011): *Chemical Biomarkers in Aquatic Ecosystems*. Princeton University Press, 392. <https://doi.org/10.2138/am.2012.592>
- Blaauw, M. and Christen, J.A. (2011): Flexible paleoclimate age-depth models using an autoregressive gamma process. *Bayesian Anal.* 6. <https://doi.org/10.1214/11-BA618>
- Blondel, P. (2009): *The Handbook of Sidescan Sonar*. Springer Berlin Heidelberg, Berlin, Heidelberg, 316. <https://doi.org/10.1007/978-3-540-49886-5>

- Blott, S.J. and Pye, K. (2001): Gradstat: A grain size distribution and statistics package for the analysis of unconsolidated sediments. *Earth Surf. Process. Landforms* 26, 1237–1248. <https://doi.org/10.1002/esp.261>
- Blum, M., Martin, J., Milliken, K. and Garvin, M. (2013): Paleovalley systems: Insights from Quaternary analogs and experiments. *Earth-Science Rev.* 116, 128–169. <https://doi.org/10.1016/j.earscirev.2012.09.003>
- Blum, M.D. and Hattier-Womack, J. (2009): Climate Change, Sea-Level Change, and Fluvial Sediment Supply to Deepwater Depositional Systems, In: Kneller, B., Martinsen, O.J., McCaffrey, B. (Eds.), *External Controls of Deep-Water Depositional Systems*. SEPM (Society for Sedimentary Geology), pp. 15–39. <https://doi.org/10.2110/sepm.092.015>
- Blum, M.D. and Törnqvist, T.E. (2000): Fluvial responses to climate and sea-level change: a review and look forward. *Sedimentology* 47, 2–48. <https://doi.org/10.1046/j.1365-3091.2000.00008.x>
- Boetto, G. and Radić Rossi, I. (2012): Šivani brod u uvali Caski na otoku Pagu: Rezultati istraživačke kampanje 2011. *Histria Antiq.* 21, 609–622.
- Bonacci, O., Andrić, I. and Roje-Bonacci, T. (2017): Hydrological analysis of Skradinski Buk tufa waterfall (Krka River, Dinaric karst, Croatia). *Environ. Earth Sci.* 76, 669. <https://doi.org/10.1007/s12665-017-7023-9>
- Bonacci, O., Jukić, D. and Ljubenković, I. (2006): Definition of catchment area in karst: case of the rivers Krčić and Krka, Croatia. *Hydrol. Sci. J.* 51, 682–699. <https://doi.org/10.1623/hysj.51.4.682>
- Boschi, F. (2011): Geophysical Survey of the Burnum Archaeological Site, Croatia. *Archaeol. Prospect.* 18, 117–126. <https://doi.org/10.1002/arp.410>
- Boyd, R., Dalrymple, R. and Zaitlin, B.A. (1992): Classification of clastic coastal depositional environments. *Sediment. Geol.* 80, 139–150. <https://doi.org/10.1016/0037->

0738(92)90037-R

- Boyd, R., Dalrymple, R.W. and Zaitlin, B.A. (2006): Estuarine and Incised-Valley Facies Models, in: *Facies Models Revisited*. SEPM (Society for Sedimentary Geology), 171–235. <https://doi.org/10.2110/pec.06.84.0171>
- Brown, C.J., Beaudoin, J., Brissette, M. and Gazzola, V. (2019): Multispectral multibeam echo sounder backscatter as a tool for improved seafloor characterization. *Geosci.*, 126. <https://doi.org/10.3390/geosciences9030126>
- Brunović, D. (2020): Morska i jezerska sedimentacija u potopljenom krškom bazenu: Taložni sustav Lošinjskoga kanala tijekom kasnog kvartara. Doctoral Thesis, Faculty of Science, University of Zagreb, 355.
- Brunović, D., Hasan, O., Miko, S., Georgiou, N., Geraga, M., Christodoulou, D., Dimas, X., Ilijanić, N. and Papatheodorou, G. (2024): High-resolution seismic record of the Quaternary palaeoenvironments along a Dalmatian-type coast (Lošinj Channel, Adriatic Sea). *Mar. Geol.* 474, 107325. <https://doi.org/10.1016/j.margeo.2024.107325>
- Brunović, D., Miko, S., Hasan, O., Papatheodorou, G., Ilijanić, N., Miserocchi, S., Correggiari, A. and Geraga, M. (2020): Late Pleistocene and Holocene paleoenvironmental reconstruction of a drowned karst isolation basin (Lošinj Channel, NE Adriatic Sea). *Palaeogeogr. Palaeoclimatol. Palaeoecol.* 544, 109587. <https://doi.org/10.1016/j.palaeo.2020.109587>
- Brunović, D., Miko, S., Ilijanić, N., Peh, Z., Hasan, O., Kolar, T., Šparica Miko, M and Razum, I. (2019): Holocene foraminiferal and geochemical records in the coastal karst dolines of Cres island, Croatia. *Geol. Croat.* 72, 19–42. <https://doi.org/10.4154/gc.2019.02>
- Bufarale, G., O’Leary, M., Stevens, A. and Collins, L.B. (2017): Sea level controls on palaeochannel development within the Swan River estuary during the Late Pleistocene to Holocene. *CATENA* 153, 131–142. <https://doi.org/10.1016/j.catena.2017.02.008>
- Buhl-Mortensen, L., Buhl-Mortensen, P., Dolan, M.F.J. and Holte, B. (2015): The MAREANO

- programme – A full coverage mapping of the Norwegian off-shore benthic environment and fauna. *Mar. Biol. Res.* 11, 4–17. <https://doi.org/10.1080/17451000.2014.952312>
- Buljan, M. (1969): Neka hidrografska svojstva estuarnih područja rijeka Krke i Zrmanje. *Krš jugoslavije* 20, 303–326.
- Burić, Z., Cetinić, I., Viličić, D., Mihalić, K.C., Carić, M. and Olujić, G. (2007):. Spatial and temporal distribution of phytoplankton in a highly stratified estuary (Zrmanja, Adriatic Sea). *Mar. Ecol.* 28, 169–177. <https://doi.org/10.1111/j.1439-0485.2007.00180.x>
- Carlotto, M.J. (2009): Effect of errors in ground truth on classification accuracy. *Int. J. Remote Sens.* 30, 4831–4849. <https://doi.org/10.1080/01431160802672864>
- Cattaneo, A. and Steel, R.J. (2003): Transgressive deposits: a review of their variability. *Earth-Science Rev.* 62, 187–228. [https://doi.org/10.1016/S0012-8252\(02\)00134-4](https://doi.org/10.1016/S0012-8252(02)00134-4)
- Cesarik, N. (2018): Pre-Roman and Roman Burnum: Some Remarks, and New Evidence of the Auxiliary Fort at Čučevo. *J. Anc. Hist. Archaeol.* 5. <https://doi.org/10.14795/j.v5i4.349>
- Chaumillon, E., Proust, J.-N., Menier, D. and Weber, N. (2008): Incised-valley morphologies and sedimentary-fills within the inner shelf of the Bay of Biscay (France): A synthesis. *J. Mar. Syst.* 72, 383–396. <https://doi.org/10.1016/j.jmarsys.2007.05.014>
- Chaumillon, E., Tessier, B. and Reynaud, J.Y. (2010): Stratigraphic records and variability of incised valleys and estuaries along French coasts. *Bull. la Société Géologique Fr.* 181, 75–85. <https://doi.org/10.2113/gssgfbull.181.2.75>
- Chayes, F. (1960): On correlation between variables of constant sum. *J. Geophys. Res.* 65, 4185–4193. <https://doi.org/10.1029/JZ065i012p04185>
- Chen, J., Zhang, D.D., Wang, S., Xiao, T. and Huang, R. (2004): Factors controlling tufa deposition in natural waters at waterfall sites. *Sediment. Geol.* 166, 353–366. <https://doi.org/10.1016/j.sedgeo.2004.02.003>

- Cimerman, F. and Langer, M.R. (1991): Mediterranean Foraminifera. Slov. Akad. Znan. Ljubljana.
- Cindrić, A.-M., Garnier, C., Oursel, B., Pižeta, I. and Omanović, D. (2015): Evidencing the natural and anthropogenic processes controlling trace metals dynamic in a highly stratified estuary: The Krka River estuary (Adriatic, Croatia). *Mar. Pollut. Bull.* 94, 199–216. <https://doi.org/10.1016/j.marpolbul.2015.02.029>
- Clark, P.U., Dyke, A.S., Shakun, J.D., Carlson, A.E., Clark, J., Wohlfarth, B., Mitrovica, J.X., Hostetler, S.W. and McCabe, A.M. (2009): The Last Glacial Maximum. *Science*, 325, 710–714. <https://doi.org/10.1126/science.1172873>
- Clark, P.U., McCabe, A.M., Mix, A.C. and Weaver, A.J. (2004): Rapid Rise of Sea Level 19,000 Years Ago and Its Global Implications. *Science*, 304, 1141–1144. <https://doi.org/10.1126/science.1094449>
- Clark, P.U., Shakun, J.D., Baker, P.A., Bartlein, P.J., Brewer, S., Brook, E., Carlson, A.E., Cheng, H., Kaufman, D.S., Liu, Z., Marchitto, T.M., Mix, A.C., Morrill, C., Otto-Bliesner, B.L., Pahnke, K., Russell, J.M., Whitlock, C., Adkins, J.F., Blois, J.L., Clark, J., Colman, S.M., Curry, W.B., Flower, B.P., He, F., Johnson, T.C., Lynch-Stieglitz, J., Markgraf, V., McManus, J., Mitrovica, J.X., Moreno, P.I. and Williams, J.W. (2012): Global climate evolution during the last deglaciation. *Proc. Natl. Acad. Sci.* 109. <https://doi.org/10.1073/pnas.1116619109>
- Coggan, R., Populus, J., White, J., Sheehan, K., Fitzpatrick, F. and Piel, S. (2007): Review of standards and protocols for seabed habitat mapping. *Mesh* 244.
- Collier, J. and McGonigle, C. (2011): Examining the relationship between acoustic backscatter and physical properties of the seabed, Final Report MEFP 09/P80, 213.
- Combourieu-Nebout, N., Peyron, O., Bout-Roumazeilles, V., Goring, S., Dormoy, I., Joannin, S., Sadori, L., Siani, G. and Magny, M. (2013): Holocene vegetation and climate changes in the central Mediterranean inferred from a high-resolution marine pollen record (Adriatic Sea). *Clim. Past* 9, 2023–2042. <https://doi.org/10.5194/cp-9-2023-2013>

- Cooper, J.A.G., Green, A.N. and Wright, C.I. (2012): Evolution of an incised valley coastal plain estuary under low sediment supply: a 'give-up' estuary. *Sedimentology* 59, 899–916. <https://doi.org/10.1111/j.1365-3091.2011.01284.x>
- Correggiari, A., Cattaneo, A. and Trincardi, F. (2005): The modern Po Delta system: Lobe switching and asymmetric prodelta growth. *Mar. Geol.* 222–223, 49–74. <https://doi.org/10.1016/j.margeo.2005.06.039>
- Correggiari, A., Roveri, M. and Trincardi, F. (1996): Late Pleistocene and Holocene evolution of the North Adriatic continental shelf (Italy). *Il Quat.* 9, 697–704.
- Croudace, I.W. and Rothwell, R.G. (2015): *Micro-XRF Studies of Sediment Cores, Developments in Paleoenvironmental Research*. Springer Netherlands, Dordrecht. <https://doi.org/10.1007/978-94-017-9849-5>
- Croudace, I.W., Rindby, A. and Rothwell, R.G. (2006): ITRAX: description and evaluation of a new multi-function X-ray core scanner. *Geol. Soc. London, Spec. Publ.* 267, 51–63. <https://doi.org/10.1144/GSL.SP.2006.267.01.04>
- Crusius, J., Calvert, S., Pedersen, T. and Sage, D. (1996): Rhenium and molybdenum enrichments in sediments as indicators of oxic, suboxic and sulfidic conditions of deposition. *Earth Planet. Sci. Lett.* 145, 65–78. [https://doi.org/10.1016/S0012-821X\(96\)00204-X](https://doi.org/10.1016/S0012-821X(96)00204-X)
- Cukrov, N. and Barišić, D. (2006): Spatial distribution of ^{40}K and ^{232}Th in recent sediments of the Krka River Estuary. *Croat. Chem. Acta* 79, 115–118.
- Cukrov, N., Cuculić, V., Barišić, D., Lojen, S., Mikelić, I.L., Oreščanin, V., Vdović, N., Fiket, Ž., Čermelj, B. and Mlakar, M. (2013): Elemental and isotopic records in recent fluvio-lacustrine sediments in karstic river Krka, Croatia. *J. Geochemical Explor.* 134, 51–60. <https://doi.org/10.1016/j.gexplo.2013.07.011>
- Cukrov, N., Cindrić, A.-M., Omanović, D. and Cukrov, N. (2024): Spatial Distribution, Ecological Risk Assessment, and Source Identification of Metals in Sediments of the

Krka River Estuary (Croatia). *Sustainability* 16, 1800.

<https://doi.org/10.3390/su16051800>

Cukrov, N., Doumandji, N., Garnier, C., Tucaković, I., Dang, D.H., Omanović, D. and Cukrov, N. (2020): Anthropogenic mercury contamination in sediments of Krka River estuary (Croatia). *Environ. Sci. Pollut. Res.* 27, 7628–7638. <https://doi.org/10.1007/s11356-019-07475-y>

Cukur, D., Krastel, S., Çağatay, M.N., Damcı, E., Meydan, A.F. and Kim, S.P. (2015): Evidence of extensive carbonate mounds and sublacustrine channels in shallow waters of Lake Van, eastern Turkey, based on high-resolution chirp subbottom profiler and multibeam echosounder data. *Geo-Marine Lett.* 35, 329–340. <https://doi.org/10.1007/s00367-015-0410-x>

Cundy, A. (2003): Reconstructing historical trends in metal input in heavily-disturbed, contaminated estuaries: studies from Bilbao, Southampton Water and Sicily. *Appl. Geochemistry* 18, 311–325. [https://doi.org/10.1016/S0883-2927\(02\)00127-0](https://doi.org/10.1016/S0883-2927(02)00127-0)

Dalrymple, Robert W., Zaitlin, Brian A. and Boyd, R. (1992): Estuarine facies models: conceptual basis and stratigraphic implications. *J. Sediment. Petrol.* 62, 1130–1146. [https://doi.org/0022-4472/92/0062-1130/\\$03.0](https://doi.org/0022-4472/92/0062-1130/$03.0)

Dalrymple, R.W., Boyd, R. and Zaitlin, B.A. (1994): History of Research, Types and Internal Organisation of Incised-Valley Systems: Introduction to the Volume, In: *Incised-Valley Systems: Origin and Sedimentary Sequences*. SEPM Society for Sedimentary Geology. <https://doi.org/10.2110/pec.94.12.0003>

Dalrymple, R.W., Zaitlin, B.A. and Boyd, R. (1992): Estuarine facies models; conceptual basis and stratigraphic implications. *J. Sediment. Res.* 62, 1130–1146. <https://doi.org/10.1306/D4267A69-2B26-11D7-8648000102C1865D>

Davis, L.G., Punke, M.L., Hall, R.L., Fillmore, M. and Willis, S.C. (2004): A Late Pleistocene Occupation on the Southern Coast of Oregon. *J. F. Archaeol.* 29, 7–16. <https://doi.org/10.1179/jfa.2004.29.1-2.7>

- de Carvalho Gomes, F., Godoy, J.M., Godoy, M.L.D.P., de Carvalho, L.Z., Tadeu Lopes, R., Sanchez-Cabeza, J.A., de Lacerda, D.L. and Wasserman, C.J. (2009): Metal concentrations, fluxes, inventories and chronologies in sediments from Sepetiba and Ribeira Bays: A comparative study. *Mar. Pollut. Bull.* 59, 123–133.
<https://doi.org/10.1016/j.marpolbul.2009.03.015>
- De Falco, G., Carannante, A., Del Vais, C., Gasperini, L., Pascucci, V., Sanna, I., Simeone, S. and Conforti, A. (2022): Evolution of a single incised valley related to inherited geology, sea level rise and climate changes during the Holocene (Tirso river, Sardinia, western Mediterranean Sea). *Mar. Geol.* 451, 106885.
<https://doi.org/10.1016/j.margeo.2022.106885>
- Dearing, J. (1987): Environmental magnetism. *Quat. Sci. Rev.* 6, 71–72.
[https://doi.org/10.1016/0277-3791\(87\)90024-2](https://doi.org/10.1016/0277-3791(87)90024-2)
- Dearing, J.A., Dann, R.J.L., Hay, K., Lees, J.A., Loveland, P.J., Maher, B.A. and O’Grady, K. (1996): Frequency-dependent susceptibility measurements of environmental materials. *Geophys. J. Int.* 124, 228–240. <https://doi.org/10.1111/j.1365-246X.1996.tb06366.x>
- Debenay, J.P. and Guillou, J.J. (2002): Ecological transitions indicated by foraminiferal assemblages in paralic environments. *Estuaries* 25, 1107–1120.
<https://doi.org/10.1007/BF02692208>
- Debret, M., Desmet, M., Balsam, W., Copard, Y., Francus, P. and Laj, C. (2006): Spectrophotometer analysis of Holocene sediments from an anoxic fjord: Saanich Inlet, British Columbia, Canada. *Mar. Geol.* 229, 15–28.
<https://doi.org/10.1016/j.margeo.2006.01.005>
- Deiana, G., Lecca, L., Melis, R., Soldati, M., Demurtas, V. and Orrù, P. (2021): Submarine Geomorphology of the Southwestern Sardinian Continental Shelf (Mediterranean Sea): Insights into the Last Glacial Maximum Sea-Level Changes and Related Environments. *Water* 13, 155. <https://doi.org/10.3390/w13020155>
- Domínguez-Villar, D., Vázquez-Navarro, J.A., Cheng, H. and Edwards, R.L. (2011): Freshwater

tufa record from Spain supports evidence for the past interglacial being wetter than the Holocene in the Mediterranean region. *Glob. Planet. Change* 77, 129–141.
<https://doi.org/10.1016/j.gloplacha.2011.04.006>

Dunn, J.R. (1953): The origin of the deposits of tufa in Mono Lake [California]. *J. Sediment. Res.* 23, 18–23. <https://doi.org/10.1306/D4269530-2B26-11D7-8648000102C1865D>

Durn, T. (2020): Aktivnost A.2.2. Priprema i analiza arhivskih geofizičkih podataka, Report, Croatian Geological Survey, 16.

Dyer, S.E., Green, A.N., Cooper, J.A.G., Hahn, A. and Zabel, M. (2021): Response of a wave-dominated coastline and delta to antecedent conditioning and fluctuating rates of postglacial sea-level rise. *Mar. Geol.* 434, 106435.
<https://doi.org/10.1016/j.margeo.2021.106435>

Edwards, R. (2006): Sea levels: change and variability during warm intervals. *Prog. Phys. Geogr. Earth Environ.* 30, 785–796. <https://doi.org/10.1177/0309133306071959>

Egozcue, J. J., Pawlowsky-Glahn, V., Mateu-Figueras, G. and Barceló-Vidal, C. (2003): Isometric Logratio Transformations for Compositional Data Analysis. *Mathemtical Geol.* 35, 279–300. <https://doi.org/doi.org/10.1023/A:1023818214614>

Elbaz-Poulichet, F., Guan, D.M. and Martin, J.-M. (1991): Trace metal behaviour in a highly stratified Mediterranean estuary: the Krka (Yugoslavia). *Mar. Chem.* 32, 211–224.
[https://doi.org/10.1016/0304-4203\(91\)90039-Y](https://doi.org/10.1016/0304-4203(91)90039-Y)

Ellam, R. (2016): *Isotopes: A Very Short Introduction*. Oxford University Press.
<https://doi.org/10.1093/actrade/9780198723622.001.0001>

Emery, K.O. (1981): Geological limits of the continental shelf. *Ocean Dev. Int. Law* 10, 1–11.
<https://doi.org/10.1080/00908328109545671>

Emiliani, C. (1955): Pleistocene Temperatures. *J. Geol.* 63, 538–578.
<https://doi.org/10.1086/626295>

- Fairbanks, R.G. (1989): A 17,000-year glacio-eustatic sea level record: influence of glacial melting rates on the Younger Dryas event and deep-ocean circulation. *Nature* 342, 637–642. <https://doi.org/10.1038/342637a0>
- Faivre, S., Fouache, E., Kovačić, V. and Glušćević, S. (2010): Geomorphological and archaeological indicators of Croatian shoreline evolution in the last two thousands years. *GeoActa* 35, 125–133.
- Faivre, S., Lončar, N., Tomljenović, B., Sečanj, M., Herak, M. and Barešić, J. (2024): Impact of coseismic uplifting on relative sea level change in the Southern Adriatic during the past 4.5000 years – New evidence from Dubrovnik epicentral area based on analysis of algal rims and tidal notches. *Geomorphology* 460. 1-20.
<https://doi.org/10.1016/j.geomorph.2024.109262>
- Faivre, S., Bakran-Petricioli, T., Barešić, J. and Horvatinčić, N. (2015): New Data on Marine Radiocarbon Reservoir Effect in the Eastern Adriatic Based on Pre-Bomb Marine Organisms from the Intertidal Zone and Shallow Sea. *Radiocarbon* 57, 527–538.
https://doi.org/10.2458/azu_rc.57.18452
- Faivre, S., Bakran-Petricioli, T., Horvatinčić, N. and Sironić, A. (2013): Distinct phases of relative sea level changes in the central Adriatic during the last 1500years — influence of climatic variations? *Palaeogeogr. Palaeoclimatol. Palaeoecol.* 369, 163–174.
<https://doi.org/10.1016/j.palaeo.2012.10.016>
- Faivre, S., Fouache, E., Ghilardi, M., Antonioli, F., Furlani, S. and Kovačić, V. (2011): Relative sea level change in western Istria (Croatia) during the last millennium. *Quat. Int.*
<https://doi.org/10.1016/j.quaint.2010.05.027>
- Faust, J.C. and Knies, J. (2019): Organic Matter Sources in North Atlantic Fjord Sediments. *Geochemistry, Geophys. Geosystems* 20, 2872–2885.
<https://doi.org/10.1029/2019GC008382>
- Felja, I. (2017): Karstic estuaries along the eastern Adriatic coast: Late-Quaternary evolution of the Mirna and Neretva River mouths. Doctoral Thesis, Faculty of Science, University

of Zagreb, 169.

Felja, I., Fontana, A., Furlani, S., Bajraktarević, Z., Paradžik, A., Topalović, E., Rossato, S., Ćosović, V. and Juračić, M. (2015): Environmental changes in the lower Mirna River valley (Istria, Croatia) during Upper Holocene. *Geol. Croat.* 68, 209–224.

<https://doi.org/10.4154/GC.2015.16>

Filipčić, A. (2000): Razgraničenje Köppenovih klimatskih tipova Cf i Cs u Hrvatsko. *Acta Geogr. Croat.* 35, 7–17.

Fleming, K., Johnston, P., Zwartz, D., Yokoyama, Y., Lambeck, K. and Chappell, J. (1998): Refining the eustatic sea-level curve since the Last Glacial Maximum using far- and intermediate-field sites. *Earth Planet. Sci. Lett.* 163, 327–342.

[https://doi.org/10.1016/S0012-821X\(98\)00198-8](https://doi.org/10.1016/S0012-821X(98)00198-8)

Folk, R.L. and Ward, W.C. (1957): Brazos River Bar: A Study in the Significance of Grain Size Parameters. *J. Sediment. Petrol.* 27, 3–26.

Ford, T.D. and Pedley, H.M. (1996): A review of tufa and travertine deposits of the world.

Earth-Science Rev. 41, 117–175. [https://doi.org/10.1016/S0012-8252\(96\)00030-X](https://doi.org/10.1016/S0012-8252(96)00030-X)

Frančičković-Bilinski, S., Barišić, D., Vertačnik, A., Bilinski, H. and Prohić, E. (2004):

Characterization of tufa from the Dinaric Karst of Croatia: mineralogy, geochemistry and discussion of climate conditions. *Facies* 50, 183–193.

<https://doi.org/10.1007/s10347-004-0015-8>

Francke, A., Wagner, B., Leng, M.J. and Rethemeyer, J. (2013): A Late Glacial to Holocene record of environmental change from Lake Dojran (Macedonia, Greece). *Clim. Past* 9, 481–498. <https://doi.org/10.5194/cp-9-481-2013>

Furlani, S., Cucchi, F., Biolchi, S. and Odorico, R. (2011): Notches in the Northern Adriatic Sea: Genesis and development. *Quat. Int.* 232, 158–168.

<https://doi.org/10.1016/j.quaint.2010.06.010>

Gao, X., Yang, Y. and Wang, C. (2012): Geochemistry of organic carbon and nitrogen in

surface sediments of coastal Bohai Bay inferred from their ratios and stable isotopic signatures. *Mar. Pollut. Bull.* 64, 1148–1155.

<https://doi.org/10.1016/j.marpolbul.2012.03.028>

García-del-Cura, M.Á., Benavente, D., Martínez-Martínez, J. and Cueto, N. (2012): Sedimentary structures and physical properties of travertine and carbonate tufa building stone. *Constr. Build. Mater.* 28, 456–467.

<https://doi.org/10.1016/j.conbuildmat.2011.08.042>

Gasparon, M., Ehrler, K., Matschullat, J. and Melles, M. (2007): Temporal and spatial variability of geochemical backgrounds in the Windmill Islands, East Antarctica: Implications for climatic changes and human impacts. *Appl. Geochemistry* 22, 888–905.

<https://doi.org/10.1016/j.apgeochem.2006.12.018>

GEOTEK (2014): Multi-Sensor Core Logger, Manual, 154.

Golubić, S., Violante, C., Plenković-Moraj, A. and Grgasović, T. (2008): Travertines and calcareous tufa deposits: an insight into diagenesis. *Geol. Croat.* 61, 363–378.

Gomes, M.P., Vital, H., Stattegger, K. and Schwarzer, K. (2016): Bedrock control on the Assu Incised Valley morphology and sedimentation in the Brazilian Equatorial Shelf. *Int. J. Sediment Res.* 31, 181–193. <https://doi.org/10.1016/j.ijsrc.2015.04.002>

Gopal, V., Krishnamurthy, R.R., Vignesh, R., Sabari Nathan, C., Anshu, R., Kalaivanan, R., Mohana, P., Magesh, N.S., Manikanda Bharath, K., Ekoa Bessa, A.Z., Abdelrahman, K. and Abioui, M. (2023): Assessment of heavy metal contamination in the surface sediments of the Vedaranyam coast, Southern India. *Reg. Stud. Mar. Sci.* 65, 103081. <https://doi.org/10.1016/j.rsma.2023.103081>

Goudie, A.S., Viles, H.A. and Pentecost, A. (1993): The late-Holocene tufa decline in Europe. *The Holocene* 3, 181–186. <https://doi.org/10.1177/095968369300300211>

Green, A.N., Dladla, N. and Garlick, G.L. (2013): Spatial and temporal variations in incised valley systems from the Durban continental shelf, KwaZulu-Natal, South Africa. *Mar.*

Geol. 335, 148–161. <https://doi.org/10.1016/j.margeo.2012.11.002>

Gržetić, Z., Precali, R., Degobbis, D. and Škrivanić, A. (1991): Nutrient enrichment and phytoplankton response in an Adriatic karstic estuary. *Mar. Chem.* 32, 313–331. [https://doi.org/10.1016/0304-4203\(91\)90046-Y](https://doi.org/10.1016/0304-4203(91)90046-Y)

Gu, Y.-G., Ouyang, J., Ning, J.-J. and Wang, Z.H. (2017): Distribution and sources of organic carbon, nitrogen and their isotopes in surface sediments from the largest mariculture zone of the eastern Guangdong coast, South China. *Mar. Pollut. Bull.* 120, 286–291. <https://doi.org/10.1016/j.marpolbul.2017.05.013>

Hafsten, U. (1970): A sub-division of the Late Pleistocene period on a synchronous basis, intended for global and universal usage. *Palaeogeogr. Palaeoclimatol. Palaeoecol.* 7, 279–296. [https://doi.org/10.1016/0031-0182\(70\)90097-0](https://doi.org/10.1016/0031-0182(70)90097-0)

Harris, P.T. (2012): Seafloor Geomorphology—Coast, Shelf, and Abyss, in: *Seafloor Geomorphology as Benthic Habitat*. Elsevier, pp. 109–155. <https://doi.org/10.1016/B978-0-12-385140-6.00006-2>

Hasan, O. (2017): Paleookolišna rekonstrukcija slivova Karinskoga mora, Novigradskoga mora i Velebitskoga kanala tijekom holocena. Doctoral Thesis, Faculty of Mining, Geology and Petroleum Engineering, University of Zagreb, 564.

Hasan, O., Miko, S., Brunović, D., Papatheodorou, G., Christodolou, D., Ilijanić, N. and Geraga, M. (2020): Geomorphology of Canyon Outlets in Zrmanja River Estuary and Its Effect on the Holocene Flooding of Semi-enclosed Basins (the Novigrad and Karin Seas, Eastern Adriatic). *Water* 12, 2807. <https://doi.org/10.3390/w12102807>

Hasan, O., Smrkulj, N., Miko, S., Brunović, D., Ilijanić, N. and Šparica Miko, M. (2023): Integrated Reconstruction of Late Quaternary Geomorphology and Sediment Dynamics of Prokljan Lake and Krka River Estuary, Croatia. *Remote Sens.* 15, 2588. <https://doi.org/10.3390/rs15102588>

Hayes, M.O. (1975): Morphology of Sand Accumulation in Estuaries: An Introduction to the

- Symposium. In: *Geology and Engineering*. Elsevier, pp. 3–22.
<https://doi.org/10.1016/B978-0-12-197502-9.50006-X>
- Heaton, T.J., Köhler, P., Butzin, M., Bard, E., Reimer, R.W., Austin, W.E.N., Bronk Ramsey, C., Grootes, P.M., Hughen, K.A., Kromer, B., Reimer, P.J., Adkins, J., Burke, A., Cook, M.S., Olsen, J. and Skinner, L.C. (2020): Marine20—The Marine Radiocarbon Age Calibration Curve (0–55,000 cal BP). *Radiocarbon* 62, 779–820.
<https://doi.org/10.1017/RDC.2020.68>
- Helland-Hansen, W. and Hampson, G.J. (2009): Trajectory analysis: concepts and applications. *Basin Res.* 21, 454–483. <https://doi.org/10.1111/j.1365-2117.2009.00425.x>
- Helmke, J.P., Schulz, M. and Bauch, H.A. (2002): Sediment-Color Record from the Northeast Atlantic Reveals Patterns of Millennial-Scale Climate Variability during the Past 500,000 Years. *Quat. Res.* 57, 49–57. <https://doi.org/10.1006/qres.2001.2289>
- Herak, D., Herak, M., Prelogović, E., Markušić, S. and Markulin, Ž. (2005): Jabuka island (Central Adriatic Sea) earthquakes of 2003. *Tectonophysics*.
<https://doi.org/10.1016/j.tecto.2005.01.007>
- Herman, J.S. and Lorah, M.M. (1988): Calcite precipitation rates in the field: Measurement and prediction for a travertine-depositing stream. *Geochim. Cosmochim. Acta* 52, 2347–2355. [https://doi.org/10.1016/0016-7037\(88\)90292-X](https://doi.org/10.1016/0016-7037(88)90292-X)
- Horne, D.J., Cohen, A. and Martens, K. (2002): Taxonomy, morphology and biology of Quaternary and living ostracoda. pp. 5–36. <https://doi.org/10.1029/131GM02>
- Horvatinčić, N., Čalić, R. and Geyh, M.A. (2000): Interglacial Growth of Tufa in Croatia. *Quat. Res.* 53, 185–195. <https://doi.org/10.1006/qres.1999.2094>
- Hršak, V., Šegota, V. and Sedlar, Z. (2023): Vascular flora of Krka National Park (Croatia). *Glas. Hrvat. Bot. društva* 10, 6–53. <https://doi.org/10.46232/glashbod.10.1-2.1>
- Hua, Q. (2009): Radiocarbon: A chronological tool for the recent past. *Quat. Geochronol.* 4,

378–390. <https://doi.org/10.1016/j.quageo.2009.03.006>

- Hunt, C., Demšar, U., Dove, D., Smeaton, C., Cooper, R. and Austin, W.E.N. (2020): Quantifying Marine Sedimentary Carbon: A New Spatial Analysis Approach Using Seafloor Acoustics, Imagery, and Ground-Truthing Data in Scotland. *Front. Mar. Sci.* 7, 1–11. <https://doi.org/10.3389/fmars.2020.00588>
- Hus, P. (2023): Paleookolišna rekonstrukcija estuarija rijeke Krke tijekom holocena temeljem bentoskih krednjaka (Foraminifera). Master Thesis, Faculty of Science, University of Zagreb, 67.
- Ilijanić, N. (2014): Minerali glina u jezerskim sedimentima istočno Jadranske obale kao pokazatelji promjena okoliša tijekom kasnog pleistocena i holocena. Doctoral Thesis, Faculty of Science, University of Zagreb, 382.
- Ilijanić, N., Miko, S., Ivkić Filipović, I., Hasan, O., Šparica Miko, M., Petrinec, B., Terzić, J. and Marković, T. (2022): A Holocene Sedimentary Record and the Impact of Sea-Level Rise in the Karst Lake Velo Blato and the Wetlands on Pag Island (Croatia). *Water* 14, 342. <https://doi.org/10.3390/w14030342>
- Imbrie, J., Hays, J. D., Martinson, D. G., McIntyre, A., Mix, A. C., Morley, J. J., Pisias, N. G., Prell, W. L. and Shackleton, N.J. (1984): The orbital theory of Pleistocene climate: support from a revised chronology of the marine $\delta^{18}O$ record. In: *Milankovitch and Climate (Part 1)*. Reidel Publishing Company, Dordrecht, Netherlands, pp. 269–305.
- Janowski, Ł., Tęgowski, J. and Nowak, J. (2018): Seafloor mapping based on multibeam echosounder bathymetry and backscatter data using Object-Based Image Analysis: a case study from the Rewal site, the Southern Baltic. *Oceanol. Hydrobiol. Stud.* 47, 248–259. <https://doi.org/10.1515/ohs-2018-0024>
- Jerbić, K. (2019): Zambratija: A 6000-year-old pile-dwelling submerged under the Adriatic Sea. Doctoral Thesis, Flinders University, 374.
- Joannin, S., Brugiapaglia, E., de Beaulieu, J.-L., Bernardo, L., Magny, M., Peyron, O., Goring,

- S. and Vanni re, B. (2012): Pollen-based reconstruction of Holocene vegetation and climate in southern Italy: the case of Lago Trifoglietti. *Clim. Past* 8, 1973–1996. <https://doi.org/10.5194/cp-8-1973-2012>
- Jones, R.T. and Marshall, J.D. (2002): Lacustrine Oxygen Isotopic Records from Temperate Marl Lakes. *PAGES news* 10, 17–19. <https://doi.org/10.22498/pages.10.2.17>
- Juggins, S. (2003): C2 user guide: Software for ecological and palaeoecological data analysis and visualization. Univ. Newcastle, Newcastle upon Tyne, UK, 73.
- Jura i , M. and Prohi , E. (1991): Mineralogy, sources of particles and sedimentation in the Krka River estuary (Croatia). *Geološki Vjesn.* 44, 195–200.
- Kamenski, A. and Korbar, T. (2023): Platform-to-Basin Evolution of a Tectonically Indistinct Part of a Multiple Foreland—Analysis of a 3D Seismic Block in the Northern Adriatic Sea (Croatian Offshore). *Geosci.*, 1-22. <https://doi.org/10.3390/geosciences13110323>
- Kelts, K. and Talbot, M. (1990): Lacustrine Carbonates as Geochemical Archives of Biotic / Abiotic Interactions. Springer-Verlag Berlin Heidelberg, 288–315.
- Kemp, A.L.W. (1971): Organic Carbon and Nitrogen in the Surface Sediments of Lakes Ontario, Erie and Huron. *J. Sediment. Petrol.* 41, 537–548.
- Kennish, M.J. (2016): *Encyclopedia of Estuaries*, Encyclopedia of Earth Sciences Series. Springer Netherlands, Dordrecht, 760. <https://doi.org/10.1007/978-94-017-8801-4>
- Kent, D. V, Rio, D., Massari, F., Kukla, G. and Lanci, L. (2002): Emergence of Venice during the Pleistocene. *Quat. Sci. Rev.* 21, 1719–1727. [https://doi.org/10.1016/S0277-3791\(01\)00153-6](https://doi.org/10.1016/S0277-3791(01)00153-6)
- Korbar, T. (2009): Orogenic evolution of the External Dinarides in the NE Adriatic region: a model constrained by tectonostratigraphy of Upper Cretaceous to Paleogene carbonates. *Earth-Science Rev.* 96, 296–312. <https://doi.org/10.1016/j.earscirev.2009.07.004>

- Korlević, M., Šupraha, L., Ljubešić, Z., Henderiks, J., Ciglonečki, I., Dautović, J. and Orlić, S. (2016): Bacterial diversity across a highly stratified ecosystem: A salt-wedge Mediterranean estuary. *Syst. Appl. Microbiol.* 39, 398–408.
<https://doi.org/10.1016/j.syapm.2016.06.006>
- Kuperman, W. and Roux, P. (2007): Underwater Acoustics, in: Springer Handbook of Acoustics. Springer New York, New York, NY, pp. 149–204.
https://doi.org/10.1007/978-0-387-30425-0_5
- Kwokal, Ž. and Lovrić, M. (2006): Vertical distribution of mercury in the Krka river estuary. *Int. J. Environ. Anal. Chem.* 86, 905–914. <https://doi.org/10.1080/03067310600739723>
- Kylander, M.E., Ampel, L., Wohlfarth, B. and Veres, D. (2011): High-resolution X-ray fluorescence core scanning analysis of Les Echets (France) sedimentary sequence: new insights from chemical proxies. *J. Quat. Sci.* 26, 109–117.
<https://doi.org/10.1002/jqs.1438>
- Lacerda, L.D., Fernandez, M.A., Calazans, C.F. and Tanizaki, K.F. (1992): Bioavailability of heavy metals in sediments of two coastal lagoons in Rio de Janeiro, Brazil. *Hydrobiologia* 228, 65–70. <https://doi.org/10.1007/BF00006477>
- Lamb, A.L., Wilson, G.P. and Leng, M.J. (2006): A review of coastal palaeoclimate and relative sea-level reconstructions using $\delta^{13}\text{C}$ and C/N ratios in organic material. *Earth-Science Rev.* 75, 29–57. <https://doi.org/10.1016/j.earscirev.2005.10.003>
- Lambeck, K. and Chappell, J. (2001): Sea Level Change Through the Last Glacial Cycle. *Science* (80-.). 292, 679–686. <https://doi.org/10.1126/science.1059549>
- Lambeck, K., Rouby, H., Purcell, A., Sun, Y. and Sambridge, M. (2014): Sea level and global ice volumes from the Last Glacial Maximum to the Holocene. *Proc. Natl. Acad. Sci.* 111, 15296–15303. <https://doi.org/10.1073/pnas.1411762111>
- Lambeck, K., Yokoyama, Y. and Purcell, T. (2002): Into and out of the Last Glacial Maximum: sea-level change during Oxygen Isotope Stages 3 and 2. *Quat. Sci. Rev.* 21, 343–360.

[https://doi.org/10.1016/S0277-3791\(01\)00071-3](https://doi.org/10.1016/S0277-3791(01)00071-3)

Langlet, D., Geslin, E., Baal, C., Metzger, E., Lejzerowicz, F., Riedel, B., Zuschin, M., Pawlowski, J., Stachowitsch, M. and Jorissen, F.J. (2013): Foraminiferal survival after long-term in situ experimentally induced anoxia. *Biogeosciences* 10, 7463–7480. <https://doi.org/10.5194/bg-10-7463-2013>

Lasanta, T., García-Ruiz, J., Pérez-Rontomé, C. and Sancho-Marcén, C. (2000): Runoff and sediment yield in a semi-arid environment: the effect of land management after farmland abandonment. *CATENA* 38, 265–278. [https://doi.org/10.1016/S0341-8162\(99\)00079-X](https://doi.org/10.1016/S0341-8162(99)00079-X)

Legović, T. (1991): Exchange of water in a stratified estuary with an application to Krka (Adriatic Sea). *Mar. Chem.* [https://doi.org/10.1016/0304-4203\(91\)90032-R](https://doi.org/10.1016/0304-4203(91)90032-R)

Legović, T., Petricioli, D. and Žutić, V. (1991): Hypoxia in a pristine stratified estuary (Krka, Adriatic Sea). *Mar. Chem.* 32, 347–359. [https://doi.org/10.1016/0304-4203\(91\)90048-2](https://doi.org/10.1016/0304-4203(91)90048-2)

Legović, T., Žutić, V., Gržetić, Z., Cauwet, G., Precali, R. and Viličić, D. (1994): Eutrophication in the Krka estuary. *Mar. Chem.* 46, 203–215. [https://doi.org/10.1016/0304-4203\(94\)90056-6](https://doi.org/10.1016/0304-4203(94)90056-6)

Leng, M.J. (2006): *Isotopes in Palaeoenvironmental Research, Developments in Paleoenvironmental Research*. Springer Netherlands, Dordrecht. <https://doi.org/10.1007/1-4020-2504-1>

Leng, M.J., Jones, M.D., Frogley, M.R., Eastwood, W.J., Kendrick, C.P. and Roberts, C.N. (2010): Detrital carbonate influences on bulk oxygen and carbon isotope composition of lacustrine sediments from the Mediterranean. *Glob. Planet. Change* 71, 175–182. <https://doi.org/10.1016/j.gloplacha.2009.05.005>

Leng, M.J. and Marshall, J.D. (2004): Palaeoclimate interpretation of stable isotope data from lake sediment archives. *Quat. Sci. Rev.* 23, 811–831. <https://doi.org/10.1016/j.quascirev.2003.06.012>

- Li, Y., Zhang, H., Tu, C., Fu, C., Xue, Y. and Luo, Y. (2016): Sources and fate of organic carbon and nitrogen from land to ocean: Identified by coupling stable isotopes with C/N ratio. *Estuar. Coast. Shelf Sci.* 181, 114–122. <https://doi.org/10.1016/j.ecss.2016.08.024>
- Lionello, P. (2012): *The Climate of the Mediterranean Region*, The Climate of the Mediterranean Region. Elsevier. <https://doi.org/10.1016/C2011-0-06210-5>
- Liu, J., Hrustić, E., Du, J., Gašparović, B., Čanković, M., Cukrov, N., Zhu, Z. and Zhang, R. (2019): Net Submarine Groundwater-Derived Dissolved Inorganic Nutrients and Carbon Input to the Oligotrophic Stratified Karstic Estuary of the Krka River (Adriatic Sea, Croatia). *J. Geophys. Res. Ocean.* 124, 4334–4349. <https://doi.org/10.1029/2018JC014814>
- Liu, M., Hou, L.J., Xu, S.Y., Ou, D.N., Yang, Y., Yu, J. and Wang, Q. (2006): Organic carbon and nitrogen stable isotopes in the intertidal sediments from the Yangtze Estuary, China. *Mar. Pollut. Bull.* 52, 1625–1633. <https://doi.org/10.1016/j.marpolbul.2006.06.008>
- Lobo, F.J., Dias, J.M.A., Hernández-Molina, F.J., González, R., Fernández-Salas, L.M. and Díaz Del Río, V. (2005): Late Quaternary shelf-margin wedges and upper slope progradation in the Gulf of Cadiz margin (SW Iberian Peninsula). *Geol. Soc. London, Spec. Publ.* 244, 7–25. <https://doi.org/10.1144/GSL.SP.2005.244.01.02>
- Lobo, F.J., García, M., Luján, M., Mendes, I., Reguera, M.I. and Van Rooij, D. (2018): Morphology of the last subaerial unconformity on a shelf: insights into transgressive ravinement and incised valley occurrence in the Gulf of Cádiz. *Geo-Marine Lett.* 38, 33–45. <https://doi.org/10.1007/s00367-017-0511-9>
- Loeblich, A. R. and Tappan, H. (1988): *Foraminiferal Genera and Their Classification*, 1st ed. ed. Springer, 869.
- Lojen, S., Cukrov, M. and Cukrov, N. (2014): Variability of Stable Isotope Fingerprints of the Serpulid *Ficopomatus enigmaticus* Within a Permanently Stratified Estuary: Implications for (Palaeo)environmental Interpretations. *Estuaries and Coasts* 37, 436–448. <https://doi.org/10.1007/s12237-013-9685-1>

- Lojen, S., Trkov, A., Ščančar, J., Vázquez-Navarro, J.A. and Cukrov, N. (2009): Continuous 60-year stable isotopic and earth-alkali element records in a modern laminated tufa (Jaruga, river Krka, Croatia): Implications for climate reconstruction. *Chem. Geol.* 258, 242–250. <https://doi.org/10.1016/j.chemgeo.2008.10.013>
- Loring, D.H. and Rantala, R.T.T. (1992): Manual for the geochemical analyses of marine sediments and suspended particulate matter. *Earth-Science Rev.* 32, 235–283. [https://doi.org/10.1016/0012-8252\(92\)90001-A](https://doi.org/10.1016/0012-8252(92)90001-A)
- Lowe, J.J. and Walker, M. (2014): *Reconstructing Quaternary Environments*. Routledge. <https://doi.org/10.4324/9781315797496>
- Mamužić, P. (1975): Tumač za osnovnu geološku kartu 1 : 100 000 list Šibenik K 33-8.
- Marcinek, S., Cindrić, A.M., Pađan, J. and Omanović, D. (2022): Trace Metal Partitioning in the Salinity Gradient of the Highly Stratified Estuary: A Case Study in the Krka River Estuary (Croatia). *Appl. Sci.* 12, 1–13. <https://doi.org/10.3390/app12125816>
- Marini, M., Maselli, V., Campanelli, A., Foglini, F. and Grilli, F. (2016): Role of the Mid-Adriatic deep in dense water interception and modification. *Mar. Geol.* 375, 5–14. <https://doi.org/10.1016/j.margeo.2015.08.015>
- Maselli, V. and Trincardi, F. (2013): Large-scale single incised valley from a small catchment basin on the western Adriatic margin (central Mediterranean Sea). *Glob. Planet. Change* 100, 245–262. <https://doi.org/10.1016/j.gloplacha.2012.10.008>
- Maselli, V., Trincardi, F., Cattaneo, A., Ridente, D. and Asioli, A. (2010): Subsidence pattern in the central Adriatic and its influence on sediment architecture during the last 400 kyr. *J. Geophys. Res. Solid Earth* 115. <https://doi.org/10.1029/2010JB007687>
- Masselink, G., Hughes, M. and Knight, J. (2014): *Introduction to Coastal Processes and Geomorphology*. Routledge. <https://doi.org/10.4324/9780203785461>
- Mayer, L.M. (1994): Surface area control of organic carbon accumulation in continental shelf sediments. *Geochim. Cosmochim. Acta* 58, 1271–1284. [263](https://doi.org/10.1016/0016-</p></div><div data-bbox=)

7037(94)90381-6

Meisch, C. (2000): *Freshwater Ostracoda of Western and Central Europe*. Spektrum, 522.

Mendušić, M. and Marguš, D. (2007): *Oziđana Pećina – Rezultati Arheoloških Istraživanja*. *Subterranea Croat.* 5, 31–35.

Menning, D.M., Wynn, J.G. and Garey, J.R. (2015): Karst estuaries are governed by interactions between inland hydrological conditions and sea level. *J. Hydrol.* 527, 718–733. <https://doi.org/10.1016/j.jhydrol.2015.05.021>

Mesić, S. (2004): *Antropogeni utjecaj na geokemijski sastav holocenskih sedimenata Vranskog jezera na Cresu*. Doctoral Thesis, Faculty of Science, University of Zagreb, 186.

Mesquita-Joanes, F., Smith, A.J. and Viehberg, F.A. (2012): The Ecology of Ostracoda Across Levels of Biological Organisation from Individual to Ecosystem, in: *Developments in Quaternary Science*. pp. 15–35. <https://doi.org/10.1016/B978-0-444-53636-5.00002-0>

Meyers, P.A. (1994): Preservation of elemental and isotopic source identification of sedimentary organic matter. *Chem. Geol.* 114, 289–302. [https://doi.org/10.1016/0009-2541\(94\)90059-0](https://doi.org/10.1016/0009-2541(94)90059-0)

Meyers, P.A. and Ishiwatari, R. (1993): Lacustrine organic geochemistry—an overview of indicators of organic matter sources and diagenesis in lake sediments. *Org. Geochem.* 20, 867–900. [https://doi.org/10.1016/0146-6380\(93\)90100-P](https://doi.org/10.1016/0146-6380(93)90100-P)

Meyers, P.A. and Teranes, J.L. (2001): *Sediment Organic Matter*, in: *Tracking Environmental Change Using Lake Sediments*. Kluwer Academic Publishers, Dordrecht, pp. 239–269. https://doi.org/10.1007/0-306-47670-3_9

MGDAPAI (2013): *Marine Geophysics Data Acquisition, Processing and Interpretation*.

Micallef, A., Foglini, F., Le Bas, T., Angeletti, L., Maselli, V., Pasuto, A. and Taviani, M. (2013): *The submerged paleolandscape of the maltese Islands: Morphology, evolution and*

relation to quaternary environmental change. *Mar. Geol.* 335, 129–147.

<https://doi.org/10.1016/j.margeo.2012.10.017>

Mikac, N., Kwokal, Z., May, K. and Branica, M. (1989): Mercury distribution in the Krka river Estuary (Eastern Adriatic Coast). *Mar. Chem.* 28, 109–126.

[https://doi.org/10.1016/0304-4203\(89\)90190-4](https://doi.org/10.1016/0304-4203(89)90190-4)

Miko, S., Durn, G., Adamcova, R., Covic, M., Dubikova, M., Skalsky, R., Kapelj, S. and Ottner, F. (2003): Heavy metal distribution in karst soils from Croatia and Slovakia. *Environ. Geol.* 45, 262–272. <https://doi.org/10.1007/s00254-003-0878-y>

Miko, S., Mesić, S., Šparica Miko, M. and Hasan, O. (2008): A record of anthropogenic Pb deposition in a Mediterranean karst catchment (Lake Vrana, Cres Island, Croatia).

Mineral. Mag. 72, 455–460. <https://doi.org/10.1180/minmag.2008.072.1.455>

Milović, M. (2016): A new contribution to the knowledge of the vascular flora of the Krka National Park (North Dalmatia, Croatia). *Glas. Hrvat. Bot. društva* 4, 22–29.

Mitchum, R.M., Vail, P.R. and Sangree, J.B. (1977): Seismic Stratigraphy and Global Changes of Sea Level, Part 6: Stratigraphic Interpretation of Seismic Reflection Patterns in Depositional Sequences, in: *Seismic Stratigraphy — Applications to Hydrocarbon Exploration*. American Association of Petroleum Geologists.

<https://doi.org/10.1306/M26490C8>

Mocochain, L., Audra, P., Clauzon, G., Bellier, O., Bigot, J.-Y., Parize, O. and Monteil, P. (2009): The effect of river dynamics induced by the Messinian Salinity Crisis on karst landscape and caves: Example of the Lower Ardèche river (mid Rhône valley).

Geomorphology 106, 46–61. <https://doi.org/10.1016/j.geomorph.2008.09.021>

Montereale Gavazzi, G., Madricardo, F., Janowski, L., Kruss, A., Blondel, P., Sigovini, M. and Foglini, F. (2016): Evaluation of seabed mapping methods for fine-scale classification of extremely shallow benthic habitats – Application to the Venice Lagoon, Italy. *Estuar. Coast. Shelf Sci.* 170, 45–60. <https://doi.org/10.1016/j.ecss.2015.12.014>

- Moore, D.M. and Reynolds Jr, R.C. (1997): X-Ray Diffraction and the Identification and Analysis of Clay Minerals.
- Morang, A., Larson, R. and Gorman, L. (1997): Monitoring the Coastal Environment; Part III: Geophysical and Research Methods. *J. Coast. Res.* 13, 17.
- Moreira-Turcq, P., Martin, J.M. and Fleury, A. (1993): Chemical and biological characterization of particles by flow cytometry in the Krka estuary, Croatia. *Mar. Chem.* [https://doi.org/10.1016/0304-4203\(93\)90219-E](https://doi.org/10.1016/0304-4203(93)90219-E)
- Morelli, G., Gasparon, M., Fierro, D., Hu, W.P. and Zawadzki, A. (2012): Historical trends in trace metal and sediment accumulation in intertidal sediments of Moreton Bay, southeast Queensland, Australia. *Chem. Geol.* 300–301, 152–164. <https://doi.org/10.1016/j.chemgeo.2012.01.023>
- Moscon, G., Correggiari, A., Stefani, C., Fontana, A. and Remia, A. (2015): Very-high resolution analysis of a transgressive deposit in the Northern Adriatic Sea (Italy). *Alp. Mediterr. Quat.* 28, 121–129.
- Murray-Wallace, C. V. and Woodroffe, C.D. (2014): Quaternary Sea-Level Changes. Cambridge University Press, 484. <https://doi.org/10.1017/CBO9781139024440>
- Murray, J.W. (2006): Ecology and Applications of Benthic Foraminifera, Ecology and Applications of Benthic Foraminifera. Cambridge University Press, 426. <https://doi.org/10.1017/CBO9780511535529>
- Murray, M.R. (2002): Is laser particle size determination possible for carbonate-rich lake sediments? *J. Paleolimnol.* 27, 173–183. <https://doi.org/10.1023/A:1014281412035>
- Nordfjord, S., Goff, J.A., Austin, J.A. and Gulick, S.P.S. (2006): Seismic facies of incised-valley fills, New Jersey continental shelf: Implications for erosion and preservation processes acting during latest Pleistocene-Holocene transgression. *J. Sediment. Res.* 76, 1284–1303. <https://doi.org/10.2110/jsr.2006.108>
- Novak, A., Šmuc, A., Poglajen, S. and Vrabec, M. (2020): Linking the high-resolution acoustic

and sedimentary facies of a transgressed Late Quaternary alluvial plain (Gulf of Trieste, northern Adriatic). *Mar. Geol.* 419, 106061.

<https://doi.org/10.1016/j.margeo.2019.106061>

Ortiz, J., Mix, A., Harris, S. and O'Connell, S. (1999): Diffuse spectral reflectance as a proxy for percent carbonate content in North Atlantic sediments. *Paleoceanography* 14, 171–186. <https://doi.org/10.1029/1998PA900021>

Parać, M., Cukrov, N., Bulat, T. and Cukrov, N. (2022): Microplastics assessment in the Krka river estuary surface water. *Environ. Eng.* 9, 29–34. <https://doi.org/10.37023/ee.9.1-2.4>

Patruno, S. and Helland-Hansen, W. (2018): Clinofolds and clinofold systems: Review and dynamic classification scheme for shorelines, subaqueous deltas, shelf edges and continental margins. *Earth-Science Rev.* 185, 202–233. <https://doi.org/10.1016/j.earscirev.2018.05.016>

Pavlović, G., Prohić, E., Miko, S. and Tibljaš, D. (2002): Geochemical and petrographic evidence of meteoric diagenesis in tufa deposits in Northern Dalmatia (Zrmanja and Krupa Rivers, Croatia). *Facies* 46, 27–34. <https://doi.org/10.1007/BF02668071>

Pawłowsky-Glahn, V. and Buccianti, A. (2011): *Compositional Data Analysis, Compositional Data Analysis: Theory and Applications*. Wiley. <https://doi.org/10.1002/9781119976462>

Pawłowsky-Glahn, V., Egozcue, J.J. and Tolosana-Delgado, R. (2015): *Modelling and Analysis of Compositional Data*. Wiley. <https://doi.org/10.1002/9781119003144>

Pedley, H.M. (1990): Classification and environmental models of cool freshwater tufas. *Sediment. Geol.* 68, 143–154. [https://doi.org/10.1016/0037-0738\(90\)90124-C](https://doi.org/10.1016/0037-0738(90)90124-C)

Pellegrini, C., Asioli, A., Bohacs, K.M., Drexler, T.M., Feldman, H.R., Sweet, M.L., Maselli, V., Rovere, M., Gamberi, F., Valle, G.D. and Trincardi, F. (2018): The Late Pleistocene Po River lowstand wedge in the Adriatic Sea: Controls on architecture variability and

sediment partitioning. *Mar. Pet. Geol.* 96, 16–50.
<https://doi.org/10.1016/j.marpetgeo.2018.03.002>

Pellegrini, C., Maselli, V., Gamberi, F., Asioli, A., Bohacs, K.M., Drexler, T.M. and Trincardi, F., (2017): How to make a 350-m-thick lowstand systems tract in 17,000 years: The Late Pleistocene Po River (Italy) lowstand wedge. *Geology* 45, 327–330.
<https://doi.org/10.1130/G38848.1>

Peña, J.L., Sancho, C. and Lozano, M.V. (2000): Climatic and tectonic significance of Late Pleistocene and Holocene tufa deposits in the Mijares River canyon, eastern Iberian Range, northeast Spain. *Earth Surf. Process. Landforms* 25, 1403–1417.
[https://doi.org/10.1002/1096-9837\(200012\)25:13<1403::AID-ESP147>3.0.CO;2-N](https://doi.org/10.1002/1096-9837(200012)25:13<1403::AID-ESP147>3.0.CO;2-N)

Pentecost, A. (2005): *Travertine*. Springer-Verlag, Berlin/Heidelberg.
<https://doi.org/10.1007/1-4020-3606-X>

Pentecost, A. (1995): The quaternary travertine deposits of Europe and Asia Minor. *Quat. Sci. Rev.* 14, 1005–1028. [https://doi.org/10.1016/0277-3791\(95\)00101-8](https://doi.org/10.1016/0277-3791(95)00101-8)

Perica, D., Orešić, D. and Trajbar, S. (2005): Geomorfološka obilježja doline i poriječja rijeke Krke s osvrtom na dio od Knina do Bilušića buka. *Geoadria* 10, 131–156.
<https://doi.org/10.15291/geoadria.55>

Perillo, G.M.E. (1995): *Geomorphology and Sedimentology of Estuaries*.

Perov, G. and Bhattacharya, J.P. (2011): Pleistocene shelf-margin delta: Intradeltaic deformation and sediment bypass, northern Gulf of Mexico. *Am. Assoc. Pet. Geol. Bull.* 95, 1617–1641. <https://doi.org/10.1306/01271109141>

Philippson, B. (2013): The freshwater reservoir effect in radiocarbon dating. *Herit. Sci.* 1, 24.
<https://doi.org/10.1186/2050-7445-1-24>

Pikelj, K. and Juračić, M. (2013): Eastern Adriatic Coast (EAC): Geomorphology and Coastal Vulnerability of a Karstic Coast. *J. Coast. Res.* 29, 944–957.
<https://doi.org/https://doi.org/10.2112/JCOASTRES-D-12-00136.1>

- Piva, A., Asioli, A., Schneider, R.R., Trincardi, F., Andersen, N., Colmenero-Hidalgo, E., Dennielou, B., Flores, J. and Vigliotti, L. (2008): Climatic cycles as expressed in sediments of the PROMESS1 borehole PRAD1-2, central Adriatic, for the last 370 ka: 1. Integrated stratigraphy. *Geochemistry, Geophys. Geosystems* 9.
<https://doi.org/10.1029/2007GC001713>
- Porębski, S.J. and Steel, R.J. (2003): Shelf-margin deltas: their stratigraphic significance and relation to deepwater sands. *Earth-Science Rev.* 62, 283–326.
[https://doi.org/10.1016/S0012-8252\(02\)00161-7](https://doi.org/10.1016/S0012-8252(02)00161-7)
- Posamentier, H.W. (2001): Lowstand alluvial bypass systems: Incised vs. unincised. *Am. Assoc. Pet. Geol. Bull.* 85, 1771–1793. <https://doi.org/10.1306/8626D06D-173B-11D7-8645000102C1865D>
- Posamentier, H. W. and Allen, G.P. (1999): *Siliciclastic Sequence Stratigraphy*, SEPM Society for Sedimentary Geology. SEPM (Society for Sedimentary Geology).
<https://doi.org/10.2110/csp.99.07>
- Posamentier, H.W. and Vail, P.R. (1988): Eustatic Controls on Clastic Deposition II—Sequence and Systems Tract Models. In: *Sea-Level Changes*. SEPM (Society for Sedimentary Geology), 125–154. <https://doi.org/10.2110/pec.88.01.0125>
- Postma, D. (1982): Pyrite and siderite formation in brackish and freshwater swamp sediments. *Am. J. Sci.* 282, 1151–1183. <https://doi.org/10.2475/ajs.282.8.1151>
- Prahl, F.G., Bennett, J.T. and Carpenter, R. (1980): The early diagenesis of aliphatic hydrocarbons and organic matter in sedimentary particulates from Dabob Bay, Washington. *Geochim. Cosmochim. Acta* 44, 1967–1976.
[https://doi.org/10.1016/0016-7037\(80\)90196-9](https://doi.org/10.1016/0016-7037(80)90196-9)
- Pritchard, D.W. (1989): Estuarine Classification — A Help or a Hindrance, in: Neilson, B.J., Kuo, A., Brubaker, J. (Eds.), *Estuarine Circulation*. Humana Press, Totowa, NJ, 1–38.
https://doi.org/10.1007/978-1-4612-4562-9_1

- Prohić, E. and Juračić, M. (1989): Heavy metals in sediments—problems concerning determination of the anthropogenic influence. Study in the Krka River estuary, eastern Adriatic coast, Yugoslavia. *Environ. Geol. Water Sci.* 13, 145–151.
<https://doi.org/10.1007/BF01664699>
- Prohić, E. and Kniewald, G. (1987): Heavy metal distribution in recent sediments of the Krka River Estuary — an example of sequential extraction analysis. *Mar. Chem.* 22, 279–297.
[https://doi.org/10.1016/0304-4203\(87\)90015-6](https://doi.org/10.1016/0304-4203(87)90015-6)
- Qiu, J., Liu, J., Saito, Y., Yin, P., Zhang, Y., Liu, J. and Zhou, L. (2019): Seismic morphology and infilling architecture of incised valleys in the northwest South Yellow Sea since the last glaciation. *Cont. Shelf Res.* 179, 52–65. <https://doi.org/10.1016/j.csr.2019.04.008>
- Radić Rossi, I., Karavanić, I. and Butorac, V. (2022): Croatia: Submerged Prehistoric Sites in a Karstic Landscape. In Bailey, G., Galanidou, N., Peeters, H., Jöns, H. and Mennenga, M. (eds.), *The Archaeology of Europe's Drowned Landscapes*. Springer Nature Switzerland AG, 347–369.
- Razum, I. (2018): Paleookolišni i tefrostratigrafski sedimentni zapis kasnopleistocenskih i holocenskih okoliša otoka Mljeta. Doctoral Thesis, Faculty of Science, University of Zagreb, 210.
- Razum, I., Bajo, P., Brunović, D., Ilijanić, N., Hasan, O., Röhl, U., Miko, M.Š. and Miko, S., (2021): Past climate variations recorded in needle-like aragonites correlate with organic carbon burial efficiency as revealed by lake sediments in Croatia. *Sci. Rep.* 11, 7568.
<https://doi.org/10.1038/s41598-021-87166-2>
- Razum, I., Miko, S., Ilijanić, N., Hasan, O., Šparica Miko, M., Brunović, D. and Pawlowsky-Glahn, V. (2020): A compositional approach to the reconstruction of geochemical processes involved in the evolution of Holocene marine flooded coastal karst basins (Mljet Island, Croatia). *Appl. Geochemistry* 116, 104574.
<https://doi.org/10.1016/j.apgeochem.2020.104574>
- Reimer, P.J., Austin, W.E.N., Bard, E., Bayliss, A., Blackwell, P.G., Bronk Ramsey, C., Butzin,

M., Cheng, H., Edwards, R.L., Friedrich, M., Grootes, P.M., Guilderson, T.P., Hajdas, I., Heaton, T.J., Hogg, A.G., Hughen, K.A., Kromer, B., Manning, S.W., Muscheler, R., Palmer, J.G., Pearson, C., van der Plicht, J., Reimer, R.W., Richards, D.A., Scott, E.M., Southon, J.R., Turney, C.S.M., Wacker, L., Adolphi, F., Büntgen, U., Capano, M., Fahrni, S.M., Fogtmann-Schulz, A., Friedrich, R., Köhler, P., Kudsk, S., Miyake, F., Olsen, J., Reinig, F., Sakamoto, M., Sookdeo, A. and Talamo, S. (2020): The IntCal20 Northern Hemisphere Radiocarbon Age Calibration Curve (0–55 cal kBP). *Radiocarbon* 62, 725–757. <https://doi.org/10.1017/RDC.2020.41>

Reimer, P.J. and Reimer, R.W. (2001): A Marine Reservoir Correction Database and On-Line Interface. *Radiocarbon* 43, 461–463. <https://doi.org/10.1017/S0033822200038339>

Rickard, D. and Luther, G.W. (2007): Chemistry of Iron Sulfides. *Chem. Rev.* 107, 514–562. <https://doi.org/10.1021/cr0503658>

Riedinger, N., Pfeifer, K., Kasten, S., Garming, J.F.L., Vogt, C. and Hensen, C. (2005): Diagenetic Alteration of Magnetic Signals by Anaerobic Oxidation of Methane Related to a Change in Sedimentation Rate. *Geochim. Cosmochim. Acta* 69, 4117–4126. <https://doi.org/10.1016/j.gca.2005.02.004>

Roberts, N., Jones, M.D., Benkaddour, A., Eastwood, W.J., Filippi, M.L., Frogley, M.R., Lamb, H.F., Leng, M.J., Reed, J.M., Stein, M., Stevens, L., Valero-Garcés, B. and Zanchetta, G. (2008): Stable isotope records of Late Quaternary climate and hydrology from Mediterranean lakes: the ISOMED synthesis. *Quat. Sci. Rev.* 27, 2426–2441. <https://doi.org/10.1016/j.quascirev.2008.09.005>

Röhl, U., Brinkhuis, H., Sluijs, A. and Fuller, M. (2004): On the search for the Paleocene/Eocene boundary in the Southern Ocean: Exploring ODP Leg 189 holes 1171D and 1172D, Tasman Sea. pp. 113–125. <https://doi.org/10.1029/151GM08>

Ronchi, L., Fontana, A., Correggiari, A. and Asioli, A. (2018): Late Quaternary incised and infilled landforms in the shelf of the northern Adriatic Sea (Italy). *Mar. Geol.* 405, 47–67. <https://doi.org/10.1016/j.margeo.2018.08.004>

- Rovere, A., Raymo, M.E., Vacchi, M., Lorscheid, T., Stocchi, P., Gómez-Pujol, L., Harris, D.L., Casella, E., O'Leary, M.J. and Hearty, P.J. (2016a): The analysis of Last Interglacial (MIS 5e) relative sea-level indicators: Reconstructing sea-level in a warmer world. *Earth-Science Rev.* 159, 404–427. <https://doi.org/10.1016/j.earscirev.2016.06.006>
- Rovere, A., Stocchi, P. and Vacchi, M. (2016b): Eustatic and Relative Sea Level Changes. *Curr. Clim. Chang. Reports* 2, 221–231. <https://doi.org/10.1007/s40641-016-0045-7>
- Roychoudhury, A.N. (2007): Spatial and seasonal variations in depth profile of trace metals in saltmarsh sediments from Sapelo Island, Georgia, USA. *Estuar. Coast. Shelf Sci.* 72, 675–689. <https://doi.org/10.1016/j.ecss.2006.12.003>
- Schmidt, R., Müller, J., Drescher-Schneider, R., Krisai, R., Szeroczyńska, K. and Barić, A. (2000): Changes in lake level and trophy at Lake Vrana, a large karstic lake on the Island of Cres (Croatia), with respect to palaeoclimate and anthropogenic impacts during the last approx. 16,000 years. *J. Limnol.* 59, 113. <https://doi.org/10.4081/jlimnol.2000.113>
- Schock, S.G., Leblanc, L.R and Mayer, L.A. (1989): Chirp subbottom profiler for quantitative sediment analysis. *Geophysics* 54, 445–450. <https://doi.org/10.1190/1.1442670>
- Scott, D.B., Medioli, F.S. and Schafer, C.T. (2001): *Monitoring in Coastal Environments Using Foraminifera and Thecamoebian Indicators*. Cambridge University Press. <https://doi.org/10.1017/CBO9780511546020>
- Seyler, P. and Martin, J.M. (1991): Arsenic and selenium in a pristine river-estuarine system: the Krka (Yugoslavia). *Mar. Chem.* [https://doi.org/10.1016/0304-4203\(91\)90018-R](https://doi.org/10.1016/0304-4203(91)90018-R)
- Shackleton, N.J., Sánchez-Goñi, M.F., Paillet, D. and Lancelot, Y. (2003): Marine Isotope Substage 5e and the Eemian Interglacial. *Glob. Planet. Change* 36, 151–155. [https://doi.org/10.1016/S0921-8181\(02\)00181-9](https://doi.org/10.1016/S0921-8181(02)00181-9)
- Siddall, M., Rohling, E.J., Almogi-Labin, A., Hemleben, C., Meischner, D., Schmelzer, I. and Smeed, D.A. (2003): Sea-level fluctuations during the last glacial cycle. *Nature* 423, 853–858. <https://doi.org/10.1038/nature01690>

- Siveter, David J, Siveter, Derek J, Sutton, M.D. and Briggs, D.E. (2007): Brood care in a Silurian ostracod. *Proc. R. Soc. B Biol. Sci.* 274, 465–469.
<https://doi.org/10.1098/rspb.2006.3756>
- Smrkulj, N., Hasan, O., Brunović, D., Miko, S. and Ilijanić, N. (2024): Holocene palaeoenvironmental development of Prokljan Lake (Krka River, Croatia): Evolution from a calcareous tufa barrier system to a karst estuary. *Mar. Geol.* 476, 107370.
<https://doi.org/10.1016/j.margeo.2024.107370>
- Sondi, I., Juračić, M. and Pravdić, V. (1995): Sedimentation in a disequilibrium river-dominated estuary: the Rasa River Estuary (Adriatic Sea, Croatia). *Sedimentology* 42, 769–782. <https://doi.org/10.1111/j.1365-3091.1995.tb00408.x>
- Sperazza, M., Moore, J.N. and Hendrix, M.S. (2004): High-Resolution Particle Size Analysis of Naturally Occurring Very Fine-Grained Sediment Through Laser Diffractometry. *J. Sediment. Res.* 74, 736–743. <https://doi.org/10.1306/031104740736>
- St-Onge, G., Mulder, T., Francus, P. and Long, B. (2007): Chapter Two Continuous Physical Properties of Cored Marine Sediments. pp. 63–98. [https://doi.org/10.1016/S1572-5480\(07\)01007-X](https://doi.org/10.1016/S1572-5480(07)01007-X)
- Surić, M. (2002): Submarine Karst of Croatia - Evidence of Former Lower Sea Levels. *Acta Carsologica* 31. <https://doi.org/10.3986/ac.v31i3.381>
- Surić, M. and Juračić, M. (2010): Late pleistocene-holocene environmental changes - Records from submerged speleothems along the Eastern Adriatic coast (Croatia). *Geol. Croat.* <https://doi.org/10.4154/gc.2010.13>
- Surić, M., Juračić, M., Horvatinčić, N. and Krajcar Bronić, I. (2005): Late Pleistocene-Holocene sea-level rise and the pattern of coastal karst inundation: Records from submerged speleothems along the Eastern Adriatic Coast (Croatia). *Mar. Geol.*
<https://doi.org/10.1016/j.margeo.2004.10.030>
- Surić, M., Korbar, T. and Juračić, M. (2014): Tectonic constraints on the late Pleistocene-

- Holocene relative sea-level change along the north-eastern Adriatic coast (Croatia). *Geomorphology* 220, 93–103. <https://doi.org/10.1016/j.geomorph.2014.06.001>
- Svensen, C., Viličić, D., Wassmann, P., Arashkevich, E. and Ratkova, T. (2007): Plankton distribution and vertical flux of biogenic matter during high summer stratification in the Krka estuary (Eastern Adriatic). *Estuar. Coast. Shelf Sci.* 71, 381–390. <https://doi.org/10.1016/j.ecss.2006.07.022>
- Šegota, T. and Filipčić, A. (1991): Arheološki i geološki pokazatelji holocenskog položaja razine mora na istočnoj obali Jadranskog mora. *Rad Jugoslavenske Akad. Znan. i Umjet. Razred za Prir. Znan.* 25, 149–172
- Šolaja, D., Miko, S., Brunović, D., Ilijanić, N., Hasan, O., Papatheodorou, G., Geraga, M., Durn, T., Christodoulou, D. and Razum, I. (2022): Late Quaternary Evolution of a Submerged Karst Basin Influenced by Active Tectonics (Koločep Bay, Croatia). *J. Mar. Sci. Eng.* 10, 881. <https://doi.org/10.3390/jmse10070881>
- Tesson, M., Posamentier, H. W. and Gensous, B. (2000): Stratigraphic Organization of Late Pleistocene Deposits of the Western Part of the Golfe du Lion Shelf (Languedoc Shelf), Western Mediterranean Sea, Using High-Resolution Seismic and Core Data1. *Am. Assoc. Pet. Geol. Bull.* 84. <https://doi.org/10.1306/C9EBCD83-1735-11D7-8645000102C1865D>
- Thompson, R. and Oldfield, F. (1986): *Environmental Magnetism*. Springer Netherlands, Dordrecht. <https://doi.org/10.1007/978-94-011-8036-8>
- Tjallingii, R. (2007): Application and quality of X-Ray Fluorescence core scanning in reconstructing late Pleistocene NW African continental margin sedimentation patterns and paleoclimate variations. Doctoral Thesis, University of Bremen, 114.
- Tribovillard, N., Algeo, T.J., Lyons, T. and Riboulleau, A. (2006): Trace metals as paleoredox and paleoproductivity proxies: An update. *Chem. Geol.* 232, 12–32. <https://doi.org/10.1016/j.chemgeo.2006.02.012>

- Trincardi, F. and Field, M.E. (1991): Geometry, Lateral Variation, and Preservation of Downlapping Regressive Shelf Deposits: Eastern Tyrrhenian Sea Margin, Italy. *SEPM J. Sediment. Res.* Vol. 61. <https://doi.org/10.1306/D42677D0-2B26-11D7-8648000102C1865D>
- Trincardi, F., Correggiari, A. and Roveri, M. (1994): Late Quaternary transgressive erosion and deposition in a modern epicontinental shelf: The Adriatic semienclosed basin. *Geo-Marine Lett.* 14, 41–51. <https://doi.org/10.1007/BF01204470>
- Trobec, A., Šmuc, A., Poglajen, S. and Vrabec, M. (2017): Submerged and buried Pleistocene river channels in the Gulf of Trieste (Northern Adriatic Sea): Geomorphic, stratigraphic and tectonic inferences. *Geomorphology* 286, 110–120. <https://doi.org/10.1016/j.geomorph.2017.03.012>
- Ulm, S. (2002): Marine and estuarine reservoir effects in central Queensland, Australia: Determination of ΔR values. *Geoarchaeology* 17, 319–348. <https://doi.org/10.1002/gea.10017>
- Vaniček, V. (2013): Pleistocenske taložine u hrvatskom dijelu podmorja Jadrana. Doctoral Thesis, Faculty of Science, University of Zagreb, 219.
- Viličić, D., Legović, T. and Žutić, V. (1989): Vertical distribution of phytoplankton in a stratified estuary. *Aquat. Sci.* 51, 31–46. <https://doi.org/10.1007/BF00877779>
- Vizzini, S., Savona, B., Chi, T. D. and Mazzola, A. (2005): Spatial variability of stable carbon and nitrogen isotope ratios in a Mediterranean coastal lagoon. *Hydrobiologia* 550, 73–82. <https://doi.org/10.1007/s10750-005-4364-2>
- Vlahović, I., Tišljarić, J., Velić, I. and Matičec, D. (2005): Evolution of the Adriatic Carbonate Platform: Palaeogeography, main events and depositional dynamics. *Palaeogeogr. Palaeoclimatol. Palaeoecol.* 220, 333–360. <https://doi.org/10.1016/j.palaeo.2005.01.011>
- Volpi, V., Forlin, F., Donda, F., Civile, D., Facchin, L., Sauli, S., Merson, B., Sinza-Mendieta, K.

- and Shams, A. (2015): Southern Adriatic Sea as a Potential Area for CO₂ Geological Storage. *Oil Gas Sci. Technol. – Rev. d'IFP Energies Nouv.* 70, 713–728.
<https://doi.org/10.2516/ogst/2014039>
- Vreca, P. and Dolenc, T. (2005): Geochemical estimation of copper contamination in the healing mud from Makirina Bay, central Adriatic. *Environ. Int.* 31, 53–61.
<https://doi.org/10.1016/j.envint.2004.06.009>
- Waelbroeck, C., Labeyrie, L., Michel, E., Duplessy, J.C., McManus, J.F., Lambeck, K., Balbon, E. and Labracherie, M. (2002): Sea-level and deep water temperature changes derived from benthic foraminifera isotopic records. *Quat. Sci. Rev.* 21, 295–305.
[https://doi.org/10.1016/S0277-3791\(01\)00101-9](https://doi.org/10.1016/S0277-3791(01)00101-9)
- Wagner, B., Lotter, A.F., Nowaczyk, N., Reed, J.M., Schwalb, A., Sulpizio, R., Valsecchi, V., Wessels, M. and Zanchetta, G. (2009): A 40,000-year record of environmental change from ancient Lake Ohrid (Albania and Macedonia). *J. Paleolimnol.* 41, 407–430.
<https://doi.org/10.1007/s10933-008-9234-2>
- Wagoner, J.C. Van, Mitchum, R.M., Campion, K.M. and Rahmanian, V.D. (1990): Siliciclastic Sequence Stratigraphy in Well Logs, Cores, and Outcrops. American Association of Petroleum Geologists. <https://doi.org/10.1306/Mth7510>
- Walker, M. (2005): *Quaternary Dating Methods*. J. Wiley & Son, 304.
- Walton, A. (1967): Radioactive Dating and Methods of Low-level Counting. *Antiquity* 41, 317–318. <https://doi.org/10.1017/S0003598X00102510>
- Wang, R. (2020): Quantitative analysis of geological controls on incised- valley-fill geometry and stratigraphic architecture. Doctoral Thesis, The University of Leeds, 249.
- Wang, R., Colombera, L. and Mountney, N.P. (2020): Quantitative analysis of the stratigraphic architecture of incised-valley fills: A global comparison of Quaternary systems. *Earth-Science Rev.* 200, 102988.
<https://doi.org/10.1016/j.earscirev.2019.102988>

- Wang, X., Feng, H. and Ma, H. (2007): Assessment of Metal Contamination in Surface Sediments of Jiaozhou Bay, Qingdao, China. *CLEAN – Soil, Air, Water* 35, 62–70. <https://doi.org/10.1002/clen.200600022>
- Weiss, D., Shotyk, W., Appleby, P.G., Kramers, J.D. and Cheburkin, A.K. (1999): Atmospheric Pb Deposition since the Industrial Revolution Recorded by Five Swiss Peat Profiles: Enrichment Factors, Fluxes, Isotopic Composition, and Sources. *Environ. Sci. Technol.* 33, 1340–1352. <https://doi.org/10.1021/es980882q>
- Wolf, A.B. (2011): Determining Whether Spectrophotometer CIE L*a*b* Color Analysis is an Effective Alternative to Munsell Soil Color Charts for the Study of Burnt Bones: Insights From Analysis of Bab edh-Dhra EB II-III Burnt Bones. Oberlin College.
- Wu, Z., Yang, F. and Tang, Y. (2021): High-resolution Seafloor Survey and Applications, High-resolution Seafloor Survey and Applications. Springer Singapore, Singapore. <https://doi.org/10.1007/978-981-15-9750-3>
- Wunsam, S., Schmidt, R. and Müller, J. (1999): Holocene lake development of two Dalmatian lagoons (Malo and Veliko Jezero, Isle of Mljet) in respect to changes in Adriatic sea level and climate. *Palaeogeogr. Palaeoclimatol. Palaeoecol.* 146, 251–281. [https://doi.org/10.1016/S0031-0182\(98\)00147-3](https://doi.org/10.1016/S0031-0182(98)00147-3)
- Xu, G. and Haq, B.U. (2022): Seismic facies analysis: Past, present and future. *Earth-Science Rev.* 224, 103876. <https://doi.org/10.1016/j.earscirev.2021.103876>
- Zaitlin, B.A., Dalrymple, R.W. and Boyd, R. (1994): The Stratigraphic Organization of Incised-Valley Systems Associated with Relative Sea-Level Change, in: *Incised-Valley Systems: Origin and Sedimentary Sequences*. SEPM Society for Sedimentary Geology. <https://doi.org/10.2110/pec.94.12.0045>
- Zanchetta, G., Borghini, A., Fallick, A.E., Bonadonna, F.P. and Leone, G. (2007): Late Quaternary palaeohydrology of Lake Pergusa (Sicily, southern Italy) as inferred by stable isotopes of lacustrine carbonates. *J. Paleolimnol.* 38, 227–239. <https://doi.org/10.1007/s10933-006-9070-1>

Zaninović, K. (2006): Climate and bioclimate of national park Krka. In: Nacionalni park Krka - prirodoslovni vodič, Marguš, D. (Ed.), 37–44.

Zhi, H., Siwabessy, J., Nichol, S.L. and Brooke, B.P. (2014): Predictive mapping of seabed substrata using high-resolution multibeam sonar data: A case study from a shelf with complex geomorphology. *Mar. Geol.* 357, 37–52.
<https://doi.org/10.1016/j.margeo.2014.07.012>

Zhornyak, L.V., Zanchetta, G., Drysdale, R.N., Hellstrom, J.C., Isola, I., Regattieri, E., Piccini, L., Baneschi, I. and Couchoud, I. (2011): Stratigraphic evidence for a “pluvial phase” between ca 8200–7100 ka from Renella cave (Central Italy). *Quat. Sci. Rev.* 30, 409–417. <https://doi.org/10.1016/j.quascirev.2010.12.003>

Žutić, V. and Legović, T. (1987): A film of organic matter at the fresh-water/sea-water interface of an estuary. *Nature* 328, 612–614. <https://doi.org/10.1038/328612a0>

10. APPENDICES

Appendix 1

Results of laboratory analyses on grab samples from the Krka River estuary- EXCEL table, CD.

Appendix 2

Results of laboratory analyses on sediment core PROK-1- EXCEL table, CD.

Appendix 3

Results of laboratory analyses on sediment core PROK-2- EXCEL table, CD.

Appendix 4

Results of laboratory analyses on sediment core PROK-3- EXCEL table, CD.

Appendix 5

Results of laboratory analyses on sediment core PROK-4- EXCEL table, CD.

Appendix 6

Results of laboratory analyses on sediment cores ZLA-1 and ZLA-2- EXCEL table, CD.

Plate 1

Plate 2

PLATE 1

A *Ammonia tepida* (Cushman), umbilical view (240x)

B *Ammonia tepida* (Cushman), spiral view (240x)

C *Nonionella turgida* (Williamson, 1858) (300x)

D *Elphidium crispum* (Linnaeus, 1758) (78x)

E *Elphidium macellum* (Fichtel & Moll) (110x)

F *Porosonion subgranosum* (d'Orbigny, 1846) (240x)

G *Haynesina depressula* (Walker & Jacob) (440x)

H *Ammonia beccarii* (Linné, 1758), spiral view (130x)

I *Ammonia beccarii* (Linné, 1758), umbilical view (200x)

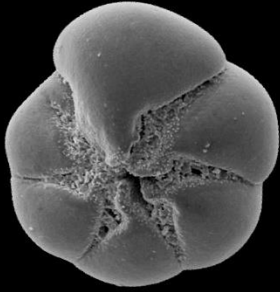
J *Haynesina germanica* (Ehrenberg, 1840) (540x)

K *Textularia bocki* Höglund, 1947 (200x)

L *Miliolinella subrotunda* (Montagu, 1803) (860x)

PLATE 1

A



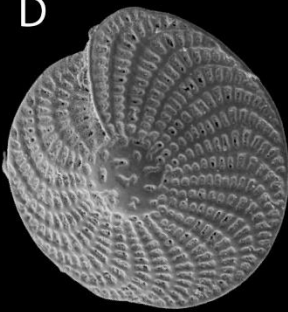
B



C



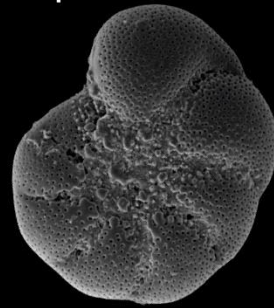
D



E



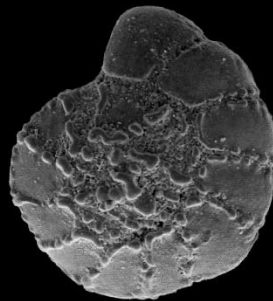
F



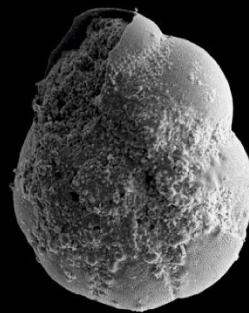
G



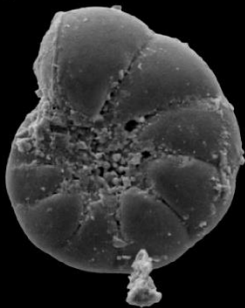
H



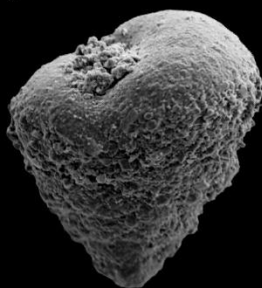
I



J



K



L

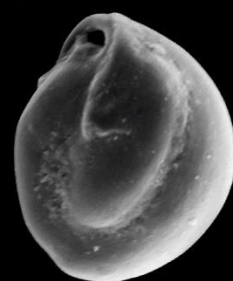


PLATE 2

A *Rectuvigerina elongatastriata* (Colom, 1952) (200x);

B *Bulimina aculeata* d'Orbigny, 1826, posterior side (600x);

C *Bulimina aculeata* d'Orbigny, 1826 (360x);

D *Elphidium translucens* Natland, 1938 (240x);

E *Siphonaperta aspera* (d'Orbigny, 1826) (320x);

F *Pyrgo* sp. DeFrance, 1824 (130x);

G *Pyrgo elongata* (d'Orbigny, 1826), aperture detail (320x);

H *Triloculina adriatica* Le Calvez & Le Calvez, 1958 (180x);

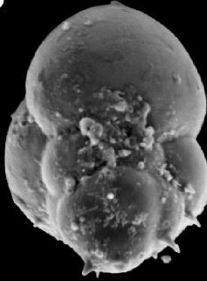
I *Triloculina adriatica* Le Calvez & Le Calvez, 1958, aperture detail (320x)

PLATE 2

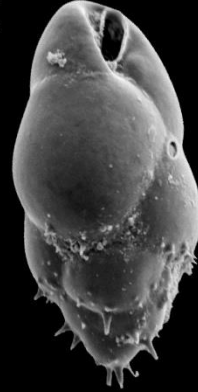
A



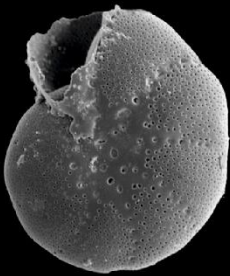
B



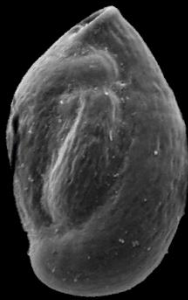
C



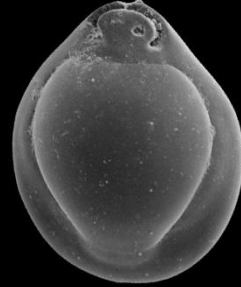
D



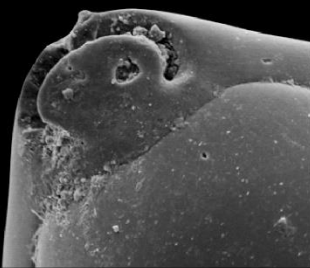
E



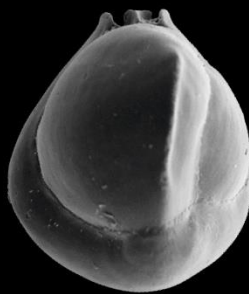
F



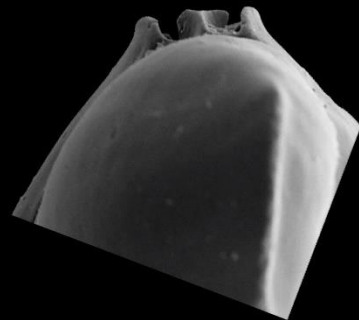
G



H



I



11. CURRICULUM VITAE

Natalia Smrkulj (Šenolt) was born on August 4, 1994, in Bjelovar, Croatia. She completed her elementary education at "Mato Lovrak" in Veliki Grđevac and attended the Grammar School in Bjelovar. In 2018, she earned her master's degree from the Department of Geology at the Faculty of Science, University of Zagreb. Since 2020, she has been working at the Department for Mineral Resources and Marine Geology (Croatian Geological Survey) as an assistant. In 2020, she enrolled in the Doctoral Study of Geology at the Faculty of Science, University of Zagreb. During her career, she has been a collaborator on the project „Sediments between source and sink during a Late Quaternary eustatic cycle: The Krka river and the Mid Adriatic Deep System“ (QMAD) funded by the Croatian Science Foundation (2020-2024), where she works as a doctoral candidate, and has also participated in the PALEOMAD project (DAAD).

During her doctoral study, she spent time at the University of Innsbruck at the Austrian Core Facility, where she conducted geochemical analyses on sediment cores using a μ XRF core scanner. She performed the interpretation of seismic data at the University of Patras (OCEANUS-lab) under the supervision of Prof. George Papatheodorou and his team of scientists.

She has published two scientific papers as the author and corresponding author in the CC database, with third paper currently under submission in Catena. Additionally, she has presented at over ten international and domestic scientific conferences as both author and co-author.

Published scientific papers:

Original scientific papers (CC base):

Hasan, O., Smrkulj, N., Miko, S., Brunović, D., Ilijanić, N. and Šparica Miko, M. (2023): Integrated Reconstruction of Late Quaternary Geomorphology and Sediment Dynamics of Prokljan Lake and Krka River Estuary, Croatia. // Remote sensing, 15 (10), <https://doi.org/10.3390/rs15102588>, 2588 doi:10.3390/rs15102588.

Smrkulj, N., Hasan, O., Brunović, D., Miko, S. and Ilijanić, N. (2024): Holocene palaeoenvironmental development of Prokljan Lake (Krka River, Croatia): Evolution from a calcareous tufa barrier system to a karst estuary. // *Marine Geology*, 476, <https://doi.org/10.1016/j.margeo.2024.107370>.

Published abstracts:

Smrkulj, N., Hasan, O., Brunović, D., Miko, S., Huang, J-J. S., Ilijanić, N., Ortler, M., Šparica Miko, M. and Hus, P. (2023): NEW MULTI-PROXY EVIDENCE OF HOLOCENE ENVIRONMENTAL AND HYDROLOGIC CHANGES FROM SEDIMENTARY INFILL OF PROKLJAN LAKE (KRKA RIVER, CROATIA). // 7. hrvatski geološki kongres, Poreč, Croatia.

Miko, S., Hasan, O., Ilijanić, N., Karavanić, I., Razum, I., Brunović, D. and Smrkulj, N. (2023): RECONSTRUCTION OF THE PLEISTOCENE AND HOLOCENE SUBMERGED PALEOENVIRONMENTS OF THE JADRO RIVER (CENTRAL DALMATIA, CROATIA).// 7. hrvatski geološki kongres, Poreč, Croatia.

Hasan, O., Miko, S., Brunović, D., Ilijanić, N., Ivkić-Filipović, I. and Smrkulj, N. (2023): GEOLOGICAL MAPPING OF THE CROATIAN ADRIATIC SEAFLOOR WITHIN THE FRAME OF EMODNET GEOLOGY INITIATIVE.// 7. hrvatski geološki kongres, Poreč, Croatia.

Smrkulj, N., Hasan, O., Miko, S., Brunović, D., Ilijanić, N., Papatheodorou, G., Geraga, M. and Christodolou, D. (2023): Reconstruction of former landscapes and Late Quaternary sea-level changes in the Krka River mouth area. // XXI Congress of the International Union for Quaternary Research (INQUA) „Time for change“, Rim, Italy.

Hasan, O., Smrkulj, N., Brunović, D., Geraga, M., Christodoulou, D., Ilijanić, N. and Miko, S. (2023): Submarine terraced landforms and paleoshorelines of the Dalmatian islands in the Eastern Adriatic Coast, Croatia. // XXI Congress of the International Union for Quaternary Research (INQUA) „Time for change“, Rim, Italy.

Hus, P., Brunović, D., Smrkulj, N., Ilijanić, N. and Miko, S. (2023): Benthic foraminifera reveal the Holocene palaeoenvironments and sea transgression in the Krka River estuary (Adriatic Sea, Croatia). // The Micropalaeontological Society Annual Conference, Southampton, United Kingdom.

- Hus, P., Brunović, D., Smrkulj, N., Ilijanić, N. and Miko, S. (2023): What Happens in the Past, Stays in the Past (or not)? // SymbioSE-27th Symposium of Biology Students in Europe, Korper, Slovenia.
- Hus, P., Brunović, D., Smrkulj, N., Ilijanić, N. and Miko, S. (2022): Benthic foraminifera as proxies of the Holocene paleoenvironmental changes in the Krka River estuary (Adriatic Sea, Croatia). // The Micropalaeontological Society Annual Conference, Bremen, Germany.
- Šenolt, N., Hasan, O., Miko, S., Brunović, D. and Ilijanić, N. (2022): Submerged karst landscape of the Prokljan Lake (Krka River estuary in the central Dalmatia). // 10th IAG International Conference on Geomorphology, Coimbra, Portugal.
- Šenolt, N., Miko, S., Hasan, O., Brunović, D., Ilijanić, N. and Šparica Miko, M. (2022): Holocene paleoenvironmental reconstruction of a karst Krka River estuary (Eastern Adriatic coast). // International Conference on Seafloor Landforms, Processes and Evolution, Valletta, Malta.
- Hasan, O., Smrkulj, N., Brunović, D., Geraga, M., Christodoulou, D., Ilijanić, N. and Miko, S. (2022): Submerged marine terraces and paleo shorelines along the eastern rim of the Mid Adriatic Deep. // International Conference on Seafloor Forms, Processes and Evolution, Valletta, Malta.
- Šenolt, N., Miko, S., Hasan, O., Brunović, D. and Ilijanić, N. (2022): Holocene evolution of the Krka River estuary. // PhD Student Symposium 2022. Zagreb, Faculty of Science, University of Zagreb, Zagreb, Croatia.
- Šenolt, N., Miko, S., Hasan, O., Brunović, D., Ilijanić, N. and Šparica Miko, M. (2021): Late Quaternary geomorphological evolution of the Prokljan Lake on the Eastern Adriatic coast (Dalmatia). // SHINE Sparking light once again over landscapes overshadowed by time, online.
- Šenolt, N., Miko, S., Hasan, O., Brunović, D., Ilijanić, N. and Šparica Miko, M. (2021): Late Quaternary seabed geomorphology of the Prokljan Lake (Krka River estuary). // 6 Regional Scientific Meeting on Quaternary Geology Seas, Lakes and Rivers, Ljubljana, Slovenia.
- Šenolt, N., Miko, S., Hasan, O., Brunović, D., Šparica Miko, M., Ilijanić, N. and Papatheodorou, G. (2021): Submerged landscape of the Prokljan Lake. // PhD Student Symposium 2021. Zagreb, Faculty of Science, University of Zagreb, Zagreb, Croatia.

- Hasan, O., Miko, S., Brunović, D., Šenolt, N., Šparica Miko, M. and Ilijanić, N. (2021): Seabed geomorphology of the Prokljan Lake – a Krka River estuary on the eastern Adriatic coast (Dalmatia). // European Geosciences Union General Assembly (EGU 2021), online. doi:10.5194/egusphere-egu21-11320.
- Miko, S., Bajo, P., akrač, K., Brunović, D., Christodoulou, D., Durn, T., Geraga, M., Hajek-Tadesse, V., Hasan, O., Hruševar, D., Ilijanić, N., Karavanić, I., Mesić, S., Mitić, B., Papatheodorou, G., Petrinec, B., Prohaska, A., Radić Rossi, I., Razum, I., Schulz, H., Šenolt, N., Šparica Miko, M. and Willerslev, E. (2021): Submerged landscapes of the eastern Adriatic – from the river across the lake all the way to the sea. // European Geosciences Union General Assembly (EGU 2021), online. doi:10.5194/egusphere-egu21-12177.
- Ilijanić, N., Miko, S., Hasan, O., Brunović, D., Šparica Miko, M., Sladović, Ž., Ivkić Filipović, I., Šenolt, N. and Goreta, G. (2021): Geomorphology of the lakebed and sediment deposition during the Holocene in Lake Visovac. // European Geosciences Union General Assembly (EGU 2021), online. doi:10.5194/egusphere-egu21-15787.